MODELING AND APPLICATION OF SOIL MOISTURE AT VARYING SPATIAL SCALES WITH PARAMETER SCALING

A Dissertation

by

NARENDRA NARAYAN DAS

Submitted to the Office of Graduate Studies of
Texas A&M University
in partial fulfillment of the requirements for the degree of

DOCTOR OF PHILOSOPHY

August 2008

Major Subject: Biological and Agricultural Engineering

MODELING AND APPLICATION OF SOIL MOISTURE AT VARYING SPATIAL SCALES WITH PARAMETER SCALING

A Dissertation

by

NARENDRA NARAYAN DAS

Submitted to the Office of Graduate Studies of
Texas A&M University
in partial fulfillment of the requirements for the degree of

DOCTOR OF PHILOSOPHY

Approved by:

Chair of Committee,	Binayak P. Mohanty
Committee Members,	Yalchin Efendiev
	Robert D. Hetland
	Vijay P. Singh
Head of Department,	Gerald Riskowski

August 2008

Major Subject: Biological and Agricultural Engineering

ABSTRACT

Modeling and Application of Soil Moisture at Varying Spatial Scales with Parameter Scaling. (August 2008)

Narendra Narayan Das, B.En., National Institute of Technology, Raipur, India;

M.S., Texas A&M University

Chair of Advisory Committee: Dr. Binayak P. Mohanty

The dissertation focuses on characterization of subpixel variability within a satellite-based remotely sensed coarse-scale soil moisture footprint. The underlying heterogeneity of coarse-scale soil moisture footprint is masked by the area-integrated properties within the sensor footprint. Therefore, the soil moisture values derived from these measurements are an area average. The variability in soil moisture within the footprint is introduced by inherent spatial variability present in rainfall, and geophysical parameters (vegetation, topography, and soil). The geophysical parameters/variables typically interact in a complex fashion to make soil moisture evolution and dependent processes highly variable, and also, introduce nonlinearity across spatio-temporal scales. To study the variability and scaling characteristics of soil moisture, a quasi-distributed Soil-Vegetation-Atmosphere-Transfer (SVAT) modeling framework is developed to simulate the hydrological dynamics, i.e., the fluxes and the state variables within the satellite-based soil moisture footprint. The modeling framework is successfully tested and implemented in different hydroclimatic regions during the research. New multiscale

data assimilation and Markov Chain Monte Carlo (MCMC) techniques in conjunction with the SVAT modeling framework are developed to quantify subpixel variability and assess multiscale soil moisture fields within the coarse-scale satellite footprint. Reasonable results demonstrate the potential to use these techniques to validate multiscale soil moisture data from future satellite mission e.g., Soil Moisture Active Passive (SMAP) mission of NASA. The results also highlight the physical controls of geophysical parameters on the soil moisture fields for various hydroclimatic regions.

New algorithm that uses SVAT modeling framework is also proposed and its application demonstrated, to derive the stochastic soil hydraulic properties (i.e., saturated hydraulic conductivity) and surface features (i.e., surface roughness and volume scattering) related to radar remote sensing of soil moisture.

DEDICATION

To my late father Shri Basant Kumar Das and my late father-in-law Shri Jivan Krishna Kanungo

ACKNOWLEDGEMENTS

First of all, I would like to thank my late father and my mother, whose love, support and inspiration gave me the mental strength and endurance to pursue higher studies and brought me to this juncture of my life. Special heartfelt thanks go to my wife, Subhashri, for her many sacrifices, constant support and contribution during my every endeavor. I would like to take this opportunity to extend my sincere thanks to my late father-in-law, my sisters, and all my friends for their motivation and support. I would like to thank Mr. P. K. Chakravorty, former Executive Director Finance of Bhilai Steel Plant, India, for giving me unstinted support during my planning phase to go for higher studies.

Gratitude also goes to my academic advisor and mentor, Dr. Binayak Mohanty, who offered tremendous help and support in every aspect. As my guide, he offered ideas and timely suggestions for my research work. In addition to continued funding, Dr. Binayak P. Mohanty always gave me ample space and liberty to conduct my research. I would also like to thank Dr. Vijay P. Singh, Dr. Yalchin Efendiev, and Dr. Robert D. Hetland for their guidance and support during my research work. I also want to extend my gratitude to Dr. Eni Njoku for introducing me to the concept and applications of microwave remote sensing of soil moisture and providing me the opportunity to visit and work in the Jet Propulsion Lab for two months. My special thanks to Dr. Amor V. M. Ines for helping me in my research and providing me with valuable input and suggestions.

Very special thanks go to my brother-in-law, Saurajit Kanungo, and his wife, Savita Kanungo, who provided encouragement and support to my family during my stay in College Station. Devdeep, Nitin, Raghu, Deb, Bikram, Surajit, Champa, Dipankar and Bhavna often provided helpful advice and moral support, and they were good company during my stay in College Station.

I wish to thank and acknowledge the support of NSIDC, USDA, NOAA, and NASA for the valuable dataset for my research. I also acknowledge the support of NSF (CMG/DMS) grant 0621113, NASA-JPL, and NASA-THP grants for my research.

Last, but definitely not the least, I would like to extend my special thanks and love to my daughter, Anjali, for her love and support.

TABLE OF CONTENTS

CHAPTER Page

LIST OF FIGURES

Page

Page

Page

Page

Page

Page

Page

LIST OF TABLES

Page

CHAPTER I

GENERAL INTRODUCTION

Soil moisture is a small proportion (only 0.15%) of freshwater on the Earth [*Dingman*, 1994]. Even with this small proportion, it is a key variable that links the water-, energy-, and carbon-cycle. Soil moisture plays a fundamental role in partitioning of incoming solar energy into latent heat and sensible heat fluxes, and precipitation into runoff and infiltration. Soil moisture is also critical for evapotranspiration process. In boreal latitudes, the switching on and off of land-atmosphere carbon exchange is influenced by the freeze/thaw of soil moisture. Long term soil moisture storage changes have been identified as a good indicator of climate change. Over the past decade, numerous studies have also recognized the importance of soil moisture in numerical weather prediction at regional- and continental-scale. Soil moisture also influences a variety of processes related to plant growth, thereby, affecting ecological patterns and agricultural production.

Hydrologic processes depending on soil moisture, such as infiltration, evapotranspiration, and runoff, occur at spatial scales on the order of 1 ~ 1000 m. Physical processes involving soil moisture that affect land-atmosphere interaction in a weather and climate dynamics take place at scales ranging from 10 ~ 100 km. This broad range of scales over which soil moisture information is needed poses a serious

---

This dissertation follows the style of *Water Resources Research.*

challenge. Therefore, it is important to develop techniques for accurate measurement/assessment of soil moisture at different spatial and temporal scales to understand the hydrological and meteorological processes that are the integral components of the water-, energy-, and carbon-cycle. The measurement of soil moisture is also crucial for various water resource management strategies (e.g., flood control and mitigation, and irrigation scheduling), and weather forecast.

In-situ (point-scale) measurements have historically been used to characterize soil moisture for the purpose of hydrologic modeling at field- to watershed-scale. Although in-situ measurements are reasonably accurate with very small support, they do not provide adequate information in terms of spatial continuity and spatial support required for regional- to continental-scale soil moisture dynamics. Maintaining an expensive high density *in-situ* network for soil moisture measurement at continental- and global-scale is almost impossible. The trade-off is to deploy satellite-based remote sensing instruments e.g., Advanced Microwave Scanning Radiometer (AMSR-E) [*Njoku, et al.*, 2003], to obtain coarse spatial scale continuous measurements with certain level of uncertainty against fairly accurate *in-situ* measurements. This makes satellite-based measurements suitable for initial/boundary condition in large scale environmental, crop, and climate model. The satellite-based remote sensor measures area-integrated properties within the sensor footprint and the soil moisture derived from these measurements are an area average, resulting in loss of underlying detail. Ground-based investigations have shown that a significant amount of variability exists within the remote sensing footprint [*Famiglietti, et al.*, 1999; *Mohanty, et al.*, 2000b]. The variability in soil moisture within

satellite-based footprint is introduced by inherent variability in rainfall, and geophysical parameters (vegetation, topography, and soil). The extent and support of satellite-based measurements have a complex spatial scale effect also. This is due to the geophysical parameters/variables (soil, topography, rainfall, and vegetation) that typically interact in a complex fashion to make soil moisture evolution and dependent processes highly variable, and introduce nonlinearity across spatio-temporal scales [*Western, et al.*, 2002]. Even with the evolution of numerous airborne- and satellite-based sensors, resulting in improvement of support, spacing, and extent of soil moisture measurements, many scale issues in soil moisture still remain unresolved.

Scale issues in soil moisture cause challenges for researchers on several fronts. The dissertation focuses on resolving questions that often arise regarding soil moisture scaling issues: How to deal and quantify subgrid-scale variability in soil moisture within a remote sensing footprint? How can remotely sensed or assimilated coarse scale soil moisture fields be downscaled for input to small scale modeling or hydrologic applications? How can remotely sensed soil moisture measurements be optimally combined with model predictions to initialize and validate coupled land-atmosphere models? Few algorithms and techniques to better understand these questions of scale-dependency and space-time dynamics of soil moisture variability within a remote sensing footprint are addressed in Chapters II-IV of this dissertation. Chapters V and VI are applications of soil moisture modeling at various scales to estimate the soil physical properties and characterize the radar backscattering used for soil moisture remote sensing, respectively.

In Chapter II, the spatio-temporal evolution of root zone soil moisture of the Walnut Gulch Experimental Watershed (WGEW) in Arizona is investigated during the Soil Moisture Experiment 2004 (SMEX04). Root zone soil moisture is estimated via assimilation of aircraft-based remotely sensed surface soil moisture into a distributed Soil-Vegetation-Atmosphere-Transfer (SVAT) model. The study also provided an opportunity to develop and test the quasi-distributed SVAT framework. An ensemble square root filter (EnSRF) based on a Kalman filtering scheme is used for assimilating the aircraft-based soil moisture observations at a spatial resolution of 800 m X 800 m. Model predictions are presented in terms of temporal evolution of soil moisture probability density function at various depths across the WGEW.

In Chapter III, a MCMC-based algorithm is developed to derive upscaled land surface parameters for a SVAT model using time series data of satellite measured atmospheric forcings (e.g., precipitation), and land surface states (e.g., soil moisture and vegetation). This study focuses especially on the evaluation of soil moisture measurements from AMSR-E aboard AQUA satellite using the new MCMC-based scaling algorithm. Soil moisture evolution is modeled at a spatial scale comparable to the AMSR-E soil moisture product, with the hypothesis that the characterization of soil microwave emissions and their variations with space and time on soil surface within the AMSR-E footprint can be represented by an ensemble of upscaled soil hydraulic parameters. The study demonstrated the potential to improve upon the AMSR-E measurements by assimilating the soil moisture evolution from the proposed upscaled SVAT model.

Chapter IV focuses on downscaling of remotely sensed coarse scale soil moisture footprint. Two approaches are proposed for soil moisture downscaling. The first approach provides the probability distribution functions at the finer scales with no information about the spatial organization of soil moisture fields. The second approach implements a multiscale ensemble Kalman filter (EnKF) that assimilates remotely sensed coarse scale soil moisture footprint, attributes of fine scale geophysical parameters/variables (i.e., soil texture: %sand, vegetation: NDVI, topography: slope, and precipitation) and coarse/fine scale simulation into a spatial characterization of soil moisture evolution at the finer scales.

New algorithm developed in Chapter V is used to assess the soil physical property i.e., saturated hydraulic conductivity. The proposed algorithm uses the Karhunen-Loève Expansion (KLE) and 3-D soil moisture modeling in conjunction with Markov Chain Monte Carlo (MCMC) technique which employs measured soil moisture values to characterize the saturated hydraulic conductivity of an agricultural field at a fine resolution. An application of soil moisture modeling at much coarser scale is demonstrated in Chapter VI. A Soil-Vegetation-Atmosphere-Transfer (SVAT) framework is employed for soil moisture estimation that is used to assess the dielectric constant of soil profile which in turn relates to radar backscattering. A new algorithm is proposed that uses the simulated radar backscattering to separate/estimate the stochastic surface roughness and vegetation backscattering components in diverse hydro-climatic regions under different combinations of geophysical parameters (i.e., soil, topography, and vegetation).

The motivation of all these studies discussed in Chapters II-VI comes from the belief that satellite-based remote sensing is the future of soil moisture estimation in a watershed-, regional-, and global-scale at a reasonable temporal frequency. In the near future, there are two major satellite missions planned which will include sensors for measuring soil moisture: Soil Moisture and Ocean Salinity (SMOS) mission by European Space Agency (ESA), and Soil Moisture Active and Passive (SMAP) mission by National Aeronautics and Space Agency (NASA). The SMOS satellite by ESA will be launched in 2009. It will monitor soil moisture, ocean salinity, the water content in vegetation, and the snow and ice cover by using a passive microwave interferometer MIRAS i.e., Microwave Imaging Radiometer using Aperture Synthesis. MIRAS will operate in the L-band, where the sensitivity to soil moisture is very high, whereas, the sensitivity to atmospheric disturbances and surface roughness is minimal. In the timeframe 2010-2013, NASA will have the SMAP mission, which will monitor soil moisture and freeze-thaw cycles and provide the data for weather and climate prediction, hydrospheric modeling and water resource availability prediction. The instrumentation will utilize both active (radar) and passive microwave (radiometers) technique in L-band to measure the dielectric characteristics of soil and vegetation.

CHAPTER II

MODELING AND ASSIMILATION OF ROOT ZONE SOIL MOISTURE USING REMOTE SENSING OBSERVATIONS

2.1. Synopsis

Soil moisture status in the root zone is an important component of the water cycle at all spatial scales (e.g., point, field, catchment, watershed, and region). In this study, the spatio-temporal evolution of root zone soil moisture of the Walnut Gulch Experimental Watershed (WGEW) in Arizona was investigated during the Soil Moisture Experiment 2004 (SMEX04). Root zone soil moisture was estimated via assimilation of aircraft-based remotely sensed surface soil moisture into a distributed Soil-Water-Atmosphere-Plant (SWAP) model. An ensemble square root filter (EnSRF) based on a Kalman filtering scheme was used for assimilating the aircraft-based soil moisture observations at a spatial resolution of 800 m X 800 m. The SWAP model inputs were derived from the SSURGO soil database, LAI (Leaf Area Index) data from SMEX04 database, and data from meteorological stations/rain gauges at the WGEW. Model predictions are presented in terms of temporal evolution of soil moisture probability density function at various depths across the WGEW. The assimilation of the remotely sensed surface soil moisture observations had limited influence on the profile soil moisture. More specifically, root zone soil moisture depended mostly on the soil type. Modeled soil moisture profile estimates were compared to field measurements made periodically during the experiment at the ground based soil moisture stations in the

watershed. Comparisons showed that the ground-based soil moisture observations at various depths were within ±1 standard deviation of the modeled profile soil moisture. Density plots of root zone soil moisture at various depths in the WGEW exhibited multi-modal variations due to the uneven distribution of precipitation and the heterogeneity of soil types and soil layers across the watershed.

2.2. Introduction

Surface and root-zone soil moisture are important state variables for hydrological and meteorological modeling. The sensitivity of energy exchange processes at the land-atmosphere boundary to root zone soil moisture is well known. These processes are important for global water circulation and carbon cycling. Passive microwave remote sensing has the potential to provide synoptic surface soil moisture measurements [*Engman and Gurney*, 1991; *Jackson*, 1993; *Jackson, et al.*, 1999; *Njoku and Entekhabi*, 1995] that are important for assessment of root-zone soil moisture over a region. These measurements describe near-surface (0~0.05 m) soil moisture [*Schmugge, et al.*, 1974; *Schmugge, et al.*, 1980; *Schmugge, et al.*, 1977]. Recognizing the importance of surface and root-zone soil moistures, major efforts are underway to develop operational soil moisture remote sensing techniques. Scientific campaigns such as Washita 1992, Southern Great Plains hydrology experiments 1997 (SGP97), and Soil Moisture Experiments 2004 (SMEX04) were conducted to validate airborne and space-borne passive microwave remote sensing platforms and thus estimating soil moisture over large spatial scales. These campaigns were conducted in selected geographical regions

representing rangeland, agricultural farmland, and semi-arid shrubland, as well as different topographic conditions such as flat, rolling/undulating, and mountainous terrains.

Kostov and Jackson [1993] suggested that a promising approach for estimating profile soil moisture is the integration of remote sensing surface soil moisture data and computational modeling. In the case of bare soil, *Entekhabi et al*. [1994] showed that it is possible to retrieve profile soil water content using passive microwave data at frequencies less than 10 GHz. In that study, the propagation of information from the surface to deeper soil layers was investigated using a multilayer model of heat and water transfer. *Houser et al.* [1998] studied the use of four-dimensional data assimilation methods in a macro-scale land hydrology model to generate surface and root zone soil moisture fields at regular space and time intervals for the Walnut Gulch Experimental Watershed (WGEW) in Arizona. Other related/similar studies have been conducted for estimation of surface and profile soil water contents using passive microwave data at watershed/regional scale during the SGP97 experiment [*Crosson, et al.*, 2002; *Crow and Wood*, 2003; *Das and Mohanty*, 2006; *Dunne and Entekhabi*, 2005; *Margulis, et al.*, 2002; *Reichle, et al.*, 2002].

The primary objective of this study is to determine the evolution of the spatial and temporal dynamics of root-zone soil moisture in semi-arid shrublands of the WGEW during the SMEX04 experiment. We have used an Ensemble Square Root Filter (EnSRF) to assimilate aircraft-based (Polarimetric Scanning Radiometer) remotely sensed surface soil moisture observations with the Soil-Water-Atmosphere-Plant

(SWAP) model for the estimation of profile soil water content. The assimilation of Polarimetric Scanning Radiometer (PSR/CX)-based surface soil moisture and modeling of root-zone soil moisture were conducted by extending the parallel non-interacting stream tube framework proposed by *Das and Mohanty* [2006] and also included run-off and run-on processes between remote sensing footprints. The temporal evolution of soil moisture measured at point-based monitoring locations and depths across the WGEW was also compared with EnSRF-based model predictions. A secondary objective of this study is to develop the probability distributions for soil moisture at various depths within the WGEW.

2.3. Materials and Methods

Description of Study Area and Forcings

The SMEX04 field campaign was conducted between August 2 and August 27, 2004 across Arizona, USA and Sonora, Mexico (http://hydrolab.arsusda.gov/smex04/). The primary focus of the field experiments in Arizona during SMEX04 was the Walnut Gulch Experimental Watershed (31º43´N, 110º41´W) near Tombstone, operated by the Agriculture Research Service (ARS), U.S. Department of Agriculture (USDA). The 150 km^2 watershed (Fig. 2.1) is part of the San Pedro river basin, and is heavily instrumented to measure rainfall and runoff. The instrumented area of the watershed comprises a dense network of 88 rain-gages (Fig. 2.1) of which 19 are collocated with soil moisture sensors. The elevation of the WGEW (Fig. 2.2) varies between 1250 m and 1585 m above the mean sea level, with an average annual temperature of 17.7ºC. It receives an

average of 350 mm of precipitation annually. The vegetation is mainly shrubs, covering about two-thirds of the watershed. The remaining one-third is mostly grassland. The soil is generally well drained, calcareous, gravelly loam with large percentages of rock and gravel at the soil surface. Natural Resources Conservation Services (NRCS) has mapped 27 soil series in this watershed. The soil classification based on dominant surface soil texture at a resolution of 800 m X 800 m is illustrated in Fig. 2.3. Complete information about the WGEW is available on the USDA-ARS website (http: //ars.usda.gov/SP2UserFiles/Place/53424500/WGBrochure.pdf). During SMEX04 campaign, the PSR/CX (Piepmeier and Gasiewski, 2001) with polarimetric channels of C and X band (5.82-10.80 GHz) was flown on the Naval Research Lab's (NRL) P3 aircraft. The P3 flight details of the remote sensing campaign are available at National Snow and Ice Data Center (NSIDC). The PSR/CX-based soil moisture snapshots for 9 days across the WGEW are illustrated in Fig. 2.4 [*Bindlish, et al.*, 2006b].

The footprint size (800 m X 800 m) of PSR/CX was used as the basis for grid resampling (by inverse-distance interpolation) for all variables resulting in a total of 224 pixels across the WGEW. The resulting daily spatially distributed hydro-climatic datasets were used as inputs to the SWAP model. For this distributed modeling and data assimilation study, we used input data from various sources including the LAI data collected during SMEX04 campaign, the soil layers and types from the SSURGO database (USDA-NRCS), and the precipitation data collected by the network of 88 weighing-type recording rain-gages arranged in a grid across the WGEW (Fig. 2.1). An inverse-distance interpolation (IDI) technique was used to create a spatial distribution of

daily accumulated precipitation on relevant dates (Fig. 2.5). It is apparent from Fig. 2.5 that during the SMEX04 period WGEW received scattered and scanty rainfall with no major precipitation event throughout the watershed. The spatial distribution of LAI (800 m X 800 m) across WGEW was also generated with IDI technique (Fig. 2.6). All other meteorological forcings (e.g., relative humidity, wind speed, and air temperature) were extracted from the Soil Climate Analysis Network (SCAN) site located within WGEW (Fig. 2.1), and were assumed to be spatially uniform for the purpose of this study. The relevant GIS and ground measurement datasets available at NSIDC were used for distributed modeling of root zone soil moisture in the WGEW.

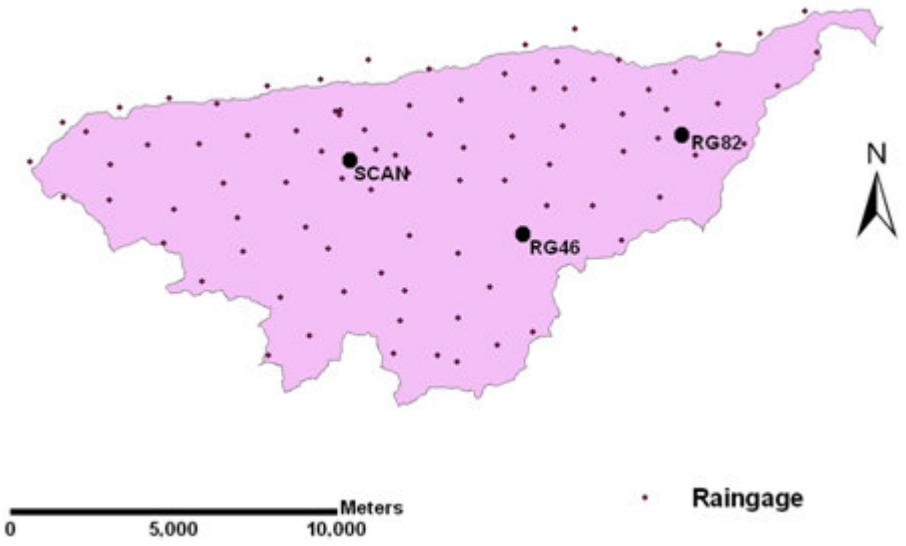

Figure 2.1. Walnut Gulch Experimental Watershed (WGEW) with rain gages, SCAN, RG46, and RG82 sites used in the study.

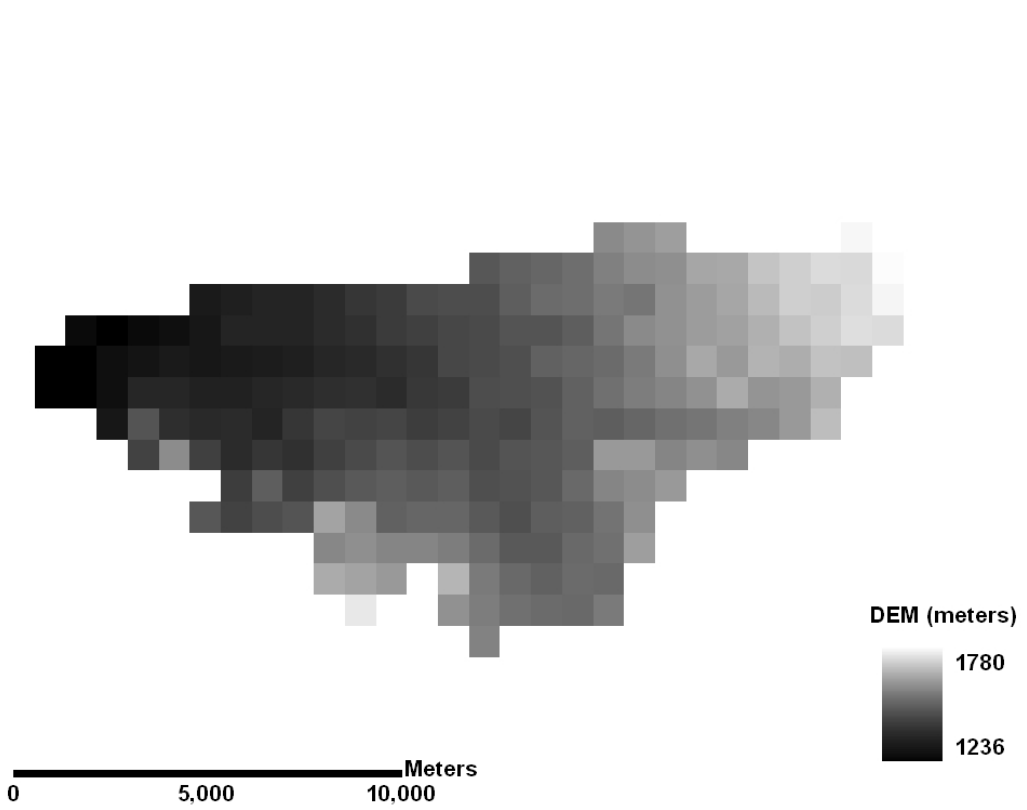

Figure 2.2. Walnut Gulch Experimental Watershed (WGEW) digital elevation model (DEM) at resolution of 800 m X 800 m, resampled from 30 m X 30 m DEM. Data source: USDA geospatial-data-gateway.

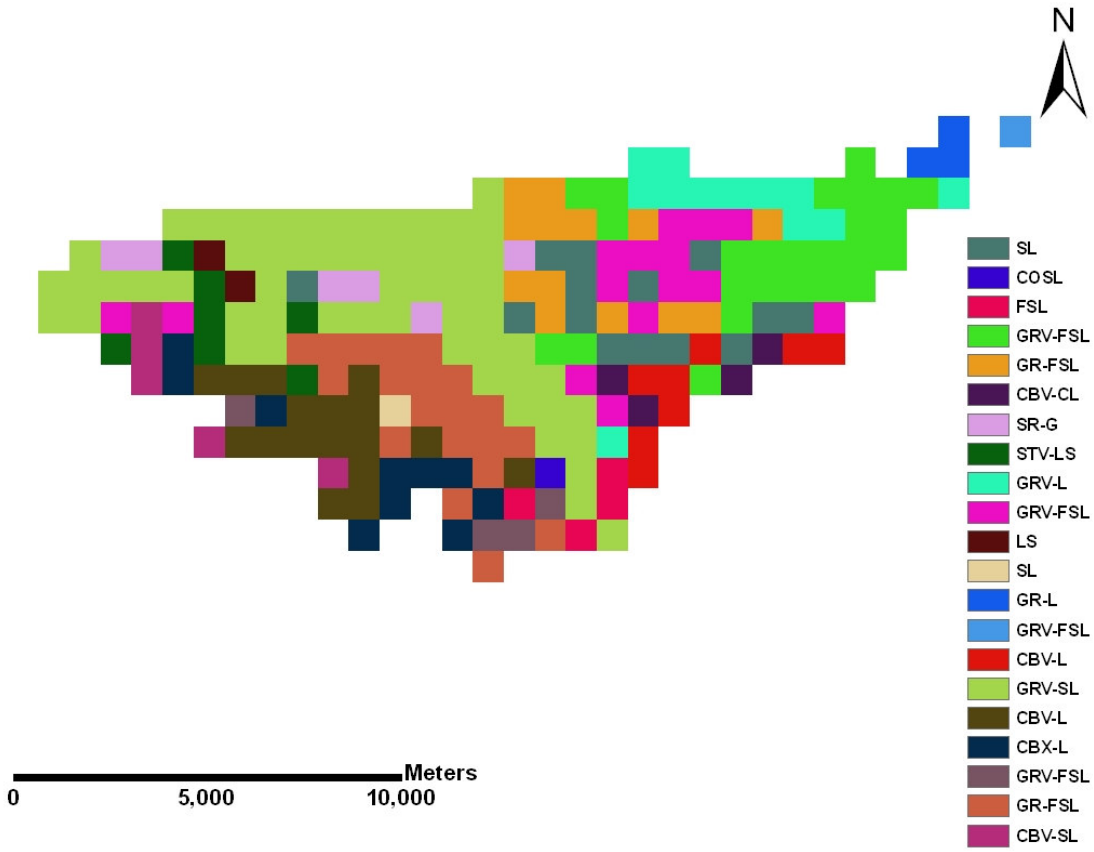

Figure 2.3. Walnut Gulch Experimental Watershed (WGEW) surface soil texture at resolution 800 m X 800 m (SL: Sandy Loam; COSL: Coarse Sandy Loam; FSL: Fine Sandy Loam; GRV-FSL: Very Gravelly Fine Sandy Loam; GR-FSL: Gravelly Fine Sandy Loam; CBV-CL: Very Cobblly Clay Loam; SR-G: Stratified Gravel; STV-LS: Very Stony Loamy Sand; GRV-L: Very Gravelly Loam; LS: Loamy Sand; GR-L: Gravelly Loam; CBV-L: Very Cobblly Loam; GRV-SL: Very Gravelly Sandy Loam; CBX-L: Extremely Cobbly Loam; CBV-SL: Very Cobblly Sandy Loam).

Data source: http://soildatamart.nrcs.usda.gov/County.aspx?State=AZ

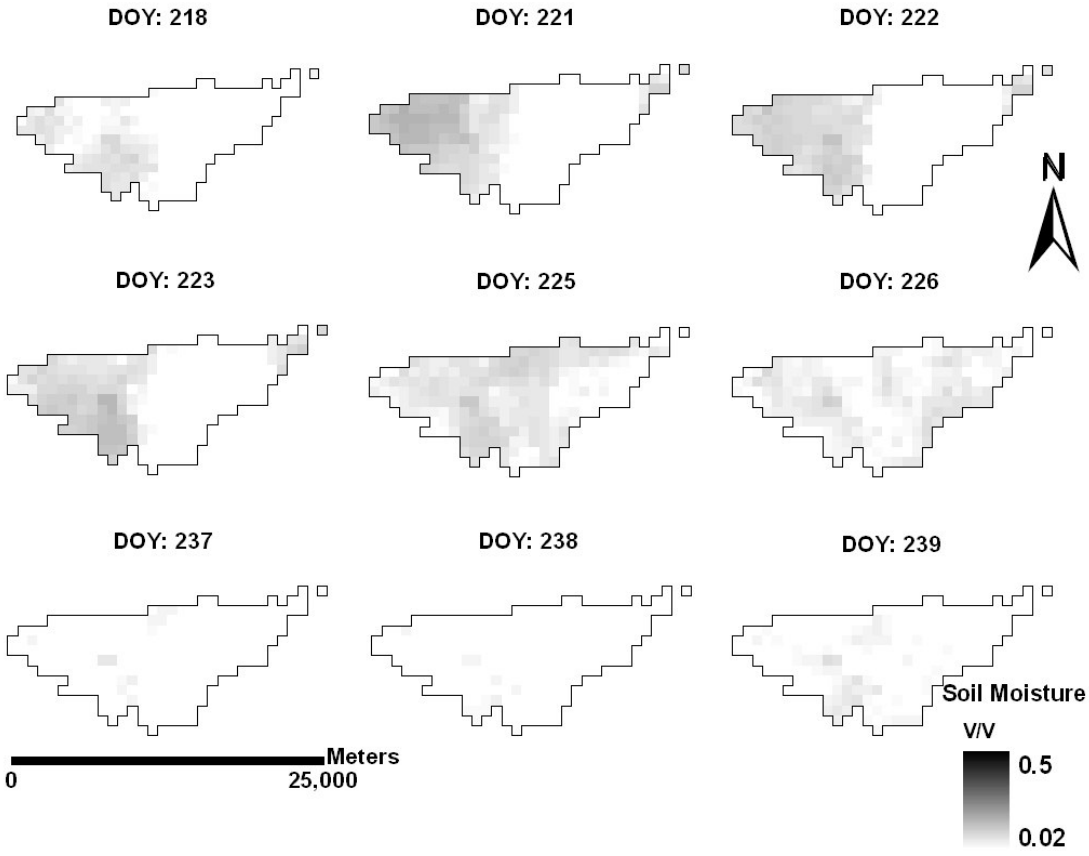

Figure 2.4. Walnut Gulch Experimental Watershed (WGEW) PSR/CX snapshots of soil moisture for Day of Year (DOY) 218, 221, 222, 223, 225, 226, 237, 238, and 239 at resolution of 800 m X 800 m.

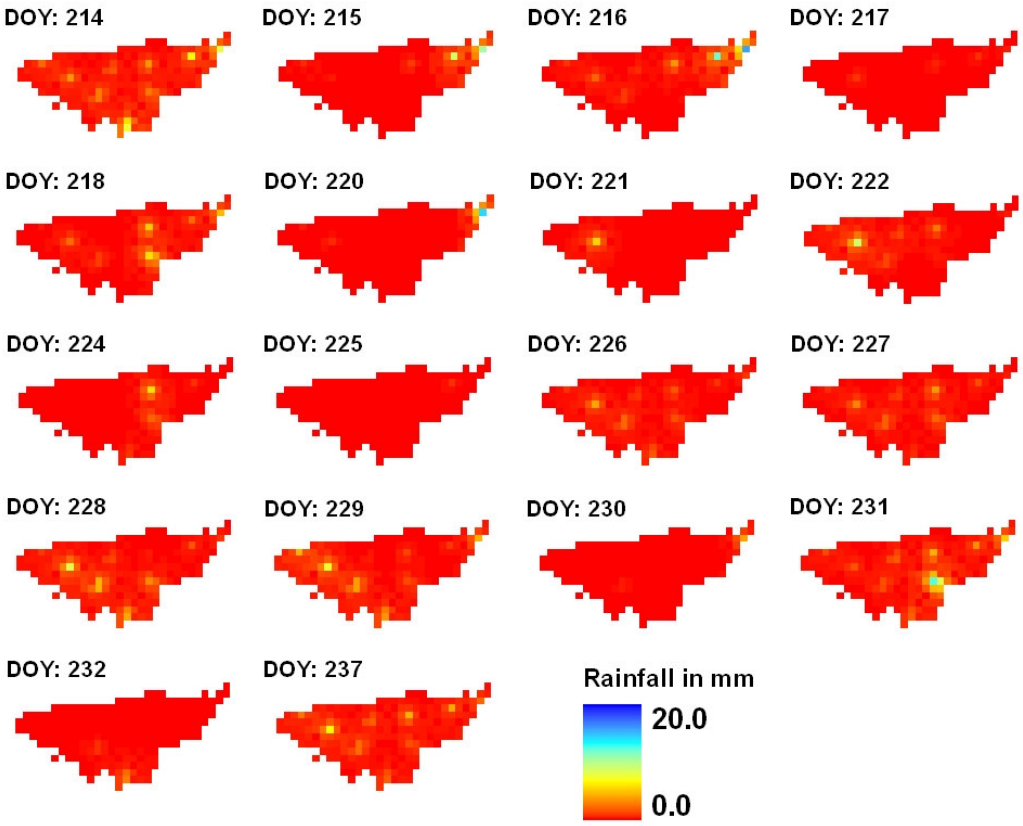

Figure 2.5. Spatial distribution of precipitation at resolution of 800 m X 800 m created with inverse distance interpolation (IDI) of measurements from 88 raingages in Walnut Gulch Experimental Watershed (WGEW).

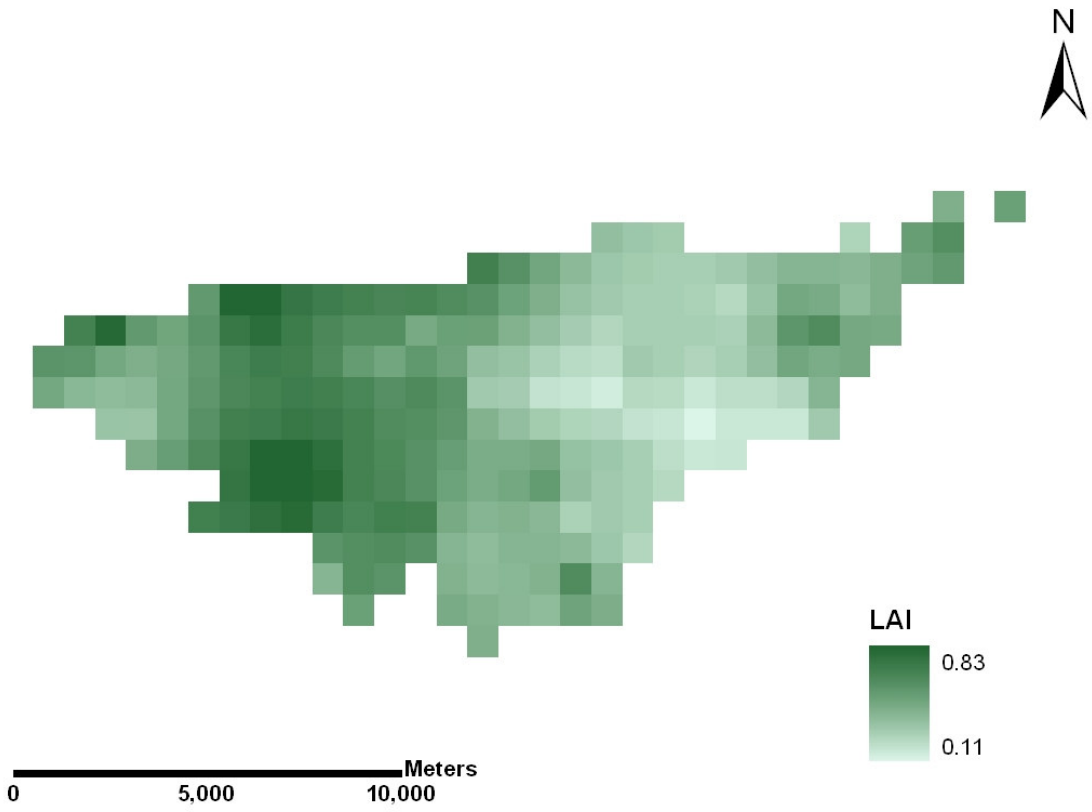

Figure 2.6. Walnut Gulch Experimental Watershed (WGEW) Leaf Area Index (LAI) at resolution of 800 m X 800 m.

Soil-Water-Atmosphere-Plant (SWAP) Model

SWAP [*Van Dam, et al.*, 1997] is a robust physically-based field scale eco-hydrological model used to simulate the processes occurring in the soil-water-atmosphere-plant system. SWAP is an open source hydrological model and is the successor of the SWATR model [*Feddes, et al.*, 1978]. SWAP is available at http://www.swap.alterra.nl/. The model simulates both the soil water quantity and quality with daily temporal resolution. SWAP can account for several combinations of

the top and bottom boundary conditions. Ines and Honda [2005] have successfully used SWAP in their study for quantifying surface and root-zone soil water contents from low resolution remote sensing data. Since SWAP was not originally designed for distributed modeling, it was adapted into a framework developed by *Das and Mohanty* [*Das and Mohanty*, 2006]. This framework was developed on ArcGIS platform for distributed hydrological modeling. It uses geophysical variables in grid format as inputs to the hydrologic model (SWAP). The framework is capable of producing soil moisture outputs at watershed-scale at various depths in a grid format. For this study, run-on and run-off routing were also included in the framework by extracting flow-accumulation, flow-direction, and flow-length information from the digital elevation model (DEM) (Fig. 2.2) of the WGEW with a steepest descent technique. Note, however, the DEM of 800 m X 800 m resolution (resampled from 30 m X 30 m resolution) may introduce some scale uncertainty while evaluating flow-accumulation, flow-direction, and flow length.

The governing equation of SWAP solves the 1-D Richards' equation (eq. 2.1) to simulate partially-saturated water movement in the soil profile.

$$\frac{\partial \theta}{\partial t} = \frac{\partial}{\partial z}[K(\frac{\partial h}{\partial z} + 1)] - S_a(h) \tag{2.1}$$

where θ is the soil water content (m^3/ m^3), z is the soil depth (m), h is the soil water pressure head (m), K is the unsaturated hydraulic conductivity (m/day), and S_a(h) is the root water uptake (m/day). The maximum possible root water uptake over the rooting depth is equal to potential transpiration rate, T_p (m/day), which is governed by atmospheric conditions. The potential root water uptake at a certain depth, $S_p(z)$, may be

determined by the root length density, $l_{root}(z)$ (m/m^3), as a fraction of the integrated root length density.

$$S_p(z) = \frac{l_{root}(z)}{\int_{D_{root}}^{0} l_{root}(z)dz} T_p \tag{2.2}$$

where D_{root} is the root layer thickness. In practice the distribution of $l_{root}(z)$ is often not available. Therefore in SWAP, a uniform root length density distribution is assumed.

$$\frac{l_{root}(z)}{\int_{D_{root}}^{0} l_{root}(z)dz} = \frac{1}{D_{root}} \tag{2.3}$$

which leads to the simplification of eq. (2.2) (Feddes et al., 1978), as

$$S_p(z) = \frac{T_p}{D_{root}} \tag{2.4}$$

The actual root water uptake $S_a(h)$, is calculated from

$$S_a(h) = \alpha_w \int_{0}^{Droot} S_p(z)\, dz \tag{2.5}$$

α_w is the reduction factor as a function of h that accounts for water stress [*Feddes, et al.*, 1978]. Penman-Monteith equation [*Monteith*, 1965] was used to calculate potential evapotranspiration. The potential transpiration (T_p) and the soil evaporation (E_p) were partitioned using LAI. The potential evaporation rate of soil under standing vegetation is derived from Penman-Monteith equation by neglecting the aerodynamic term. Thus, the only source of soil evaporation is net radiation that reaches the soil surface. Assuming

that the net radiation inside the canopy decreases according to an exponential function, we can derive

$$E_p = E_{po}\, e^{-\kappa_{gr} LAI} \tag{2.6}$$

where κ_{gr} is the extinction coefficient of global solar radiation and E_{po} (m/day) is potential evaporation. SWAP calculates the daily average T_p (m/day),:

$$T_p = (1.0 - W_{frac})\, ET_{po} - E_p \tag{2.7}$$

where W_{frac} (-) is ratio of the daily amount of intercepted precipitation and potential evaporation rate of the water intercepted by the vegetation. In eq (2.7) ET_{p0} (m/day) is potential evapotranspiration rate of a dry canopy.

In the SWAP model soil moisture retention and hydraulic conductivity functions are defined by the Mualem-van Genuchten equation,

$$S_e = \frac{\theta(h) - \theta_r}{\theta_s - \theta_r} = \left[\frac{1}{1 + |\alpha h|^n}\right]^m \tag{2.8}$$

$$K(S_e) = K_o S_e^{\,l} \{1 - [1 - S_e^{\,n/(n-1)}]^{1-1/n}\}^2 \tag{2.9}$$

where S_e is the relative saturation (-), θ_s and θ_r are the saturated and residual water content (m^3/ m^3) respectively, α (m^{-1}), n (-), m (-) are the shape parameters of the soil water retention function and $m = 1 - 1/n$, K_o is the matching point at saturation (m/s), and parameter l (-) is an empirical pore tortuosity/connectivity parameter.

SWAP Modeling Domain and Parameters

The spatially and temporally variable atmospheric forcings, soil hydraulic properties, and vegetation interact in a highly nonlinear manner to produce

heterogeneous soil moisture at the soil surface and in the root-zone. In this paper, we mainly focused on watershed-scale representations of the root-zone soil moisture at a coarser spatial resolution of 800 m X 800 m and temporal resolution of one day. Therefore, the disparity of scales between the horizontal (spatial resolution: 800 m X 800 m) and vertical (soil depth: 3.86 m) extents of the root-zone was the key consideration in formulating the framework for watershed-scale root-zone hydrology. For SWAP model simulation, the 3.86 m thick soil profile (available soil depth in SURRGO database) at every remote sensing footprint was discretized into 50 nodes, with finer discretization near the soil layer interfaces and at the land-atmosphere boundary. Finer discretization near the top boundary and layer interfaces were used to handle the steep pressure gradient for the numerical simulations. Time-dependent flux-type top boundary conditions for each parallel soil column (matching the remote sensing footprints) were used with precipitation distribution across the WGEW. A unit vertical hydraulic gradient (free drainage) condition was used at the bottom boundary of the soil columns because of deep groundwater table (45 m to 150 m) condition across the WGEW. No flow bottom boundary condition was imposed where impervious layers (i.e., bedrocks) were encountered in 3.86 m of the soil profile. Runoff and runon between adjacent footprints due to topography was considered on the land surface. The runoff from the one or more adjacent pixels of steepest descent according to flow routing was used as runon for the pixel under consideration. Given the relatively coarse horizontal scale with shallow root-zone, the parallel soil columns model ignores the lateral water fluxes across the adjacent soil columns and only predicts the vertical fluxes

including infiltration, evapotranspiration, runoff, and deep percolation as parallel non-interacting stream-tubes concept in distributed vadose zone hydrology. We also assumed that 1-D Richards' equation is an appropriate physical model to simulate vertical partially-saturated flow and partitioning of fluxes at the spatial scale of 800 m X 800 m. Numerical studies conducted by *Mantoglou*, [1992], and *Zhang*, [1999] on general upscaled Richards' equations have shown that at large spatial scales and in the absence of interflow vadose zone flow can be represented by one-dimensional Richards' equation.

A probabilistic approach was adopted in the distributed modeling environment across the WGEW. An ensemble of state variables (profile soil moistures) was created for all the 224 (800 m x 800 m) PSR/CX footprints in the WGEW. A state augmentation technique was applied by concatenating uncertain soil properties to state variables, forming composite vectors in the ensemble. The soil hydraulic properties (θ_s, θ_r, and K_{sat}) from the SSURGO database were used to introduce uncertainty in the ensemble. The van-Genuchten shape parameters (α, and n) for the soil textural classes given by *Carsel and Parrish* [1988] were used with ±20% uncertainty. The purpose of including uncertain soil properties in the ensemble is to address the assumption that it simulates model errors and subpixel variability present within a PSR/CX footprint.

For best computational efficiency, one hundred members (composite vectors) were populated in the ensemble. The soil moisture in the discretized soil profile was assigned an initial value of 50% relative saturation according to the soil texture on the onset of model simulation. A Gaussian noise of 20% to 5% of the initial soil moisture (in

decreasing order from top to bottom of the soil profile) was introduced in all the ensemble members with an assumption of decreasing variability in soil moisture with increasing depth. The SWAP model was run a month ahead of the SMEX04 campaign (August 2nd, 2004 through August 27th, 2004), to tune the state of initial soil moisture profile. PSR/CX-measured surface soil moisture was assimilated with the SWAP model predictions (across the 3.86 m of soil layer) through the ensemble square root filter (EnSRF) updating scheme described below. At each time step, final states were determined by averaging the ensemble of the one hundred replicated predictions made by the model.

Ensemble Square Root Filter (EnSRF)

An enduring problem in many hydrologic situations is to forecast the state of a system given a set of observations and a hydrologic model. While the use of deterministic models has significantly addressed this problem, it now appears that much more promising solutions lie with probabilistic forecasting and data assimilation. In hydrology, the ensemble Kalman filters (EnKF) [*Evensen*, 2003; *Houtekamer and Mitchell*, 1998] based on the Monte-Carlo approach are generally used [*Crosson, et al.*, 2002; *Crow and Wood*, 2003; *Das and Mohanty*, 2006; *Dunne and Entekhabi*, 2005; *Margulis, et al.*, 2002; *Reichle, et al.*, 2002]. Use of the Kalman filter system implicitly assumes that the observations are related to the true state x^t through

$$y = Hx^t + \varepsilon \tag{2.10}$$

where ε is a Gaussian random error vector with a mean of zero and measurement error covariance R, and H is the operator that maps the model variable space to the observation space. Furthermore, the forecast of x_t is Gaussian with mean $x^f_{t=k}$ and error covariance $P^f_{t=k}$. Using these assumptions, the estimated state of the profile soil moisture and error covariance is updated as

$$x^a_{t=k} = x^f_{t=k} + K(y - Hx^f_{t=k}) \text{ and} \tag{2.11}$$

$$P^a_{t=k} = (I - KH)P^f_{t=k}. \tag{2.12}$$

Here, the superscripts f and a represent the respective prior (forecast) and posterior (analysis/updated) estimates, the subscript t represents time, y is the observation vector, I is the identity matrix, and K is the Kalman gain matrix defined as:

$$K = P^f_{t=k} H^T (HP^f_{t=k} H^T + R)^{-1} \tag{2.13}$$

The EnKF forecast and analysis error covariance comes directly from an ensemble of model simulations as:

$$P^f H^T = (N_e - 1)^{-1} \sum_{n=1}^{N_e} (x^f_n - \bar{x}^f)(Hx^f_n - H\bar{x}^f)^T \tag{2.14}$$

N_e is the number of ensemble members, and the subscript n represents each individual ensemble member. The overbar represents the ensemble mean, which is sampled as

$$\bar{x}^f = N_e^{-1} \sum_{n=1}^{N_e} x^f_n \tag{2.15}$$

The ensemble is generated by perturbing a first-guess value so that ensemble mean is equal to the first-guess value. The variance is specified based on the uncertainty in the

first-guess. In this system, ensemble members are integrated independently and updated in accordance with the Kalman filter methods when new observations become available. An alternate version of the EnKF approach is required in our study to ensure that the analysis error covariance does not become unrealistically low. Burgers et al. (1998) demonstrated that P^a is underestimated by a factor of *I-KH* when observations are not treated as random variables. This can cause the EnKF to reject observations in favor of the ensemble forecast. This leads the analysis incrementally further away from reality, resulting in filter divergence [*Burgers, et al.*, 1998; *Houtekamer and Mitchell*, 1998; *Mitchell and Houtekamer*, 2000; *Whitaker and Hamill*, 2002]. *Whitaker and Hamill* [2002] showed that adding random noise to observations further skews the distribution of P^a, and this results in a more erroneous analysis even though the covariance is increased. They suggested an alternative ensemble square root filter (EnSRF) where the ensemble mean is still updated by eq. 2.11, but deviations from the mean are updated by

$$x'^{a}_{t=k} = x'^{f}_{t=k} + K'(Hx'^{f}_{t=k}) \tag{2.16}$$

where

$$K' = \alpha K \tag{2.17}$$

and

$$\alpha = \left(1 + \sqrt{\frac{R}{HPH + R}}\right)^{-1} \tag{2.18}$$

Using this method, the analysis error covariance is guaranteed to be exactly equal to that in eq. 2.11, and perturbed observations are no longer necessary ($y' = 0$). This scalar

version of EnKF for the assimilation of a single observation at a time was implemented in this study.

2.4. Results and Discussion

Modeling and Verification

The model run for the period of SMEX04 resulted in soil moisture estimation up to a profile depth of 3.86 m in all 224 pixels of the WGEW. Figure 2.7 illustrates the evolution of average (from pixel ensemble) soil moisture fields at the depths of 0.05, 0.20, 1.00, and 3.50 m for August 8th, 2004 (Day of Year, DOY, 221). To evaluate the model performance, model outputs were compared with soil moisture observations from the SCAN and Hydra sites (RG46 and RG82) at WGEW (highlighted in Fig. 2.1). The modeled footprint-scale profile soil moisture at a particular depth was compared with the corresponding local (point-scale) profile soil moisture data measured at these three sites. It is suggested that the ensemble variability of soil moisture within a pixel (800 m X 800 m) reflects the variability at the subpixel/point scale at the respective depth. The evolution of profile soil moisture states at corresponding footprint-scale and local/point-scale were greatly influenced by the soil layers, antecedent moisture conditions, soil hydraulic properties, and precipitation (Fig. 2.8). Table 2.1 shows the layer depth (z), saturated hydraulic conductivity (K_{sat}), residual water content (θ_r), saturated water content (θ_s), and soil texture for various soil layers (from SSURGO database) up to 3.86 m depth at the SCAN and Hydra sites representing typical conditions of the WGEW.

The following discussion elaborates the comparisons of modeled and observed profile soil moisture values at these three sites.

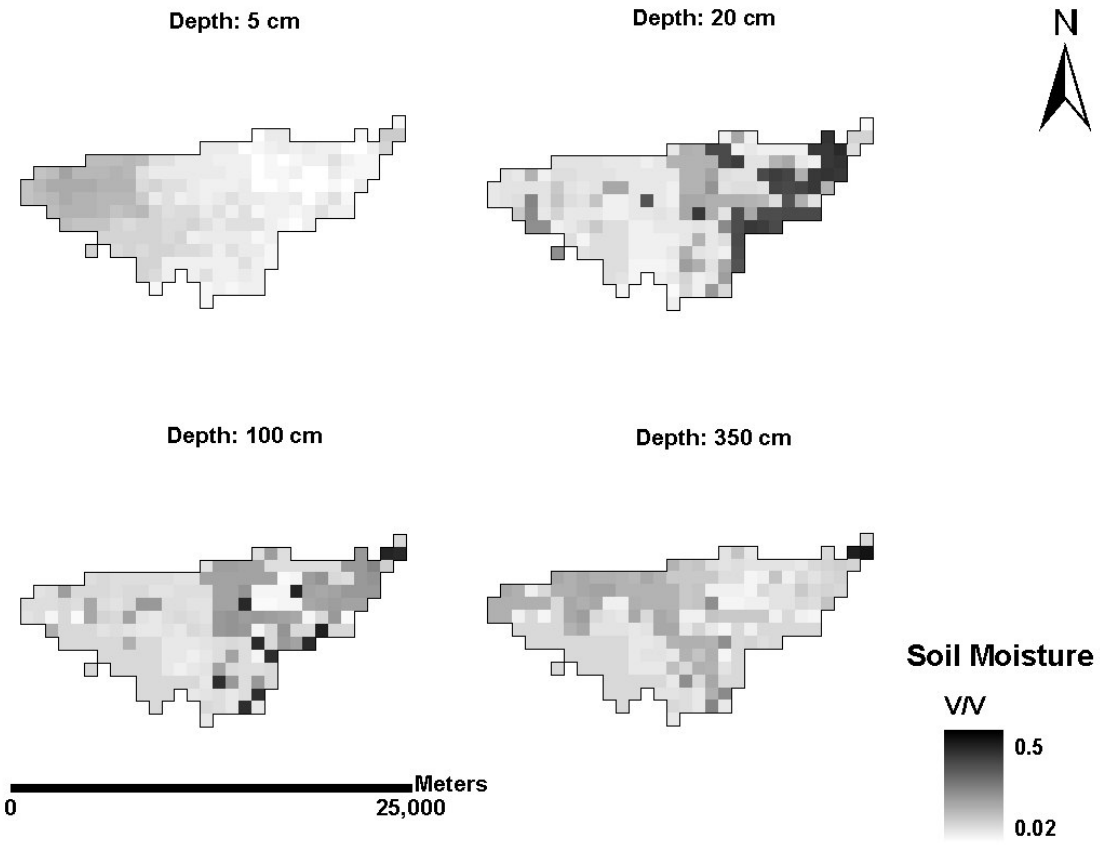

Figure 2.7. Walnut Gulch Experimental Watershed (WGEW) model (with assimilation) simulated soil moisture for Day of Year (DOY) 219 at depth 0.05 m, 0.20 m, 1.00 m, and 3.50 m at resolution of 800 m X 800 m.

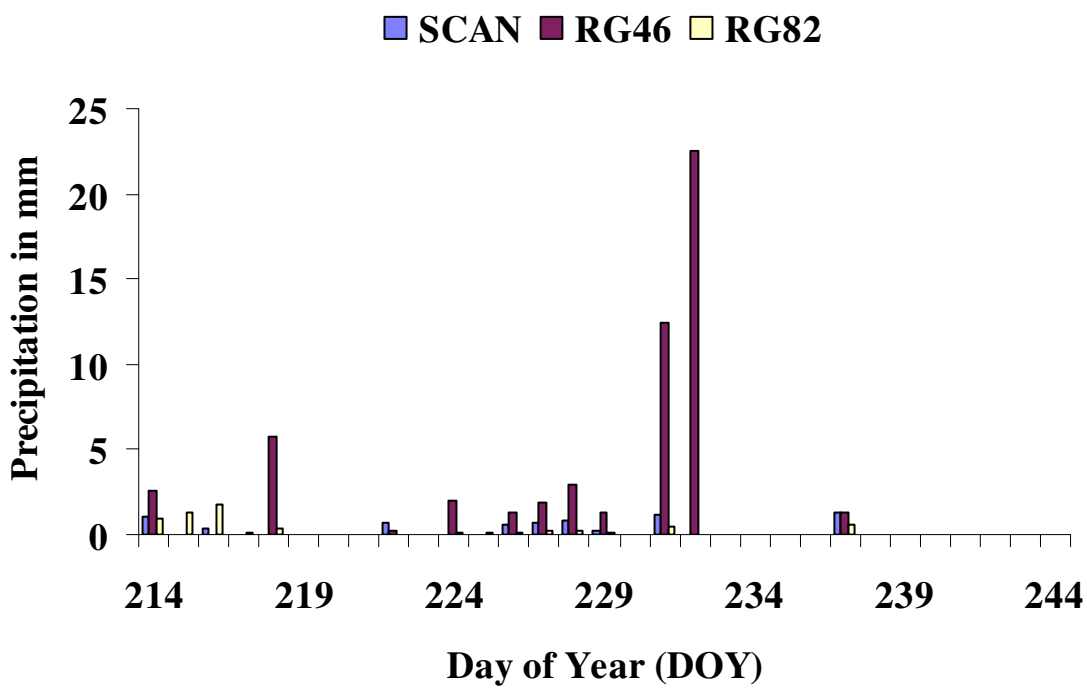

Figure 2.8. Precipitation in mm observed in three sites (SCAN, RG46 and RG82).

Table 2.1. Saturated hydraulic conductivity, water content (residual and saturated), and soil texture of various soil layers at the SCAN site and the Hydra sites of Walnut Gulch Experimental Watershed (WGEW).

	Soil layers depth (m)		Ksat (m/day)			Water Content (%)		Soil texture
Site	**top**	**bottom**	**min.**	**avg.**	**max.**	**residual**	**saturated**	**description**
SCAN	0	0.127	1.20	2.41	3.62	3.9	25	very gravelly sandy loam
	0.127	0.83	1.20	2.41	3.62	5.7	33	gravelly sandy loam
	0.83	2.00	1.20	2.41	3.62	6.6	40	sandy loam
	2.00	251.46	1.20	2.41	3.62	5.5	33	gravelly sandy loam
	2.51	3.86	0.34	0.77	1.20	6.1	37	gravelly loam
RG46	0	0.07	1.20	2.41	3.62	8	41	fine sandy loam
(Hydra)	0.07	0.45	0.12	0..23	0..34	17.5	44	sandy clay loam
	0.45	2.51	0..03	0.17	0.34	20	49	clay Loam
	2.51	3.86	0.12	0.23	0.34	12.2	45	sandy clay loam
RG82	0	0.12	1.20	2.41	3.62	7.1	33	gravelly fine sandy loam
(Hydra)	0.12	2.26	0.12	0.23	0.34	13.8	36	gravelly sandy clay loam
	2.26	3.86	1.20	2.41	3.62	7.8	39	sandy loam

SCAN Site

The SCAN site is a semiarid shrubland located at an altitude of 1362 m above the sea level. The SCAN site is typical of WGEW with very gravelly sandy soil texture and high saturated hydraulic conductivity (Table 2.1). The site has 5 distinct soil layers up to the depth of 3.86 m. The top 4 layers at the site have similar K_{sat}, but dissimilar θ_r and θ_s due to different degrees of compaction. The SCAN site observations at the depths of 0.05, 0.10, 0.20, 0.50 and 1.00 m are plotted in Fig. 2.9a-e. Model prediction with PSR/CX-based data assimilation and open-loop (model prediction without data assimilation) are also plotted in these figures. The subpixel variability in the PSR/CX-

assimilated prediction is shown as ±1 standard deviation (SD) in the plots. From Fig. 2.9a, it is clear that at 0.05 m depth, SCAN observations and PSR/CX observations disagree for the initial study period. During the initial dry days (DOY: 214-220) the model predictions (with and without data assimilation) were close to θ_r (0.039 based on SSURGO), whereas SCAN observations are much below this value and were beyond the ±1 SD. One explanation for such low SCAN observations is the presence of rock and gravel fraction in the top 0.13 m of soil depth. High rock and gravel fraction influence the soil hydraulic characteristics making them highly nonlinear with very high saturated hydraulic conductivity, which drains the soil rapidly. The other reason for the discrepancy between the SCAN point-scale (observation) and PSR pixel-scale (modeled) soil moisture is that the SCAN site received scanty rainfall during SMEX04 (Fig. 2.8). In dry conditions the model was constrained due to the lower limit set by θ_r (from SSURGO dataset). Thus, on DOY 219, assimilating PSR/CX observations made the model prediction deviate further away from the SCAN observations (Fig. 2.9a). During the rest of the SMEX04 experiment (DOY: 222 to 244), with the increase in soil moisture at 0.05 m depth, the model prediction trend matches reasonably well with the SCAN observations. At the depths of 0.10, 0.20, and 0.50 m (Fig. 2.9b-d) the SCAN observations are close to ±1 SD of the model predictions with data assimilation using PSR-based data. The deepest SCAN site observations at 1.00 m depth show a uniform state of soil moisture and the trend matches with both the models (assimilated and open-loop), and are also contained completely within ±1 SD of assimilated model predictions. Most SCAN observations lie within ±1 SD of the assimilated model predictions. This

provides some evidence that the spatial variability is well represented by the model ensemble for the particular pixel. The open-loop model also performed somewhat similar to the assimilated model at the deeper depths (Fig. 2.9b-e), demonstrating the dominant effect of soil texture in the evolution of soil moisture distribution at the deeper depths, irrespective of the model. Figures 2.9a-e also show that the propagation of EnSRF Kalman gain through the land surface model reaches deeper with diminishing effect when the soil layers are nearly similar. In other words, the results from this site show the benefits of providing better soil layer (textural heterogeneity) information as open loop simulation performs reasonably well. At 0.10 m depth, soil moisture values were constrained due to residual water content of the soil layer. Data assimilation could not improve over open-loop and they are almost similar. Whereas, at 0.20 m depth, soil moisture values are slightly more than the residual water content and data assimilation adjusts the soil moisture and deviate it further from SCAN observations. This effect exhibits another good example of having very gravelly sandy soil and how it influences the soil moisture observations and data assimilation. It is quite apparent from Fig 2.9d-e, that data assimilation did improve the prediction over open-loop.

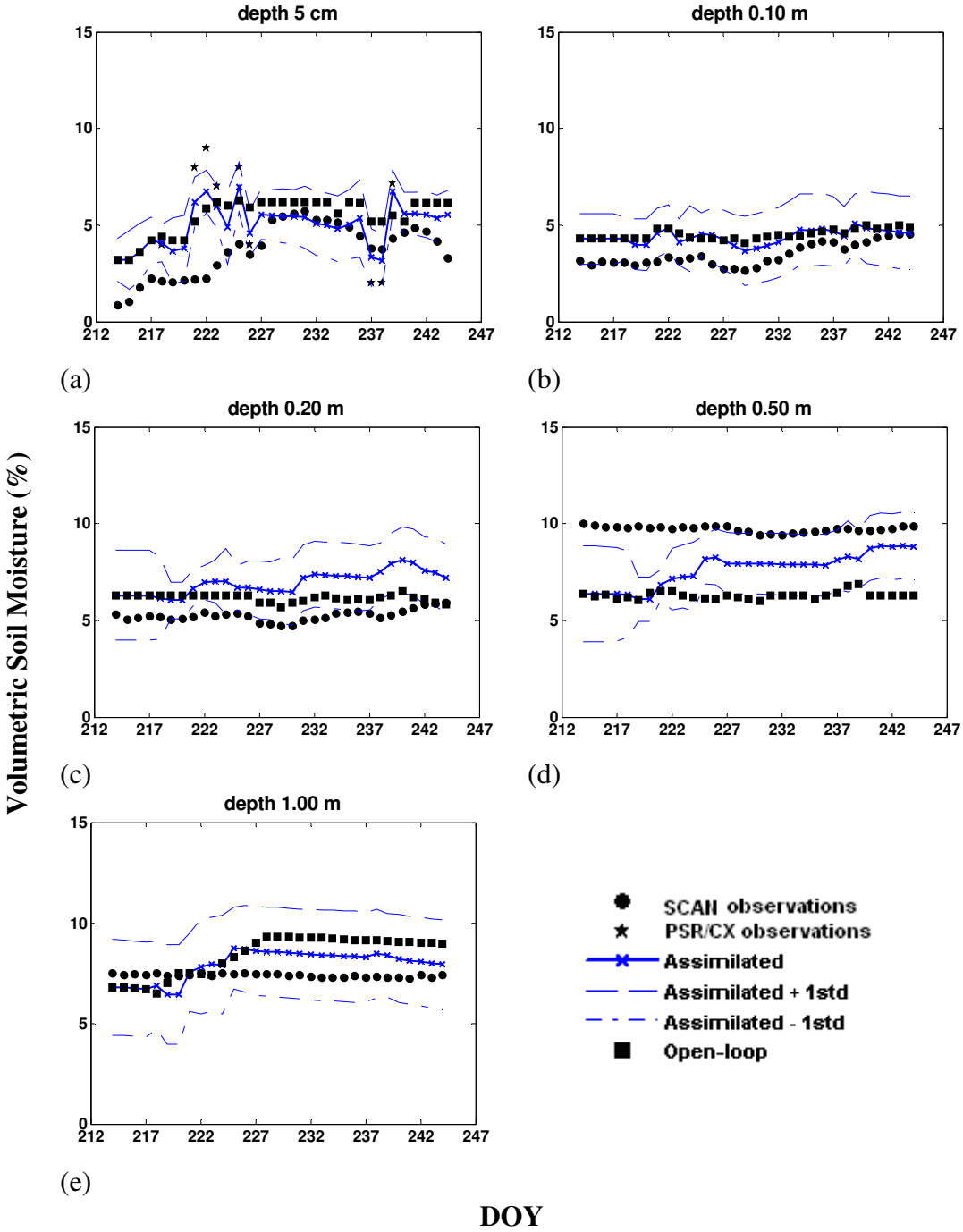

Figure 2.9. Comparison of SCAN soil moisture observations with model (with assimilation) simulated soil moisture at depth of (a) 0.05 m, (b) 0.10 m, (c) 0.20 m, (d) 0.50 m, and (e) 1.00 m of Walnut Gulch Experimental Watershed (WGEW).

Hydra Site (RG46)

This rain-gauge site (RG46) is situated in a shrubland at an altitude of 1442 m above the sea level. Figure 2.8 shows the amount of precipitation received at this site during the SMEX04 experiment. Hydra soil moisture sensors are installed at 0.13, 0.38, and 0.76 m depths at this site. The top two sensors are in the second soil layer (Table 2.1: sandy clay loam), and the sensor at 0.76 m is in the third soil layer (Table 2.1: clay loam). The states of soil moisture at these depths (Fig. 2.10a-c) were predominantly influenced by the clay loam (CL) texture of the layers (Table 2.1). The PSR/CX-based surface soil moisture observations for the pixel at this site are very low, ranging from 2 to 3% by volume, which is much below θ_r for the surface soil used in the modeling. Very low remotely sensed surface soil moisture for the pixel could be attributed to rock fraction on the surface. The effect of PSR/CX data assimilation is clearly visible at the depth of 0.13 m (Fig. 2.10a). However, the effect of data assimilation diminishes at the deeper depths of 0.38 and 0.76 m (Fig. 2.10b-c). It is also important to note that starting the model for a month before SMEX04 primed the initial conditions in both the assimilated and open-loop models quite close to the Hydra measurements. For the entire SMEX04 duration, the Hydra measurements for this site were within the bounds of ±1 SD of the assimilated model predictions.

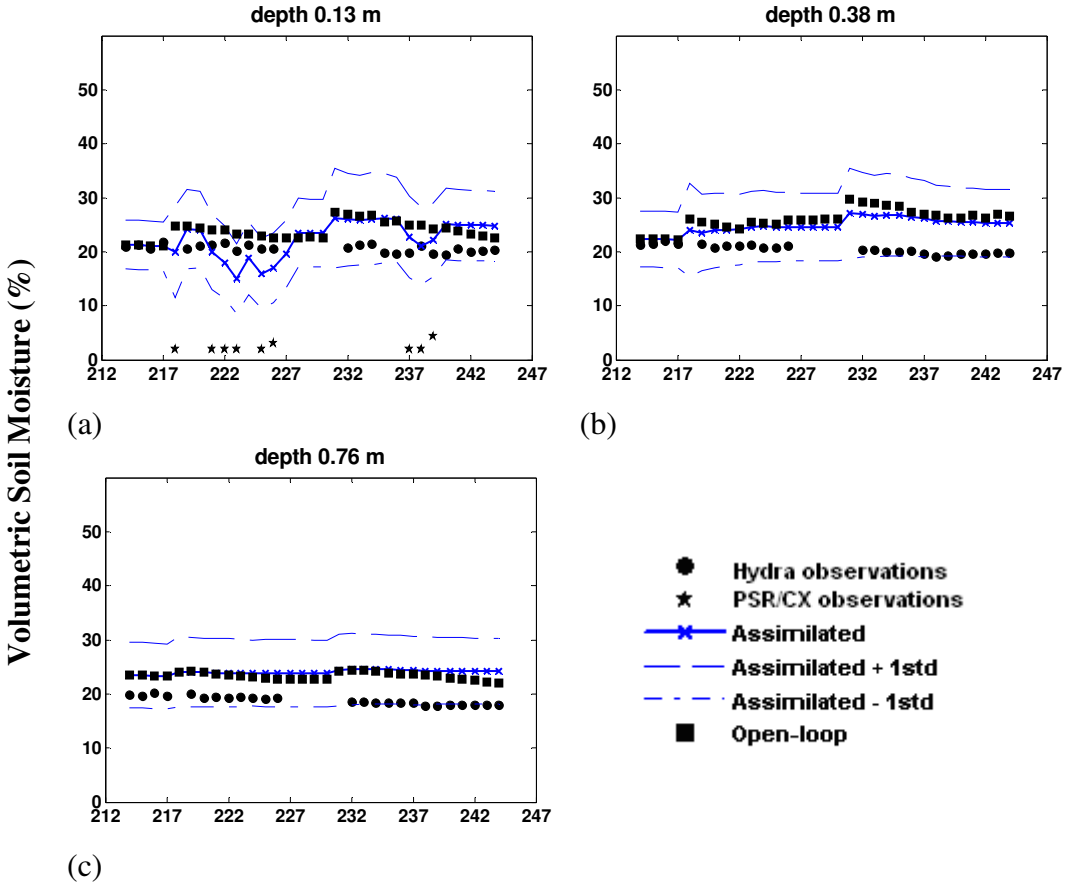

Figure 2.10. Comparison of Vitel (RG46) soil moisture observations with model (with assimilation) simulated soil moisture at depth of (a) 0.13 m, (b) 0.38 m, and (c) 0.76 m of Walnut Gulch Experimental Watershed (WGEW).

Hydra Site (RG82)

The RG82 site is at 1518 m above the sea level and located in a shrubland. The site received small amount of precipitation during the SMEX04 period (Fig. 2.8). As for the other sites, the PSR/CX measurements for this site were influenced by the gravelly sandy loam texture at the soil surface. As illustrated in Fig. 2.11a PSR/CX measurements are very low (much below θ_r of soil surface from SSURGO) which was due to overall rock fraction on the soil surface in the pixel. Of the three soil layers considered in modeling this site, the middle layer contained clay (Table 2.1) that impeded water movement. All the three Hydra soil moisture sensors at the depths 0.13, 0.38, and 0.76 m are installed in the middle soil layer (gravelly sandy clay loam). Figures 2.11a-c show very small fluctuations in soil moisture as a result of high retention by the clay content. In the time stability study, *Vachaud et al.* [1985] described the relation between soil water content and soil texture and demonstrated that locations with the high clay content remain most wet at all times. The assimilated and open-loop models performed equally well in describing the soil moisture trend. Comparisons of Hydra measurements with assimilated and open-loop models show a good agreement at all the three depths and the match improved with depth. At this site the Hydra observations were completely contained within ±1 SD of the assimilated model predictions.

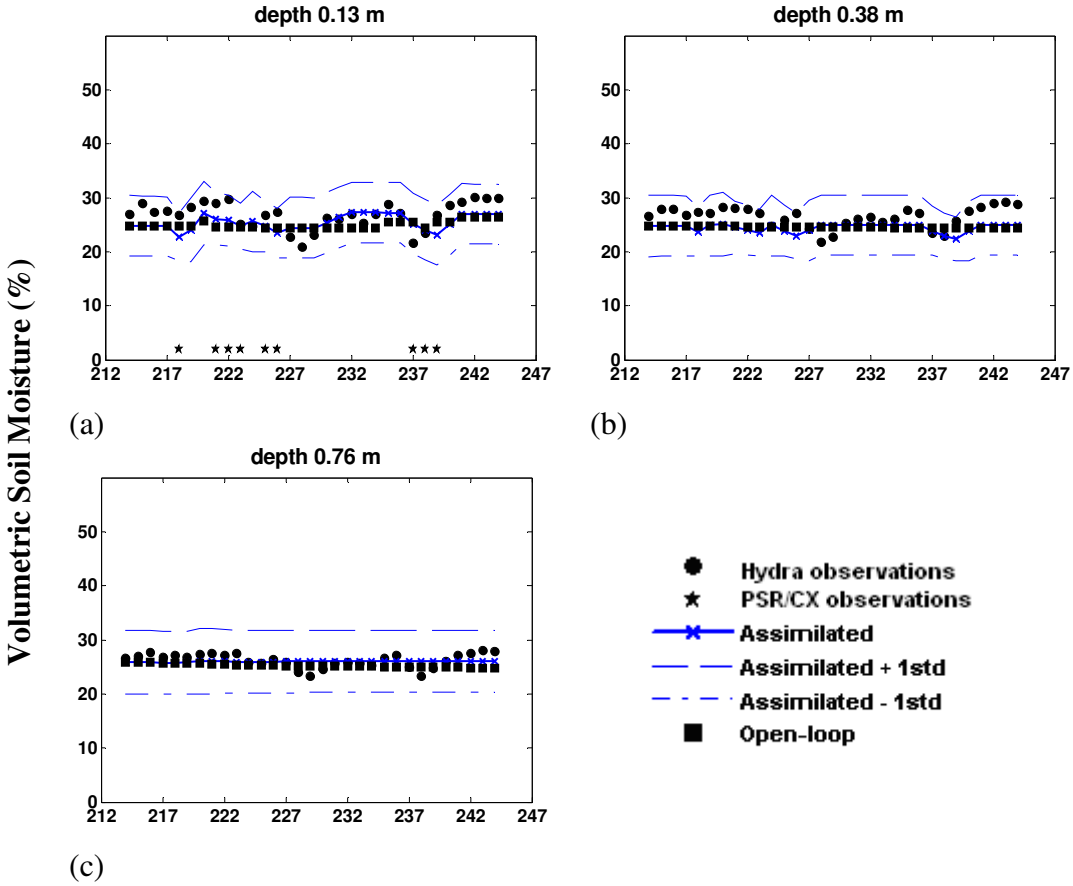

Figure 2.11. Comparison of Vitel (RG82) soil moisture observations with model (with assimilation) simulated soil moisture at depth of (a) 0.13 m, (b) 0.38 m, and (c) 0.76 m of Walnut Gulch Experimental Watershed (WGEW).

Spatio-Temporal Variability of Soil Moisture in WGEW

From the results presented above for the three test sites, it is evident that the assimilated model ensembles for a particular pixel reasonably describe the variability present at the respective depths. The averages from these ensembles for 224 different pixels are used to characterize the soil moisture states at various depths across the

WGEW (Figs. 2.12). Western et al. (2002) showed that the normal distribution fits best for spatial representation of soil moisture. A kernel smoothing technique [*Silverman*, 1981] was used to compute the normal probability density of soil moisture at the depths of 0.01, 0.05, 0.10, 0.20, 0.50, 0.75, 1.00, 1.50, and 3.50 m at the WGEW scale. At each depth 31 (daily) realizations of probability density (Fig. 2.12) from DOY 214 to 244 (August 1st to August 31st 2004) are presented using 22400 (224 footprints X 100 ensembles) soil moisture estimates.

Figures 2.12a-i reveal the transition of soil moisture probability densities and describe the temporal variability across the soil profiles in the WGEW. For most of the days between DOY 214 to 244, unimodality in soil moisture probability density was observed in the top 0.05 m depth (Fig. 2.12a-b). Variation in magnitude of the peak densities for 31 days is apparent at the depth of 0.01 m (Fig. 2.12a). We suggest that the change in the mean and variance of the daily soil moisture probability densities at the 0.01 m depth (Fig. 2.12a) is due to the highly variable (localized) convective summer precipitation patterns across the WGEW. However, at 0.05 m depth, the variation in soil moisture probability density peaks is less pronounced as compared to the probability density at the 0.01 m depth. [*Western, et al.*, 2002] found that the bounded normal probability densities of soil moisture become skewed and less variable as the means approach the lower bound i.e., residual water content. In our study, as the Gaussian kernel estimates at shallow depths (0.01 and 0.05 m, Fig. 2.12a-b) approach the lower boundary, probability densities become positively skewed with small spread/variation. This behavior is also consistent with the findings of [*Famiglietti, et al.*, 1999]. It is

noteworthy that during the SMEX04 period no shift was observed from positively skewed (dry: near lower bounds) to moderate (midrange of wetness) or negatively skewed (wet: near upper bounds) probability densities at 0.01 m and 0.05 m depths. This limited variation in soil moisture skewness indicates an absence of uniform rainfall events over the whole watershed domain as illustrated in Fig. 2.5. Further, positively skewed narrow densities with little or no variation were attributed to a very conductive (sandy texture) top soil layer and little precipitation at WEGW.

With increasing depth (0.10 m to 3.50 m), realizations with multi-modal kernel density estimates were observed (Fig. 2.12c-i). Mixture of distinct Gaussian probability density functions (PDFs) was apparent in these multimodal densities. The persistence of these distinct Gaussian PDFs in the multimodal densities was observed at specific soil moisture values. Little difference in mean and variance was observed in the distinct Gaussian PDFs across the DOYs (Fig. 2.12c-i). Also, multimodality of probability density was much more pronounced for the deeper depths than near the soil surface (Fig 2.12). A spike in probability distribution was detected at the depth 1.50 m (Fig. 2.12h). A logical explanation for this spike is internal drainage or redistribution. During redistribution, relatively deeper layer (at 1.50 m) draw soil moisture from the upper layers. It is apparent from Fig. 2.12e-g, that nominal spikes were also present for DOY 214-225 at the depths of 0.50 m, 0.75 m, and 1.00 m. The time-varying rate of redistribution depends not only on the hydraulic properties of the conducting soil but also on the initial soil moisture status (wetting front depth and the relative dryness of the deeper layers). When the initial wetting front depth is small and the underlying soil is

relatively dry, the hydraulic gradient augmenting the gravitational gradient are likely to be strong and hence induce a rapid rate of redistribution.

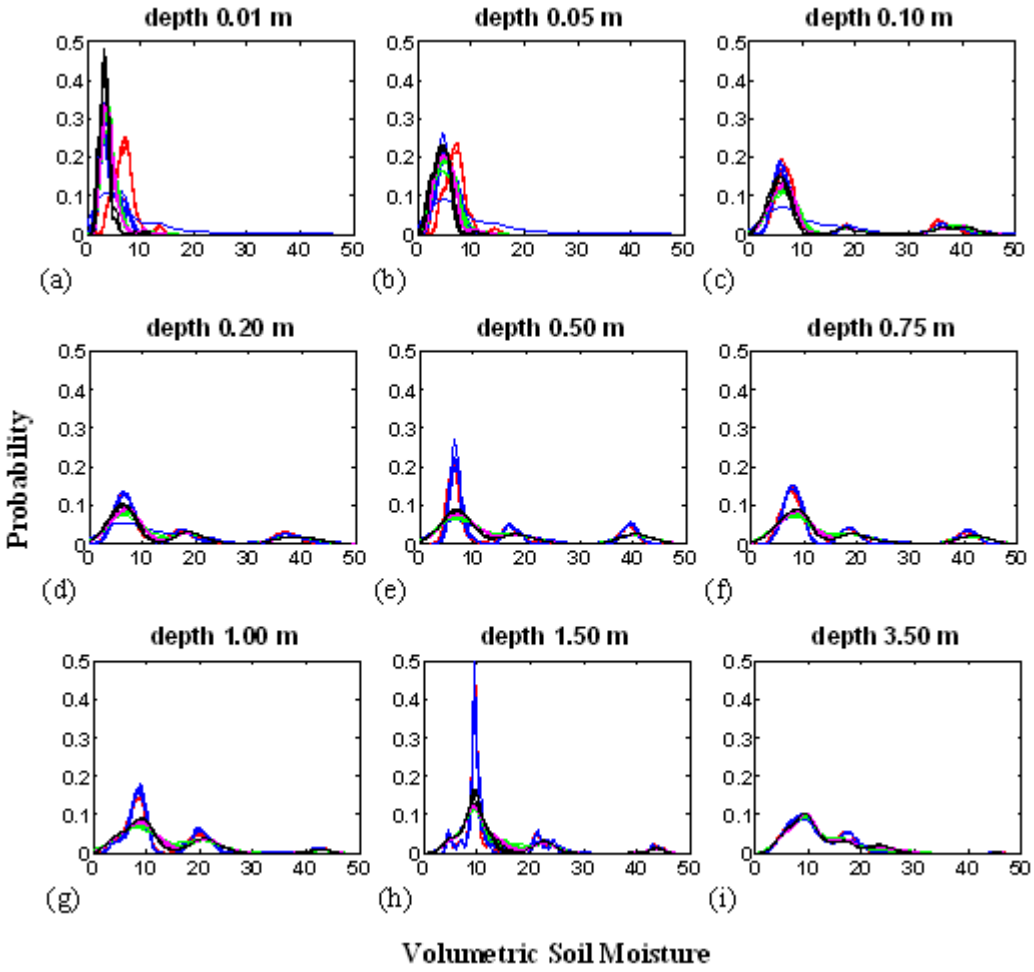

Figure 2.12. Walnut Gulch Experimental Watershed (WGEW) soil moisture densities at depth of (a) 0.01 m, (b) 0.05 m, (c) 0.10 m, (d) 0.20 m, (e) 0.50 m, (f) 0.75 m, (g) 1.00 m, (h) 1.50 m, and (i) 3.50 m at resolution of 800 m X 800 m.

To understand the spatial variability of soil moisture across the WGEW, *kmean* clustering [*Jain and Dubes*, 1988] was conducted on 22400 (224 footprints X 100 ensembles) soil moisture estimates at the depths of 0.01, 0.05, 0.10, 0.20, 0.50, 0.75, 1.00, 1.50, and 3.50 m for all 31 days of SMEX04. Table 2.2 shows the number of spatial clusters of soil moisture at specified depths in WGEW. Table 2.2 also provide spatial clustering of texture related soil hydraulic properties i.e., saturated hydraulic conductivity (K_{sat}), residual water content (θ_r), and saturated water content (θ_s) across the WGEW. Number of clusters of θ_r and θ_s are nearly similar at all the specified depths, whereas in case of K_{sat} the number of spatial clusters increases with the depth. The smaller number of K_{sat} spatial clusters (4 clusters for 0.05 m depth) corroborate with the presence of large percentages of rock and gravel fraction on the soil surface. Based on the groupings of saturated hydraulic conductivity and soil moisture spatial clusters, three distinct depth-dependent zones (i) 0-0.05 m, (ii) 0.05-0.75 m, and (iii) below 0.75 m can be identified in the soil profile. The number of clusters in the spatial distributions of soil moisture for the depths of 0.01 m, 0.05 m, and 0.75 m were somewhat matching to the modality in the respective probability distributions in Fig. 2.12. Also note that a sudden increase in the number of soil moisture spatial clusters was observed below 1.00 m depth. The numbers of spatial clusters found at these deeper depths were close to the number of soil textures encountered at these specific depths. Based on these findings we suggest that soil texture takes control of soil moisture evolution and spatial distribution with increasing depth and with lesser influence from forcings and feedbacks at the land-atmosphere boundary. At the depths between 0.05 and 1.00 m, plant roots play a major

role in describing the status of soil moisture. In our SWAP model simulations the maximum rooting depth was prescribed to be 1.00 m. Plant root water uptake is largely controlled by soil water status and spatial (horizontal-vertical) variability of soil moisture. Root-soil interaction tends to equalize soil water content in the root-zone. The tendency of homogenization of soil moisture at these depths resulted in three spatial clusters which could be attributed to root dynamics of various vegetation types present in the WGEW. The phenomenon of homogenizing soil moisture in the root zone also reduces soil water flux variability.

Table 2.2. Spatial clusters (SC) of soil moisture and hydraulic parameters across WGEW at specified depths.

Soil profile depth in m	Soil moisture SC	Saturated Hydraulic Conductivity (K_{sat}) SC	Residual Water Content (θ_r) SC	Saturated Water Content (θ_s)SC
0.01	1	4	14	11
0.05	2	4	14	13
0.10	3	7	12	14
0.20	3	8	13	11
0.50	3	9	14	13
0.75	3	9	10	12
1.00	8	10	12	12
1.50	9	10	11	11
3.50	12	10	10	10

Based on the above results it is clear that a coarse spatial resolution of 800 m X 800 m and daily time scale for model simulations influence the evolution of profile soil moisture and other hydrologic responses in WGEW during SMEX04. Furthermore, because of the scanty and scattered nature of rainfall within WGEW during the SMEX04 period and highly conductive nature of the top soil layer, no significant surface runoff

and runon were observed at a coarse resolution of 800 m X 800 m. The topographic control on spatial distribution of soil moisture was not apparent due to sustained dry period. This finding agrees with those of *Chang and Islam* [2003], where they demonstrated that soil physical properties and topography control spatial variations of soil moisture over large areas. They have shown that topographical control dictates soil moisture distribution under wet conditions, and soil physical properties control variations of soil moisture under drier conditions. Based on these arguments and our results we suggest that at the remote sensing pixel scale the effect of topography and patchy rainfall on the spatio-temporal distribution of soil moisture at the soil surface and deeper depths was not found to be as significant as that of soil texture in the WGEW during SMEX04.

2.5. Summary and Conclusion

The distribution, behavior, and evolution of soil moisture at various depths in the Walnut Gulch Experimental Watershed, Arizona, during SMEX04 were studied. Aircraft based remotely sensed surface soil moisture for the WGEW was assimilated using EnSRF to model root zone soil moisture up to a depth of 3.86 m. The modeled root zone soil moisture was evaluated with *insitu* measurements from several Hydra and SCAN sites. The comparison shows significant benefits of providing better soil layer/property information, and the propagation of EnSRF Kalman gain through the land surface model SWAP. Reasonable agreement was observed for the shallow depths (0-0.50 m). Most of the measurements at these depths were within ±1 standard deviation of the modeled soil

moisture. The models with assimilation and without assimilation (open-loop) performed equally well at deeper depths using soil layer information from the SSURGO database. The results also demonstrated the impact of data assimilation of PSR/CX-based surface soil moisture measurements reaching deeper layers having similar hydraulic properties. In case of the presence of deeper soil layers (with different hydraulic properties from the surface soil layer) the propagation of information during data assimilation from the soil surface to deeper layers was found to be ineffective. The ensembles from the PSR/CX-assimilated model output were used for characterizing the probability densities of soil moisture at several depths. The soil moisture probability densities revealed the temporal evolution across the soil profile in the WGEW. Unimodality in soil moisture densities was observed for the top 0.05 m of soil, whereas multimodality was observed for the deeper soil layers for all 31 days of SMEX04. Multimodality in probability density became more pronounced with depth across the soil profile. Almost no appreciable temporal variation in soil moisture probability densities were observed at any depth between 0.01 and 3.50 m. An increase in the number of soil moisture spatial clusters with depth was found and could to be related to the number of soil textures encountered at the deeper depths (below 1.00 m). An increase in soil moisture spatial clusters suggests that soil texture took control of space-time evolution with increasing depth, while the impact of land-atmosphere interaction diminished. With a coarser resolution of 800 m X 800 m and a temporal resolution of one day, the effect of existing conditions of geophysical factors (e.g., topography, rainfall) on the distribution of soil moisture at deeper depths were found to be less significant in the WGEW during SMEX04.

Further investigation is warranted involving different data assimilation schemes and how they affect the evolution of root-zone soil moisture with the use of single layer as opposed to multilayer soil information in different hydroclimatic conditions. Besides, we need to develop an improved modeling/assimilation framework to accommodate higher spatial and temporal resolutions to study diurnal variations in precipitation and other meteorological forcings (e.g., air temperature, wind speed) which may be present at the study site.

CHAPTER III

A MCMC ALGORITHM FOR UPSCALED SVAT MODELING TO EVALUATE SATELLITE-BASED SOIL MOISTURE MEASUREMENT

3.1. Synopsis

A Markov Chain Monte Carlo (MCMC) based algorithm was developed to derive upscaled land surface parameters for a Soil-Vegetation-Atmosphere-Transfer (SVAT) model using time series data of satellite measured atmospheric forcings (e.g., precipitation), and land surface states (e.g., soil moisture and vegetation). This study focuses especially on the evaluation of soil moisture measurements of the AQUA satellite based AMSR-E instrument using the new MCMC-based scaling algorithm. Soil moisture evolution was modeled at a spatial scale comparable to the AMSR-E soil moisture product, with the hypothesis that the characterization of soil microwave emissions and their variations with space and time on soil surface within the AMSR-E footprint can be represented by an ensemble of upscaled soil hydraulic parameters. We demonstrated the features of the MCMC based parameter upscaling algorithm (from field to satellite footprint scale) within a SVAT model framework to evaluate the satellite-based brightness temperature/soil moisture measurements for different hydroclimatic regions, and identified the temporal effects of vegetation (LAI) and other environmental factors on AMSR-E based remotely sensed soil moisture data. The SVAT modeling applied for different hydroclimatic regions revealed the limitation of AMSR-E measurements in high vegetation regions. The study demonstrated the potential to

improve upon the AMSR-E measurements by assimilating the soil moisture evolution from the proposed upscaled SVAT model. The technique also has the potential to derive upscaled parameters of other geophysical properties used in remote sensing of land surface states. The developed MCMC algorithm with SVAT model can be very useful for land-atmosphere interaction studies and further understanding of the physical controls responsible for soil moisture dynamics at different scales.

3.2. Motivation

Studies [*Claussen*, 1998; *Delworth and Manabe*, 1989; *Foley*, 1994; *Texier, et al.*, 1997] have shown that the initial/boundary (I/BC) values of state variables (e.g., soil moisture, soil temperature, vegetation water content) at various spatial and temporal scales in the land surface exert strong controls on hydrologic, climatic and weather related processes. Hence, measuring these state variables is crucial for flood forecasting, natural resource management, agronomic crop management, and regional/global climate simulation. There are various ways to measure the state variables depending upon the spatial scale of interest. In-situ techniques provide reasonably accurate measurements of state variables at the local-scale, at desired time intervals. Direct incorporation of in-situ measurements as I/BC in large scale models has limitations due to its very small spatial support. Satellite-based remote sensors measure spatially integrated measurements of state variables with temporal sampling that depends upon the orbital placement of the satellites. This makes satellite-based measurements suitable for I/BC in large scale modeling. However, the quality of satellite-based land parameter measurements is often

questionable due to uncertainties introduced by atmospheric attenuation, clouds, rainfall, and the inherent variability present in geophysical properties and state variables, which influence the measurements and their calibration and validation. The extent and spatial resolution of satellite-based measurements can also introduce complex scale effects [*Western, et al.*, 2002]. Conventionally, satellite-based measurements are validated using ground-based measurements, but this approach is also limited in accounting for scale effects and heterogeneity within the large footprints. In this study we focus primarily on developing a physically-based soil hydrologic model at the satellite footprint scale, including parameter upscaling and a soil moisture data assimilation scheme.

The Advanced Microwave Scanning Radiometer (AMSR-E) on the Earth Observing System Aqua satellite is currently used for global soil moisture mapping [*Njoku, et al.*, 2003]. AMSR-E measures radiation at six frequencies in the range 6.9–89 GHz with dual polarization. It covers the globe in approximately two days or less with a swath of 1445 km. The spatial resolution at the surface varies from approximately 60 km at 6.9 GHZ to 5 km at 89 GHz [*Njoku, et al.*, 2003]. The current ASMR-E soil moisture algorithm is based on a change detection approach using polarization ratios (PR) of the calibrated AMSR-E channel brightness temperatures [*Njoku and Chan*, 2006]. The accuracy of the soil moisture algorithm has been investigated on short time scales during calibration/validation field campaigns of the Soil Moisture Experiments in 2002, 2003, and 2004 (SMEX02, SMEX03, and SMEX04) [*Bindlish, et al.*, 2006a; *Bindlish, et al.*, 2005; *Jackson, et al.*, 2005a]. Results show some level of consistency and calibration stability of the observed brightness temperatures at specific locations. However there

have been concerns regarding the spatial variability of the retrieved soil moisture biases over areas with different amounts of vegetation. AMSR-E measurements have shallow measurement depth (1 cm or less) and coarse spatial resolution (~60 km x 60 km) which, combined with subgrid and grid scale variability, also impose limitations on the retrieval algorithm and its operational accuracy.

Measurements of microwave emissions show sensitivity to soil moisture through the effects of moisture on the dielectric constant and hence emissivity of the soil [*Ulaby, et al.*, 1986]. The large contrast between the real part of the dielectric constant of water and that of dry soil translates into a difference of up to 100 K or more in brightness temperature between very dry and very wet soils [*Njoku and Kong*, 1977; *Wang*, 1980; *Wang and Choudhury*, 1995]. The surface geophysical properties, i.e., soil characteristics (surface roughness and soil texture) and vegetation, also affect the microwave emissivity. Vegetation acts as an attenuating and emissive layer over the soil [*Jackson and Schmugge*, 1991; *Njoku and Chan*, 2006; *Ulaby and Wilson*, 1985] and is characterized mainly by its water content and geometrical structure. The net effect of vegetation is a reduction in sensitivity that makes it more difficult to estimate soil moisture accurately over vegetated terrain. At AMSR-E frequencies (6.6 GHz and higher) the sensitivity to soil moisture becomes very low when the leaf area index (LAI) exceed 2.0 [*Njoku and Li*, 1999]. Surface roughness adds another dimension of complexity due to surface scattering [*Choudhury, et al.*, 1979; *Njoku and Chan*, 2006] which affects the emissivity. The net effect of surface roughness can be difficult to establish, especially when dealing with inhomogeneous elements. Soil texture, ranging

from sand to clay, also influences the emissivity of the soil. Sandy-textured soil has the highest emissivity at all frequencies which is influenced by least specific surface area of soil that leads to lowest bound water [*Wang and Schmugge*, 1980].

The uncertainty in estimating microwave emissivity at the AMSR-E footprint scale is affected also by the heterogeneity of the vegetation, surface roughness, and soil moisture within the footprint. Soil moisture exhibits heterogeneity due to variability in a number of geophysical parameters (soil properties, vegetation, topography, and precipitation). The soil moisture distribution at a particular spatio-temporal scale within an AMSR-E footprint evolves from complex interactions among these geophysical parameters [*Dubayah, et al.*, 1997; *Western, et al.*, 2002]. Soil properties always exhibit significant spatial variability that characterizes the soil moisture status and transport processes. For example, *Rodriguez-Iturbe, et al.* [1995] suggested that the spatial organization of soil moisture is a consequence of the soil properties; *Tomer et al.* [2006] found significant correlation between soil properties and soil moisture at the watershed scale; and [*daSilva, et al.*, 2001] showed that temporal stability in soil moisture patterns can be associated with the arrangement of soil types and textures at the landscape scale. Soil texture is also related to topographical attributes such as surface curvature, slope, and elevation. *Mohanty and Mousli* [2000], *Pachepsky et al.* [2001], and *Leij et al.* [2004] demonstrated that soil hydraulic properties relate to relative landscape positions in topographically complex landscapes, and [*Chang and Islam*, 2003] demonstrated that soil physical properties and topography together control spatial variations of soil moisture over large areas. They showed that topographical control dictates the soil

moisture distribution under wet conditions, and soil physical properties control variations of soil moisture under relatively dry conditions. Infiltration properties of soil are influenced by vegetation at the plant scale [*Seyfried and Wilcox*, 1995] or tillage/cropping practice at the field scale [*Mohanty et al.,* [1994b]. In a recent study, *Sharma et al*. [2006] discovered that including remotely sensed vegetation parameters in addition to soil texture and topographic features improved the predictability of soil hydraulic properties across Little Washita watershed in Oklahoma using artificial neural networks. These spatially overlapping geophysical attributes define the functional organization of soil hydrological processes, and in turn soil moisture variability. The evolution of the soil moisture state within the AMSR-E footprints is primarily forced by precipitation. For this study subgrid variability of precipitation is not considered. The partitioning and transport of the water above and below the land surface is mainly controlled by soil hydraulic properties which are in turn influenced by soil types, texture, topography, and vegetation. In summary, the emitted microwave radiation (brightness temperature) of the soil observed at the 60 km x 60 km AMSR-E footprint scale is a weighted integral of the soil moisture distribution, as influenced by the variability in soil hydraulic properties within the footprint. *Camillo et al.* [1986] have also shown that remotely-sensed soil moisture may be inverted to estimate soil hydraulic properties using a microwave emission model and soil moisture and temperature profiles generated by moisture and energy balance equations. Application of such approaches on a regional scale may generate large-scale soil properties for input into mesoscale land-atmosphere models. Regional soil properties may be estimated by inversion of dynamic one-

dimensional soil-water-vegetation model in conjunction with soil moisture obtained from microwave remote sensing.

Based on the above discussion we hypothesize that an ensemble of soil hydraulic properties describing the soil moisture dynamics within the AMSR-E footprint can be used to determine the microwave emission from the surface soil layer. In other words, the ensemble of soil hydraulic properties can suitably characterize the variability present within the AMSR-E footprint. Although at a field scale, *Burke et al*. [1997] demonstrated retrieval of soil hydraulic properties from the time series of the measured brightness temperature over agricultural fields. There could be some concern, however, about the validity of using an ensemble of local soil hydraulic properties to represent conditions at the remote sensing footprint scale. Soil hydraulic properties are defined at the point to field scale, whereas soil is conceptualized as a hierarchical heterogeneous medium with discrete spatial scales, e.g., *Roth et al.* [1999]. It is argued that the natural pattern of soil variability may exhibit embedded, organizational structures that lead to non-stationary soil hydraulic properties and processes. With an increase in spatial scale (extent), soil hydraulic properties typically become non-stationary. The soil hydraulic properties may change from deterministic at smaller scale to more random at larger scale, with the small scale soil properties filtered out by larger scale soil related processes [*Kavvas*, 1999]. Thus, upscaling of soil properties is required to understand the physical processes, and characterize the evolution of soil moisture and in turn soil emissivity, at the AMSR-E footprint scale.

The primary objective of this study is to develop a procedure, using a Markov Chain Monte Carlo (MCMC) algorithm, for estimating upscaled land surface parameters to be used in a SVAT model for evaluating satellite-based land surface state measurements. The performance of the upscaled parameters and SVAT model can then be tested using selected AMSR-E footprints in three different hydroclimatic conditions to evaluate the satellite-based soil moisture product.

3.3. Approach

Effective soil hydraulic parameters are a representative set of parameters that characterize a footprint-scale domain and approximate the flux equivalent to the aggregated flux obtained from distributed modeling within the domain [*Kabat, et al.*, 1997; *Zhu and Mohanty*, 2003]. Footprint-scale effective soil hydraulic parameters are vital to hydroclimatic studies since such studies commonly use soil-vegetation-atmosphere-transfer (SVAT) models whose sub-surface flow components are based on the Darcian flow equation [*Demarty, et al.*, 2005]. The soil hydraulic parameters used in SVAT models are physically defined at a local measurement scale (mostly at point to field scale). Therefore, soil hydraulic parameter upscaling from field scale to hydroclimate grid or satellite footprint scale is critical for SVAT model performance at these scales. The difficulty of upscaling soil hydraulic parameters to the footprint scale stems from the inherent spatial variability of soil properties and the non-linear dependence of soil moisture. Our strategy here is to develop a new approach for estimating upscaled soil hydraulic parameters. We follow a method that derives upscaled

hydraulic parameters directly from explicit information on the soil moisture state at the AMSR-E footprint scale and the stochastic variability of soil hydraulic parameters at the much smaller (local) scale within the footprint. Using ensembles of upscaled soil hydraulic parameters, large scale fluxes and states at the land surface can be determined that are compatible with the microwave emission from the surface soil layer at the footprint scale.

The algorithm developed for this approach uses a Bayesian methodology that provides an effective and efficient tool for combining two or more discrete sources of information, model output and observed data. The algorithm is used to merge prior information on an arbitrary number of soil hydraulic parameters, with the information content of the related soil moisture data, to find SVAT model parameter estimates. The algorithm is particularly useful when extracting target (soil hydraulic property) characteristics from remotely sensed (e.g., AMSR-E soil moisture) data. The Bayesian technique can produce full probability distributions for an arbitrary number of parameters. In practice, the probability distributions can be considered to represent either the imprecise knowledge regarding the true value of the parameter, the natural variability of the parameter, or a combination of the both. In the procedure, the inference about the set of soil hydraulic parameters is obtained after integrating all possible combinations of the soil hydraulic parameters in the full joint probability posterior distribution. In this study the integration is performed on the set of parameters using a Markov Chain Monte Carlo (MCMC)-based numerical method.

MCMC Algorithm

Bayesian methods provide a framework within which pre-existing knowledge about the parameters of a model can be combined with observed data and model output. These results in a probability distribution of the parameter space (posterior distribution) that summarizes uncertainty about the parameters based on the combination of pre-existing (or prior) knowledge and the sampled data values. In this study, the uncertainties in accurately determining the parameters of the nonlinear soil water retention function for large scale hydrological modeling is the focus of the development of the Bayesian framework. The Bayesian approach takes the parameters of the model as random variables [*Gelman, et al.*, 1995] with particular probability density functions (pdfs). Thus, in addition to the determination of a likelihood function, the process of Bayesian inference may require the specification of prior pdfs that summarize the prior knowledge. Figure 3.1 illustrates the methodology of the Bayesian framework. Here, the likelihood function is the time series of AMSR-E derived soil moisture data D = $\{\theta_1, \theta_2,.., \theta_t\}$ at a particular grid point. The priors are defined as the soil hydraulic parameters (shown in eq. 3.1) of the dominant soil types based on Soil Survey Geographic (SSURGO) database within the particular AMSR-E footprint. These soil hydraulic parameters are used in the Mualem-van Genuchten functions [*Mualem*, 1976; *van Genuchten*, 1980]:

$$S_e = \frac{\theta(h) - \theta_{res}}{\theta_{sat} - \theta_{res}} = \left[\frac{1}{1 + |\alpha h|^n}\right]^m \tag{3.1}$$

$$K(S_e) = K_o S_e^{\,l}\{1 - [1 - S_e^{\,n/(n-1)}]^{1-1/n}\}^2 \tag{3.2}$$

where, water content θ is a nonlinear function of pressure head h, S_e is the relative saturation (-), θ_{res} and θ_{sat} are the residual and saturated water contents (cm^3 cm^{-3}) respectively, α (cm^{-1}), n (-), m (-) and λ (-) are shape parameters of the retention and the conductivity functions, K_{sat} is the saturated hydraulic conductivity (cm d^{-1}), and m=1-1/n. The values of these parameters are distinct amongst soil (textural) types and are defined at the local or field scale. By virtue of the variability in soil types within an AMSR-E footprint, very relaxed pdfs (high standard deviations, σ) were defined for the soil parameters as priors. A normal distribution was assigned to all parameters, e.g., θ_{res} ~ N($\mu_{\theta res}$, $\sigma_{\theta res}$) based on the UNSODA database [*Nemes, et al.*, 2001]. In principle, non-normal priors could be used as well, but the computational complexity would increase considerably. If no prior information from the SSURGO database is available for the soil parameters except for their ranges, uniform pdfs are assigned in the valid ranges. For computational simplicity, random samples are drawn independently from the pdfs of different soil hydraulic parameters to form a field scale parameter set (θ_{res}, θ_{sat}, α, n, K_{sat}). A scaling parameter β (with a uniform distribution between 0 and 1) is introduced in our algorithm to account for the scale disparity. Thus, β relates the soil hydraulic parameters at the field scale to the effective soil hydraulic parameters at the ASMR-E footprint scale. The general relationship used in this study for upscaling of any of the soil hydraulic parameters in the Mualem-van Genuchten relationship (eq. 3.1), can be written as (e.g., for θ_{res})

$$(\theta_{res})_{eff} = (\theta_{res})^{\beta} \tag{3.3}$$

where $(\theta_r)_{eff}$ is the effective value of the residual water content at the ASMR-E footprint

scale. Thus, for upscaling the field-scale parameters, eq. 3.3 was used to form a set of upscaled parameters, $z_i = (\theta_{res}^{\beta i}, \theta_{sat}^{\beta i}, \alpha^{\beta i}, n^{\beta i}, K_{sat}^{\beta i})_i$, where i is a realization of the MCMC and the upscaling parameter βi represents the corresponding upscaling parameter drawn randomly from a uniform distribution between 0 and 1.

By applying Bayes' theorem, the conditional posterior pdf, $P(Z|D)$, given the measured values of D, is described as:

$$P(Z \mid D) = \frac{P(Z)\,P(D \mid Z)}{P(D)} \tag{3.4}$$

where $P(Z)$ is the prior joint pdf for the upscaled soil hydraulic parameters $Z = \{z_1, z_2, \ldots, z_m\}$. The $P(D)$ is a normalization factor and $P(D|Z)$ is the likelihood derived from measured AMSR-E soil moisture footprint values given Z. To describe the AMSR-E data, a normal (pdf) likelihood was introduced. Once the joint pdf is obtained, given specific values for D**,** the marginal posterior pdf that retains exclusively the dependence on one parameter (e.g., θ_{res}^{β}) can be obtained as follows:

$$P(\theta_{res}^{\beta} \mid D) = \frac{\int\int\int\int P(D \mid Z)\,P(Z)\,d\theta_{sat}^{\beta} d\alpha^{\beta}\, dn^{\beta}\, dK_{sat}^{\beta}}{P(D)} \tag{3.5}$$

$$P(D \mid Z) \propto \prod \frac{exp(\frac{(D - \theta(h))^2}{2\sigma^2})}{\sigma} \tag{3.6}$$

$$P(Z) \propto exp(-\frac{1}{2}(Z - \mu)^T \Sigma^{-1} (Z - \mu)) \tag{3.7}$$

where, Σ is the covariance matrix of the soil hydraulic parameters, and μ is the vector of means of the parameters. This marginalization could potentially be an intractable task

because of the high-dimensional integration in eq. 3.5. This could happen when the retrieval process is applied to situations where there are more than two soil parameters to be estimated, and when the resulting pdf does not have a standard form. A possible solution is to estimate the form of the posterior pdf by generating samples by means of the Markov Chain Monte Carlo (MCMC) method [*Brooks and Roberts*, 1998]. The mean, variance, and higher order moments for the parameters can be calculated from the numerically approximated pdf's of the MCMC. We use the MCMC to perform the integration required for the evaluation of eq. 3.5. More specifically, we used the Metropolis algorithm for the Markov Chain Monte Carlo (MCMC) method with a simple random walk to describe the posterior distribution, representing the ensemble of soil hydraulic parameters for the AMSE-E footprint. The Metropolis algorithm [*Metropolis and Ulam*, 1949] has been widely used in Bayesian applications because of its simplicity and its efficiency. Its principle can be summarized as follows: starting from a vector generated at iteration i-1, a new candidate vector is generated based on a symmetric jump distribution. The SVAT model (addressed below) is run with the new candidate vector (proposed soil hydraulic parameters) and the surface soil moisture generated from the model is compared with the AMSR-E measurements. If this new candidate vector leads to an increased probability of the target distribution, it is accepted as the generated value at iteration i. Otherwise, the ratio between the new and the previous value of the target distribution is computed, and used as the acceptance probability of the candidate vector. In case of rejection, the generated vector at iteration i remains the same as that at iteration i-1. The Metropolis algorithm was used in this paper

with a Gaussian jump distribution with covariance matrix $\sum$. The MCMC algorithm used in the study is summarized below:

i. Choose a starting point of candidate vector $\pi(0)$ with a covariance matrix $\sum$.

ii. Iterate $i = 1, \ldots, N_{iter}$.

1. Generate a candidate vector based on $\pi^* \sim N(\pi^{(i-1)}, \sum)$

2. If $p(\pi^*|X) \geq p(\pi^{(i-1)}|X)$, set $\pi(i) = \pi^*$, else accept the candidate vector ($\pi(i)=\pi^*$) with probability $r = \frac{p(\pi^*|X)}{p(\pi^{i-1}|X)}$ or reject it ($\pi(i) = \pi^{(i-1)}$) with probability (1-r).

In order to avoid numerical overflows, it is useful to consider the logarithm of the posterior distribution, and to compute the posterior ratio as $r = exp(log(p(\pi^*|X))-log(p(\pi^{(i-1)}|X)))$. Moreover, this ratio is made invariant by multiplying the posterior distribution by a constant, which implies that the Metropolis algorithm can be applied to a non-normalized target distribution. The MCMC algorithm generates a Markov chain (k_n) whose stationary distribution is $\pi(k)$. The posterior distributions of parameters obtained from the MCMC algorithm are further subjected to a process of thinning. The objective of thinning is to decrease the autocorrelation (increasing independence) between samples. Thinning a Markov chain necessitates that the chain be long enough to obtain a sample of the desired size. Thinning was implemented in the algorithm by periodic selection of samples from the MCMC chain at a specified rate to form an ensemble of soil hydraulic parameters.

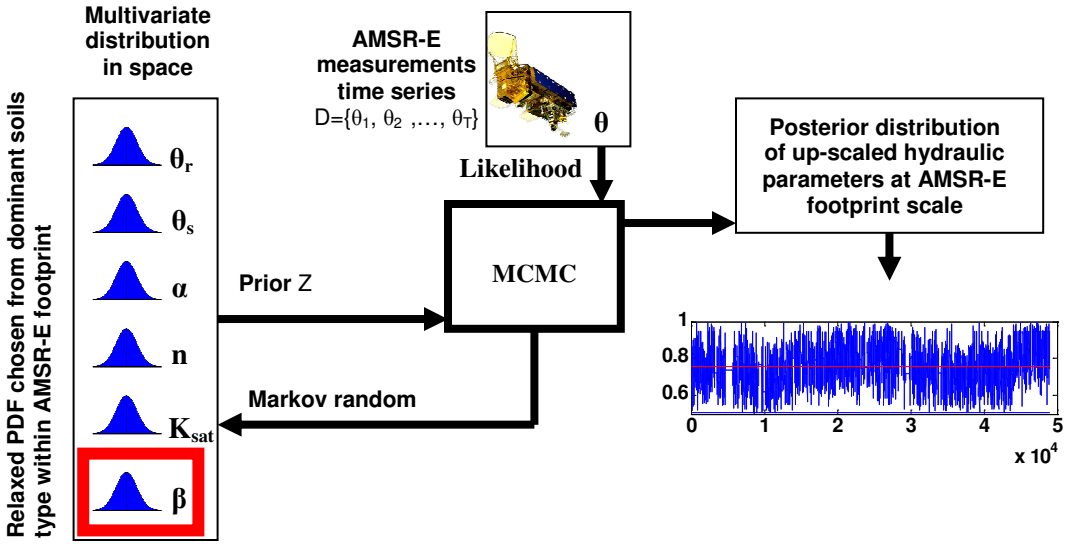

Figure 3.1. Markov Chain Monte Carlo (MCMC) based schematic for deriving upscaled soil hydraulic parameters.

SVAT Modeling for Soil Moisture Estimation

Key challenges in using SVAT models for very coarse scale (e.g., AMSR-E footprint scale) hydrologic modeling are the selection of governing flow equations, setting accurate boundary conditions, and defining the modeling domain. For this study, we used the parallel non-interacting soil column approach [*Milly*, 1988; *Peck, et al.*, 1977] that allows a variety of modeling concepts for soil water processes in heterogeneous conditions. In this stream-tube approach, the horizontal spatial heterogeneity is represented by an ensemble of upscaled soil hydraulic parameters and is conceptualized as bundle of independent parallel soil columns. At the large spatial scale, the stream tube approach suits well the hypothesis of negligible lateral interflow across

adjacent soil columns within the modeling domain. In a previous study, *Zhu and Mohanty* [2002] analyzed the magnitude of the lateral flow component in parallel soil columns and found them of minor importance. We also assumed that the 1-D Richards' equation is an appropriate physical model to simulate the vertical partially-saturated flow and partitioning of fluxes at such coarse spatial scale. Numerical studies conducted by *Mantoglou* [1992], and *Zhang* [1999] on general upscaled Richards' equations have shown that at large spatial scales and in the absence of lateral flow, vadose zone flow can be represented by the one-dimensional Richards' equation. We used the SWAP model [*Van Dam, et al.*, 1997] to simulate the processes of the soil-water-atmosphere-plant system. SWAP is a physically-based, hydrologic model that numerically solves the one-dimensional Richards' equation for simulating the soil moisture dynamics in the soil profile under different climatic and environmental conditions. Irrespective of scale, for transient isothermal unsaturated water flow in non-swelling soil, Richards' equation as used in SWAP is described by

$$\frac{\partial \theta}{\partial t} = \frac{\partial}{\partial z}\left[K\left(\frac{\partial h}{\partial z} + 1\right)\right] - S_a(h) \qquad (3.8)$$

where θ is the soil water content (m^3/ m^3), z is the soil depth (m), h is the soil water pressure head (m), K is the unsaturated hydraulic conductivity (m/day), and $S_a(h)$ is the root water uptake (m/day). The Penman-Monteith equation [*Monteith*, 1965] was used to calculate potential evapotranspiration, while potential transpiration (T_p) and soil evaporation (E_p) were partitioned using LAI. In the SWAP model, soil moisture retention and hydraulic conductivity functions are defined by the Mualem-van Genuchten equations, shown in eq. 3.1 and 3.2, respectively.

Modeling Domain

SWAP is a numerical water management tool that can accommodate several combinations of top and bottom boundary conditions. Availability of satellite data to characterize the upper boundary condition as well as the vegetation cover allows study of regional/footprint scale soil water processes. The SWAP model simulates both the soil water quantity and quality with a temporal resolution of one day, along with other state variables. The model has been used in various applications in the past, and has been well validated under different climatic and environmental conditions [*Ines and Droogers*, 2002; *Ines and Mohanty*, 2006; *Wesseling and Kroes*, 1998]. For more detailed descriptions of SWAP the reader can refer to [*Van Dam*, 2000].

A rooting depth of 50 cm for the soil profile with a parallel soil columns concept was used to characterize the AMSR-E soil moisture footprints, keeping in view the scope and objective of this study. For the SWAP model simulations, the 50 cm thick soil profile at each remote sensing footprint was discretized into 50 nodes, with finer discretization near the soil layer interfaces and at the land-atmosphere boundary. Finer discretizations near the top boundary and at layer interfaces were used to handle the steep pressure gradients for the numerical simulations. A time-dependent flux-type top boundary condition was applied for each parallel soil column matching the AMSR-E footprint. A unit vertical hydraulic gradient (free drainage) condition was used at the bottom boundary of the soil profile because of shallow root-zone (50 cm). Given the relatively coarse horizontal scale with shallow root-zone, the parallel soil column model ignores the lateral water fluxes across the adjacent soil columns and only predicts

infiltration, evapotranspiration, and deep percolation following the parallel non-interacting stream-tubes concept of distributed vadose zone hydrology.

Site Description

To study the MCMC based parameter upscaling and SVAT modeling for evaluating soil moisture dynamics in large space-borne AMSR-E footprints, diverse hydroclimatic regions within the USA were selected. As illustrated in Fig. 3.2, large regional area in Arizona (semi-arid), Oklahoma (grassland/pastures), and Iowa (agricultural) regions were selected for the study. All of these regions have been included in previous hydrologic field campaigns (e.g., Southern Great Plains 1997 (SGP97), 1999 (SGP99), Soil Moisture Experiment 2002 (SMEX02), 2003 (SMEX03), 2004 (SMEX04), and 2005 (SMEX05)) whose objectives included calibration and validation of remotely sensed geophysical variables, especially soil moisture. The selected Arizona region comprises 42 AMSR-E footprints covering nearly 26,250 km^2. The landscape consists of perennial shrub cover with low LAI (< 1 m^2/m^2), well drained gravelly sandy loam soil, and moderately rocky and hilly terrains. The Oklahoma regional site encompasses 45 AMSR-E footprints covering nearly 28,125 km^2. Grassland and pasture with rolling topography dominates the landscape, with LAI averaging between 3 and 4 m^2/m^2 and attaining peak value between late spring and summer. Loamy sand, sandy loam, loam, and silty loam are the predominant surface soil textures in the Oklahoma region. The Iowa region, with 35 AMSR-E footprints spanning 21,825 km^2, has mainly a row crop agricultural landscape (nearly 60% corn and 40% soybean in

2002). This site is considered as the pothole region of Iowa because of its undulating terrain. The soil on the surface is mainly silty clay loam with a large percentage of organic matter. During the peak crop growing condition the LAI for this region reaches a high of 4-6 m^2/m^2.

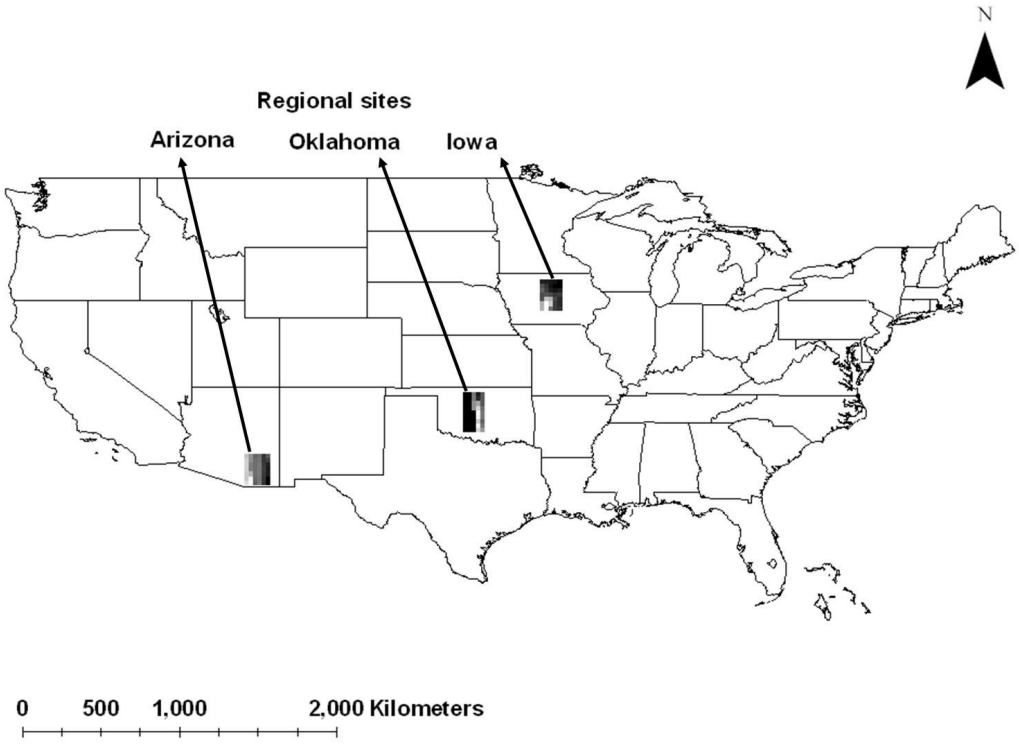

Figure 3.2. Three selected study regions (Arizona, Oklahoma, and Iowa) within the continental United States of America.

Data

AMSR-E soil moisture product

For this study we used two years (2004-2005) of AMSR-E Level-2B gridded data extracted for the three regions (AZ, OK, IA) to evaluate the quality of the AMSR-E soil

moisture product. This Level-2B land surface product includes daily measurements of surface soil moisture, vegetation water content interpretive information, and quality control variables. The data values correspond to a 56 km mean spatial resolution, resampled to a global cylindrical 25 km Equal-Area Scalable Earth Grid (EASE-Grid) spacing. The more reliable night-time AMSR-E data [*Njoku, et al.*, 2003] were used, as soil moisture and temperature profiles remain more uniform, and soil-vegetation temperature differences are smaller during the night than the early afternoon. In other words the soil moisture retrieval algorithm is expected to have less error and be more representative of deeper soil layers using the night-time data.

TRMM and other GPCP calibrated data for precipitation

Precipitation is arguably the most critical input for accurate soil moisture modeling. We used Tropical Rainfall Measuring Mission (TRMM) and other Global Precipitation Climatology Project (GPCP) calibration rainfall product 3B-42 (available at: http://disc.sci.gsfc.nasa.gov/data/datapool/TRMM/01_Data_Products/02Gridded/index. html). The combined instrument rain calibration algorithm (3B-42) uses an optimal combination of products from other satellites to adjust instantaneous rain (IR) estimates from geostationary IR observations. The rainfall data product used in this study has a spatial resolution of 0.25^{o} x 0.25^{o} grid for every 3 hours.

MODIS data for LAI

Eight-day composite LAI data (from the MODIS instrument on the Terra satellite) (http://nsidc.org/~imswww/pub/imswelcome/index.html) with 1-km spatial resolution were used for the study. For soil moisture modeling, the MODIS data was averaged up from 1 km to 56 km resolution to match the AMSR-E footprint.

NCEP/NCAR reanalysis data for atmospheric forcings

The atmospheric forcing data such as relative humidity, air temperature, etc. required for soil moisture modeling was acquired from the 40 years reanalyses products of NCEP (http://www.cdc.noaa.gov/cdc/data.ncep.reanalysis.surfaceflux.html). The NCEP/NCAR 40 years reanalysis uses a state-of-the-art global data assimilation system and a complete available database [*Kalnay, et al.*, 1996].

SSURGO data for soil texture

Soil texture information (fraction of sand, silt, and clay) was required for generating the ensemble of upscaled soil hydraulic parameters. The data was obtained from the Soil Survey Geographic (SSURGO) database (http://www.ncgc.nrcs.usda.gov/products/datasets/ssurgo/). SSURGO is the most detailed level of soil mapping done by the Natural Resources Conservation Service (NRCS). Mapping scales generally range from 1:12,000 to 1:63,360.

3.4. Results and Discussion

Upscaled Soil Hydraulic Parameters

The approach described above was applied in the Arizona, Oklahoma, and Iowa regions, each encompassing several AMSR-E footprints. The SVAT model was run within the MCMC framework for one complete year (2004). The soil moisture evolutions from first two months (January and February, 2004) were not used in evaluating the proposal probability distribution of soil hydraulic parameters during the MCMC runs (as mentioned in previous section). This was necessary to eliminate the effects of initial conditions imposed across the profile of soil layers. Soil moisture states at the land surface were selected for 30 days in 2004 coinciding with the AMSR-E footprints to evaluate the proposal probability in MCMC sampling. A key issue in successful implementation of MCMC sampling is the number of runs (steps) until the chain approaches stationarity (length of the burn-in period). A poor choice of starting values and/or proposal probability distribution of soil hydraulic parameters can greatly influence the required burn-in time. The use of the SSURGO database for soil texture information, and corresponding parameter distributions from the UNSODA database, eliminated the possibility of choosing poor starting values from proposed parameter distributions. For this study, the MCMC chain was run 50,000 times, and the first 5,000 burn-in were discarded. An acceptance ratio of nearly 7-10% was realized during MCMC for all the AMSR-E footprints used in the study. For illustration, the mixing of chain (evolution of soil hydraulic parameters from MCMC) for upscaled parameters $(\theta_{res}^{\beta}, \theta_{sat}^{\beta}, \alpha^{\beta}, n^{\beta})$ selected randomly at the AMSR-E footprint scale from the Arizona,

Iowa, and Oklahoma regions are shown in Fig. 3.3(a-d), 3.4(a-d), and 3.5(a-d), respectively. Visual examination of these plots indicates reasonably good mixing i.e., sampling from all valid probability space. However, the length is too large (45,000) to rely upon visual inspection. Hence, we considered convergence diagnostics based on the Geweke test [*Geweke*, 1992]. The Geweke test splits the MCMC chain (after removing the burn-in period) into two parts. The first part comprises the beginning 10% of the chain and the second part is the last 50% of the chain. If the chain is at stationarity, the mean of the two parts should be equal, and the resulting test statistic is often referred to as the Geweke z-score. A value of greater than 2 for the Geweke z-score indicates that the mean of the series is still drifting, and a longer burn-in period is required. During the MCMC process for parameter upscaling, convergence diagnostics of the Geweke test detected no z-score greater than 2. A z-score less than 2 is also indicative of time invariant soil parameters within the footprint. The accepted proposals were extracted from the MCMC chain and subjected to a thinning process to reduce autocorrelation. From the thinning process an ensemble of upscaled soil hydraulic parameters were prepared for the SVAT model simulation.

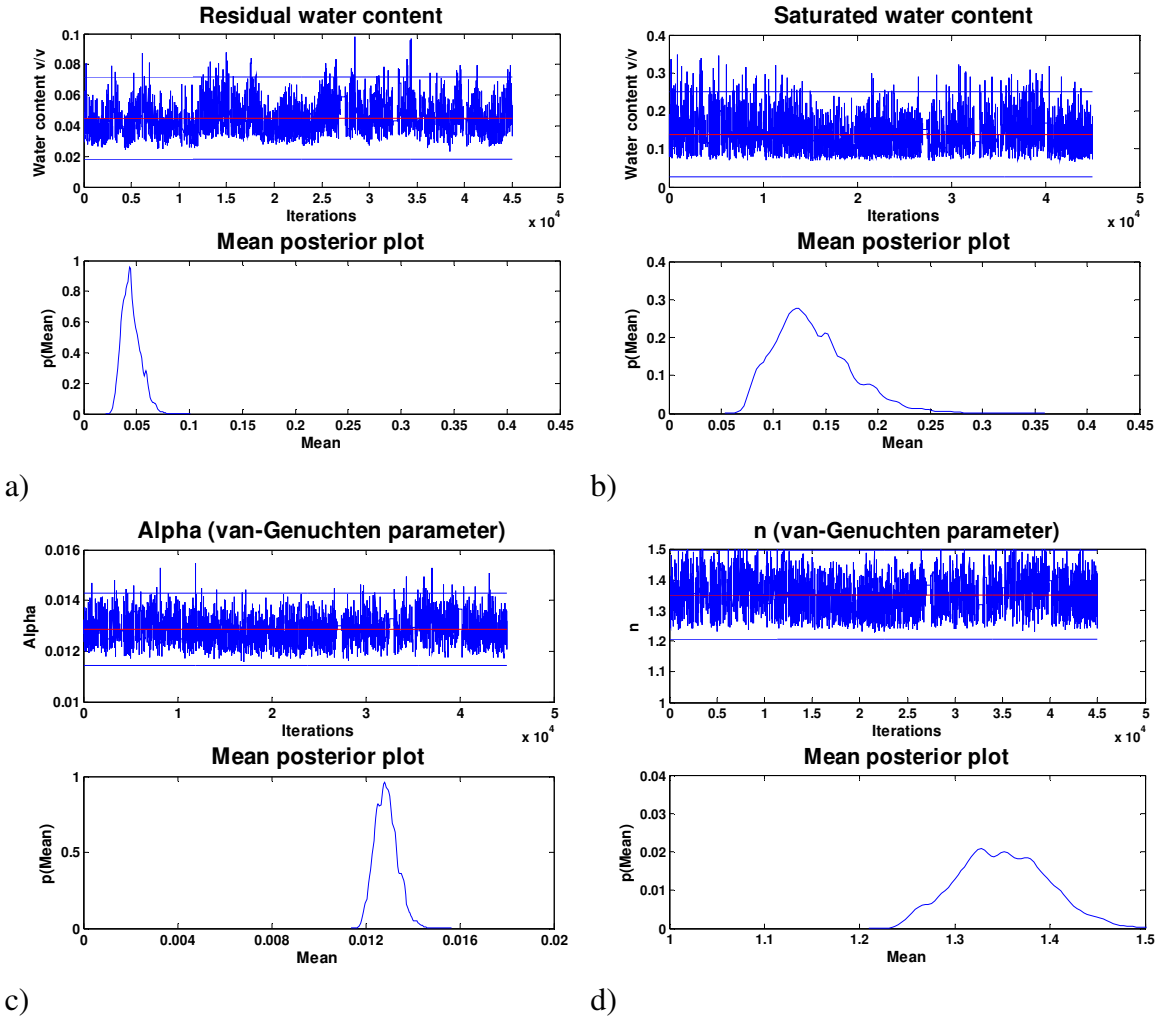

Figure 3.3. Posterior density plots for upscaled van Genuchten parameters, for a particular footprint in the Arizona regional site.

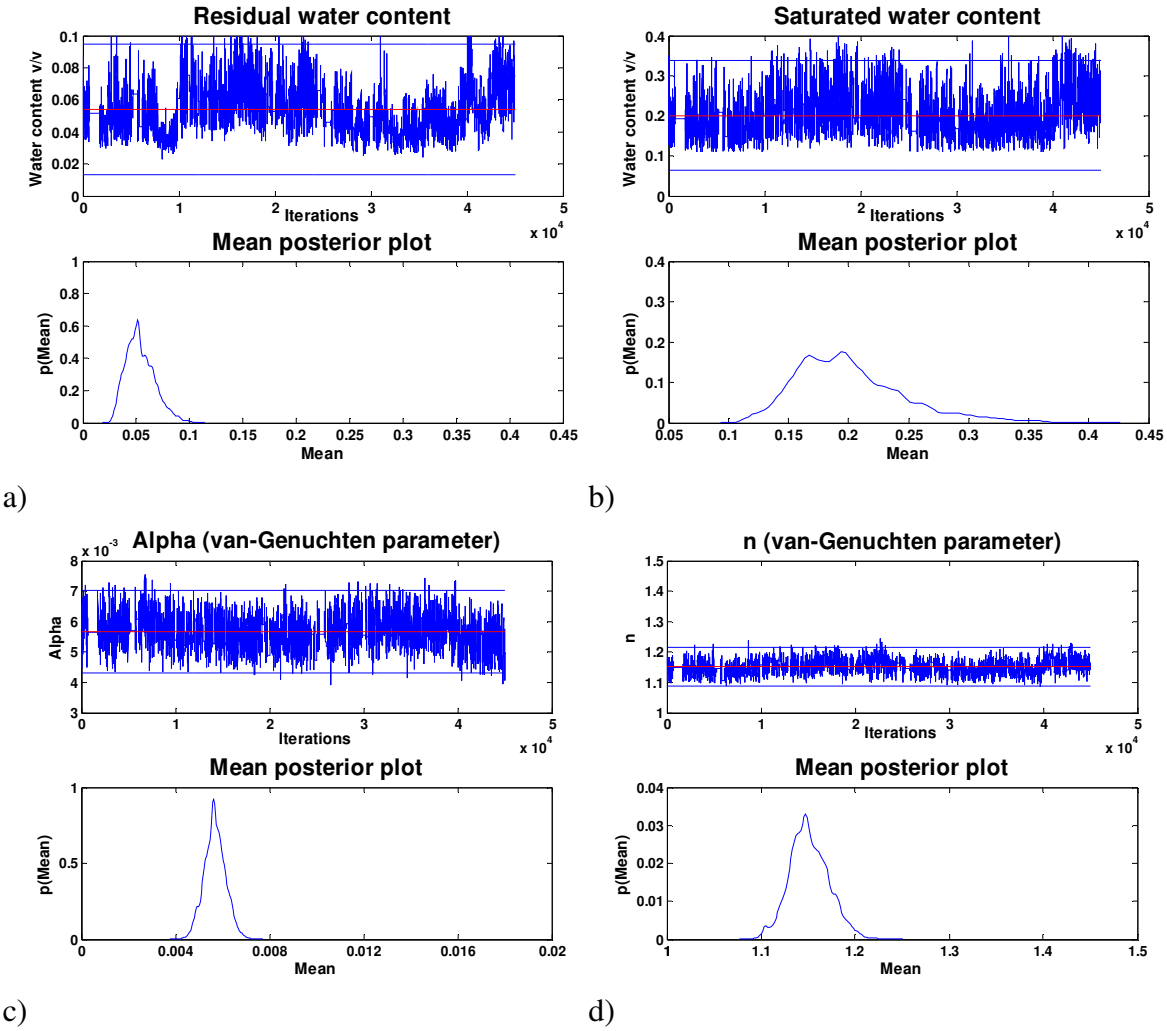

Figure 3.4. Posterior density plots for upscaled van Genuchten parameters, for a particular footprint in the Iowa regional site.

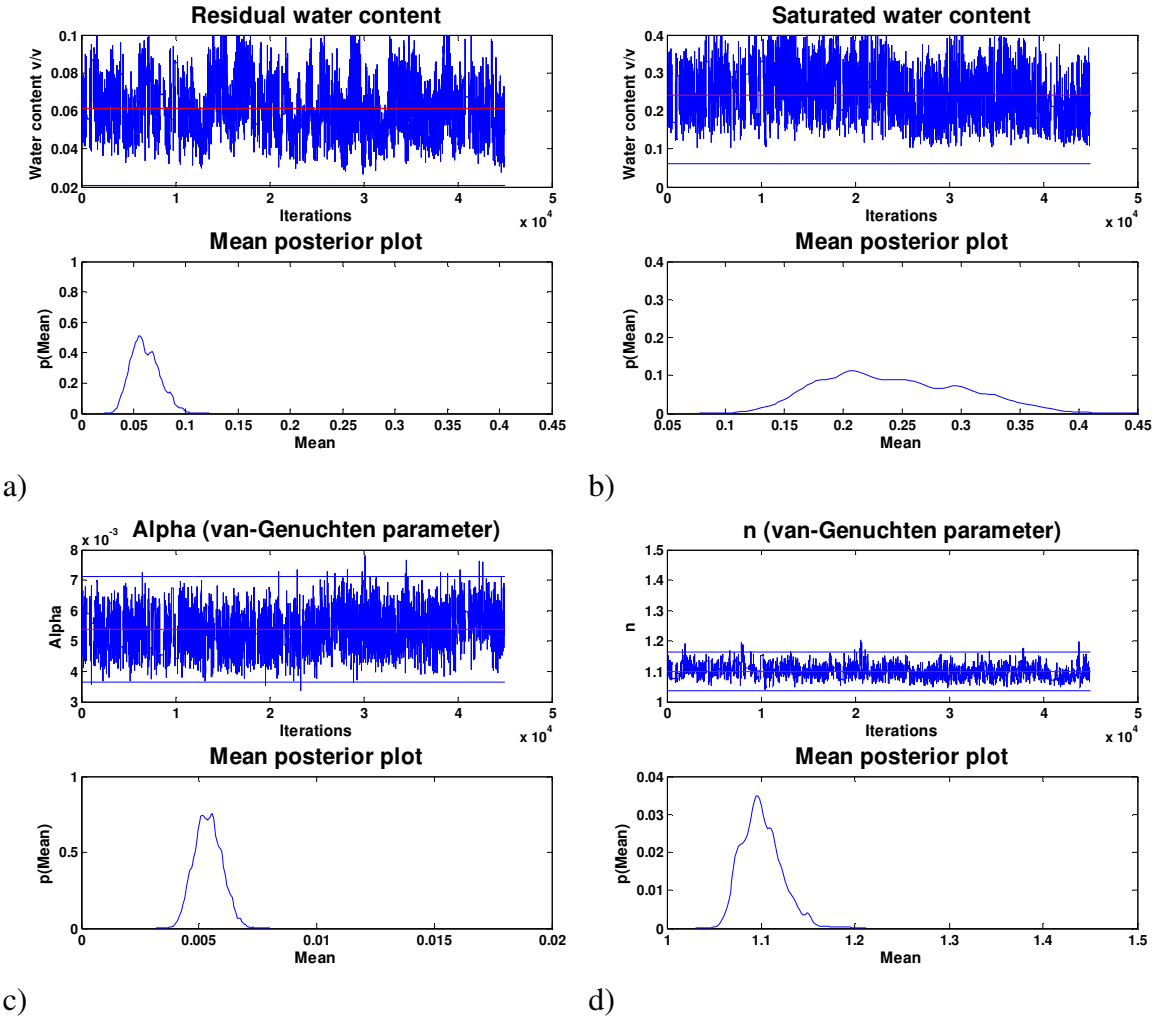

Figure 3.5. Posterior density plots for upscaled van Genuchten parameters, for a particular footprint in the Oklahoma regional site.

The upscaled soil hydraulic parameters of the study regions from the MCMC process were greatly influenced by the initial proposal distributions of the parameters. For the Arizona region, the initial parameter space was defined based on the dominant soil type i.e., mostly sandy loam with a high percentage of gravel. On the other hand, the Iowa region top soil is mostly silty clay and loam, and in the Oklahoma region the top soil layer is dominated by fine sandy loam, clay and occasional loam. Although, the initial distributions of the parameters were predefined, the Markov random process drew samples from a very relaxed search space provided for all the parameters. The signature of soil types for the three regions is clearly visible in the pdfs of the hydraulic parameters, shown in Fig. 3.3(a-d), 3.4(a-d), and 3.5(a-d). As expected the mean upscaled residual water content θ_{res}^{β} in Arizona was the lowest of the three regions. As illustrated in Fig. 3.5a, the effect of clay and fine sandy loam soil in Oklahoma region is also evident with highest mean θ_{res}^{β}. The observed variance of upscaled residual water content θ_{res}^{β} was quite low and very similar for all the three regions. Similarly, increasing trend for saturated water content θ_{sat}^{β} was also observed from sand and gravel dominated soil in Arizona to clayey and fine sandy loam soils in Oklahoma, revealing the influence of the parameter space in the MCMC algorithm. The variance of θ_{sat}^{β} encountered was also larger for the Oklahoma region than for the other two regions, determined primarily by the soil texture present in the regions. The van-Genuchten parameters (α^{β}, n^{β}) show a trend with the highest mean observed for the Arizona region and lowest for the Oklahoma region, consistent with the dominant soil texture for each region. The

characteristics of the hydraulic parameters shown in Fig. 3.3(a-d), 3.4(a-d), and 3.5(a-d) is typical of these particular regions. Of all the van-Genuchten parameters, the saturated hydraulic conductivity (K_{sat}^{β}) was the most variable and uncertain parameter obtained from the upscaling algorithm. Figure 3.6 illustrates the probability distribution of K_{sat}^{β} for a typical footprint from the Arizona region. Unlike other parameters, K_{sat}^{β} shows a multimodal distribution in space. Similar multimodal pdfs were also observed for the Iowa and the Oklahoma regional sites. Studies have shown that saturated hydraulic conductivity is a highly uncertain parameter that varies widely at the field scale [*Mohanty, et al.*, 1994a]. The wide range of K_{sat}^{β} in a footprint scale is a fair estimation keeping in view the size of the spatial domain of this study. The MCMC-based upscaling of soil hydraulic parameters results in an effective ensemble of parameter sets that is specific to regional hydroclimatic conditions, vegetation and soil type. Influence of topography on upscaling of soil hydraulic parameters was not considered in this framework. However, with the parallel stream-tube concept and the large horizontal spatial extent (60 km x 60 km) compared to the vertical range of topographic variations, the effect of topography on soil hydraulic parameters is greatly diminished.

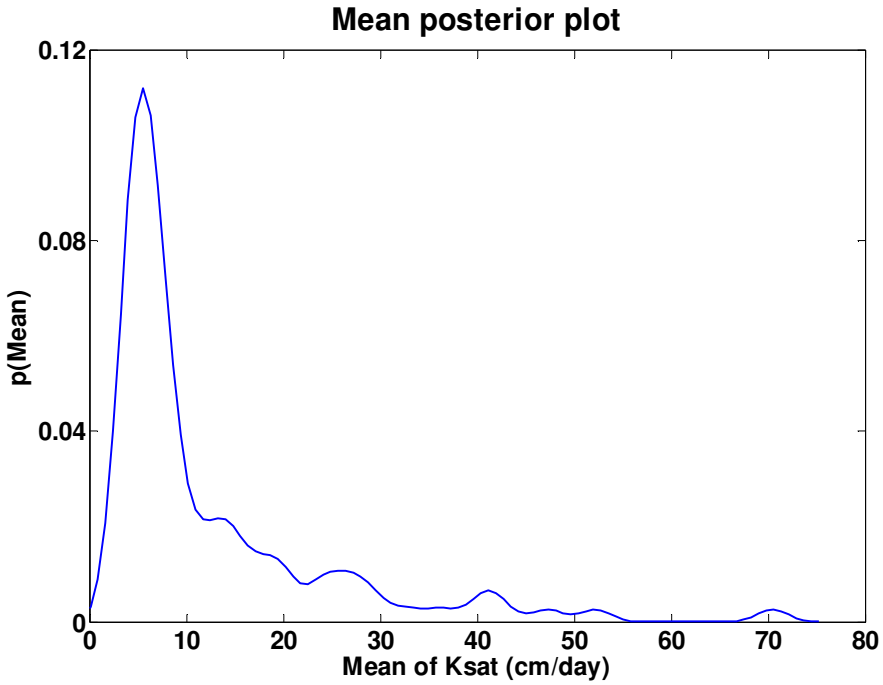

Figure 3.6. A typical example of probability distribution for upscaled saturated hydraulic conductivity (K_{sat}^{β}), from the Arizona regional site.

Figure 3.7a-c illustrates the posterior distribution of the upscaling parameter β for the three study regions. It also exhibits typical characteristic behavior as influenced by the parameter search space of the field-scale soil hydraulic parameters. For flat homogenous bare soil the value of β is 1 and the parameter values are independent of spatial scale. With heterogeneity the value of β remains no longer equal to unity and in fact can be larger or smaller than 1. In this study the upscaling parameter β is smaller than 1 due to heterogeneity introduced by soil types, vegetation and atmospheric forcings with increasing spatial scale. Essentially, all the nonlinearity encountered in the physical processes with increasing spatial scale is lumped in the upscaling factor β. As shown in Fig. 3.7, the MCMC converges to a stationary distribution of β with a mean of nearly 0.8, 0.85, and 0.9 for the Arizona, Iowa and Oklahoma region, respectively. Mean value of β may depend upon the individual AMSR-E footprint as every footprint is unique due to complex combination of topography, vegetation, soil, and other geophysical processes. Further investigation is required to study the influence of individual as well as different combinations of geophysical parameters (soil type, topography, vegetation, and atmospheric forcings) on the behavior of β with increasing spatial scale.

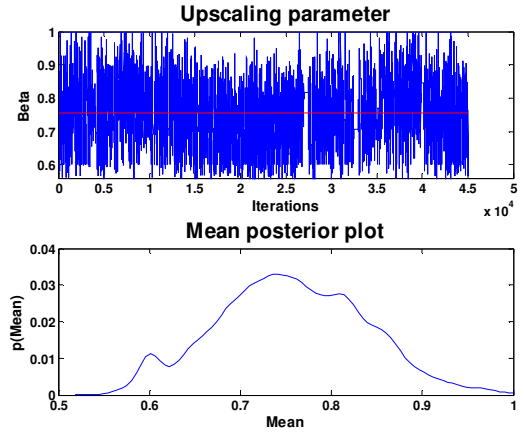

a)

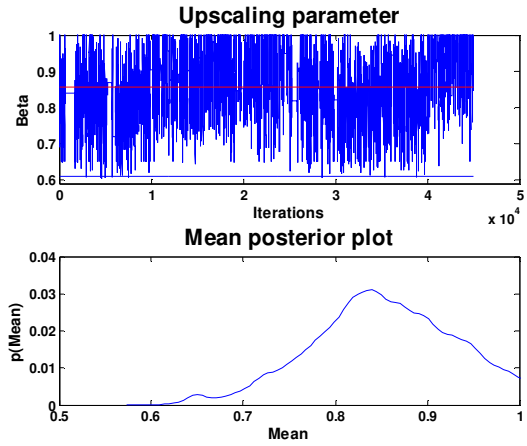

b)

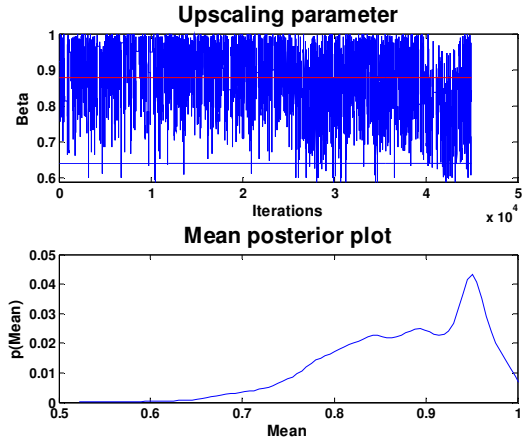

c)

Figure 3.7. Posterior density plots for upscaling parameter for a) Arizona region, b) Iowa region, and c) Oklahoma region.

Comparison of Modeled and Remotely Sensed Soil Moisture

Arizona regional site

The Arizona regional site is ideal for satellite-based passive microwave remote sensing of soil moisture because of sparse vegetation (LAI < 1 m^2/m^2). Studies [*Njoku and Li*, 1999; *Paloscia, et al.*, 1993] have demonstrated that at the AMSR-E frequency of 10.7 GHz used for soil moisture sensing, the sensitivity of brightness temperature (T_b) to variations in soil moisture strongly decreases when the soil is covered with well developed vegetation. Also, the predominant sandy texture soil with sparse vegetation of this region is suitable for microwave remote sensing. Therefore, we used this regional site as a testbed to evaluate the MCMC algorithm developed for upscaling of soil hydraulic parameters. One hundred ensemble members (each member representing one set of upscaled van Genuchten parameters) were selected from the thinning operation of the MCMC chain (posterior distribution). Modeled soil moistures from the top 1 cm depth of the soil profile from all 42 AMSR-E footprints in the region were compared with the AMSR-E measurements. Three out of 42 footprints in the region were randomly selected to display the results of SVAT modeling of the 100 ensemble members (Fig. 3.8a-c) at 60 km x 60 km resolution for 2004-2005. As illustrated in Fig. 3.8a-c, most of the times the ensemble of SVAT simulated soil moisture matches very well with the AMSR-E footprint measurements and are always within the bounds of the ensemble of SVAT simulated soil moisture. However, few discrepancies were also observed as reflected in Fig. 3.8b. Close examination of these discrepancies reveal that the AMSR-E soil moisture data did not respond to the TRMM-based precipitation data. The reason

may be the precipitation event occurring after the overpass time of the Aqua satellite (descending: 1 AM) and vice-versa. The top soil, which mostly contributes to the microwave emission, has high rock and gravel fraction with sandy texture. This influences the soil hydraulic characteristics making them highly nonlinear with very high saturated hydraulic conductivity, which drains the soil rapidly and the signature of the precipitation event is lost from the top soil. During the SMEX04 field campaign, *Das et al.* [2008] also observed similar behavior in Walnut Gulch watershed situated within this Arizona regional site. A high correlation (average R of 0.91) was observed between the AMSR-E soil moisture and the mean of SVAT ensembles for all the 42 footprints during the summer seasons of 2004-2005. However, lower correlation was observed for winter periods of 2004-2005, with an average R of 0.65. The Arizona region experiences most of the precipitation during winter by North American monsoon which is mostly widespread and is unlike convective thunderstorms during summer. The SVAT model showed high soil moisture during such major precipitation events, whereas the AMSR-E footprints showed a weak response. This also degraded the correlation value observed during the winter periods. Co-registration of satellite-based precipitation and soil moisture measurement may minimize such anomalies. The estimated upscaled hydraulic parameters for this region reasonably modeled the soil moisture evolution at a footprint scale. These upscaled parameters also retained the typical characteristics of the sandy soil at large scales. The good performance of SVAT model (using MCMC based upscaled parameters) with AMSR-E measurements in semiarid Arizona region is further

evaluated in agricultural landscapes with high biomass (Iowa region), and grass/pasture (Oklahoma region).

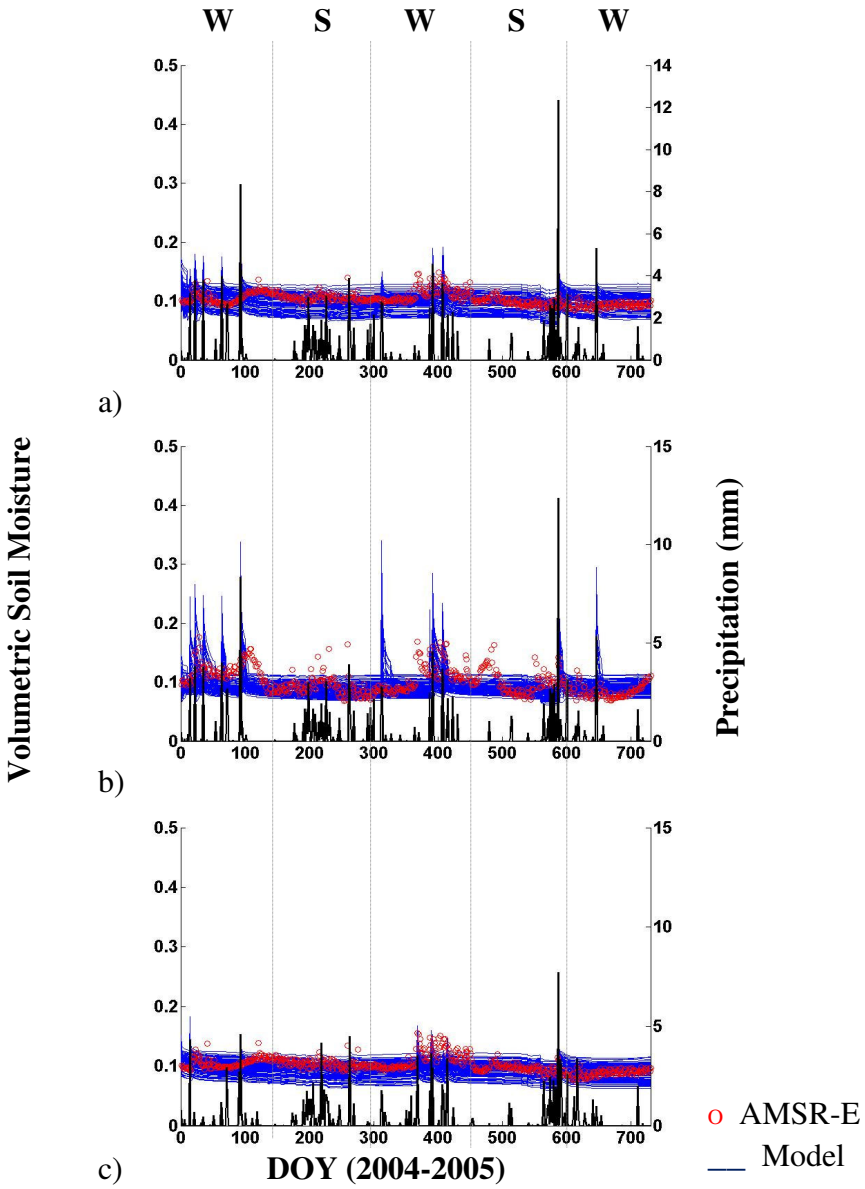

Figure 3.8. Comparison of randomly selected footprints of soil moisture evolution from ensemble of upscaled soil hydraulic parameters using SVAT model and AMSR-E measurements for 2004-2005, from Arizona region (where W: winter, and S: summer).

Iowa regional site

The Iowa regional site is a typical example of agricultural landscape (LAI of 3-6 m^2/m^2). Using data from a soil moisture experiment (SMEX02) in June-July 2002 in this region, *Bindlish et al.* [2006b] reported a satisfactory validation of the space-borne AMSR-E soil moisture using an airborne Polarimetric Scanning Radiometer (PSR). However, in this region, our study found contrasting results for 2004-2005. Performance of AMSR-E soil moisture product was evaluated against the SVAT model simulated soil moisture for 35 footprints. Results from three randomly selected footprints in the region are illustrated in Fig. 3.9a-c. Figure 3.9a shows that AMSR-E did not respond to the precipitation events, especially during the summer months. This behavior was also found in many other footprints in the region (results not shown here). During summer, in such agricultural regions mid- to late-stage corn and soybean crops of high LAI (3-6 m^2/m^2) attenuate microwave emission from soil and themselves emit essentially depolarized microwave radiations [*Wang and Choudhury*, 1995]. The attenuation of microwave emission from soil introduces masking effect observed by remote sensors and uncertainty in soil moisture process dynamics at the soil surface. Soil moisture values with very little variations or decreasing trend was found in AMSR-E measurements with the increase of LAI during the summers in the Iowa region. Contrarily, the SVAT model predictions responded with high soil moisture in the top soil layer on the day of precipitation events.

Consequently, a very low average R (0.15) was recorded between AMSR-E soil moisture product and SVAT simulated values. A slightly higher correlation (R = 0.23) was observed for the winter seasons. In few occasions, AMSR-E soil moisture was found much higher during the winters, which may be due to wet ice. A noticeable feature in Fig. 3.9c is high soil moisture measured by AMSR-E during the summer of 2005. This happened after small precipitation events, when the canopy interception due to high LAI reduces emissions to a large extent. At the same time little increase in simulated soil moisture values was observed. Due to such uncertainties and overall variability, the SVAT model ensemble trajectory for the two years did not match well with the trend of AMSR-E measurements. A noticeable feature of this regional site is high average and large variability in soil moisture content than the Arizona site. This finding signifies that the proposed MCMC algorithm, which retained the basic nature of the soil type after upscaling, highlights the discrepancies of SVAT modeled soil moisture evolution with the AMSR-E measurements.

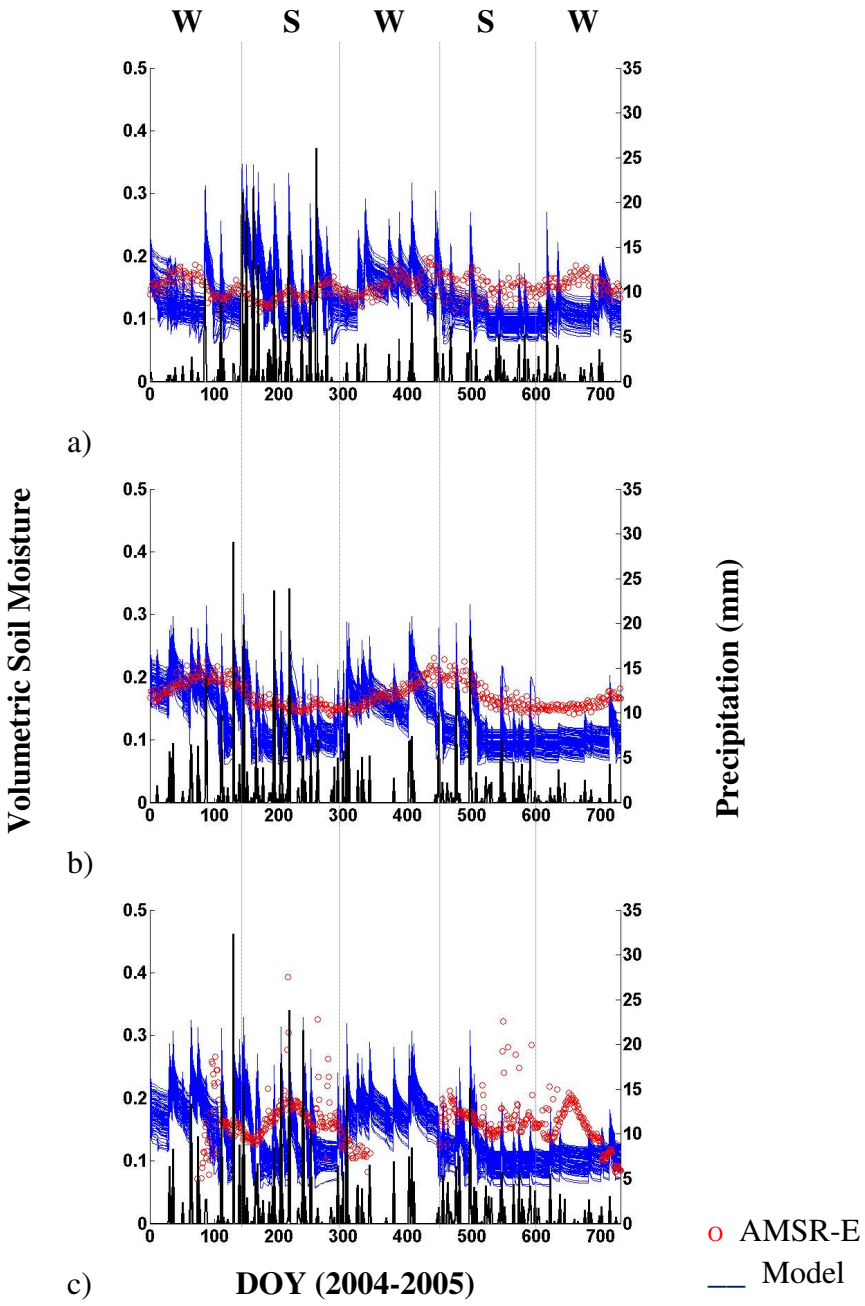

Figure 3.9. Comparison of randomly selected footprints of soil moisture evolution from ensemble of upscaled soil hydraulic parameters using SVAT model and AMSR-E measurements for 2004-2005, from Iowa region (where W: winter, and S: summer).

Oklahoma regional site

Studies showing AMSR-E instrument validation for this region is not available to date. Other studies [*Hu, et al.*, 1998; *Hu, et al.*, 1997; *Nykanen and Foufoula-Georgiou*, 2001; *Oldak, et al.*, 2002; *Peters-Lidard, et al.*, 2001; *Rodriguez-Iturbe, et al.*, 1995] conducted in this region, using airborne remote sensing (Electronically Scanned Thinned Array Radiometer, ESTAR) soil moisture data during SGP97 field campaign, reported nonstationarity and multiscaling properties with increasing spatial scale. Our MCMC-based upscaled hydraulic parameters in the SVAT model were used for 45 footprints in this region and ensemble trajectories of soil moisture evolution for three (randomly selected) AMSR-E footprints are presented in Fig. 3.10a-c. The SVAT model did reasonably well as compared to the Iowa regional site. An average R value of 0.51 for the summers and 0.39 for the winters in 2004-2005 was recorded for the Oklahoma region. As shown in the Iowa sites the AMSR-E footprints for Oklahoma in many occasions show no effects of major precipitation events. During the summer months, LAI of this region grows up to 3-5 m^2/m^2, which hampers the sensitivity of AMSR-E 10.7 GHz frequency, resulting in low soil moisture values of AMSR-E footprints. It was also observed that for this regional site, the model ensemble trajectories capture the AMSR-E measurements most of the time.

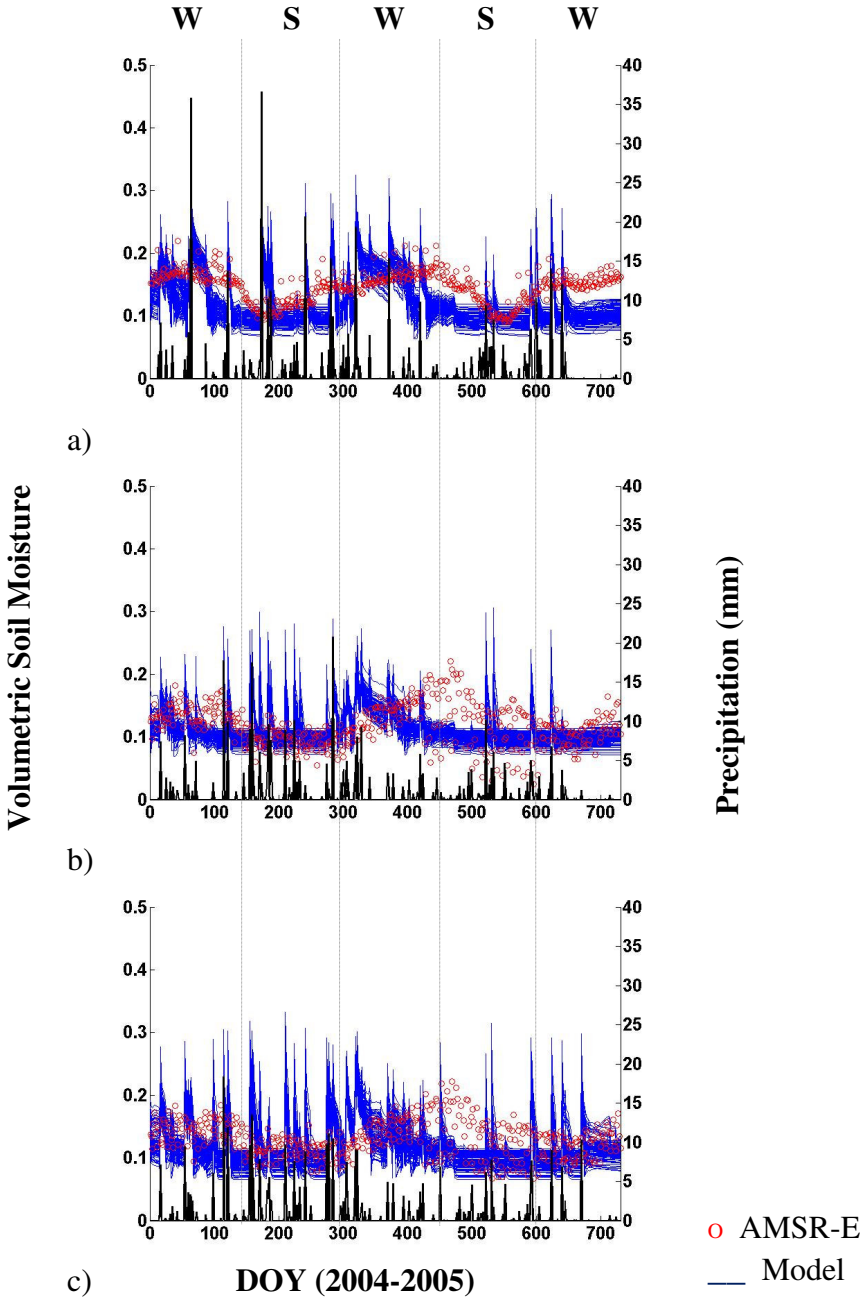

Figure 3.10. Comparison of randomly selected footprints of soil moisture evolution from ensemble of upscaled soil hydraulic parameters using SVAT model and AMSR-E measurements for 2004-2005, from Oklahoma region (where W: winter, and S: summer).

Comparison of Ground-Based, Remotely-Sensed, and Modeled Soil Moisture

Extensive regional scale field campaigns for surface soil moisture measurement (with point scale support) were conducted during the SMEX04 (in Arizona regional site) and the SMEX05 (in Iowa regional site). The time period of our modeling study (2004-2005) overlapped with the duration of these field campaigns. Figures 3.11 and 3.12 illustrate the comparison of surface soil moisture from SVAT model predictions, AMSR-E observations, and ground measurements (local/point scale) for Arizona and Iowa region, respectively. For comparison, simple average was evaluated for the all ground measurements within the specific AMSR-E grid. Note, however, the local/point scale soil moisture data (theta-probe measurements) supports a depth of 5 cm, whereas the SVAT model evolution are from top 1 cm and AMSR-E soil moisture data with footprint scale support is valid up to 1 cm depth. In Fig. 3.11, the AMSR-E observations and the SVAT model predictions having footprint scale (60 km x 60 km) support maintains a steady trend without much variation, as observed in the local/point scale surface soil moisture data in the Arizona region. This is because at the footprint scale most of the local variations were homogenized which were captured by local point scale surface soil moisture data. Also, *Das et al.* [2008] found that the change in the mean and variance of daily soil moisture probability densities at the 1 cm depth was due to the highly variable (localized) convective summer precipitation patterns across the Walnut Gulch watershed in the Arizona region. However, in the Arizona regional site the difference in mean of the surface soil moisture with SVAT model and AMSR-E soil moisture data (Fig. 3.11) were not prominent as in the Iowa regional site (Fig. 3.12).

This was due to the prevailing dry conditions with a very conductive top soil in Arizona region. The less difference in mean soil moisture was due to no major precipitation event throughout the region during SMEX04. Therefore, the wetting and subsequent drydown phase is missing in Fig. 3.11. Whereas, in the Iowa region, the mean of *insitu* surface (0-5 cm) soil moisture data is much higher than the SVAT model predictions, and the AMSR-E soil moisture data. As already discussed in the previous section, high soil moisture which was measured by point-scale gravimetric sample in the clayey textured top soil was completely masked by high LAI in the agricultural region for the AMSR-E measurements. In the Iowa region, however, the SVAT model prediction clearly responds to the precipitation events, which is not observed in the case of AMSR-E measurements because of microwave emission attenuation/manipulation by high vegetation. Another noticeable feature in Fig. 3.12 is the difference in correlation of soil moisture of the SVAT model predictions and the point-scale measurements on wet days (e.g., DOY: 176) versus dry/drydown days. This finding reflects the simple spatial scaling characteristics for the wet day as opposed to the multiscaling properties for the drydown period which corroborates with the findings of *Das and Mohanty* [2008] during SMEX02 campaign in the Iowa region. This comparison further strengthen the notion of parameter upscaling requirements and validity of using our proposed MCMC based upscaled SVAT model to record the hydrological processes within large AMSR-E footprints.

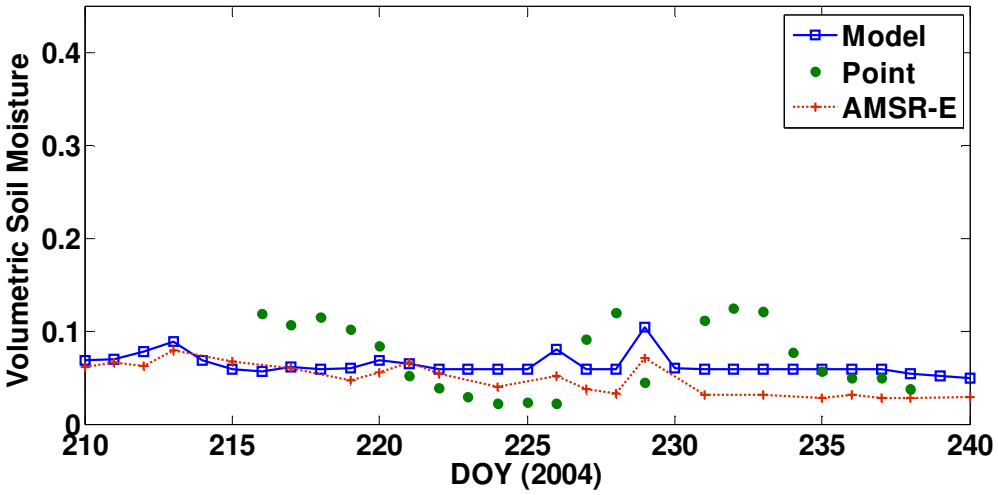

Figure 3.11. Comparison of field scale, SVAT model, and AMSR-E soil moisture data from Soil Moisture Experiment 2004 (SMEX04).

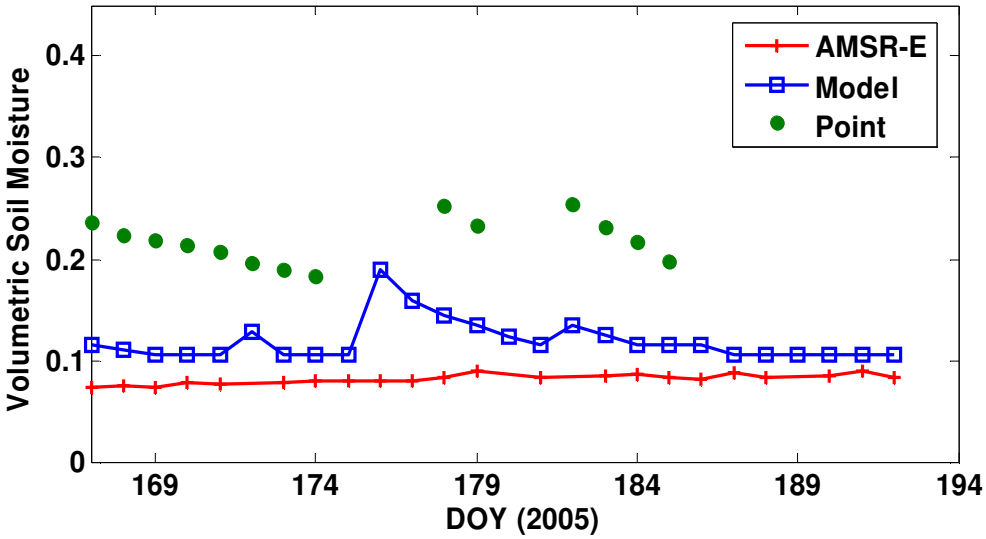

Figure 3.12. Comparison of field scale, SVAT model, and AMSR-E soil moisture data from Soil Moisture Experiment 2002 (SMEX02).

3.5. Conclusions

It has been demonstrated that upscaling of soil hydraulic parameters from field scale to satellite footprint scale has potential for modeling soil moisture evolution at the footprint scale and for evaluating the uncertainty and limitations involved in satellite based soil moisture data. A simple MCMC-based algorithm was developed with priors from existing field scale soil parameters and likelihood from AMSR-E based soil moisture data to generate a posterior set of upscaled hydraulic parameters. The SVAT model used these upscaled soil hydraulic parameters in three different hydroclimatic regions to simulate the surface soil moisture for two years (2004-2005). A high correlation between AMSR-E soil moisture data and simulated soil moisture values was

observed for the semi-arid region of Arizona attesting to the use of upscaled parameters in SVAT models at the AMSR-E footprint scale. In the agricultural landscapes of the Iowa region, the SVAT model revealed the limitation in the AMSR-E soil moisture product under dense vegetative conditions. A very low correlation was observed in the summers of 2004-2005 for the Iowa regional site. The SVAT model did reasonably well in grass/pasture lands of Oklahoma as compared to the Iowa agricultural sites. High vegetation during summers was found to degrade the AMSR-E soil moisture detection sensitivities. One constraint encountered during this study was the precipitation inputs from TRMM, which were not co-registered with AMSR-E footprints. This led to the mismatch of soil moisture evolution from SVAT model and AMSR-E soil moisture product. Our approach, using remotely sensed data to calibrate a SVAT model to mimic the evolution of land surface state variable as soil moisture, may be used in future for improving the remotely sensed products through data assimilation. The technique also has the potential to derive upscaled parameters for geophysical properties.

CHAPTER IV

A NEW MULTISCALE DATA ASSIMILATION ALGORITHM TO DOWNSCALE SATELLITE-BASED SURFACE SOIL MOISTURE DATA

4.1. Synopsis

The study focuses on downscaling of soil moisture from coarse remote sensing footprints to finer scales. Two approaches are proposed for soil moisture downscaling. The first approach provides the probability distribution functions at the finer scales with no information about the spatial organization of soil moisture fields. The second approach implements a multiscale ensemble Kalman filter (EnKF) that assimilates remotely sensed coarse scale soil moisture footprint, attributes of fine scale geophysical parameters/variables (i.e., soil texture: %sand, vegetation: NDVI, topography: slope, and precipitation) and coarse/fine scale simulation into a spatial characterization of soil moisture evolution at the finer scales. To downscale the remotely sensed coarse scale soil moisture to another spatial scale, the multiscale EnKF uses a bridging model. The bridging model infers the pixel-specific scaling coefficient from the compatible geophysical parameters/variables that influence the soil moisture evolution process at that particular spatial scale. Data from diverse hydroclimatic regions from the semiarid Arizona, the agricultural landscape of Iowa, and the grassland/rangeland of Oklahoma are used in the study to implement the multiscale downscaling algorithm. The results demonstrate that the bridging model of multiscale EnKF helps to characterize the evolution of soil moisture within the remotely sensed footprint. Validation conducted at

the finest scale also shows reasonable agreement between the measured field data and the simulated downscaled soil moisture evolution.

4.2. Introduction

Soil moisture is recognized as an important state variable that greatly influences hydrological/meteorological processes occurring at micro- (pore) to macro-(continental) scale involved in the global water and energy cycles. Therefore, knowledge of soil moisture at varying spatial scales is essential for better understanding of hydrological and meteorological processes. However, in general soil moisture is observed at two very contrasting spatial scales i.e., in-situ techniques (at cm scale) and satellite-based (> several km resolution) measurements. This enormous gap in spatial scales of the observations does not capture the characteristics of soil moisture spatial evolution occurring at the intermediate scales for different environmental, hydrological, water management, and geohazard mitigation applications.

The evolution of soil moisture at a particular spatio-temporal scale develops from nonlinear interactions among different geophysical parameters/variables i.e, soil, topography, rainfall, and vegetation [*Western, et al.*, 2002]. A number of studies about the influence of these geophysical parameters on soil moisture variability are reported in the past. For example, soil was conceptualized as a hierarchical heterogeneous medium with discrete spatial scale by *Cushman* [1990], and *Roth et al*. [1999]. They argued natural pattern of soil variability may exhibit embedded, organizational structures that lead to non-stationary soil properties and processes. *Rodriguez-Iturbe et al*. [1995]

suggested that the spatial organization of soil moisture is a consequence of soil properties. With respect to topography, studies [*Famiglietti, et al.*, 1998; *Hawley, et al.*, 1983] have shown topographical characteristics (slope and elevation) manifest control on spatial variation of soil moisture through runon, runoff, lateral flow, and water accumulation. *Chang and Islam* [2003] demonstrated that soil physical properties and topography control spatial variations of soil moisture over large areas. They have shown, topographical control will dictate soil moisture distribution under wet conditions, and soil physical properties control variations of soil moisture under relatively dry conditions. Similarly, vegetation types also influences soil moisture spatio-temporal variability through evapotranspiration [*Mohanty, et al.*, 2000a]. Infiltration properties of soil are influenced by vegetation at the plant scale [*Seyfried and Wilcox*, 1995]. With the increase in spatial scale, soil moisture variability is affected by variation in vegetation shifts from plant to patch to the community scale. Of all the geophysical variables, precipitation primarily forces spatio-temporal variability in soil moisture evolution by its inherent highly stochastic space-time characteristics at the ground level [*Gupta and Waymire*, 1990; *Kumar and Foufoula-Georgiou*, 1993]. Sellers et al. [1995] also presented spatial heterogeneity in soil moisture evolution introduced by rainfall and removed through dry-down dynamics.

The influence of the geophysical parameters/variables also reflects in studies conducted to investigate spatio-temporal variability of soil moisture. *Famiglietti et al*. [1999] found significant variability in soil moisture because of different combinations of soil type, vegetation cover, management practice, and rainfall gradient within six

selected Electronically Scanned Thinned Array Radiometer (ESTAR) footprints during the Southern Great Plains 1997 (SGP97) experiment. *Mohanty and Skaggs* [2001] also used ground-based datasets of SGP97 to show the characteristic differences in the space-time dynamics of soil moisture within several remote sensing footprints with various combinations of soil texture, slope and vegetation type. Another investigation of the spatial structure of soil moisture for Washita'92 and Washita'94 was presented by *Peters-Lidard et al*. [2001]. They conducted scaling analysis of both measured and modeled soil moisture pattern and found multiscaling properties. *Oldak et al*. [2002] studied the statistical properties of remotely sensed soil moisture field of Washita '92 and SGP97 experiments. They showed that the shape of scaling dependencies remains the same during drydowns, consequently reducing the volume of observations needed to predict scaling of surface soil moisture. Using SGP97 data, *Crow and Wood* [1999] showed that a multiscale analysis reveals a qualitatively different relationship between soil moisture means and soil moisture spatial variances when variability is sampled at fine (<1 km) versus coarse (>10 km) spatial scales. Recently, *Das and Mohanty* [2008] reported about spatial scaling characteristic of soil moisture in the agricultural region of Iowa using remotely sensed data of Polarimetric Scanning Radiometer (PSR) of ~0.8 km resolution from Soil Moisture Experiment 2002 (SMEX02) [*Bindlish, et al.*, 2005]. They used wavelet-based multiresolution analysis on the PSR data and found that the region exhibits multiscaling properties for drying fields and simple scaling for wet fields.

It is apparent from the above mentioned studies that measurements taken at different spatial scales may vary significantly in their mean and variance and depend

greatly on interactions among the geophysical parameters/variables. The soil moisture measurement available through satellite-based remote sensing offers product over large spatial scale that resembles an integrated value of the footprint e.g., remotely sensed soil moisture footprints of Advanced Microwave Scanning Radiometer (AMSR-E) aboard the Aqua satellite [*Njoku, et al.*, 2003]. The underlying heterogeneity introduced by geophysical parameters is completely masked in such remotely sensed measurements. Numerous studies [*Crow, et al.*, 2005; *Houser, et al.*, 1998; *Margulis, et al.*, 2002; *Reichle and Koster*, 2005; *Reichle, et al.*, 2004] have used coarse scale remotely sensed soil moisture data in land-surface modeling having a data assimilation scheme. The solutions of states and fluxes from these land-surface modeling exercises are valid at the respective spatial scale of the input data. Also, land-surface and energy balance models that uses remotely sensed soil moisture measurements, operates over regional, continental to global domains at a very coarse spatial resolution. Therefore, it is nearly impossible to obtain accurate fine scale spatially continuous soil moisture estimation in large extent on a consistent basis from these models, and will likely to remain so through the next generation of soil moisture remote sensors e.g., Soil Moisture Active Passive (SMAP) of NASA.

This study provides a way to predict subfootprint/subgrid variability present within a satellite-based remotely sensed coarse scale soil moisture footprint. Two approaches are proposed for soil moisture downscaling. The first approach provides the probability distribution functions (pdfs) at the finer scales with no information about the spatial organization of soil moisture fields. The second approach implements a multiscale

ensemble Kalman filter (EnKF) that assimilates information from remotely sensed coarse scale soil moisture footprint, attributes of fine scale geophysical parameters/variables (i.e., soil texture: %sand, vegetation: NDVI, topography: slope, and precipitation) and simulation outputs from coarse and fine scale modeling into a spatial characterization of soil moisture evolution at the finer scales. To downscale the remotely sensed coarse scale soil moisture footprint to the pixel of a particular scale, the multiscale EnKF algorithm uses a bridging model. The bridging model infers the fine scale pixel specific spatial scaling coefficient from the compatible geophysical parameters/variables that influence the soil moisture evolution process. The multiscale EnKF technique results in optimal solution and spatial organization of the soil moisture fields at the finer scales.

4.3. Prediction of High Resolution Soil Moisture

Tradionally, in hydrology, data assimilation is employed with a dynamical system models ‘M’ and observations ‘O’, as shown in Fig 4.1. The figure presents an ideal situation and is entirely uncoupled across scales. The data assimilation in this case have observations at a given scale that is assimilated only with simulated states at that particular scale, and predictions and updating in different scales are actually independent of each other. However, most of the time the explicit system models and observations are not available simultanously at desired scales. For example, remotely sensed soil moisture (AMSR-E data) is avaiable at a very coarse scale of ~60 km resolution, in contrast to in-situ measurements that are valid in meters scale. The large gap in observation scales impose constraint to assess soil moisture at intermediate scales.

Therefore, the question arises, how do we obtain assessment of soil moisture fields at interim scales that are consistent with the remotely sensed soil moisture measurements at the coarse scale? Our motivation is to formulate an algorithm to infer subfootprint/subgrid variability from satellite-based remotely sensed soil moisture measurement that will provide assessment at finer scales. We propose two methods: 1) estimation of probability density function (pdf) at intermediate scales, and 2) estimation of soil moisture field at intermediate scales.

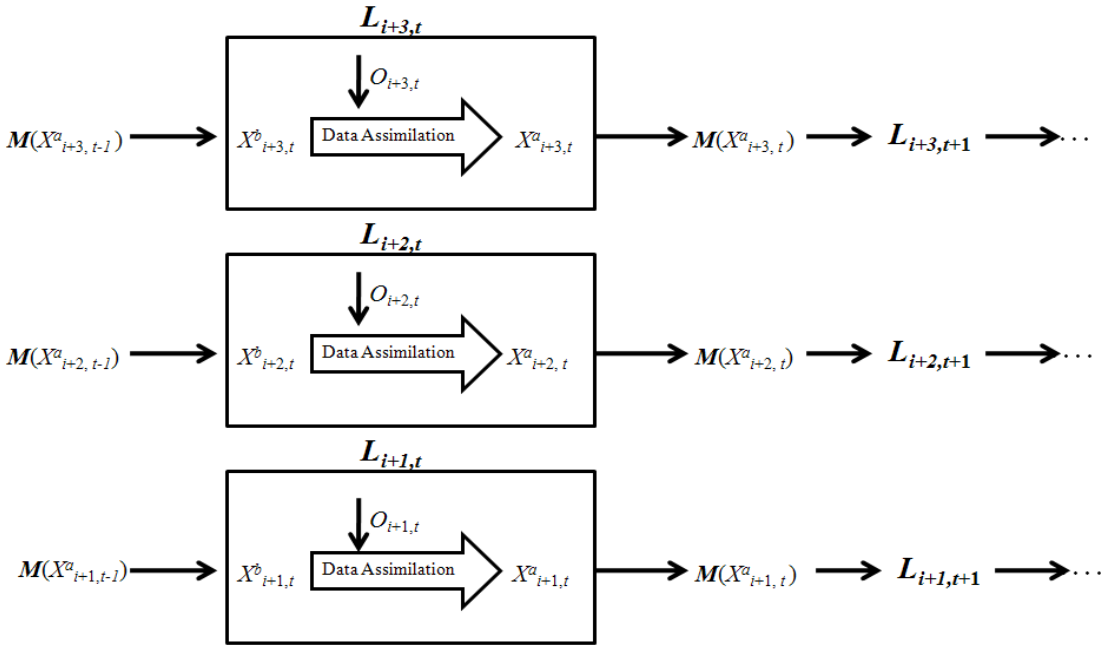

Figure 4.1. A traditional way of Ensemble Kalman Filter (EnKF) based data assimilation in hydrology with model and observation given in all scales. *M*: Hydrologic model, *O*: Observation, *X*: State variable, *L*: Data Assimilation, *i*: spatial scale, *t*: time, *b*: background/prior, and *a*: optimal solution or analysis.

In both the methods, modeling at coarse and fine scales are required. The AMSR-E soil moisture data at ~60 km resolution is chosen as reference for the coarsest scale. A Markov Chain Monte Carlo (MCMC) based algorithm developed in Das et al. [2008b] is used to derive an ensemble of upscaled soil hydraulic parameters for a Soil-Vegetation-Atmosphere-Transfer (SVAT) model at the AMSR-E footprint scale. Soil moisture evolution is simulated using SVAT model at a spatial scale comparable to the AMSR-E soil moisture product (~60 km), with the hypothesis that the characterization of soil microwave emissions and their variations with space and time on soil surface within the AMSR-E footprint can be represented by the derived ensemble of upscaled soil hydraulic parameters. As suggested in Das et al. [2008b], the simulated soil moisture from the SVAT model is further subjected to ensemble Kalman filter (EnKF) based data assimilation with AMSR-E data to improve the soil moisture estimate.

For the finest scale, the Nexrad-based precipitation data of ~4 km resolution is selected as the reference. The selection of finest scale at ~4 km is done keeping in perspective the spatio-temporal continuity, and availability of precipitation data that is arguably the most important geophysical variable for evolution of soil moisture. A quasi-distributed, physically-based SVAT model is setup to model profile soil moisture at ~4 km. We mainly focus on the root-zone soil moisture at spatial resolution of ~4 km and at a temporal resolution of one day. The disparity of scales between the horizontal (~4 km) and vertical (1 m) extents of the root-zone was the key consideration in formulating the framework. The implementation of the model setup is similar to Das et al. [2008a]. Brief overview of the modeling framework at fine scale is provided here for the relevance of

this study. For SVAT model simulation, the root-zone at every Nexrad footprint within the AMSR-E footprint is vertically discretized, with finer discretization near the soil layer interfaces and at the land-atmosphere boundary. Finer discretization near the top boundary and layer interfaces are used to handle the steep pressure gradient for the numerical simulations. Time-dependent flux-type top boundary conditions for each parallel soil column (matching the Nexrad footprints) are used with precipitation distribution within the AMSR-E footprint. Runoff and runon between adjacent pixels due to topography was considered on the land surface. The runoff from the one or more adjacent pixels of steepest descent according to flow routing is used as runon for the pixel under consideration. Given the relatively coarse horizontal scale with shallow root-zone, the parallel soil columns in the SVAT model ignores the subsurface lateral water fluxes across the adjacent soil columns and only predicts the vertical fluxes (infiltration, deep percolation and evapotranspiration) and surface runoff. This results in a parallel non-interacting stream-tubes concept with distributed modeling framework within a AMSR-E footprint. A probabilistic approach is adopted, by using an ensemble of state variables (profile soil moistures) for all the Nexrad-based pixels (~4 km) within the coarse scale soil moisture footprint. A state augmentation technique is applied by concatenating uncertain soil properties to the state variables, forming composite vectors in the ensemble. The dominant soil types from the CONUS soil database and the van-Genuchten shape parameters for the soil textural class given by Unsaturated Soil Hydraulic Database (UNSODA) are used with ±20% uncertainty. The purpose of including uncertain soil properties in the ensemble is to address the assumption that it

simulates subpixel variability present within a Nexrad footprint. For best computational efficiency, one hundred members (composite vectors) were populated in the ensemble of individual Nexrad footprint. The SVAT models at the finest and coarsest scale are run 6 months ahead of the year 2005, to tune the state of initial soil moisture profile. At each time step, final states (soil moisture) are determined by the ensemble of the one hundred replicated predictions made by the SVAT model for every Nexrad footprint at finest scale. The soil moisture fields realized at finest- (~4 km) and coarsest-scale (~60 km) for a particular time-step is represented as $\left[X_{4,t}^{b}\right]$ and $X_{60,t}^{a}$, respectively. The subscripts indicate the spatial scale in kilometers and the time (t) in day of year (DOY). The superscript b is an indicator of prior knowledge before assimilation, and superscript a represent the analysis or optimal solution. The SVAT model used in the soil moisture modeling scheme is described briefly as follows.

We use the SWAP model [*Van Dam, et al.*, 1997] to simulate the processes of the soil-water-atmosphere-plant system. SWAP is a physically-based, hydrologic model that numerically solves the one-dimensional Richards' equation for simulating the soil moisture dynamics in the soil profile under different climatic and environmental conditions. Irrespective of scale, transient isothermal unsaturated water flow in non-swelling soil, Richards' equation used in SWAP is described by

$$\frac{\partial \theta}{\partial t} = \frac{\partial}{\partial z}\left[K\left(\frac{\partial h}{\partial z} + 1\right)\right] - S_a(h) \tag{4.1}$$

where θ is the soil water content (m^3/ m^3), z is the soil depth (m), h is the soil water pressure head (m), K is the unsaturated hydraulic conductivity (m/day), and $S_a(h)$ is the root water uptake (m/day). Penman-Monteith equation [*Monteith*, 1965] was used to

calculate potential evapotranspiration. The potential transpiration (T_p) and the soil evaporation (E_p) were partitioned using LAI. In the SWAP model soil moisture retention and hydraulic conductivity functions are defined by the Mualem-van Genuchten model [*van Genuchten*, 1980].

The modeling procedures at coarsest and finest scale mentioned above are used in the two methods proposed for downscaling satellite-based soil moisture information. The first downscaling scheme makes use of soil moisture estimates at the coarsest (i.e., AMSR-E footprint scale ~60 km), and the finest (i.e., Nexrad footprint scale ~4 km) scale to describe the probability distribution of soil moisture at intermediate scales. The second method uses the soil moisture (with SVAT) modeling at coarsest and finest scales within a data assimilation framework to assess the soil moisture fields at intermediate scales.

Method 1: Estimation of Probability Density Function (PDF) at Interim Scale

Understanding the statistical distribution of soil moisture in varying space is important for a range of applications in hydrology, remote sensing, and land-atmosphere interactions. One approach to characterize statistical distribution of soil moisture is by developing probability density functions (pdfs). Ryu and Famiglietti [2005] studied behavioral features of satellite footprint-scale (~60 km) soil moisture pdfs obtained by aggregating airborne remotely sensed data (~ 0.8 km resolution) and suggested that normal distribution is reasonable for soil moisture pdf. Therefore, from the modeling exercise of this study, normal pdf is assessed at respective coarsest (~60 km) and finest

(~4 km) scale. To obtain pdf at an intermediate scale (e.g., ~8 km, ~15 km, or ~30 km) a weighted combination of pdfs at coarsest and finest scale is used. The hypothesis of such combination of pdfs is that the parameters of probability distribution functions of the interim scales are located somewhere between the parameters of coarsest and finest scales. The following description briefly explains the algorithm of parameters estimation for the pdfs at intermediate scales. The normal probability distribution from modeling at the coarsest scale is given by $X_{60} \sim N(\mu_{60}, \sigma_{60}^2)$, where μ_{60} is the mean and σ_{60}^2 is the variance of soil moisture estimate from $X_{60,t}^a$. Similarly, $X_4 \sim N(\mu_4, \sigma_4^2)$ is the normal probability distribution of soil moisture at the finest scale $\left[X_{4,t}^b\right]$, and μ_4 is the mean and σ_4^2 is the variance at ~4 km resolution, within the AMSR-E footprint. To determine the interim scale pdf, for example at ~30 km resolution is given by

$$X_{30} \sim N\{(a * \mu_{60} + b * \mu_4), (a^2 * \sigma_{60}^2 + b^2 * \sigma_4^2)\} \quad (4.2)$$

In eq. 4.2 the coefficient *a* and *b* are described as

$$a = \frac{A - x_1}{A}, \text{ and } b = \frac{A - x_2}{A} \quad (4.3)$$

where, *A* in eq. 4.3 is the difference between the area (3600 km^2) of coarsest scale (~60) and the area (~16 km2) of finest spatial scale (~4 km). In eq. 4.3, x_1 is the difference between the area of desired spatial scale and the area of finest spatial scale (~16 km2), in this case it is (|900 km^2 – 16 km^2|), and x_2 is the difference between the corarest scale (~60) and the desired spatial scale i.e., (|3600 km^2 – 900 km^2|). The advantage of this downscaling method is to obtain an approximate estimate of mean and variance at a particular interm spatial scale. However, it is incapable to describe the essential spatial organization of the soil moisture evolution at the interm scales within the satellite

footprint. The second method proposed for spatial downscaling of soil moisture imparts the capability of spatial organization of soil moisture evolution at the finer scales.

Method 2: Estimation of Soil Moisture Fields at Interim Scales

Given the optimal solution of soil moisture $X^{a}_{60,t}$ at footprint scale (~60 km) and simulated soil moisture fields $\left[X^{b}_{4,t}\right]$ at finest scale (~4 km), the problem of estimating the soil moisture fields at intermediate scales (~4 km, ~8 km, ~15 km, and ~30 km) has been addressed through the development of multiscale Ensemble Kalman Filter (EnKF) algorithm. Keeping in mind the multiscale nature of the problem and exchange of information required across spatial scales, the algorithm of multiscale EnKF is divided in two parts, a) Upward sweep, i.e., traversing from fine-to-coarse scale, and b) Downward jump, i.e., traversing from coarse-to-fine scale. This mechanism of upward and downward sweep ensures that the soil moisture fields at the finer scales possess the attributes of finest and coarsest scales. Figure 4.2 illustrates the scheme, and is explained below

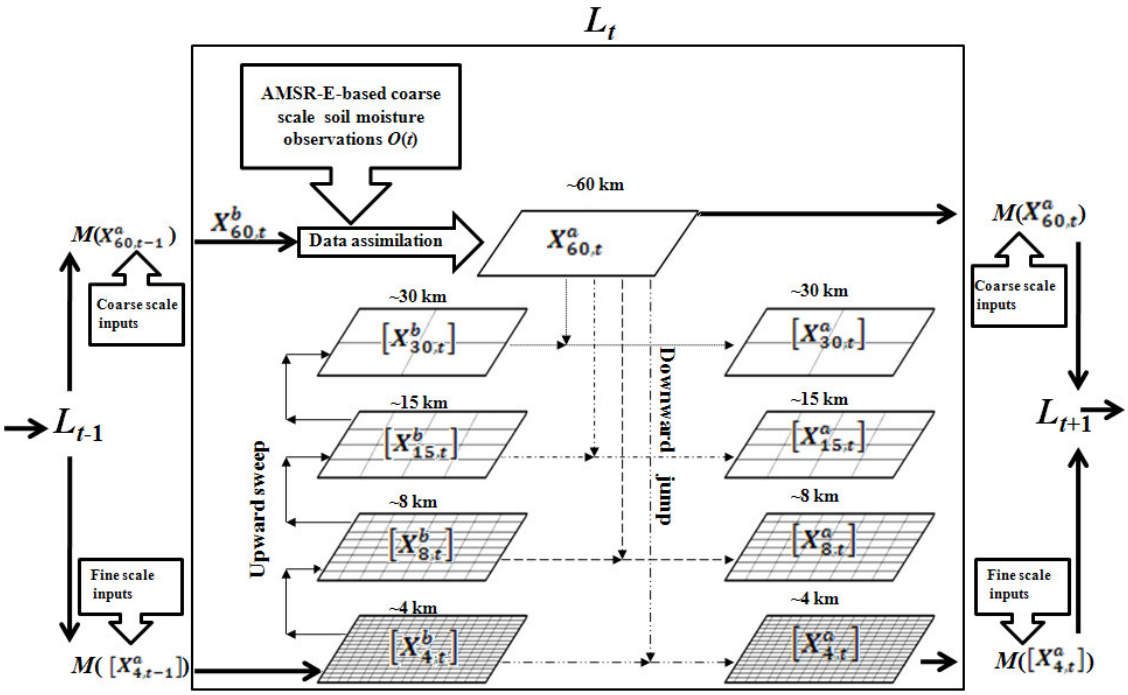

Figure 4.2. Schematic of proposed approach having an upward sweep that provides the priors and downward jumps that provide the likelihood of soil moisture estimate across spatial scales within the satellite-based soil moisture footprint for multiscale data assimilation. *M*: Hydrologic model, *O*: Observation, *X*: State variable i.e., soil moisture, *L*: multiscale data assimilation, *t*: time, b: background/prior, and *a*: optimal solution or analysis.

Upward sweep

The rationale of using upward sweep is to propogate soil moisture information (having influence of fine scale geophysical parameters/variables and hydrologic processes) from finest scale to coarser scales. Basically, it is an smoothing operation

from finest to coarser scales that provides estimate (background/prior information for data assimilation) of soil moisture fields at intermediate scales. In the study, the upward sweep from the finest scale is implemented by subjecting the simulated soil moisture fields to Haar-based scaling filter [*Haar*, 1910]. The Haar-based spatial scaling is preferred because it conserves the amount of information within multiresolution analysis. The Haar scaling $\varphi(x)$ function is the simplest of all orthogonal (orthonormal) scaling [*Kumar and Foufoula-Georgiou*, 1997] and is given as:

$$\phi_{m,\mathrm{n}}(x) = \begin{cases} 1 & 0 \le x < 1 \\ 0 & otherwise \end{cases} \tag{4.4}$$

where,

$$\phi_{m,n}(x) = 2^{-m/2}\,\phi(2^{-m}x - n) \tag{4.5}$$

For the soil moisture field $f(x)$ at finest resolution, the coefficients $C_{m,n} = \int \phi_{m,n}(x)\, f(x)\, dx$ give the discrete sampled values of $f(x)$ at scale m and location n. For Haar scaling function, $m_0 = 2$, and the scale parameter is dyadic series i.e., $m = 2,4,8,\ldots$, and the location n is incremented in steps that depends on the scale parameter so that $x = nx_0m_0^{\mathrm{m}}$, here x_0 is the soil moisture field at highest available resolution. Figure 4.2 illustrates the configuration of soil moisture field upward sweep using Haar scaling function, here $f(x)$ is represented as a field of soil moisture $\left[X_{4,t}^{b}\right]$ at ~4 km resolution. At each level of upsweep, the smoothed nonstationary soil moisture fields become more homogenous and the anisotropy is captured by the stationary fluctuation components of Haar wavelets filter. Three intermediate soil moisture fields

of resolution ~8 km: $\left[X_{8,t}^{b}\right]$, ~15 km: $\left[X_{15,t}^{b}\right]$, and ~30 km: $\left[X_{30,t}^{b}\right]$ are realized from the finest resolution (~4 km) soil moisture field of $\left[X_{4,t}^{b}\right]$.

Downward jump

As already mentioned that satellite-based passive microwave remote sensing of soil moisture provides vast horizontal support of ~60 km. The data reflects integrated information of the intrinisic neighborhood variability and dynamics in terms of large scale soil moisture processes. Thus, the downward jump produces finer scale estimates that incorporate the information of the entire remote sensing footprint (~60 km). In other words, the downward jump carries the large scale information to finer scales.

Before conducting downward jump, the optimal solution is obtained at satellite footprint scale from EnKF-based data assimilation of coarse scale SVAT model (*M*) forecast and AMSR-E obervation *O* (suggested by Das et al. [2008b] and also mentioned in Chapter II) as shown in Fig 4.2 and is described in eq. 4.6.

$$X_{60,t}^{a} = X_{60,t}^{b} + K_{60,t}\{O_t - X_{60,t}^{b}\} \quad (4.6)$$

where, $X_{60,t}^{b}$ is the forecast/background at time *t* obtained from $M(X_{60,t-1}^{b})$, O_t is the AMSR-E observation at time *t*, $K_{60,t}$ is the Kalman gain, and $X_{60,t}^{a}$ is the analysis or the optimal solution at the coarsest scale (~60 km) at time *t* (Fig. 4.2).

The optimal solution $X_{60,t}^{a}$ is subjected to downscaling during downward jump at time *t*. The derived scaling parameters $\beta_{s,t}$ (the subscript *s* is an indicator of particular spatial scale), downscales $X_{60,t}^{a}$ to the finer scales. The downscaled soil moisture i.e., $\beta_s * X_{60,t}^{a}$

is assimilated using EnKF with the smoothed soil moisture estimate from the upward sweep operation. For example, the estimate at ~30 km resolution is given by

$$X^a_{30,t} = X^b_{30,t} + K_{30,t}\{\beta_{30,t} * X^a_{60,t} - X^b_{30,t}\} \quad (4.7)$$

$$K_{30,t} = \frac{P_{30,t}}{P_{30,t} + \beta_{30,t} * R_{60,t}} \quad (4.8)$$

where, $X^b_{30,t}$ is the smoothed soil moisture value from upward sweep, $K_{30,t}$ is the Kalman gain at ~30 km scale, $\beta_{30,t} * X^a_{60,t}$ is the soil moisture downscaled to ~30 km scale from the coarsest scale (~60 km), $P_{30,t}$ is the background error of $X^b_{30,t}$, $R_{60,t}$ is the error covariance of the optimal solution at the coarsest scale, and $X^a_{30,t}$ is the analysis or the optimal solution at ~30 km resolution. This multiscale EnKF-based data assimilation is conducted individually for all the pixels at ~30 km resolution. Similar approach is applied to finer scale soil moisture field (~4km, ~8 km, and 15 km) to get optimal solution at their respective scales. At the finest scale (~4 km), the optimal solution of soil moisture at the soil surface is propagated to root-zone using the covariance matrix of the profile soil moisture that evolves over time. This ensure to vertically extrapolate surface soil moisture solution from data assimilation to soil moisture states at deeper depths that are not directly involved in the data assimilation scheme. The advantage of updating root-zone is to carry on the information gained forward in time that influence the evolution of profile soil moisture to the next time step while modeling at finest scale.

The key to this multiscale data assimilation is the bridging model for scaling parameter $\beta_{s,t}$ that provides the coupling mechanism. The scale parameter $\beta_{s,t}$ embodies the influence of geophysical parameters/variables on spatio-temporal evolution of soil

moisture in the particular scale. The relation of geophysical parameters and variables with $\beta_{s,t}$ is given by the model

$$\beta_{s,t} = \left\{1 + \frac{(1 - Sf) * NDVI_t + |1 - 1/e^{slp}|}{(1 + e^{pcp_t})}\right\}^{\log(\log(s))} \quad (4.9)$$

where, Sf is the average sand fraction (-) in soil texture, $NDVI_t$ is the Normalized Difference Vegetative Index (-) at time t, slp is the average slope (-), and pcp_t is the amount of daily precipitation (mm) in the particular pixel of spatial scale ratio s. The s (-) is the ratio of area of coarsest scale to the area of desired spatial scale (e.g., with the coarsest scale ~60 km and for the desired scale ~30 km, s = [(60*60)/(30*30)] = 4). For a desired scale, geophysical parameters and precipitation data are obtained from Haar-based multiresolution technique that provided the pixel based values from the fine scale data that are used in eq. 4.9.

The formulation of scaling parameter $\beta_{s,t}$ is empirical in nature and is always ≥ 1. Studies e.g., Das and Mohanty [2008], Hu et al. [1997], and Oldak et al. [2002] have shown that the mean value of soil moisture increases with increasing resolution having multiscaling characteristics and remains almost the same during simple scaling. The satellite-based remote sensor (AMSR-E) footprint is considered the base scale in development of the model for scale parameter $\beta_{s,t}$. Therefore, in eq. 4.9, $\beta_{s,t}$ is equal to 1 for the coarsest resolution (in this study for ~60 km resolution) and for fine scales $\beta_{s,t}$ have values greater than or equal to 1 depending upon the spatial and temporal evolution of geophysical factors that affect its evolution. The geophysical parameters (Sf, $NDVI_t$ and slp), that espescially influence $\beta_{s,t}$, have two space and time invariant factors (Sf and slp) and one time variant factor ($NDVI_t$) for all the desired scale. The contribution of

these factors are further described to elaborate their significance in eq. 4.9. The term (1-*Sf*) exhibits the physical control of soil on $\beta_{s,t}$. It is well established that *Sf* influences infiltration into the soil; greater the *Sf*, higher is the infiltration rate. This leads to less runoff generation, that means less nonlinearity in surface soil moisture. Soils with high *Sf* have better subsurface flow and have more uniform distribution of soil moisture. Typically, sandy soils rarely become water logged and allow most of the water to percolate downward more rapidly than clayey soils. Consequently, homogenity in soil moisture field is observed in the soil type having higher *Sf*. The term (1- *Sf*) also represents the silt and clay portion of the soil that shows high water retention/holding capacity, resulting in more runoff and higher nonlinearity in the system. Reduction in *Sf* displays this attribute and affects by increasing the value of scaling parameter $\beta_{s,t}$. The soil characteristics and vegetation are closely related in the proposed model of $\beta_{s,t}$. When *Sf* is 1 (i.e., 100% sand), the model mimics an arid (desert) condition which does not support any form of vegetation. Hence, the term [(1-*Sf*) * $NDVI_t$] in the numerator of eq. 4.9 becomes zero, and has no contribution in downscaling soil moisture from the coarsest scale. In other words, the downscaling of soil moisture is not required, if the effect of *slp* and pcp_t are ignored. It is hypothesized that soil with *Sf* less < 1 is capable of supporting vegetation. Therefore, the effect of $NDVI_t$ increases with the reduction of *Sf*. However, the contribution of $NDVI_t$ to $\beta_{s,t}$ value is significant in its own respect. Evapotranspiration through vegetation canopy (represented in the model as $NDVI_t$) introduces variability in spatial evolution of soil moisture that imparts nonlinear scaling characteristics. The $NDVI_t$ value in eq. 4.9 also reflects the effects of vegetation that

creates macpores due to biomass and roots in the soil profile leading to uneven distribution of soil moisture and consequently affecting the scaling charateristics. Overall, the term [(1-*Sf*)* $NDVI_t$] in eq. 4.9 accounts for interaction between soil and vegetation and their combined effect on spatial scaling of soil moisture.

The term $|1-1/e^{slp}|$ in eq. 9 represents the topographic effects on soil moisture spatial scaling. Note, *slp* is described in fraction i.e., (topographic relief)/100. Higher averege slope exhibits rough terrain and complex overland and subsurface/lateral flow within the pixel of particular scale. Terrain-based simulations have shown typical soil moisture patterns (i.e., wet conditions in lower elevation and dry conditions at higher elevation) that are correlated with the topographic attributes. This effect is even more prominent after precipitation events. Studies (e.g., [*Yeakley, et al.*, 1998]) have also found that topograhic effects on soil moisture is more predominant in the upper layer of the soil. Overall, the topographic control on soil moisture manifests itself in the form of spatial variability. In Eq.9, a value of zero is realized for the term $|1-1/e^{slp}|$ having $slp = 0$ that represents a flat surface, and the value then increases correspondingly with the increase in average slope that leads to nonlinear scaling for rough terrain.

In the numerator of eq. 4.9, the two terms $|1-1/e^{slp}|$ and [(1-*Sf*) * *NDVI*] express the variability and scaling requirement of soil moisture for the finer resolution pixels within satellite-based footprint. However, the term in the denominator $(1 + e^{pcp_t})$ of eq. 4.9 negates this effect in the event of precipitation. In $\beta_{s,t}$, fractional (i.e., subpixel variability) precipitation within the pixel is ignored. Therefore, the precipitation is considered uniform within the pixel which tends to remove the soil moisture variability

from the concerned pixel. It is obvious from $(1 + e^{pcp_t})$ that higher the amount of precipitation, lesser is the value of $\beta_{s,t}$, and as it gets closer to 1 indicating simple scaling in soil moisture. This phenomenon takes place on the day of precipitation event. However, in the absence of precipitation, sand fraction, NDVI, and slope should entirely describe the soil moisture scaling characteristics. The term $(1 + e^{pcp_t})$ also has a normalizing tendency i.e., with no precipitation ($pcp_t = 0$) the value is 2 that averages out the effect of the two terms in the numerator $\beta_{s,t}$ formulation. On the day of precipitation, the magnitude of $(1 + e^{pcp_t})$ is greater than 2 and is directly proportional to the amount of precipitation that sytematically mitigates the effects of sand fraction, NDVI, and slope.

The physical significance of the term $log(log(s))$ in eq. 4.9 is to exemplify the spatial scaling effects, when traversing from the coarsest scale to finer scales. The term $log(log(s))$ embodies the effect of contributing pixels at a particular scale in describing the state at the coarsest scale. The spatial area ratio s in the term $log(log(s))$ also represents the number of pixels at a finer scale that is contained within the coarsest scale. In this study, the magnitude of s at finer scale i.e., at ~30 km resolution is 4, at ~15 km is 16, at ~8 km is 56, and at ~4 km is 225. The value of s also represents the heterogenity factor due to number of pixels within the coarsest scale. The ultimate effect of the term $log(log(s))$ is to spatially downscale the optimal solution at coarsest scale to the finer scale pixel based on the interaction of the three physically-based terms i.e, $|1-1/e^{slp}|$, $[(1-Sf) * NDVI]$, $(1 + e^{pcp_t})$ as given by eq. 4.9.

The geophysical parameters in eq. 4.9 are the dominant factors among others that influence soil moisture scaling. However, other parameters like bulk density of soil, vegetation types, and elevation are likely candidates that may also influence the spatio-temporal evolution of soil moisture. These factors are, however, ignored in the formulation of $\beta_{s,t}$ (eq. 4.9) due to apparent correlations between *Sf* and bulk density, and between slope and elevation. We tried to keep the soil moisture scaling function as simple as possible using geophysical parameters that are easily obtained through remote sensing, or from existing databases.

4.4. Study Region and Data

Study Region

As illustrated in Fig. 4.3, large areas in Arizona (semi-arid), Iowa (agricultural), and Oklahoma (grassland/pastures) regions are selected for the study. These regions are selected for the sake of consistency with Das et al. [2008b], as this study is an extension. An important aspect of selection of these study regions is the diversity in hydroclimatic regions that helps understand the spatial scaling issues under different combinations of geophysical parameters/scenarios. The region from Arizona comprises perennial shrub cover with low LAI (< 1 m^2/m^2), well drained gravelly sandy loam soil, and moderately rocky and hilly terrains. The Iowa region has mainly a row crop agricultural landscape (nearly 60% corn and 40% soybean). This site is considered as the pothole region of Iowa because of its undulating terrain. The soil on the surface is mainly silty clay loam with a large percentage of organic matter. During the peak crop growing condition, the LAI for this region reaches a high of 4-6 m^2/m^2. The Oklahoma region is dominated by

grassland and pasture with rolling topography, with LAI averaging between 3 and 4 m^2/m^2 and attaining peak value between late spring and summer. Loamy sand, sandy loam, loam, and silty loam are the predominant surface soil textures in the Oklahoma region.

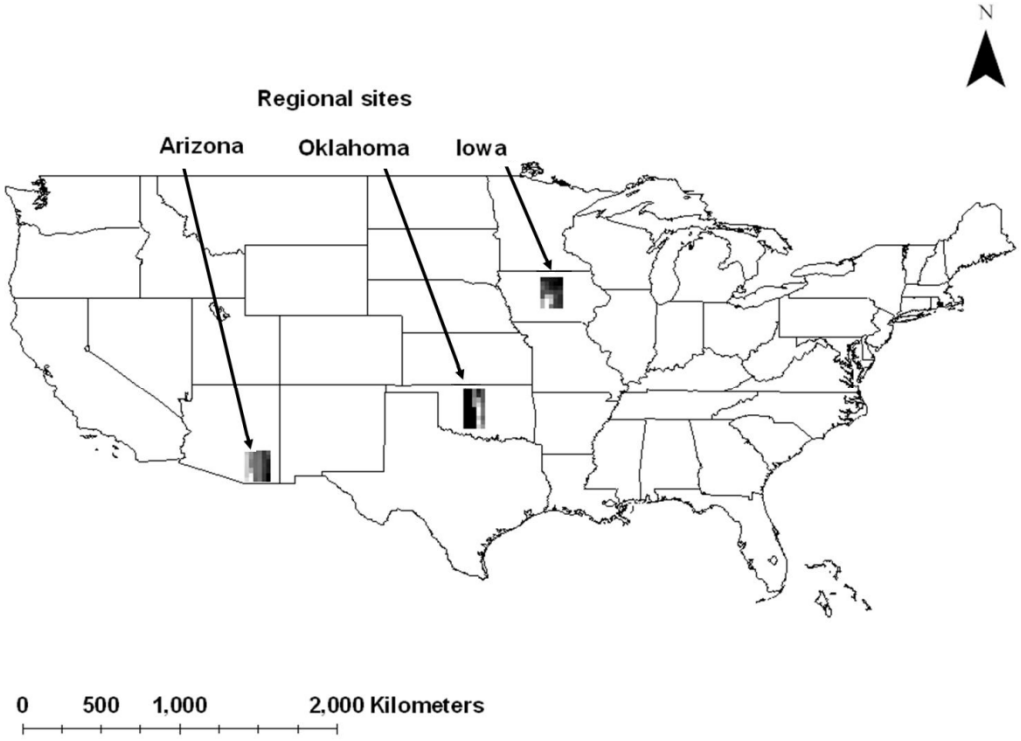

Figure 4.3. Three selected study regions (Arizona, Oklahoma, and Iowa) within the continental United States of America.

AMSR-E Data

For this study, we used one year (2005) of AMSR-E Level-2B gridded data extracted for the three regions (AZ, OK, IA) to downscale the AMSR-E soil moisture product. The data values correspond to a ~60 km mean spatial resolution. The more reliable night-time AMSR-E data [*Njoku, et al.*, 2003] are used, as soil moisture and temperature profiles remain more uniform, and soil vs. vegetation temperature differences are smaller during the night than the early afternoon. In other words, the soil moisture retrieval algorithm is expected to have less error and be more representative of deeper soil layers using the night-time data.

Soil

The soil data for the study was derived from CONUS-SOIL (available at http://www.soilinfo.psu.edu/),a multilayer soil characteristic dataset, comprises of requisite soil parameters (e.g., % sand, % clay, bulk density and saturated hydraulic conductivity) for the study. The % sand (*Sf*) data of ~1 km resolution is further subjected to the Haar-based scaling to obtain *Sf* at ~4 km, ~8 km, ~15 km, and ~30 km resolutions.

NDVI and LAI

MODIS derived 16 day composite data of *NDVI* and *LAI* at ~1 km spatial resolution is used for the study. The *NDVI* data for the study period is resampled further to ~4 km, ~8 km, ~15 km, and ~30 km resolutions using the Haar-based scaling.

Precipitation

The spatial resolution of ~4 km NEXRAD (WSR-88D) precipitation data is the most suitable for soil moisture modeling at finest resolution used in the study. Quality-controlled ~4 km precipitation data [*Seo and Breidenbach*, 2002] that is multi-sensor (radar WSR-88D and rain gauge) estimates is obtained from National Weather Service (NWS) River Forecast Centers (RFCs) and scaled to ~8 km, ~15 km, and ~30 km spatial resolution using the Haar-based scaling function.

Meteorological Forcings

Other important forcings (e.g., min and max air temperature, relative humidity and incoming solar radiation) that are relatively spatially homogenous are extracted from the North American Regional Reanalysis (NARR) dataset. The NARR dataset of ~32 km resolution are further resampled to ~4 km to suit the soil moisture modeling at finest resolution.

4.5. Results and Discussion

The proposed methods are applied in the study regions to demonstrate the application of algorithm (mentioned in Section 4.3) for estimation of soil moisture at varying spatial scales. The study period is for the year 2005. The results are discussed region wise to highlight the impact of hydroclimatic diversity on soil moisture evolution across spatial scales.

Arizona Regional Site

The SVAT modeling framework developed for this study is used to estimate soil moisture at the finest scale (~4 km). Figure 4.4 illustrates the mean estimated soil moisture ($\left[X_{4,t}^{b}\right]$) at ~4 km resolution (encompassed within the coarsest scale) plotted against the assimilated soil moisture estimates ($X_{60,t}^{a}$) for a AMSR-E footprint in the Arizona regional site for the year, 2005. A good agreement is observed between the two although with a systematic bias. Das et al. [2008b] also found high correlation between AMSR-E data and SVAT simulated soil moisture estimates at the AMSR-E footprint scale using upscaled soil hydraulic parameter for this semiarid region. In this study, the bias observed in Fig. 4.4 is a manifestation of spatial scaling between ~4 km and ~60 km. Even with the bias, the shape of scaling dependencies remains the same throughout the year. The linearity in Fig. 4.4 also suggests less volume of observations needed to predict surface soil moisture across spatial scale. This is also visible in the probability distribution functions (pdfs) shown on Fig. 4.5 that are created using $[X_4^b]$ and $[X_{60}^a]$ according to the proposed method 1 in Section 4.3. The spatial scaling attributes

are more prominent during the drydown period (Fig. 4.5b) as compared to dry day (Fig. 4.5a) and wet day ((Fig. 4.5c). With little difference in distribution parameters (mean and variance), the pdfs for dry days are almost similar across the scales. The reason for such behavior is the extreme dry condition that is mostly due to high rock and gravel fraction with sandy texture in the top soil layer, prevailing in such regions. This influences the soil hydraulic characteristics, making them highly nonlinear with high saturated hydraulic conductivity. This characteristics soil hydraulic feature drains the soil rapidly and consequently the top soil becomes very dry. High evaporation potential also contributes to the dryness of the top soil layer. The high hydraulic conductivity of the top soil layer also influences during the wet days in this region. As shown in Fig. 4.5c, the surface soil moisture could not attain a mean more than 10% v/v across the spatial scale within the ~60 km AMSR-E footprint for the particular wet day. Another noteworthy feature in Fig. 4.5c is the parameters (mean and variance) of the pdfs are almost similar for all the scales. Overall, for the region, these pdfs provide an impression that given an estimate or measurement in one scale between ~4 km and ~60 km gives a fair idea of surface soil moisture estimates in the other scale. The predictions of soil moisture distributions using method 1 (Section 4.3) at finer scale shows the uncertainties within a scale but lacks in describing the spatial organization of soil moisture and therefore, are of limited use.

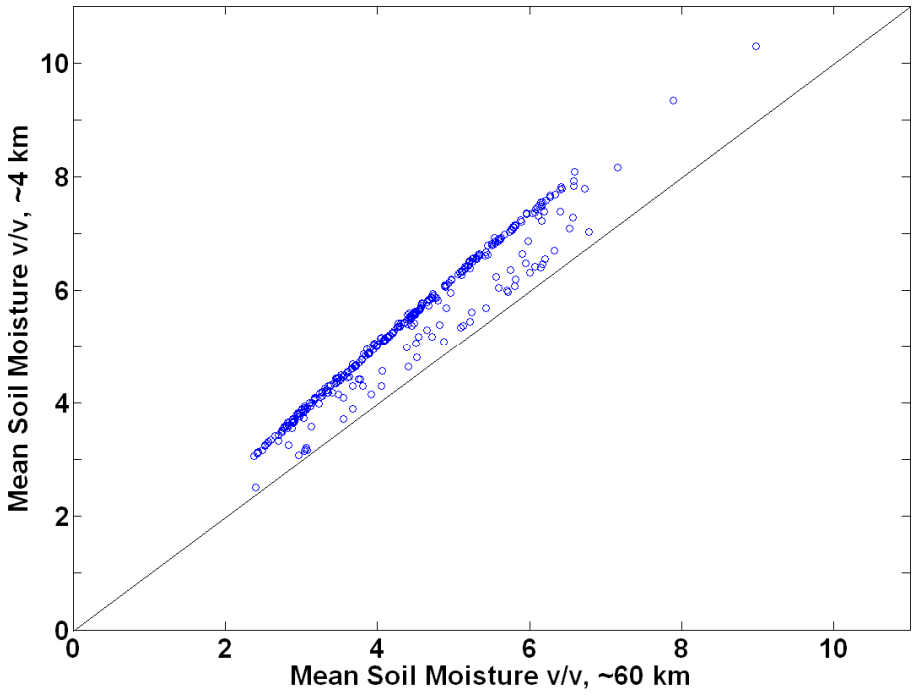

Figure 4.4. Plot of daily mean soil moisture v/v at ~60 km resolution against mean soil moisture v/v at ~4 km, for year 2005, for a randomly selected AMSR-E footprint from the Arizona study region.

The method 2 described in Section 4.3 is used to assess the soil moisture spatial organization. As elaborated in this method, the upsweep step provides the prior soil moisture estimates across increasing spatial scales. The downward jump uses the proposed bridging model (eq. 4.9) to obtain the likelihoods for the multiscale EnKF-based data assimilation. Table 4.1 provides the statistics of geophysical parameters/variables used in eq. 4.9. The bridging model (eq. 4.9) of downward jump results in scaling parameters $\beta_{s,t}$ for the region and the mean values are shown in Fig. 4.6. The scale parameter $\beta_{s,t}$ exhibits typical characteristics for this region. It remains

almost constant throughout the year, except for the days of precipitation events. Such characteristics in $\beta_{s,t}$ is attributed to the geophysical variables like $NDVI_t$ that remains almost constant (≈ 0.24) due to sparse semiarid vegetation throughout the year. A low value of $NDVI_t$ and very high mean (≈ 45 %) of *Sf* (sand fraction) at all finer scales indicates minimal scaling is required for downscaling an AMSR-E soil moisture footprint. However, the model (eq. 4.9) values for scale parameter $\beta_{s,t}$ shown in Fig. 4.6 are much higher than 1 for all the spatial scales except for days of high precipitation events. This is due to high value of the invariant geophysical parameter i.e., the slope (≈ 20˚) of the terrain within the pixels of finer resolutions. The value of the scale parameter $\beta_{s,t}$ also increases consistently with increase in spatial resolution (Fig. 4.6) because of inherent heterogenity factor (*s*) that is involved with increase in spatial resolution. Although, the geophysical parameter *slp* (slope) imparts high value to the scale parameter, the effect of spatial scaling is not visible in the soil moisture values. As illustrated in Fig. 4.7, within AMSR-E footprint of this region, for a particular wet day the surface soil moisture do not attain high values that is attributed to very high conducting top soil layer. This undermines the effects of scale parameter $\beta_{s,t}$, when downscaling the AMSR-E footprint soil moisture values in the downward jump operation.

Table 4.1. Statistics of sand fraction (*Sf*) and slope (*slp*) at different spatial scales for the Arizona regions.

		Arizona				
		mean	**min**	**max**	**std**	**mode**
~4 km	***Sf***	45.60	17.00	58.00	7.90	48.50
	slp	18.89	1.14	64.36	8.92	1.14
	wd	7.68	6.29	9.40	0.57	6.29
	ddp	5.54	4.89	6.92	0.42	4.89
	dd	4.05	3.57	5.20	0.35	3.57
~8 km	***Sf***	45.60	33.00	54.50	5.20	35.00
	slp	18.89	5.98	42.94	7.18	5.98
	wd	7.41	6.61	8.24	0.40	6.61
	ddp	5.34	4.88	6.08	0.30	4.88
	dd	3.88	3.61	4.50	0.24	3.61
~15 km	***Sf***	45.55	35.50	54.50	4.26	35.50
	slp	20.10	8.34	39.50	6.62	8.34
	wd	7.14	6.60	7.73	0.27	6.60
	ddp	5.17	4.92	5.49	0.19	4.92
	dd	3.73	3.56	4.09	0.17	3.56
~30 km	***Sf***	45.55	44.38	47.55	1.21	44.38
	slp	20.10	12.59	29.17	2.21	12.59
	wd	6.59	6.40	6.84	0.20	6.40
	ddp	4.68	4.62	4.74	0.05	4.62
	dd	3.38	3.32	3.46	0.06	3.32

Figure 4.7 displays the soil moisture fields with increasing resolution for wet and dry days from a randomly selected AMSR-E footprint of the region. Table 4.1 provides the statistics for the wet day and dry day at different resolutions that is shown in Fig. 4.7. The statistics of a randomly selected day during drydown period is also included in Table 4.1. The algorithm (Section 4.3) demonstrates its capability to capture the spatial

organization at the finer scales influenced by physical processes and geophysical factors. To validate the soil moisture evolution from the algorithm, ground data i.e., SCAN-based surface soil moisture measurements are plotted against the overlapping modeled soil moisture values at ~4 km resolution (Fig. 4.8). Overall, a reasonable agreement is found (R^2 of 0.55), however, with slight overestimation of modeled soil moisture at drier end. The overestimation resulted due to very small spatial support of the SCAN data that is representative of local-scale variability in comparison to spatial support of ~4 km. The soil hydraulic properties used for the region in the algorithm also constraint the evolution of soil moisture in extreme dry conditions by not allowing to recede below the residual water content. The errors involved in Nexrad-based precipitation and geophysical parameters at ~4 km spatial scale may also lead to such uncertainty that is shown in Fig. 4.8.

For the period of study, no specific soil moisture patterns are observed within the AMSR-E footprints. However, with sparse vegetation and highly conductive top sandy soil layer, any pattern imposed by precipitation and topography are expected to be lost immediately from the surface soil.

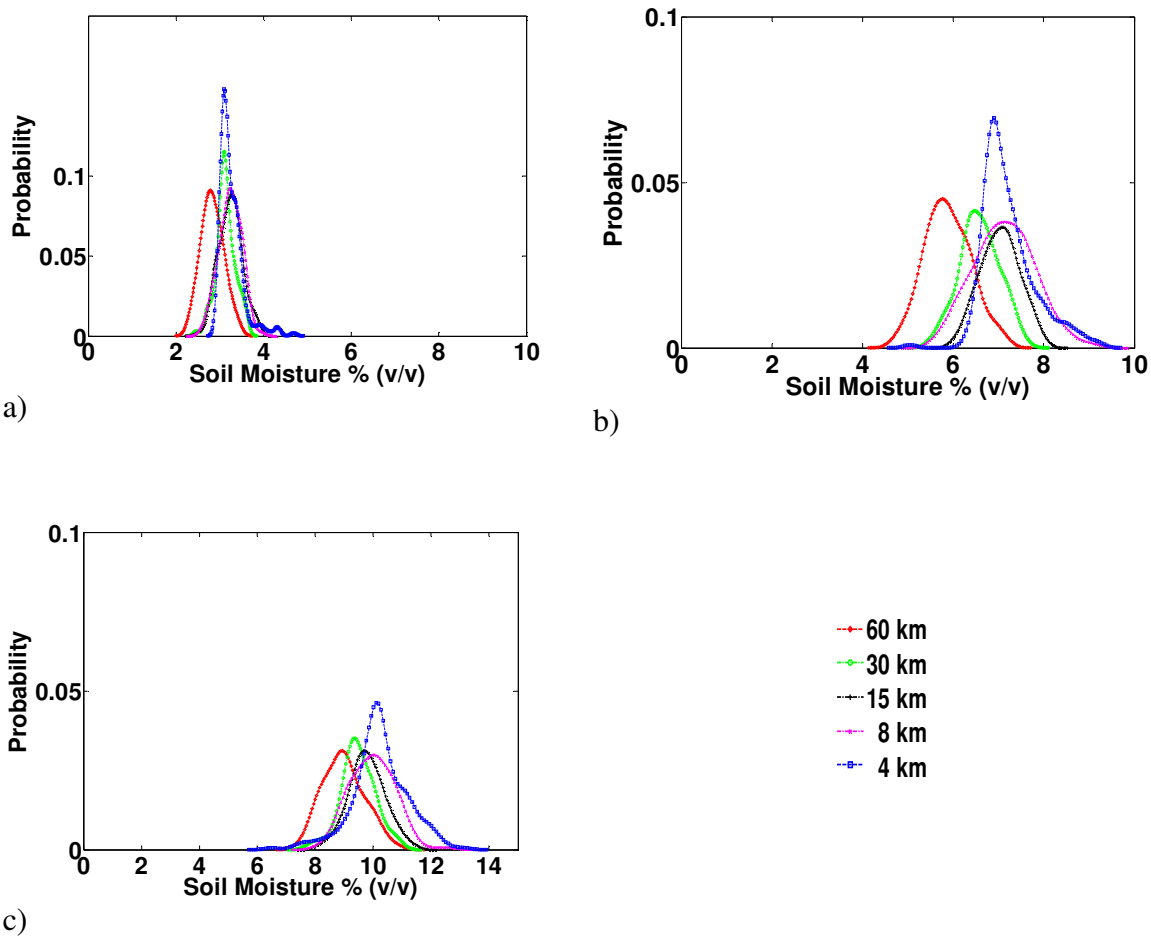

Figure 4.5. Soil moisture probability distribution functions (pdfs) at different spatial scales within a randomly selected the AMSR-E footprint, for a) dry day, b) a day during drydown period, and c) wet day, from the Arizona study region.

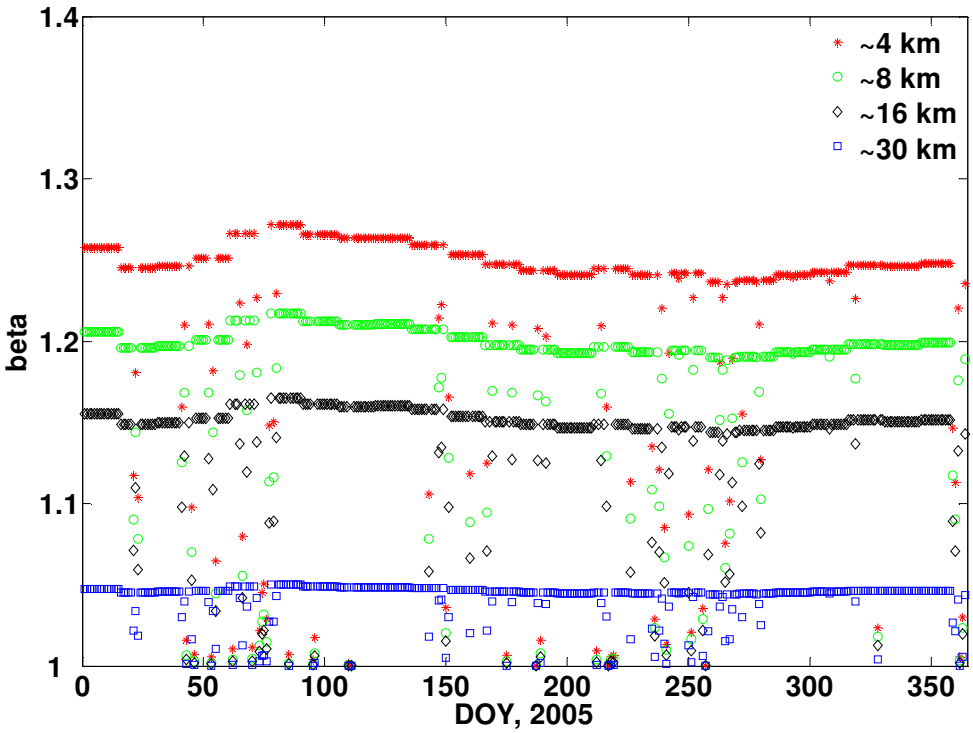

Figure 4.6. Plot of scale parameter β_s at different spatial scales, for year 2005, for a randomly selected AMSR-E footprint from the Arizona study region.

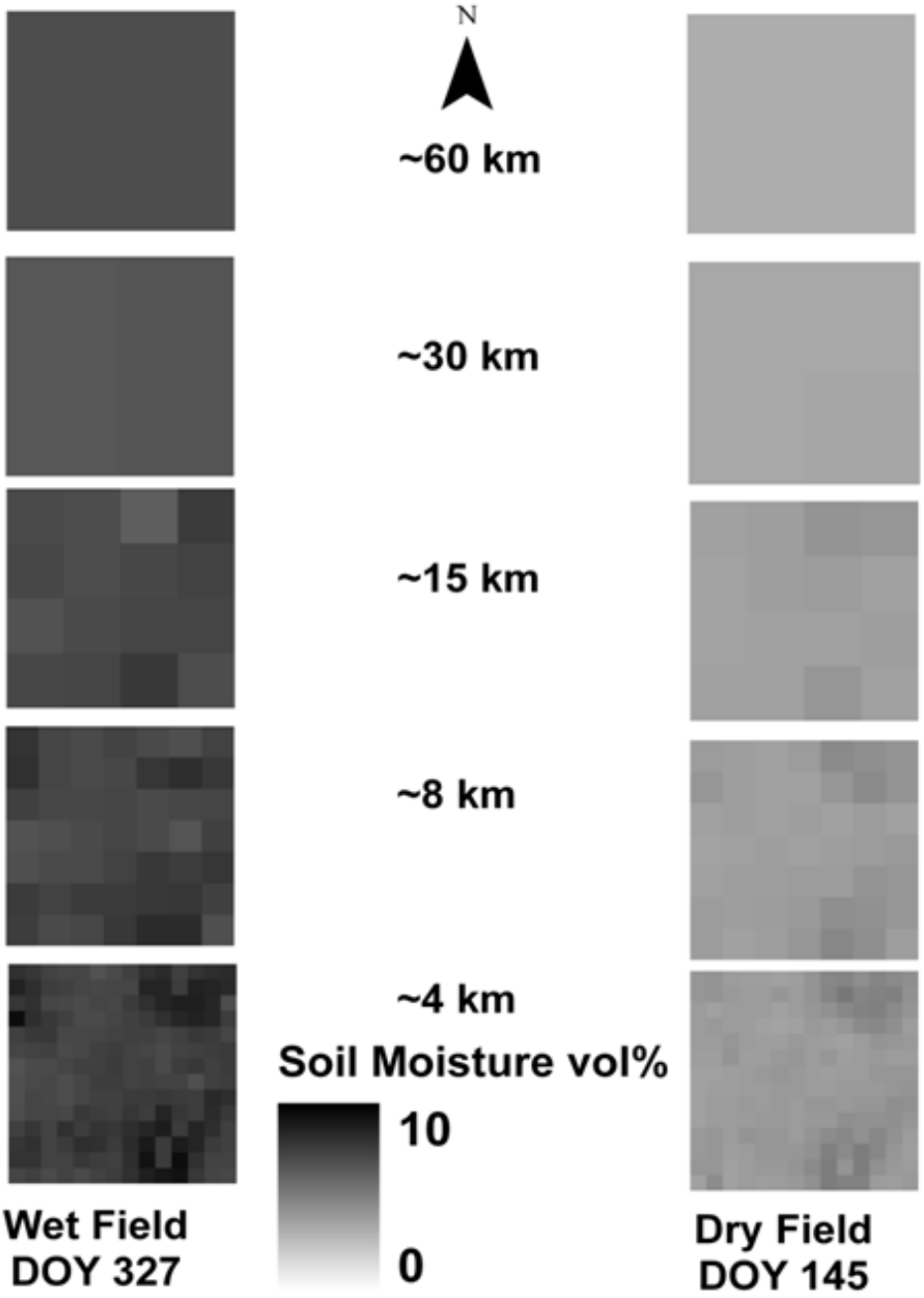

Figure 4.7. Soil moisture fields at different spatial scales, for a wet and dry day within a randomly selected AMSR-E footprint from the Arizona study region.

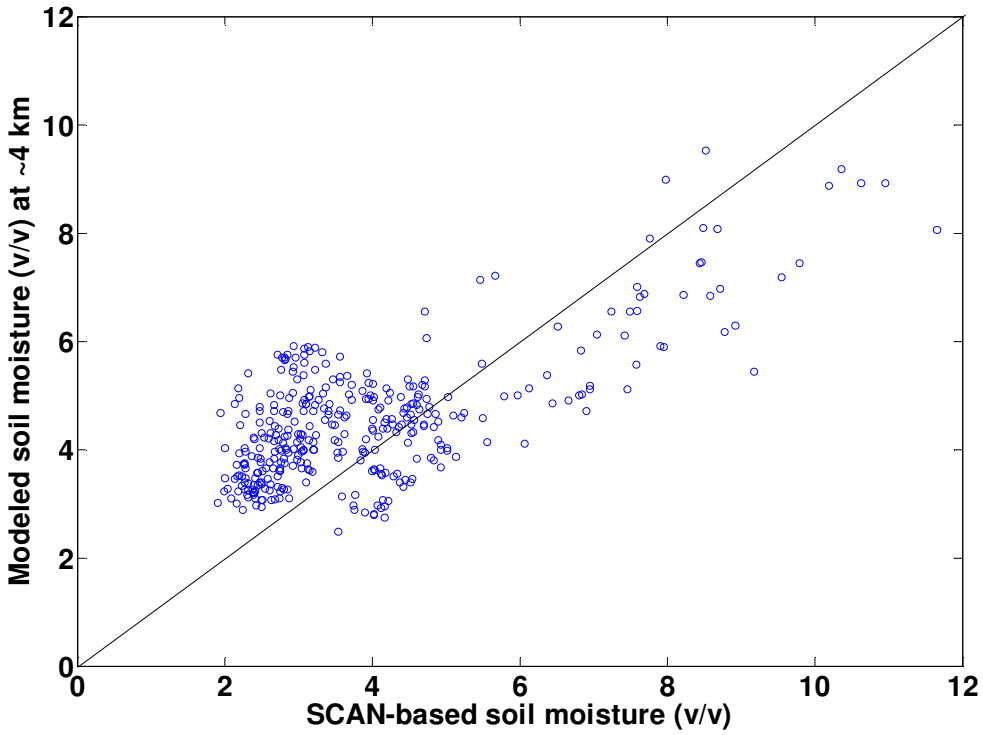

Figure 4.8. Comparison of Scan-based soil moisture data with overlapping pixel soil moisture evolution at ~4 km resolution from the proposed downscaling algorithm, in the Arizona region.

Iowa Regional Site

For a particular AMSR-E footprint of this regional site, Fig. 4.9 shows the mean of surface soil moisture simulated ($[X^b_{4,t}]$) at ~4 km resolution using SVAT modeling framework for fine scale against the assimilated surface soil moisture ($X^a_{60,t}$) estimated at the footprint scale for the year, 2005. More nonlinearity is observed in Fig. 4.9 than that of the Arizona regional site (Fig. 4.4). From Fig. 4.9, it is obvious that maximum scaling bias is at the drier conditions, whereas for the wet conditions less bias is observed. The

plot (Fig. 4.9) also indicates that the shape of spatial scaling dependencies changes consistently during the study period. In other words, the mean and the variance changes with increasing spatial scale and the rate of change is subjected to the condition (wet/dry) of soil moisture field. The pdfs shown in Fig. 4.10 obtained using method 1 (Section 4.3) also elaborate this phenomenon clearly. The pdfs (Fig 4.10a-c) show few distinct characteristics of soil moisture fields for wet and dry days (during a high vegetation period) in the region that are in contrast to the Arizona region (Fig. 4.5a-c). The mean of soil moisture across spatial scale for a dry day is distinct with the distributions having considerable variance. For this region, at the time of high vegetation, the pdfs for dry days also provide an impression that given an estimate or measurement in one scale does not provide enough information about surface soil moisture estimates in the other scale. Typical attributes are also observed i.e., increase of kurtosis during drydown process (Fig. 4.10). The region also experiences a high mean surface soil moisture and large variance in soil moisture evolution for wet days that highlight the effects of vegetation (i.e., through evapotranspiration) and high percentage of clay in the top soil layer.

Table 4.2. Statistics of sand fraction (*Sf*) and slope (*slp*) at different spatial scales for the Iowa region.

		Iowa				
		mean	**min**	**max**	**std**	**mode**
~4 km	***Sf***	21.42	10.00	35.00	7.00	16.00
	slp	2.70	0.21	6.75	1.33	0.21
	wd	33.49	29.18	40.51	1.85	29.18
	ddp	18.10	11.36	25.11	2.71	11.36
	dd	13.20	9.02	20.86	2.42	9.02
~8 km	***Sf***	21.26	12.00	35.00	4.60	16.00
	slp	2.70	0.42	5.10	0.99	0.42
	wd	33.57	30.76	39.48	2.04	30.76
	ddp	17.96	13.81	22.47	2.21	13.81
	dd	12.93	10.15	16.98	1.87	10.15
~15 km	***Sf***	21.25	16.00	25.50	2.05	20.50
	slp	2.65	1.09	3.78	0.79	1.09
	wd	33.05	30.91	34.60	1.19	30.91
	ddp	17.54	13.73	19.98	1.68	13.73
	dd	12.82	10.54	15.56	1.73	10.54
~30 km	***Sf***	21.25	20.03	22.23	0.75	20.03
	slp	2.65	2.39	2.91	0.29	2.39
	wd	33.61	33.17	33.98	0.40	33.17
	ddp	17.23	14.60	20.95	2.70	14.60
	dd	12.05	10.95	14.25	1.49	10.95

Unlike the Arizona site, the region has a relatively flat topography (having average *slp* of 2.7˚) and has low average sand fraction (*Sf* ≈ 21.25). Table 4.2 shows the statistics of *slp* and *Sf* for this region across spatial scales within a particular AMSR-E footprint. As expected, the variability of these geophysical parameters (*slp* and *Sf*) reduces with increasing spatial scale. The vegetation of this region adds another unique dimension. Corn and soybean agriculture dominates the landscape giving it a diverse temporal $NDVI_t$ based on growth and decay of crop. The $NDVI_t$ reaches it maximum (≈ 0.8) in the months of June and July, and has minimum value (nearly 0) during the months of January and December. These features impart interesting results for the scale parameter $\beta_{s,t}$ across spatial scales, as illustrated in Fig. 4.11. The bridging model (eq. 4.9) results in $\beta_{s,t}$ close to 1 for all the scales within the AMSR-E footprints for the months of January and December. This is due to very low $NDVI_t$ that nullifies the term [(1-*Sf*)**NDVI*] and the flat terrain also results in a low value from the term [|1-1/e^{slp}|] of eq. 4.9. With emergence of crop, a sudden increase in $\beta_{s,t}$ is observed. An upward trend of $\beta_{s,t}$ corresponds with the growth of the crop (i.e., with increasing $NDVI_t$) and then $\beta_{s,t}$ recedes with the decay of crop. The systematic difference in $\beta_{s,t}$ across scales (Fig. 4.11) is the effect of *s* that exhibits the inherent spatial heterogenity within the respective scale. Heavy precipitation events in the region smoothen out the variability introduced by $NDVI_t$ and drydown process, and consequently, making $\beta_{s,t}$ closer to 1. It is evident from the results (Fig. 4.11) that primarily $NDVI_t$ describes the behavior of $\beta_{s,t}$ for the region and precipitation has a secondary role that influences $\beta_{s,t}$. Using method 2 (Section 4.3), the AMSR-E footprint is downscaled for the region and a randomly

selected footprint is shown in Fig. 4.12 for wet and dry days, and the statistics presented in Table 4.2. It is interesting to note that no specific pattern is evident in the respective scales within the footprint in the wet and dry soil moisture fields at the spatial range between ~4 km and 60 km. The random patterns of surface soil moisture organization on a particular day and at a particular scale is due to the effect of transient evapotranspitation and precipitation distribution at respective scale within the footprint. The soil types and the cropping pattern within the AMSR-E footprint also imparts variability in evolving soil moisture patterns.

For the region, to validate the algorithm, 13 days of field-scale (WC11 and WC12 fields from the Walnut Creek watershed, Iowa) soil moisture data collected during Soil Moisture Experiment, 2005 (SMEX05) is used instead of SCAN-based data which is not of good quality for the study period. Figure 4.13 illustrates the comparison of field scale soil moisture with the modeled soil moisture from overlapping ~4 km resolution pixel. A good agreement is observed for all the 13 days but with slight underestimation from the algorithm that could be attributed to disparity in spatial scale. It is noteworthy that the algorithm responded to the precipitation events and drydown process as observed in the WC11 and WC12 fields.

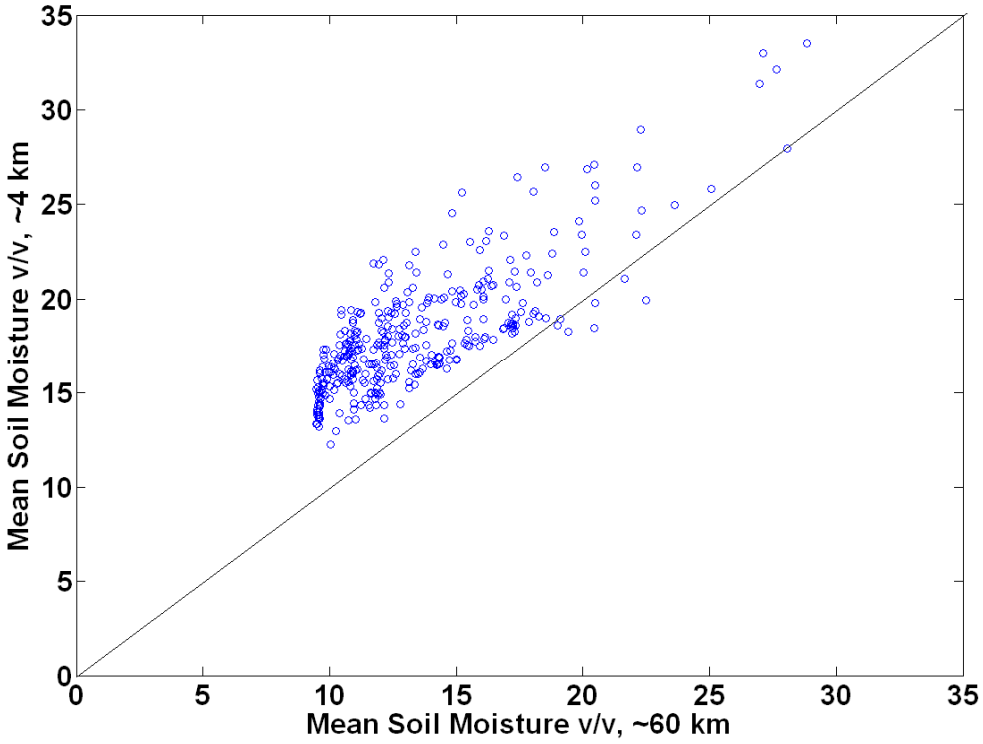

Figure 4.9. Plot of daily mean soil moisture v/v at ~60 km resolution against mean soil moisture v/v at ~4 km, for year 2005, for a randomly selected AMSR-E footprint from the Iowa study region.

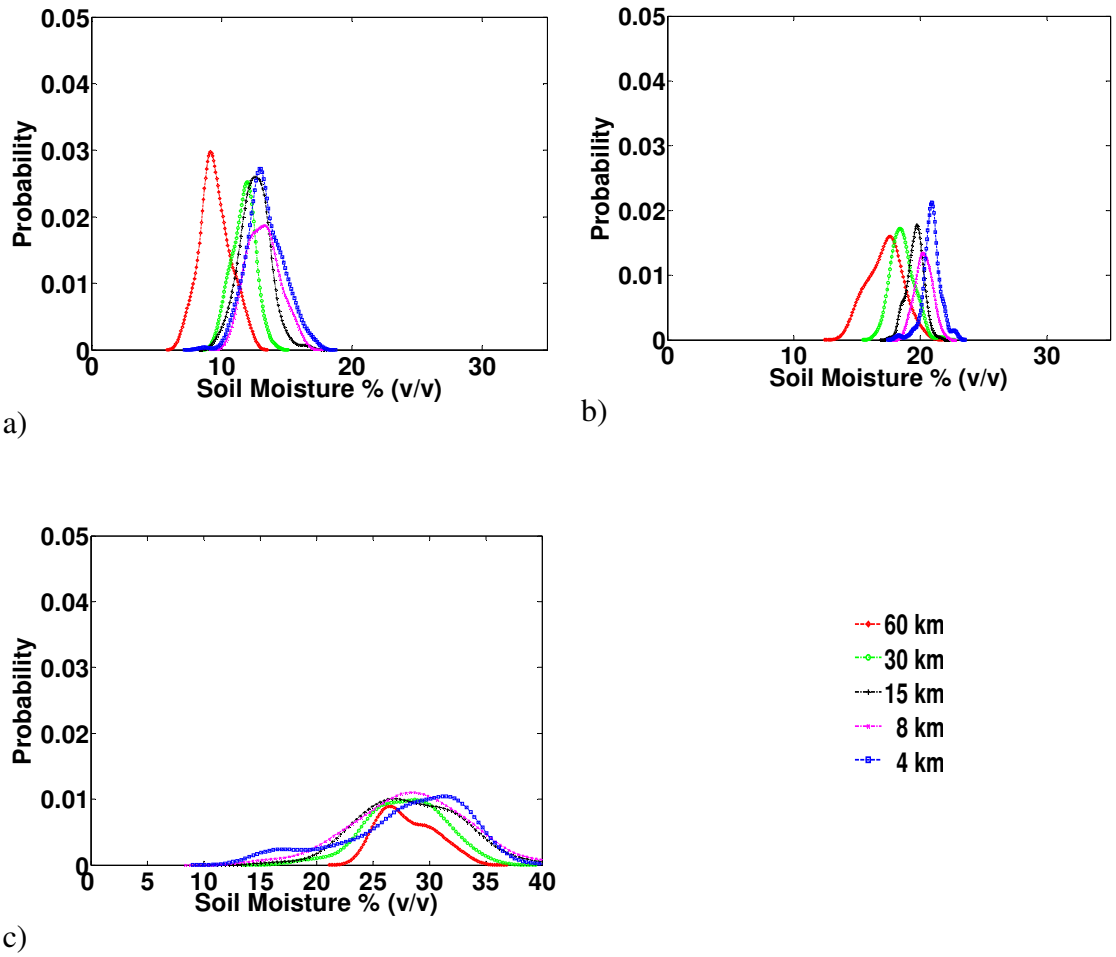

Figure 4.10. Soil moisture probability distribution functions (pdfs) at different spatial scales a randomly selected AMSR-E footprint, for a) dry day, b) a day during drydown period, and c) wet day, from the Iowa study region.

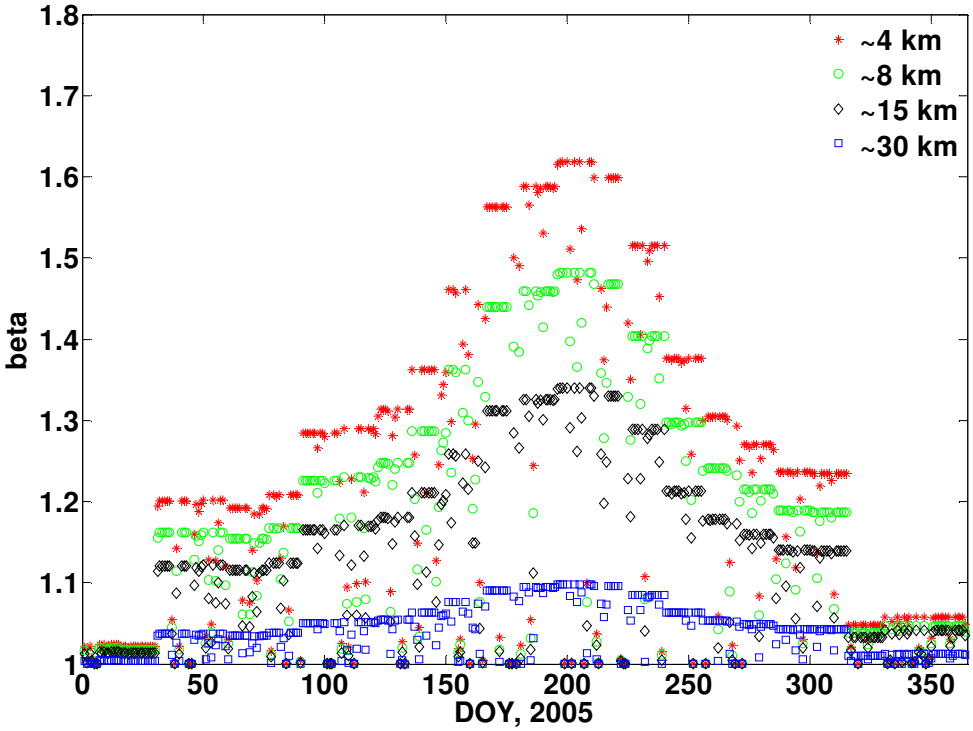

Figure 4.11. Plot of scale parameter β_s at different spatial scales, for year 2005, for a randomly selected AMSR-E footprint from the Iowa study region.

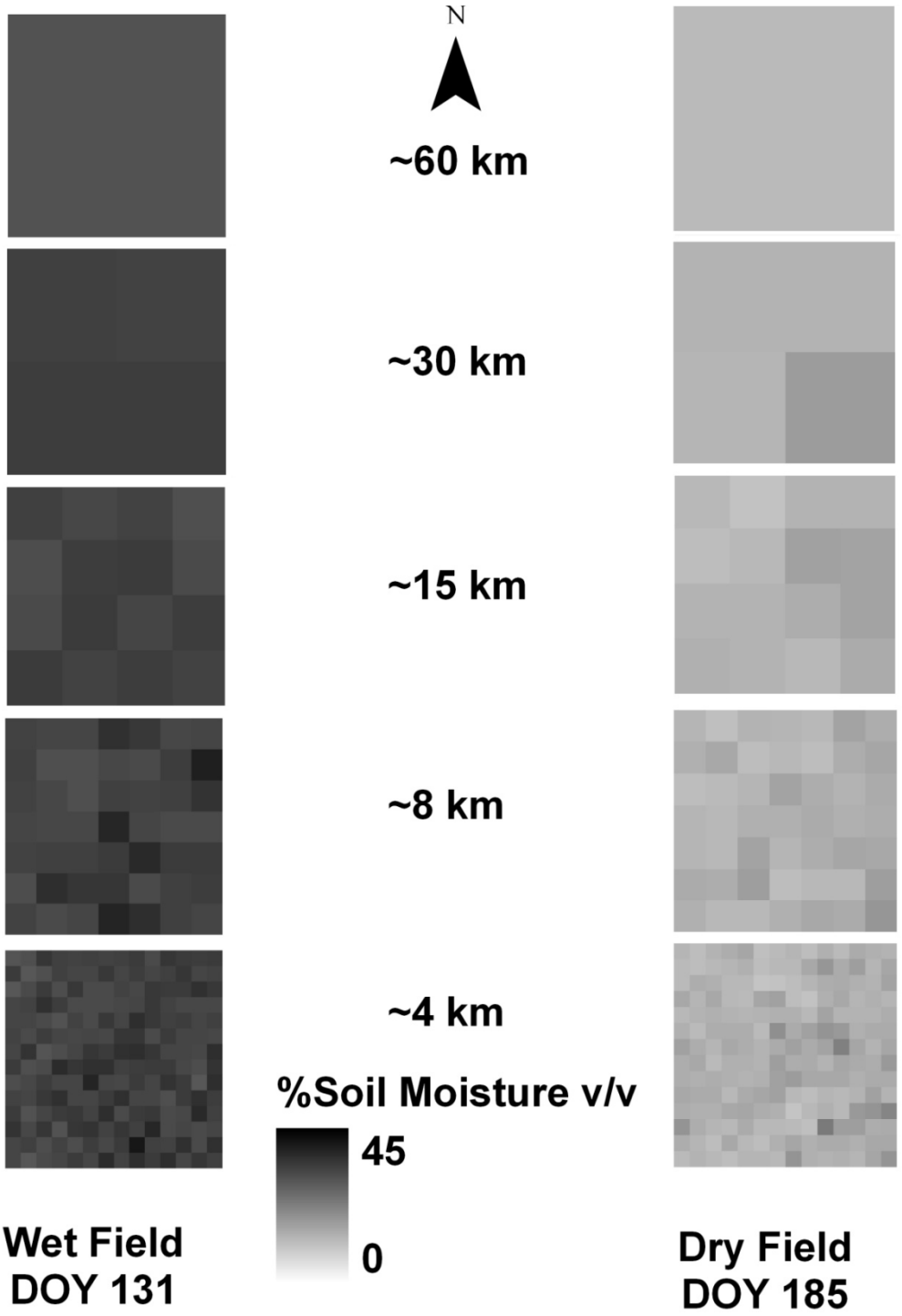

Figure 4.12. Soil moisture fields at different spatial scales, for a wet and dry day within a randomly selected AMSR-E footprint from the Iowa study region.

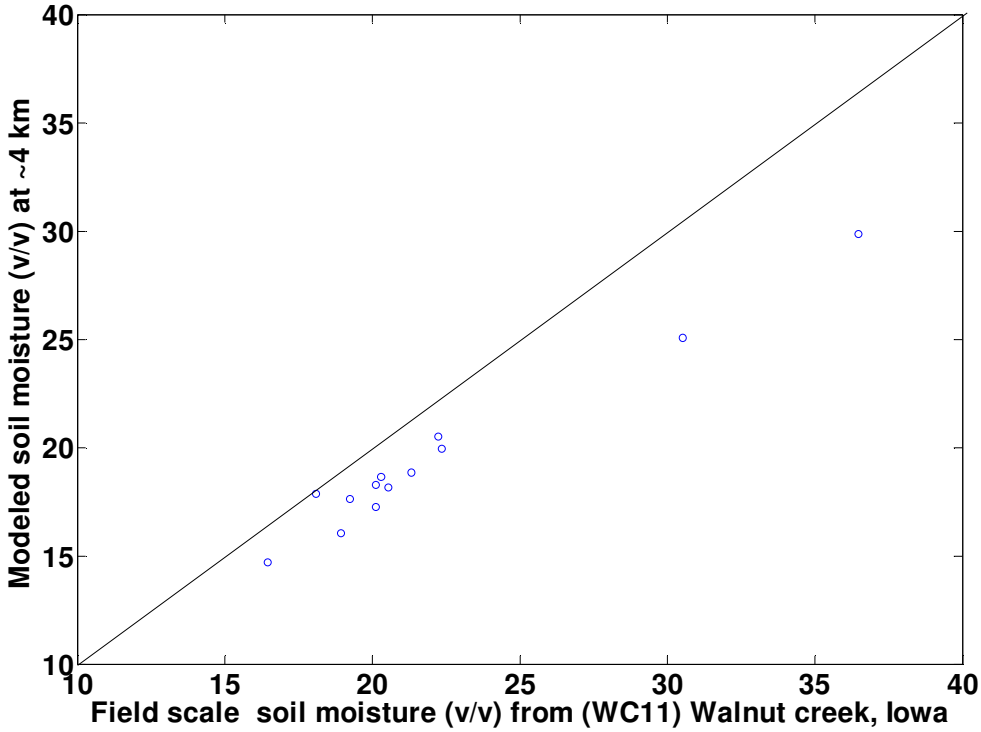

Figure 4.13. Comparison of measured field-scale (WC11 and WC12) soil moisture data with overlapping pixel soil moisture evolution at ~4 km resolution from the proposed downscaling algorithm, in the Walnut Creek watershed, Iowa.

Oklahoma Regional Site

Out of the three regional study sites, the Oklahoma region is the most diverse in terms of complex combination of soil, terrain and vegetation. The statistics in Table 4.3 for a particular footprint in the Oklahoma regional site, highlights the variety of surface soil texture with moderately high mean (≈ 30%) and standard deviation (*std*) of *Sf* for all the spatial scales within the AMSR-E footprint. The statistics of *slp* in Table 4.3 is representative of rolling topography. The region also experiences moderate to high

vegetation throughout the year. Emergence of crop/vegetation during spring and summer increases the $NDVI_t$ from average value of 0.35 to 0.6. With these factors and precipitation events, the evolution of soil moisture fields at various scales is discussed subsequently.

Table 4.3. Statistics of sand fraction (*Sf*) and slope (*slp*) at different spatial scales for the Oklahoma region.

		Oklahoma				
		mean	**min**	**max**	**std**	**mode**
~4 km	***Sf***	30.08	8.00	69.00	14.04	27.00
	slp	3.41	0.29	7.36	1.58	0.29
	wd	22.23	18.81	29.39	1.85	18.81
	ddp	17.73	8.01	24.98	3.75	8.01
	dd	14.62	6.23	22.16	3.07	6.23
~8 km	***Sf***	30.08	8.00	59.50	10.89	8.00
	slp	3.41	1.25	5.32	1.07	1.25
	wd	22.05	19.50	25.81	1.64	19.50
	ddp	17.97	13.00	22.63	2.24	13.00
	dd	14.71	8.87	18.81	1.96	8.87
~15 km	***Sf***	31.52	12.69	46.00	8.94	12.69
	slp	3.24	1.59	4.61	0.85	1.59
	wd	22.09	20.22	24.48	1.37	20.22
	ddp	17.51	15.78	20.02	1.40	15.78
	dd	14.58	10.51	17.90	1.66	10.51
~30 km	***Sf***	31.52	25.23	36.20	6.42	25.23
	slp	3.24	2.80	3.90	0.23	2.80
	wd	21.76	19.75	22.79	1.37	19.75
	ddp	16.67	16.23	16.99	0.37	16.23
	dd	14.05	12.89	14.93	0.98	12.89

The Oklahoma regional site exhibits the maximum scaling bias between the simulated mean surface soil moisture ($\left[X_{4,t}^{b}\right]$) at ~4 km and the assimilated surface soil moisture ($X_{60,t}^{a}$) estimated at ~60 km (AMSR-E footprint scale) for the year, 2005. Figure 4.14 illustrates the spatial scaling bias at ~4 km and ~60 km from a randomly selected AMSR-E footprint from the region. As expected, for wet days less scaling bias is observed. The region shows much higher scaling bias for drydown period as compared to the dry days. The evolution of soil moisture during drydown period is characterized by processes controlled by vegetation, soil and meteorological forcings and are affected by spatial scaling. However, for the dry days, soil is the primary physical control that characterizes the soil moisture fields. The fine and coarse scale SVAT model framework captures these phenomena during the drydown period and for the dry days. The pdfs of Fig. 4.15a-c obtained using method 1 (Section 4.3) substantiate this trend that is observed for wet days, drydown period and dry days. The effect of diversity in surface soil moisture evolution is also exemplified by the pdfs of ~4 km resolution that retain considerable variability irrespective of dry days (Fig. 4.15a), drydown period (Fig. 4.15b) and wet days (Fig. 4.15c). However, the spatial organizations of soil moisture across spatial scales within the AMSR-E footprint that are not captured by pdfs are obtained using method 2 (Section 4.3). The bridging model of method 2 provides the scale parameters $\beta_{s,t}$ values shown in Fig. 4.16 for a particular AMSR-E footprint of this regional site that gives a representative idea of spatial variability present across different scales. From Fig. 4.16, it is evident that the value of $\beta_{s,t}$ at a particular spatial scale is a summation of a baseline value and a transient term except for the days having

precipitation event. The baseline value of $\beta_{s,t}$ for a pixel at a particular spatial scale is imparted by *slp*, *Sf*, *s* and the minimum $NDVI_t$ value within a year. The transient part of $\beta_{s,t}$ corresponds with the $NDVI_t$ value that exceeds the minimum $NDVI_t$. For dry days, the high value of $\beta_{s,t}$ in the algorithm is compensated by the low (near residual) soil moisture values. For the wet days, $\beta_{s,t}$ value is low or close to 1, and the spatial organisation of soil misture field at a particular spatial scale is influenced by the precipitation pattern and soil moisture evolution at finest scale. The maximum influence of $\beta_{s,t}$ on spatial organization is observed during the drydown period, when the soil moisture values are in mid ranges. Based on these values of $\beta_{s,t}$, an example of the multiscale data assimilation results is shown in Fig. 4.17 for a wet and dry days, and the statistics presented in Table 4.3. Like the Iowa region, no specific trend is observed in the wet and dry soil moisture fields in the range of spatial scale between ~4 km and ~60 km. In such diverse region, the spatial organization of soil moisture within the AMSR-E footprint for any day at a particular scale does not depend on any specific physical control. In fact, the result suggests that for the region, the soil moisture patterns is influenced by process dynamics resulting from complex combination of initial soil moisture status, soil, vegetation, topography and precipitation pattern.

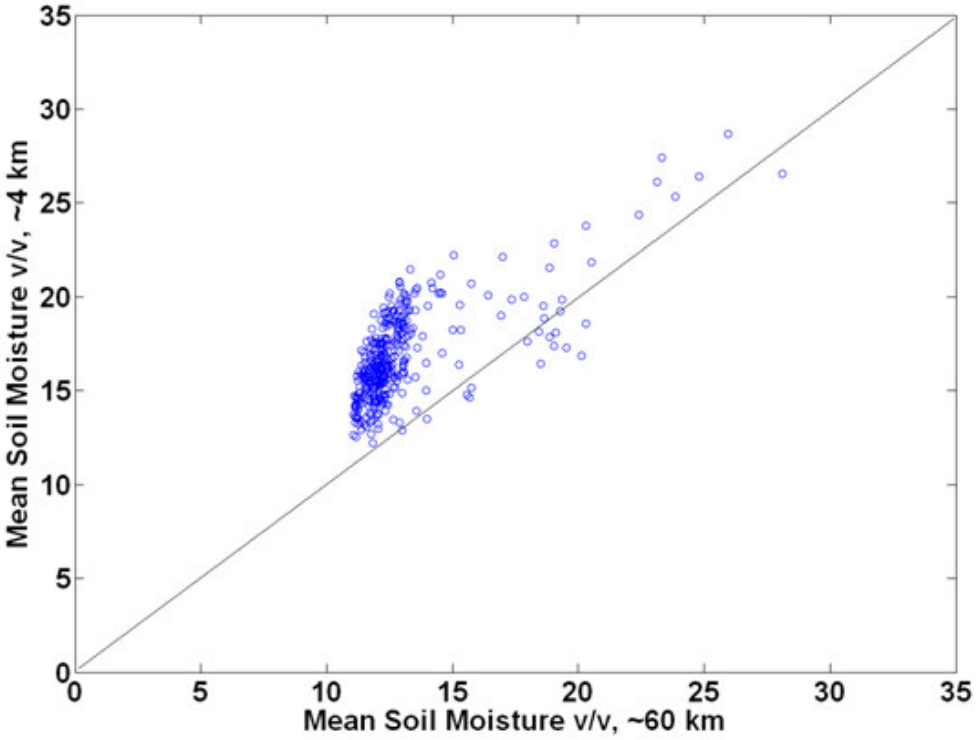

Figure 4.14. Plot of daily mean soil moisture v/v at ~60 km resolution against mean soil moisture v/v at ~4 km, for year 2005, for a randomly selected AMSR-E footprint from the Oklahoma study region.

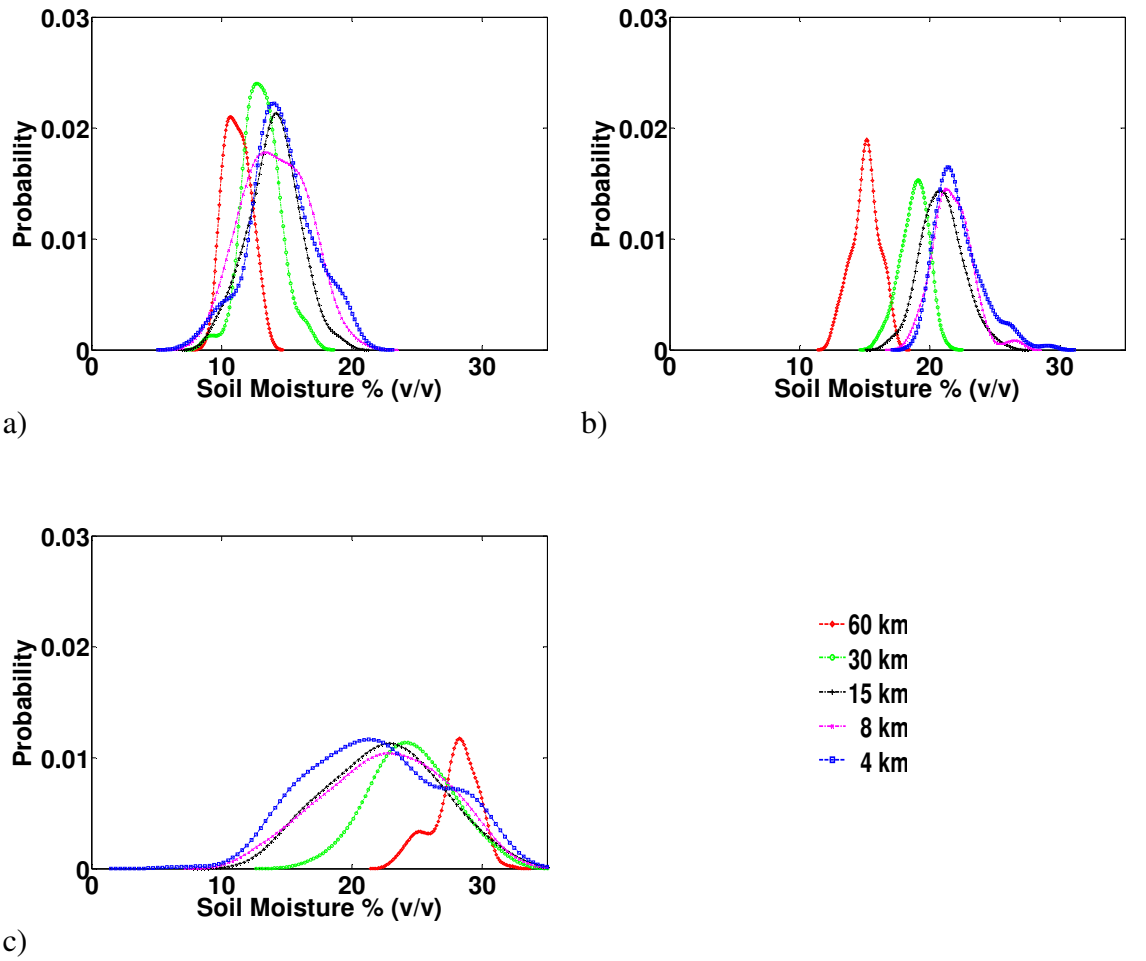

Figure 4.15. Soil moisture probability distribution functions (pdfs) at different spatial scales within a randomly selected AMSR-E footprint, for a) dry day, b) a day during drydown period, and c) wet day, from the Oklahoma study region.

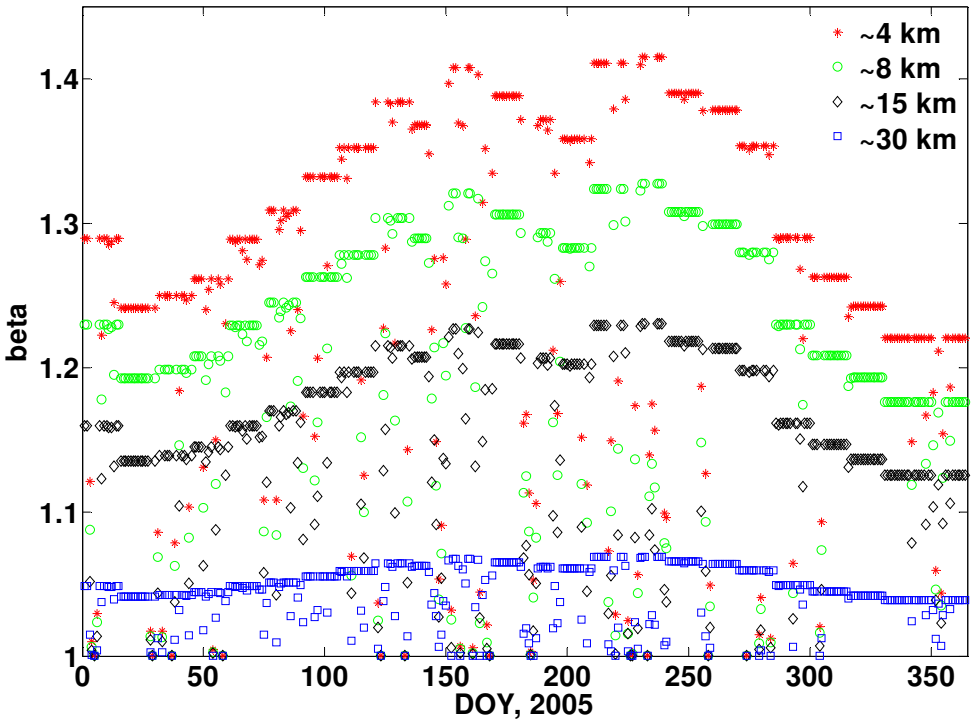

Figure 4.16. Plot of scale parameter β_s at different spatial scales, for year 2005, for a randomly selected AMSR-E footprint from the Oklahoma study region.

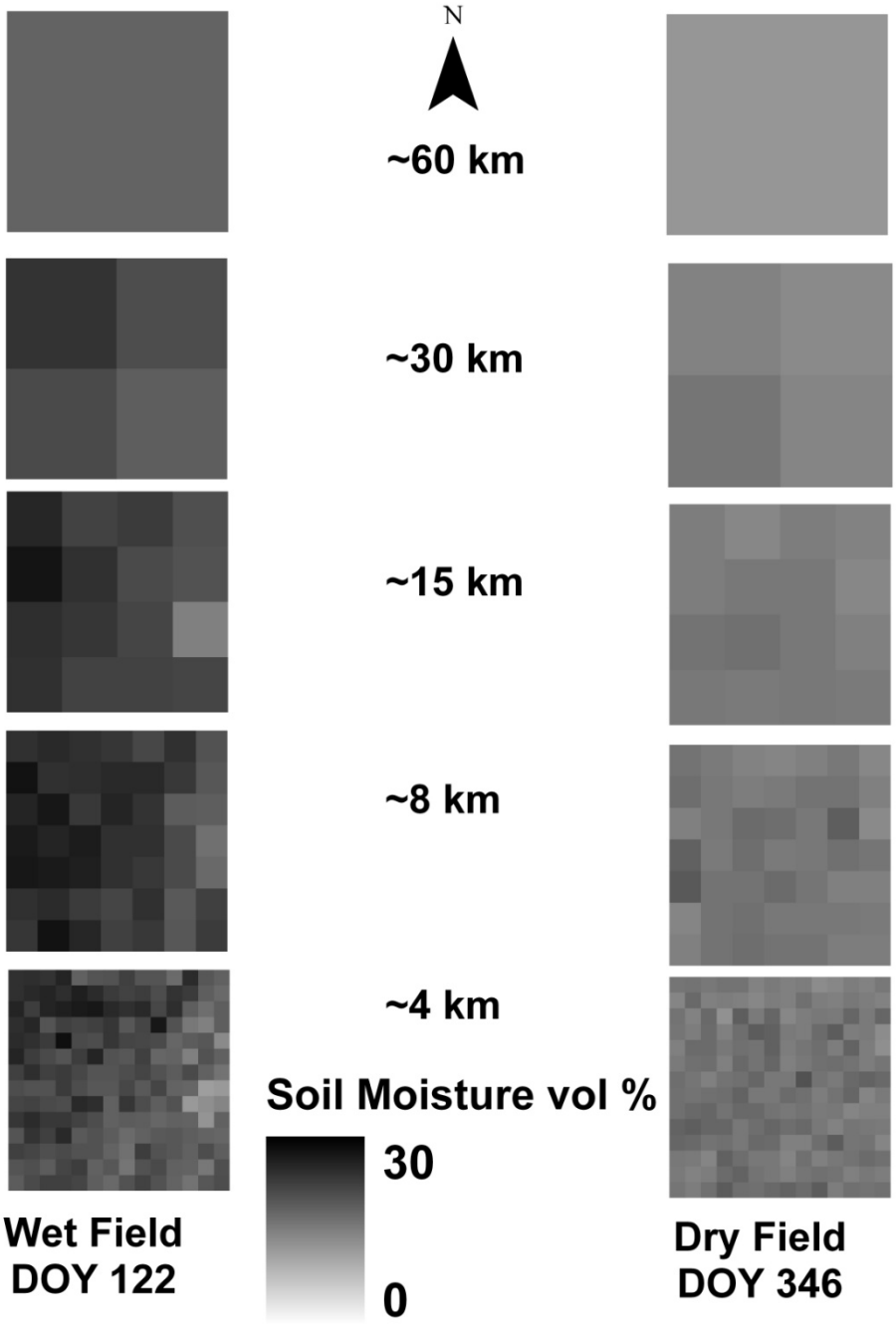

Figure 4.17. Soil moisture fields at different spatial scales, for a wet and dry day within a randomly selected AMSR-E footprint from the Oklahoma study region.

4.6. Conclusion

The study demonstrates the potential to downscale the AMSR-E-based coarse scale (~60 km) soil moisture footprint for diverse hydroclimatic regions. Two algorithms are developed to characterize the soil moisture distribution across various scales within the AMSR-E fooprint. The first algorithm results in probability distribution functions (pdfs) that provide a reasonable estimation of statistics across desired scale between coarse scale and fine scale soil moisture distributions. However, the algorithm does not account for the effects of geophysical parameters/variables on soil misture spatial evolution while evaluting the statistics for the intermediate scales. Another drawback of the first algorithm is the incapability to describe the spatial organization of soil moisture at finer scale that give rise to the footprint scale integrated soil moisture estimate. The second algorithm is a two prong multiscale data assimilation approach comprising upward sweep and downward jumps. The exchange of fine scale and coarse scale soil moisture information in a multiscale data assimilation technique resulted in a soil moisture field at the finest (i.e., ~ 4 km) and various intermediate scales (i.e., ~ 8 km, ~15 km, and ~30 km). Validation of soil moisture evolution is conducted at the finest scale (~4 km) for the study regions and reasonable agreement is observed. The validation also highlights that within the ~4 km spatial scale soil moisture variability exists and the algorithm shows a scaling bais and is not capable to describe the variability entirely. Availability of finer scale spatial continuous meteorological focings to the proposed downscaling algorithm may improve the characterization of variability, bais and uncertainty in estimation of soil moisture fields.

The bridging model of multiscale data assimilation based on the important geophysical parameters/variables that affect the soil moisture evolution and organization helps to downscale satellite-based soil moisture footprint. The robustness of the bridging model has a limitation i.e., the range of heterogenity factor or the spatial-scale ratio *s*. Excessive downscaling may lead to overestimation of downscaled satellite-based soil moisture likelihood for the multiscale data assimilation. Futher studies will be conducted to identify the valid range of the heterogenity factor or the spatial-scale-ratio *s* and will also apply the proposed algorithm for different hydroclimatic regions. The accuracy of the bridging model across spatial scales also depends on the quality of geophysical parameters/variables data and their errors involved in scaling them to match the desired resolution for estimating the soil moisture fields.

The proposed multiscale data assmilation scheme will also help to validate the fine scale soil moisture data from the future satellite platform (e.g., SMAP of NASA).

CHAPTER V

CHARACTERIZATION OF SATURATED HYDRAULIC CONDUCTIVITY IN AN AGRICULTURAL FIELD USING KARHUNEN-LOÈVE EXPANSION WITH MCMC

5.1. Synopsis

Process-based soil hydrologic models require input of saturated hydraulic conductivity (*Ksat*). However, model users often have limited access to measured data and thus use published or estimated values for many site-specific hydrologic and environmental applications. We proposed an algorithm that uses the Karhunen-Loève Expansion (KLE) in conjunction with Markov Chain Monte Carlo (MCMC) technique which employs measured soil moisture values to characterize the saturated hydraulic conductivity of an agricultural field at a fine resolution. The study domain is situated in the Walnut Creek watershed, Iowa with soybean crop (in 2005) and well defined top (atmospheric) and bottom (ground water) boundary conditions. The KLE algorithm parameterize and generates *Ksat* fields with random correlation length that is used in the SWMS_3D model for predicting soil moisture dynamics for two different scenarios: 1) the van Genuchten soil hydraulic parameters (except *Ksat*) are constant and are based on the soil type of the grid block within the domain; 2) *Ksat* is correlated with the van Genuchten parameter α, as $Ksat \propto \alpha^2$. The predicted soil moisture for both scenarios are evaluated with the measured soil moisture in the MCMC algorithm for acceptance (or rejection) of the *Ksat* fields. The accepted *Ksat* fields are evaluated and validated against

the laboratory measured *Ksat* at specific locations and the comparison shows reasonable agreement. The KLE-MCMC algorithm was further tested in the same study domain for another year (2002) having different vegetation (corn) and local forcings. The algorithm shows potential to characterize the saturated hydraulic conductivity fields at fine-scale using inexpensive and more regularly measured soil moisture measurements. Further studies are required to incorporate variability in different hydro-climatic regions and diverse topography to extend the application of this algorithm.

5.2. Introduction

Characterization of infiltration is important for better understanding of overland and subsurface water flow, and chemical transport in the vadose zone. High degree of spatial variability in local infiltration is observed due to random nature of soil property i.e., saturated hydraulic conductivity (*Ksat*) [*Nielsen, et al.*, 1973; *Sharma, et al.*, 1987; *Warrick and Nielsen*, 1980]. Saturated hydraulic conductivity is a difficult property to describe because it can change many orders of magnitude over very small distances. Numerous studies [*Loague and Gander*, 1990; *Mohanty, et al.*, 1994a; *Mohanty and Mousli*, 2000; *Nielsen, et al.*, 1973; *Sharma, et al.*, 1987] have shown large variability exhibited by *Ksat*. In an agricultural field, spatial variability of *Ksat* is influenced by soil texture, cropping/tillage practice, and growing seasons [*Azevedo, et al.*, 1998; *Mohanty, et al.*, 1994a; *Mohanty and Kanwar*, 1994]. Carsel and Parrish [1988] reported soil texture-based descriptive statistics of *Ksat*. They found the highest coefficient of variation for *Ksat* (ranged from 453.3 for silty clays to 52.4 for sands), and also observed

a large difference in the value of *Ksat* between sand and clay. Various other databases are also available that highlight the variability present in Ksat. Prominent among them is the UNSODA database [*Nemes, et al.*, 2001] that provides wide range of Ksat values for uniform, single-grain size sands to loam, and clay soils and mixtures thereof. Decayed root channels lead to the formation of macropores that ultimately enhance infiltration in soil. Meek et al. [1990] showed that alfalfa root system generates an extensive macropore flow, consequently increasing *Ksat*. Wetting/drying, freezing/thawing, and earthworm activities in agricultural fields may also contribute to macropores formation that leads to high infiltration rate. However, Wager and Denton [1989] and Mohanty et al [1994a] also found that interrow wheel tracks by farm machinery compacted the underlying soil, resulting in low infiltration capacity and leading to a great reduction in *Ksat* in tracked area as compared to untracked interrow areas.

Several laboratory and in situ techniques are available to measure *Ksat* and the results of these techniques often vary significantly [*Gupta, et al.*, 1993; *Klute and Dirksen*, 1986; *Mohanty, et al.*, 1994a; *Paige and Hillel*, 1993] based on different measurement support sizes and the governing principles. The spatial support of the measurement may be representative of few square centimeters to several square meters. Macropores also tend to increase the variability of *Ksat* measurements when small sample sizes are used [*Mohanty, et al.*, 1994b]. Variability of *Ksat* in soils has also been viewed with respect to the numerous independent processes operating at different spatial and temporal scales [*McBratney*, 1998]. Recognizing that *Ksat* represents an end result of a number of independent processes, whose complex interactions makes it impractical

to apply deterministic methods for describing the spatial continuity of *Ksat*. Studies have been conducted to characterize the stochasticity of *Ksat* by auto-correlograms and variograms [*Hillel*, 1980; *Wierenga*, 1985]. Mohanty et al. [1991] used the simplified, split-window median-polishing technique in conjunction with a robust semivariogram estimator to examine the spatial structure of *Ksat* in a glacial till material. Gupta et al. [1992] used Fourier series analysis along with autoregressive methods to model hydraulic conductivity as a stochastic process. Due to such high spatial heterogeneity, *Ksat* is often modeled as random field characterized by a lognormal probability density function with relevant spatial correlation. Thus, generally the characterization of *Ksat* requires experimental data acquisition which is time-consuming and costly.

In this study, our primary objective is to parameterize *Ksat* at a field-scale with inexpensive and more regularly observed surface soil moisture measurements. We employ a physically-based soil hydrologic modeling in conjunction with Karhunen-Loève Expansion (KLE) and Markov Chain Monte Carlo (MCMC) method to characterize the *Ksat* distribution in an agricultural field using available surface soil moisture data. With KLE, we can represent the high dimensional *Ksat* field by a small number of parameters. Furthermore, the static data (the values of *Ksat* fields at some sparse locations) can be incorporated into the KLE to further reduce the dimension of the parameter space. Imposing the values of the *Ksat* at certain locations restricts the parameter space to a subspace (hyperplane). The *Ksat* fields from KLE algorithm was used in a three dimensional hydrologic model with well defined boundary conditions to obtain the evolution of profile soil moisture in the field. The simulated profile soil

moisture and the soil moisture measurements at the field site were used in a simple MCMC-based random walk sampler to accept or reject the *Ksat* realizations from the KLE algorithm. The posterior distribution of *Ksat* fields were subjected to statistical analysis and validated against the measured *Ksat* value at specific field locations. Additionally, the algorithm was further tested in the same study domain for a separate year having different vegetative cover (i.e., corn) and local forcings.

5.3. Study Area and Data Collection

During the Soil Moisture Experiments in 2002 (SMEX02) and 2005 (SMEX05), hydro-meteorological sampling campaigns (details available at http://ars.usda.gov/Research/docs.htm) at field- and regional-scale were conducted in the Walnut Creek watershed (Fig. 5.1) and regional sites near Ames, Iowa, respectively. Our study uses field sampling data of SMEX02 and SMEX05 from Walnut Creek watershed. Approximately 95% of the watershed is used for row crop agriculture (corn and soybean). The climate of the region is humid and average annual rainfall is 835 mm. The topography has low relief and poor surface drainage characteristics, resulting from prairie potholes that are water-holding depressions of glacial origin. In the watershed, ground sampling was conducted at 32 fields, approximately 800 X 800 m, for aircraft remote sensing validation. For this study, field WC11 (Fig. 5.1) within the watershed was selected during the SMEX02 and SMEX05 experiments for intensive soil moisture sampling. The geographical location of WC11 is 41.97˚N and 93.69˚W. The WC11 had corn during the SMEX02, and soybean during the SMEX05 with a small area of corn

planted near the western edge of the field. The portion of western edge was eliminated from the study domain to obtain uniform vegetation cover that rendered it to a size of 600 m X 600 m. Average rooting depth of 30-60 cm for corn and 30-50 cm for soybean during vegetative growth and development stage [*Smajstrla*, 1990] was used. The Leaf Area Index (LAI) measured during the SMEX02 and the SMEX05 field campaigns were used in the study. The topography of the WC11 is characterized by low relief and poor surface drainage. The representative soils of the WC11 as illustrated in Fig. 5.1, are clay, loam, and silty clay loam of glacial origin, and have relatively low permeability (SSURGO database). Meteorological data was obtained from USDA-NRCS managed SCAN site (42.00^{o}N and 93.74^{o}W) near Ames, IA.

Primarily the study was conducted based on the data obtained and conditions observed in the WC11 field during the SMEX05 campaign. Data from the SMEX02 campaign was further used to validate the algorithm. Soil moisture content was measured during the SMEX02 (for 12 days) and SMEX05 (for 10 days) campaigns at the same 62 point locations in the WC11 field. Measurements were conducted between 1100 and 1500 local time (CDST). Sampling points were located at nearly 30 m intervals along four transects oriented east–west and north–south within the WC11 field (as shown in Fig. 5.1). During the experiment, volumetric soil moisture contents were measured using theta probes (HH2 device, Delta-T, Inc.). For the purpose of validating *Ksat* fields, soil cores were also collected at highlighted locations in Fig. 5.1 during SMEX05 and *Ksat* measurements were made using constant head permeameter in the soil hydrology laboratory at Texas A&M University.

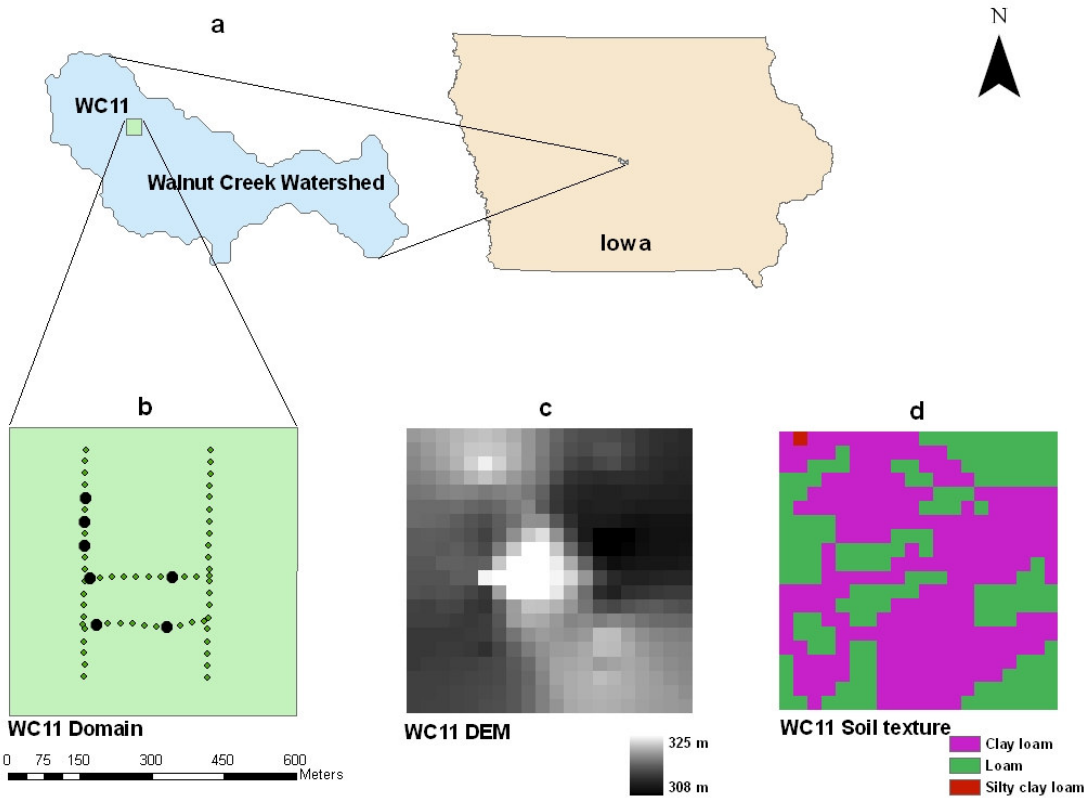

Figure 5.1. (a) Study area, (b) study domain with soil moisture sampling transect, (c) DEM, soil texture in the WC-11 field at the Walnut Creek watershed, Iowa.

5.4. Methodology

It consists of two parts. First, we present the parameterization of *Ksat* using Karhunen- Loève Expansion. This parameterization reduces the dimensionality of the uncertainty space by eliminating the modes with lower energy. Second, we present the sampling algorithm which uses Markov Chain Monte Carlo scheme.

Karhunen-Loève Expansion (KLE)

Suppose the *Ksat(x)* field is defined in the study domain Ω = 600 m X 600 m of the WC11 field (Fig. 5.2). We assume that the *Ksat* is known at some random spatial locations within the domain, and the covariance of log(*Ksat*) is also known. Thus, by discretizing the domain Ω into a rectangular mesh (of 30 m X 30 m), *Ksat(x)* is represented by a matrix, making it a high dimensional vector. Following Loève [1977], the KLE was used to generate *Ksat* field in term of an optimal L^2 basis. By truncating the expansion we can represent the *Ksat* matrix by a small number of random parameters. To impose the hard constraints (the values of the *Ksat* at prescribed locations), we find a linear subspace of our parameter space (a hyperplane) which yields the corresponding values of the *Ksat* field. For better readability, we briefly elaborate the KLE algorithm. Denote $Y(x, \omega)$ = log[*Ksat*(x, ω)], assuming *Ksat*(x) as lognormal, where the random element ω was included for the uncertainty in *Ksat(x)*. Suppose $Y(x, \omega)$ is a second order stochastic process with

$$E \int_{\Omega} Y^2(x, \omega) dx < \infty \tag{5.1}$$

where E is the expectation operator. Given an orthonormal basis $\{\varphi_k\}$ in $L^2(\Omega)$, we can expand $Y(x, \omega)$ as a general Fourier series

$$Y(x, \omega) = \sum_{k=1}^{\infty} Y_k(\omega)\varphi_k(x) \tag{5.2}$$

where

$$Y_k(\omega) = \int_{\Omega} Y(x, \omega)\varphi_k(x)\, dx \tag{5.3}$$

We are interested in the special L^2 basis $\{\varphi_k\}$ which makes the random variables Y_k uncorrelated. That is, $E(Y_iY_j) = 0$ for all $i \neq j$. Denote the covariance function of Y as $R(x, y) = E[Y(x)Y(y)]$. Then such basis functions $\{\varphi_k\}$ satisfy

$$E[Y_iY_j] = \int_\Omega \varphi_i(x)dx \int_\Omega R(x,y)\varphi_j(y)dy = 0, \qquad i \neq j.$$

Since $\{\varphi_k\}$ is a complete basis in $L^2(\Omega)$, it follows that $\varphi_i(x)$ are eigenfunctions of $R(x, y)$:

$$\int_\Omega R(x,y)\varphi_k(\mathrm{y})\mathrm{dy} = \lambda_k\varphi_k(x), \qquad \mathrm{k} = 1, 2, \ldots, \tag{5.4}$$

where $\lambda_\mathrm{k} = \mathrm{E}[Y_k^2] > 0$. Furthermore, we have

$$R(x, y) = \sum_{k=1}^{\infty} \lambda_k\varphi_k(x)\varphi_k(y) \tag{5.5}$$

Denote $\pi_k = Y_k/\sqrt{\lambda_k}$, then π_k satisfy $E(\pi_k) = 0$ and $E(\pi_i\, \pi_j) = \delta_{ij}$. It follows that

$$Y(x, \omega) = \sum_{k=1}^{\infty}\sqrt{\lambda_k}\pi_k(\omega)\varphi_k(x) \tag{5.6}$$

where φ_k and λ_k satisfy (4). We assume that the eigenvalues λ_k are ordered as $\lambda_1 \geq \lambda_2 \geq$ .... The expansion (eq. 5.6) is called the KLE. In eq. 5.6, the L^2 basis functions $\varphi_k(x)$ are deterministic and resolve the spatial dependence of the *Ksat* field. The randomness is represented by the scalar random variables π_k. After we discretize the domain by a rectangular mesh, the continuous KLE is reduced to finite terms. Generally, we only need to keep the leading order terms (quantified by the magnitude of λ_k) and still capture most of the energy of the stochastic process $Y(x, \omega)$. For an N-term KLE approximation $Y_N = \sum_{k=1}^{\infty}\sqrt{\lambda_k}\pi_k\varphi_k$, define the energy ratio of the approximation as

$$e(N) := \frac{E||Y_N||^2}{E||Y||^2} = \frac{\sum_{k=1}^{N}\lambda_k}{\sum_{k=1}^{\infty}\lambda_k} \tag{5.7}$$

If λ_k (k = 1, 2,...), decay very fast, then the truncated KLE would be a good approximation of the stochastic process in the L^2 sense. Suppose the saturated hydraulic conductivity field *Ksat*(x, ω) is a log-normal homogeneous stochastic process, then $Y(x, \omega)$ is a Gaussian process and π_k are independent standard Gaussian random variables. We assume that the covariance function of $Y(x, \omega)$ has the form

$$R(x, y) = \sigma^2 \exp\left(-\frac{|x_1-y_1|^2}{2L_1^2} - \frac{|x_2-y_2|^2}{2L_2^2}\right) \quad (5.8)$$

In the above formula, L_1 and L_2 are the correlation lengths in each dimension, and $\sigma^2 = E(Y^2)$ is a constant representing variability in *Ksat*. The eigenvalues are ordered in decreasing fashion. The rate of decay is subject to the covariance matrix of the intrinsic *Ksat* field, e.g., the shorter the correlation length; the more terms are required in the expansions. We first solve the eigenvalue problem (4) numerically on the rectangular mesh and obtain the eigenpairs $\{\lambda_k, \varphi_k\}$. For smooth Gaussian fields used here, we can sample $Y(x, \omega)$ from the truncated KLE (6) by generating Gaussian random variables π_k. In the simulations, we first generate a reference *Ksat* field using the full KLE and obtain the corresponding soil moisture using a three dimensional vadose zone mode. In our agricultural field example, to represent the discrete *Ksat* fields from the prior (unconditioned) distribution, we keep 16 terms in the KLE, which captures more than 90% of the energy of $Y(x, \omega)$. We assume that the *Ksat* field is known at 11 distinct points. This condition is imposed by setting

$$\sum_{k=1}^{16} \sqrt{\lambda}_k \pi_k(\omega) \varphi_k(\mathrm{x_j}) = \alpha_j \quad (5.9)$$

where α_j (j = 1,..., 11) are prescribed constants and x_j are prescribed locations. In the simulations we propose eleven π_k and calculate the rest of π_k by solving the linear system (9). Note that, L_1 and L_2 are assumed to be random in our simulations.

SWMS_3D Model and Domain Characteristics

The generated *Ksat* fields from KLE algorithm were used in SWMS_3D model. The SWMS_3D is a fortran-based finite element code for simulating water flow and solute transport in three-dimensional, variably saturated media [*Simunek, et al.*, 1995]. For its performances, this model was widely used by vadose zone hydrology community [*Javaux and Vanclooster*, 2006; *Javaux, et al.*, 2006; *Lewandowska, et al.*, 2004]. Water flow is solved using Richards' equation, which can be written in conventional way as

$$\frac{\partial \theta}{\partial t} = \frac{\partial}{\partial x_i}\left[K\left(K_{ij}^{A}\frac{\partial h}{\partial x_j} + K_{iz}^{A}\right)\right] - S \qquad (5.10)$$

where θ is the volumetric water content [L^3L^{-3}], h is the pressure head [L], S is a sink term [T^{-1}] (root water uptake), x_i (i=1,2,3) are the spatial coordinates [L] , t is time [T], K_{ij}^{A} are components of a dimensionless tensor K^A representing the possible anisotropic nature of the medium, and K is the unsaturated hydraulic conductivity function [LT^{-1}] given by

$$K(h,x,y,z) = Ksat(x_1,x_2,x_3)\, K_r(x_1,x_2,x_3) \qquad (5.11)$$

where K_r is the relative hydraulic conductivity [-] and *Ksat* the principal saturated hydraulic conductivity [LT^{-1}]. According to this definition, the value of K_{ij}^{A} in eq. 5.10 must be positive and less than or equal to unity. The diagonal entries of K_{ij}^{A} equal one

and the off-diagonal entries zero for an isotropic medium. Finite element schemes are used for the discretization of the flow and transport equations and the resulting equations are solved in an iterative fashion, by linearization Additional measures are taken to improve solution efficiency in transient problems, including automatic time step. The water content term is evaluated using the mass-conservative method proposed by [*Celia and Bouloutas*, 1990]. For any additional information, readers are referred to [*Simunek, et al.*, 1995].

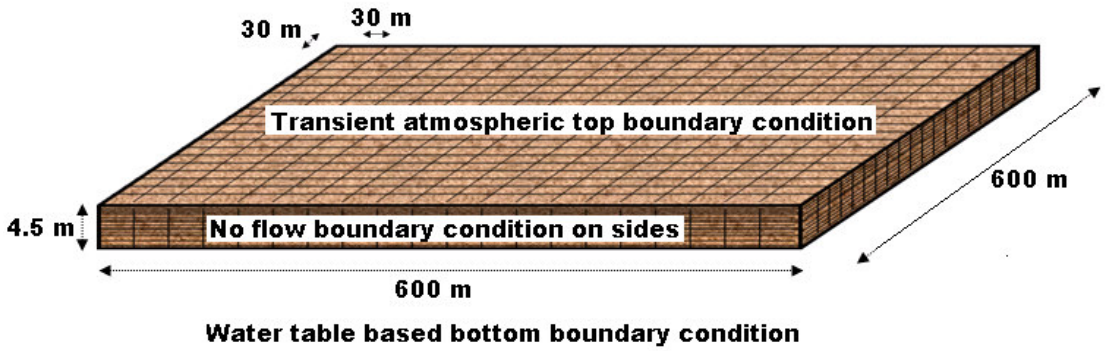

Figure 5.2. A 600 m X 600 m section of WC11 three dimensional domain configuration with horizontal discretization of 30 m X 30 m (in x and y directions) and vertical discretization comprises 55 elements (in z direction) up to the depth of 4.5 m (note: not to scale).

A 600 m X 600 m section of WC11 with soybean crop was set for model domain, as illustrated in Fig. 5.2. The domain was further discretized horizontally into grids of 30 m X 30 m (in x and y directions) resulting in 400 grid blocks. The vertical discretization

comprises 55 elements (in z direction) up to the depth of 4.5 m for all the 400 grid blocks. The 3D-domain configuration had 24255 nodal points, 21600 tetrahedral elements, and 882 boundary nodes. Atmospheric boundary condition was set for the top surface of the domain. Nodal spacings were made relatively small at the soil surface where highest head gradients and flow velocity were expected. The initial position of the groundwater was set at 3.5 m. No flow boundary condition was imposed on the sides. A rooting depth of 2 cm to 50 cm from the top surface was set with a uniform distribution of the potential water uptake. The unsaturated soil hydraulic properties including soil water retention and hydraulic conductivity were described by a set of closed-form equation, (van Genuchten [1980]). The surface soil texture information from SSURGO database was extended in vertical direction to form a homogeneous soil layer in each of the grid block. For this study, the van Genuchten parameters of residual water content θ_{res}, and saturated water content θ_{sat} were assigned based on soil texture information from SSURGO database. No stochasticity was introduced in these parameters with the assumption that they do not vary significantly at field scale. However, there are some conflicting reports in literature about the correlation among *Ksat*, α (cm^{-1}), and n (-) parameters. Smith and Diekkruger [1996] concluded that no significant correlation was observed among any of the characteristic parameters and suggested that most random variation in soil characteristic parameters could be treated as independent. However, Wang and Narasimhan [1992] indicated that *Ksat* and α were correlated with $Ksat \propto \alpha^2$. In this research, we study two cases: i) case 1 (C1), with no correlation among *Ksat*, α, and n; ii) case 2 (C2), with correlation of $Ksat \propto \alpha^2$ having n as constant. A study

conducted by Hills et al. [1992] demonstrated that the water retention characteristics could be adequately modeled using either a variable α with a constant n or a variable n with constant α, with a better result when α was variable. The KLE algorithm was used to obtain the stochastic *Ksat* fields, and for C2, the α fields are obtained from the corresponding *Ksat* fields. Analysis of existing soil hydraulic properties database (e.g., UNSODA) reveals a range of values for the constant of proportionality (P) in the correlation of $Ksat \propto \alpha^2$. The values of P between 5000 and 75000 cover a wide spectrum of soil types e.g., coarse sand, loam, sandy loam, clayey loam, clay, etc. During simulation involving C2, for constant of proportionality, specific values between 5000 and 75000 were used with an increment of 10000 to evaluate α. The simulation for both cases was conducted using SWMS_3D for 211 Julian days during 2005. The soil moisture evolution of top 5 cm from the SWMS_3D model was subjected to the MCMC algorithm (described below) to evaluate the *Ksat* fields.

MCMC Algorithm

Bayesian methods provide a rigorous framework within which pre-existing knowledge about the parameters of a model which can be combined with observed data and the model output. Here the preexisting knowledge (priors) was the soil hydraulic properties except *Ksat* that were derived from SSURGO database and the effective *Ksat* of the discretized field was obtained from KLE algorithm. The observed data (likelihood) was the measured soil moisture values from WC11, and the model output was soil moisture prediction from SWMS_3D. The results from Bayesian method is a

probability distribution of the parameter space (posterior distribution), that summarizes uncertainty about the parameters based on the combination of pre-existing knowledge and the sampled data values. The marginalization could be an intractable task in Bayesian method because of high dimensionality. We use the Metropolis algorithm within Markov Chain Monte Carlo (MCMC) method with an independent sampler to sample the posterior distribution, which were the distribution of the *Ksat* fields of WC11. The Metropolis algorithm [*Metropolis and Ulam*, 1949] has been widely used in Bayesian applications, because of its simplicity. Its principle can be summarized as follows: starting from a vector generated at iteration *i-1*, a new candidate vector is generated based on instrumental probability distribution. If this new vector leads to an increasing value of the target distribution (assuming symmetric instrumental probability distribution), it is accepted as the generated value at iteration *i*. Otherwise, the ratio between the new and the previous value of the target distribution is computed, and used as the acceptance probability of the candidate vector. In case of rejection, the generated vector at iteration *i* remains equal to that of iteration *i-1*. The Metropolis algorithm was used in this paper. As discussed above, we use the Bayes rule $P(Ksat|s) \alpha P(s|Ksat)$ $P(Ksat)$, and our goal is to sample $P(Ksat|s)$. Here *s* denotes the state variable (e.g., soil moisture) which we seek by *Ksat*. The MCMC algorithm used in the study is described below

1. Choose a starting point $Ksat(0)$ (where 0 refer to the number of iteration) and a variance $\sum$.
2. Iterate $i = 1, \ldots, N_{iter}$.

2.1. Generate a proposal candidate vector *Ksat** from q(· |*Ksat*(*i-1*))

2.2. Accept *Ksat** with probability $r = \frac{P(Ksat^* \mid s)q(Ksat(i-1) \mid Ksat^*)}{P(Ksat(i-1) \mid s)q(Ksat^* \mid Ksat(i-1))}$ or reject it with probability (1-r)

The likelihood here is described as P(*s*|*Ksat*) α $exp\left\{\frac{(-\sum_{i,j}(s_{ksat}(x_i,t_j)-s_{obs}(x_i,t_j))^2)}{\sigma^2}\right\}$. In order to avoid numerical overflows, it is useful to consider the logarithm of the posterior distribution, and to compute the posterior ratio as *r* =*exp*(*log*(*p*(*Ksat* *| *s*))-log(p(*Ksat* (i-1)| *s*))). The MCMC algorithm generates a Markov chain consisting of *Ksat* whose stationary distribution is P(*Ksat*|*s*). In our numerical simulations, $q(x \mid y)$ is a symmetric distribution (chosen by specifying the correlation lengths), $q(x \mid y) = q(y \mid x)$, and thus the acceptance probability reduces to $\frac{P(Ksat^* \mid s)}{P(Ksat(i-1) \mid s)}$.

5.5. Results and Discussion

In this study, we test for 10000 samples of *Ksat* field for each case (C1 and C2) for the 600 m X 600 m model domain of WC11 (Fig. 5.2). Note that the range of ln(*Ksat*) in these realizations are about −5.0 ~ +5.0, which means that the difference of the hydraulic conductivity is about four orders of magnitude. The statistics (mean, variance, and directional correlation length) of the generated realizations are also evaluated for the study. Each realization of the conductivity field is then used to estimate the pressure head and soil moisture fields from the SWMS_3D model with governing equations and boundary/initial conditions, i.e., (10)–(11) for both of the cases (C1 and C2). The soil

moisture evolutions of these *Ksat* realizations are compared with the measured soil moisture values within MCMC algorithm. The acceptance for these samples was nearly 2% percent (i.e., 200 from 10000 samples). In our simulations, we propose an independent realization of the saturated hydraulic conductivity field based on proposed correlation lengths. The low success rate was expected because of possibility of infinite number of combination of *Ksat* fields that could be generated from KLE algorithm. The first hundred accepted samples were discarded to eliminate the influence of starting proposal distribution and account for burn-in. Fig. 5.3 illustrates the residuals of two hundred selected samples for C1. Similar plot for C2 was also observed (not shown here). The residuals decreases initially and then becomes asymptotic to exhibit some level of convergence.

Few examples of accepted *Ksat* fields for WC11 are shown in Fig. 5.4 and Fig. 5.5 for C1 and C2, respectively. All these different *Ksat* fields demonstrated potential to describe same soil moisture dynamics with the applied initial and boundary conditions for C1 and C2. The plots in Fig. 5.4 and Fig. 5.5 also illustrate the uncertainty associated with *Ksat* in an agricultural setup. Uncertainties in hydraulic conductivity in agricultural fields were also reported in other studies. For example, in a silty loam soil, Coutadeur et al. [2002] and Logsdon and Jaynes [1996] found that tillage increased the spatial variation of *Ksat* measured with a disc infiltrometer. In WC11, uncertainty in *Ksat* fields is influenced by clustering of glacial till soil. This clustering phenomenon is due to differential deposition of soil layers by glacial drifts during its formation or subsequent incremental deposition due to wind drifts [*Mohanty, et al.*, 1991]. The impact of soil

type (hydraulic properties), and influence of lateral flow due to high water table during wet conditions also dictate considerably the realization of stochastic *Ksat* fields from the employed algorithm. This highlights the need for researchers to use caution when using *Ksat* data as model input without field validation and characterization. Also, model users need to consider both the variability/uncertainty of *Ksat* data associated with specific soil and field location and understand how the method of determination may influence its value.

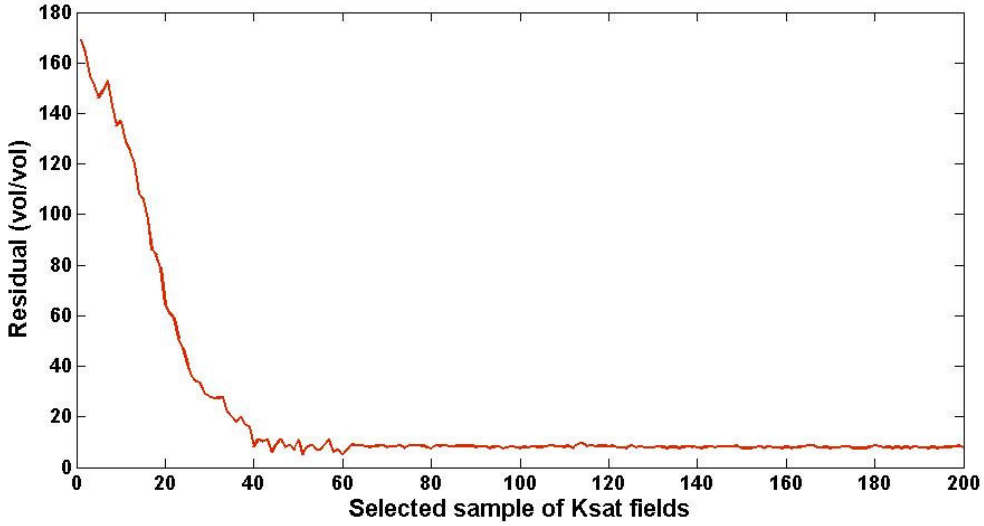

Figure 5.3. Residuals of accepted *Ksat* fields during SMEX05 from the MCMC for case 1 (C1) having no correlation among *Ksat*, α, and *n*.

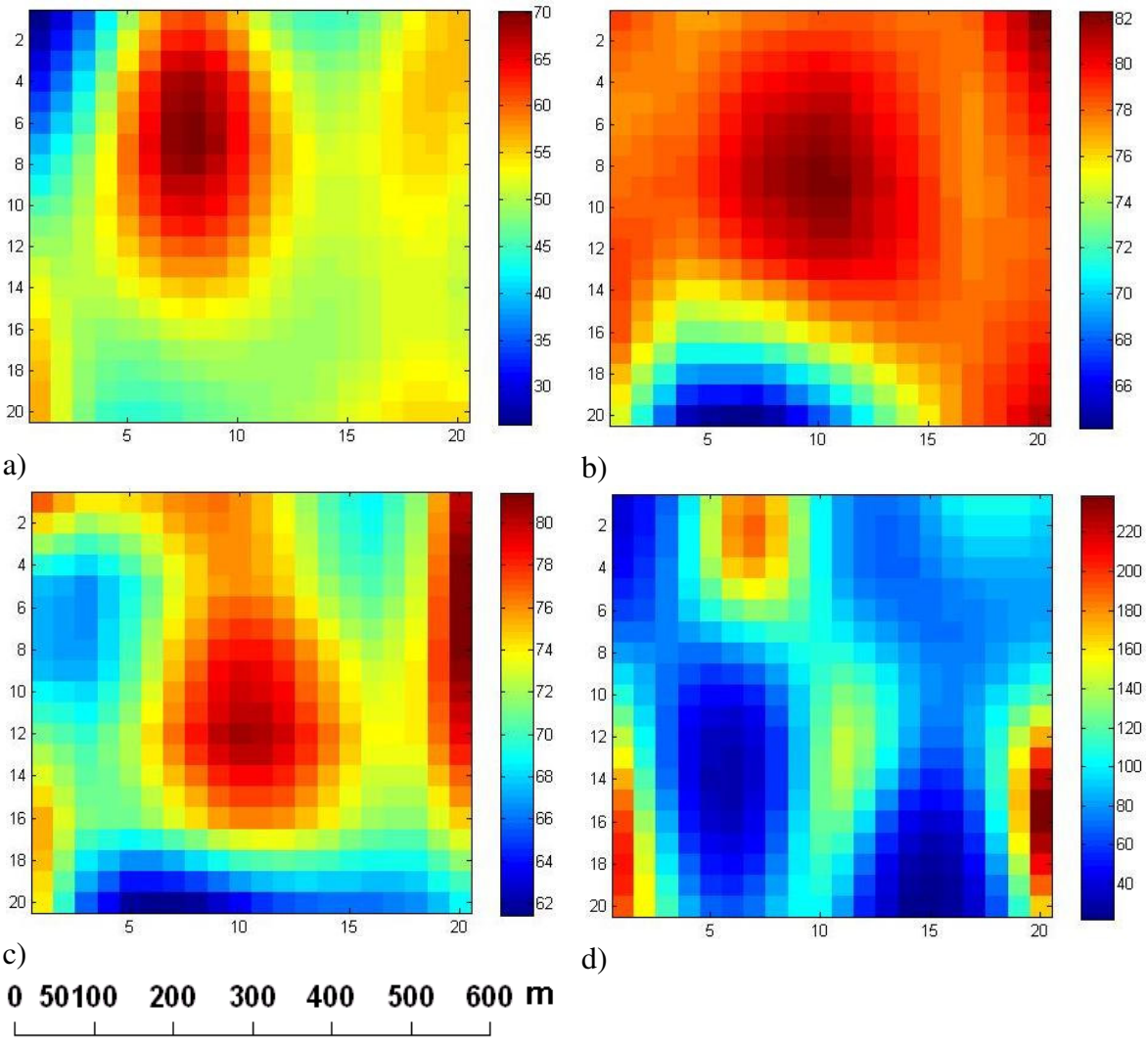

Figure 5.4. Randomly selected, highly probable Ksat fields during SMEX05 for case 1 (C1) having no correlation among *Ksat*, α, and n.

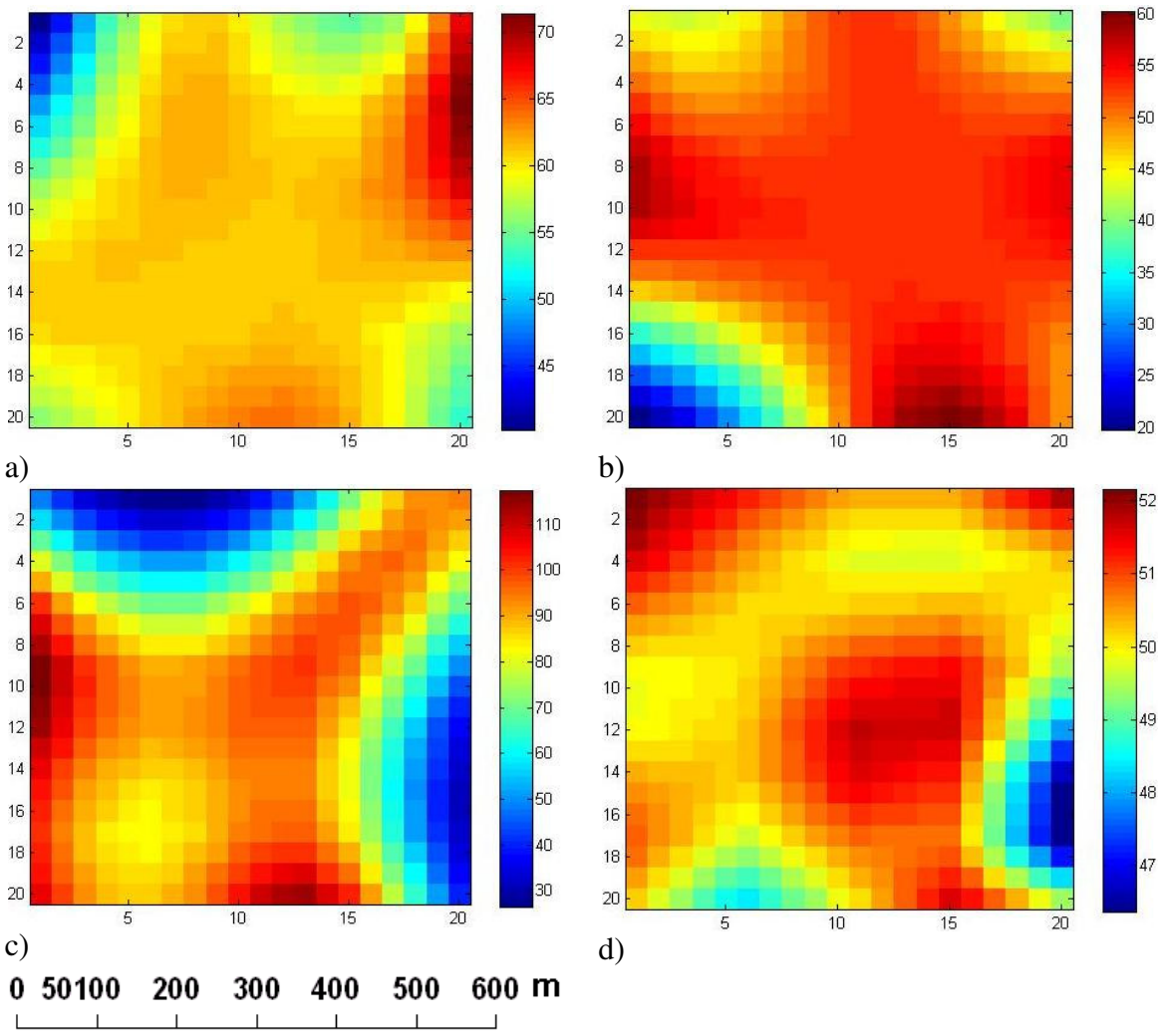

Figure 5.5. Randomly selected, highly probable Ksat fields during SMEX05 for case 2 (C2) having correlation of $Ksat \propto \alpha^2$, and n as constant.

The log saturated hydraulic conductivity Y(x) = ln(*Ksat*(x)) in the model domain is second-order stationary with a separable exponential covariance function (eq. 5.8). Various combinations of correlation length L_1 and L_2 in the horizontal directions (x_1 and

x_2 axes) from eq. 5.8 were obtained for highly probable realizations of *Ksat* fields. This exemplifies the stochastic nature of *Ksat* that give similar soil moisture evolution in WC11 for the study period. It is noteworthy that the mean horizontal correlation length of the *Ksat* is nearly 0.5 times of domain length (~300 m) in either direction (L_1 and L_2) for C1. However, in case of C2 a mean correlation length is nearly 0.65 times of domain length (i.e., 400 m). The increase in correlation length for C2 is attributed to characteristics of α fields corresponding to *Ksat* fields that introduces more flexibility i.e., degree of freedom in describing the 3-dimensional flow of water in soil profile, i.e., more water retention functions are capable to explain the nature of water movement in the soil profile within the domain. Close examination of the domain (Fig. 5.1d) also reveals spatial continuity of soil type in the range of 0.2-0.7 times of the domain length. Under similar field conditions, Mohanty et al. [1991] in their study reported a nested correlation structures with correlation lengths ranging from 23 m to 60 m and attributed the effect to the agricultural practices and soil of the same origin and/or their depositional patterns.

A mean of 20000 for *P* is observed for C2, also concur with the characteristics of the predominant soil types (clay loam and loam) within the domain. For C1, the 100 accepted *Ksat* fields show a dynamic range of 45 cm/day to 400 cm/day. In case of C2, the 100 *Ksat* fields have a much smaller range of 45 cm/day to 80 cm/day. This corroborates that the inclusion of parameter correlation (i.e., $Ksat \propto \alpha^2$) reduces the uncertainties (nonuniqueness) attached to *Ksat* within the domain. The high correlation length (L_2) for C2 also indicates this feature. The domain average *Ksat* determined from

our KLE-MCMC algorithm may suggest the presence of preferential flow due to macropores in the domain, as it is much higher than the specified values of *Ksat* in the literature for clay loam and loamy texture soil. However the influence of topography on correlation structure of *Ksat* is not apparent in this study. The domain size and variation in elevation of the WC11 is not adequate enough to capture the influence of topography in *Ksat* characterization.

Undisturbed soil cores for *Ksat* measurement collected at different locations along the soil moisture sampling transects in WC11 are shown in Fig. 5.1b. The soil cores were taken between the land surface and 30 cm depth. The purpose of measuring *Ksat* of these soil cores was to validate *Ksat* characterization and evaluate the performance of the KLE-MCMC algorithm. For comparison between the laboratory measurements and simulated values, the distribution of *Ksat* realizations at (four) particular soil hydraulic conductivity sampling locations (Fig. 5.1b) were extracted from the highly probable stochastic *Ksat* fields. Lognormal distributions of *Ksat* from the realizations of overlaying grid cell for four specific locations are shown in Fig. 5.6 and Fig. 5.7 for C1 and C2, respectively, along with the lab measured *Ksat* at the same locations. The PDFs also exhibit the amount of uncertainty involved in *Ksat* within the grid cell of the domain. Few interesting features of *Ksat* are apparent in Fig. 5.6 and Fig. 5.7. Noteworthy among them is very similar distributions with nearly same mean, standard deviation, and range for all the four locations. Similar statistics were also obtained for remaining three locations not shown here. A distinct difference is visible between C1

(Fig. 5.6) and C2 (Fig. 5.7), i.e., the overall variability is greatly reduced in case of C2. This demonstrates the decrease in uncertainty due to parameter correlation as $Ksat \propto \alpha^2$.

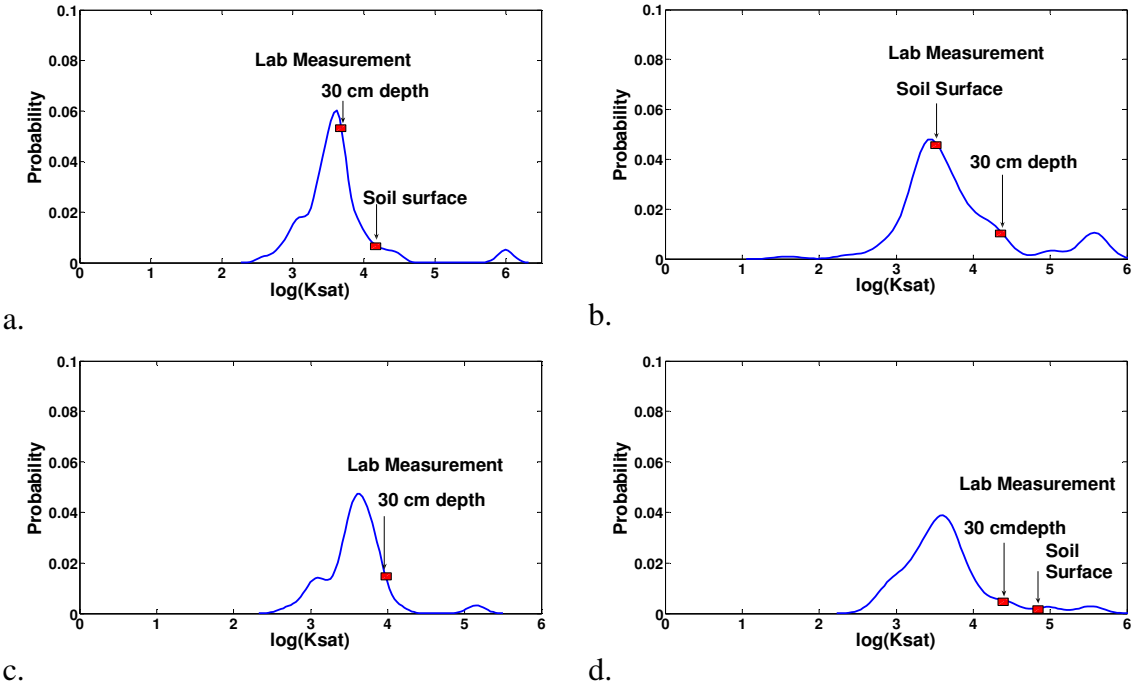

Figure 5.6. Probability distribution functions of Ksat at specific locations during SMEX05 for c*ompar*ison with field measurements for case 1 (C1) having no correlation among *Ksat*, α, and n.

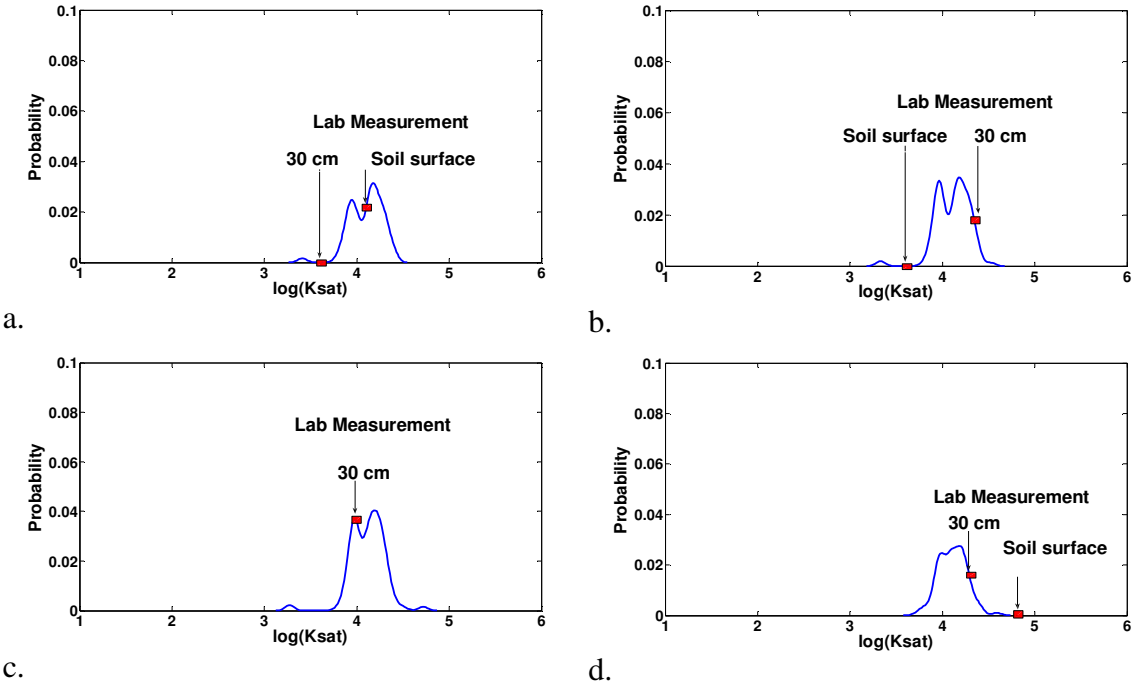

Figure 5.7. Probability distribution functions of Ksat at specific locations during SMEX05 for comparison with field measurements for case 2 (C2) having correlation of $Ksat \propto \alpha^2$, and n as constant.

The multimodality in these probability density functions (PDFs) for a clayey texture soil indicates presence of multi-modal pore size distribution including textural micropores, mesopores, and structural/biological macropores at the field locations. Preferential flow through the mesopores and macropores increase the overall effective *Ksat* of the domain. Laboratory measurements of *Ksat* for these locations also demonstrate distinct characteristics. Except in one location (Fig. 5.6b and Fig. 5.7b), the lab measured *Ksat* for soil surface is greater than that of the *Ksat* at 30 cm depth. This phenomenon is usually observed as the *Ksat* is expected to decrease with depth because

of changes in soil density, texture, and structure. One obvious feature in Figs. 5.6 and 5.7 (except in 7a) is the high probability of *Ksat* measured at 30 cm depth than at the soil surface, making it a more reliable estimate. In most of the locations the measured value of *Ksat* at 30 cm depth is closer to the mean of the predicted *Ksat*. The low probability associated with the soil surface *Ksat* is due to high measured value. This could be attributed to the presence of biological macropores and structural fractures in the core samples collected near the soil surface. Under field conditions, such macropores would be expected to terminate in the subsoil because of the decrease in porosity with depth, soil swelling, and from clay hydration, and are thus much less conductive when satiated than continuous open ended macropores in cores. At a site (Fig. 5.6b and Fig. 5.7b) the lab measured *Ksat* of soil surface is lesser than that of the *Ksat* value at 30 cm, highlights another dimension of variability. Anthropogenic manipulations (e.g., tractor tracks, trails) that lead to soil compaction may explain such occurrences. The presence of biomass and high concentration of organic matter could also impede water conduction at the soil surface. Bouma [1980] also suggested a representative elementary volume of 10000 cm^3 for clayey soil to estimate lab measured *Ksat* with less variability. However, the soil cores used for this study were much smaller than the representative elementary volume. The PDFs of KLE-MCMC predicted effective *Ksat* (Figs. 5.6 and 5.7) in selected grid cells (30 m X 30 m X 4.5 m) within the model domain that encompassed the laboratory measured values, exemplifying the existence of variability. To further assess the performance of the KLE-MCMC algorithm, conditions of the WC11 field during the SMEX02 field campaign were also applied. The importance of this

assessment is to evaluate the effects of change in vegetation cover (i.e., between corn and soybean), anthropogenic manipulation (i.e., tillage) and variation in the local forcings (i.e., atmospheric conditions) on the evolution of *Ksat* fields. The change in vegetation cover influences the status of soil moisture and ultimately modeled *Ksat* by having different evapotranspiration rates and related infiltration characteristic. Tillage and addition of biomass to the top soil also greatly manipulates the *Ksat* field. During the latter part of the SMEX02 period greater amount of precipitation was also observed that led to wetter conditions with very high soil moisture content in clayey texture soil. With these varied conditions during SMEX02 as compared to SMEX05, the *Ksat* fields modeled using the KLE-MCMC algorithm were compared. The comparison of the PDFs shows statistically insignificant difference between the overall effective *Ksat* fields estimated during the SMEX02 and SMEX05 periods. It is also noteworthy to observe similarity in the correlation length L_2 of the *Ksat* fields during SMEX02 and SMEX05 periods. This suggests that effective *Ksat* fields have experienced statistically insignificant change over time irrespective of the change in vegetation cover and anthropogenic manipulation (tillage) of the soil surface in WC11 field.

5.6. Conclusion

In this paper, we characterize and parameterize saturated hydraulic conductivity (*Ksat*) for an agricultural field (WC11) in the Walnut Creek watershed, Iowa. Soil moisture measurements taken during a field campaign were used to assess effective *Ksat*. The Karhunen-Loève Expansion (KLE) with Markov Chain Monte Carlo

(MCMC) technique in conjunction with a physically based vadose zone model (SWMS_3D) was used for the study under two different scenarios: case 1) van Genuchten soil hydraulic parameters except *Ksat* are constant and are based on the soil type of the grid block within the modeling domain; case 2) *Ksat* is correlated with the van Genuchten parameter α as $Ksat \propto \alpha^2$. The MCMC algorithm selected *Ksat* fields with a low acceptance rate, but displayed a reasonable level of convergence. The selected *Ksat* fields revealed an average spatial correlation length of nearly 400 m within a study domain of 600 m X 600 m which is quite reasonable considering the influence of clayey soil texture. Laboratory measurements of *Ksat* using soil cores collected from the WC11 at soil surface and 30 cm depth are used to validate the predicted effective *Ksat* fields. The probability distribution functions (PDFs) of the predicted effective *Ksat* for both C1 and C2 scenarios encompassed the laboratory measurements and also illustrated the variability associated within the domain. In general, the uncertainty of *Ksat* reduces when the parameter correlation, $Ksat \propto \alpha^2$, is used. The PDFs also show multimodality which indicates the presence of macropores. Furthermore, the laboratory measured *Ksat* values from the soil cores collected at 30 cm depth were found more reliable and representative of the field conditions in comparison with the predicted effective *Ksat*.

Application of the same algorithm in separate field conditions (i.e., different years) of the WC11 domain was used to assess the impact on effective *Ksat* fields due to different vegetation cover and local forcings. Results reveal statistically insignificant difference between the two years 2002 (SMEX02) and 2005 (SMEX05). The study shows that the proposed algorithm is efficient to characterize and parameterize the

evolution of effective *Ksat* for an agricultural field. Further studies are required for different hydroclimatic regions and diverse topography to extend the application of proposed algorithm. We also plan to use more efficient sampling techniques such as two-stage MCMC to sample *Ksat* in our future work.

CHAPTER VI

A NEW ALGORITHM FOR CHARACTERIZATION OF BACKSCATTER BY SURFACE FEATURES IN L-BAND MICROWAVE REMOTE SENSING OF SOIL MOISTURE

6.1. Synopsis

Satellite based remote sensing of soil moisture is generally conducted with active (radar) and passive (radiometer) microwave measurements. These methods of measurements have their own strengths (e.g., spatial/temporal continuity) and limitations (e.g., coarse spatial resolution). Particularly, the active microwave remote sensing of soil moisture is very sensitive to the presence of vegetation on soil surface. During active microwave remote sensing the backscattering from the target (i.e, the soil surface) is affected by the overlaying vegetation, consequently sending degraded signal back to the radar. This phenomenon greatly compromises the quality of remotely sensed soil moisture measurements at the footprint scale. Radar backscattering is also greatly influenced by the surface roughness characteristics. Theoretical and empirical models exist to remove such influence of vegetation and surface roughness from the radar backscattering data, however, they are complicated and mostly site specific. The proposed research presents an alternative algorithm that averts usage of such techniques. The algorithm has simple assumptions that convert the total radar backscattering equations for a particular temporal scale (i.e., the inter-strom period) into a set of simple linear equations. A Soil-Vegetation-Atmosphere-Transfer (SVAT) model is employed in

the algorithm for soil moisture estimation that is used to assess the dielectric constant of soil profile which in turn relates to radar backscattering. A major advantage of the new algorithm is its potential to separate/estimate the stochastic surface roughness and vegetation backscattering components in diverse hydro-climatic regions under different combinations of geophysical parameters (i.e., soil, topography, and vegetation) and estimate their uncertainties. Entropy-based characterization is utilized to quantify the chaos in radar backscattering. The study helped to identify the physical controls that influence the L-band radar backscattering components.

6.2. Introduction

Soil moisture is a crucial variable of the environmental continuum formed by soil, water and air that influences hydrologic, ecologic, and climatic processes. Therefore, measuring soil moisture at various spatial and temporal scales is critical for better understanding of these environmental processes. Recent advancement in remote sensing technology has demonstrated that soil moisture can be measured by variety of techniques i.e., optical (visible, near-infrared, shortwave infrared) [*Muller and Decamps*, 2001], thermal infrared [*Shih and Jordan*, 1993], active microwave [*Dubois, et al.*, 1995], and passive microwave [*Engman*, 1991; 1995; *Jackson, et al.*, 2005b; *Jackson, et al.*, 1999; *Njoku, et al.*, 2003; *Njoku and Oneill*, 1982]. Optical remote sensing of soil moisture has serious drawbacks due to limited ability to penetrate clouds and vegetation canopy, and is highly attenuated by the earth's atmosphere. Similarly, thermal infrared remote sensing has serious limitations due to presence of any vegetation. On the other hand,

microwave remote sensing is considered suitable to quantitatively measure soil moisture under variety of soil, topographic and vegetation conditions and particularly the earth's atmosphere is relatively transparent to microwave. The use of various active and passive microwave remote sensors [*Georgakakos*, 1996] has enhanced the capability for monitoring soil moisture across range of spatio-temporal scales. Microwave (active/passive) remote sensing of soil moisture, however, remains an active area of investigation because of its dependency on variety of geophysical parameters (e.g., precipitation, soil type, topography, and vegetation) and sensor configuration (system parameters: frequency, incident angle, polarization), and due to coarse spatial resolution of remote sensor that mask the underlying ground heterogeneity.

Significant progress has been made in regional/global soil moisture mapping using passive microwave sensors [*Jackson, et al.*, 1999; *Njoku, et al.*, 2003]. *Njoku and Entekhabi* [1995] have also shown that a passive microwave radiometer with less than 1˚K radio brightness noise sensitivity can measure near-surface soil moisture with a root-mean-square error of 1–2% vol/vol for bare soil. In a spaceborne satellite-based radiometer with the current technology, 1˚K radio brightness noise sensitivity can only be attained for a footprint size larger than 40 km [*Njoku, et al.*, 2003]. Having such coarse spatial resolution (>40 km) in relatively low microwave frequencies (<10.71 GHz), the spatial heterogeneity in land surface (e.g., snow cover, soil wetness, surface roughness, topography) also introduce complexity in soil moisture retrieval. Furthermore, microwave emissions are also attenuated by vegetation canopy reducing sensitivity for accurate estimation of soil moisture [*Jackson and Schmugge*, 1991; *Njoku*

and Chan, 2006]. With the available configurations and associated limitations in terms of coarse resolution of passive microwave remote sensing it is not adequate to meet the finer scale spatial resolution requirement for soil moisture in watershed, catchment, and field scale applications. The only satellite-based sensor that can meet the spatial resolution requirement for watershed and finer scale management is by using active microwave remote sensing techniques. *Dobson and Ulaby* [*Dobson and Ulaby*, 1986] in their study showed that using active microwave (radar) soil moisture (with ±3.5% vol/vol error) for spatial resolutions down to 1 km may be retrieved for soil surfaces with vegetation cover shorter than 15 cm. In active microwave remote sensing, the radar backscattering from the soil surface is adversely affected by the presence of vegetation. This is due to increased volume scattering and attenuation of electromagnetic signal [*Tansly and Millington*, 2001]. The overall impact of vegetation, surface roughness, and topography on radar signals results significantly higher root mean square error (RMSE) for soil moisture retrieval [*Dobson and Ulaby*, 1986]. Currently, there are three operational Synthetic Aperture Radar (SAR) satellite systems that have capability to measure soil moisture: ESA ERS 2 (C-band) [*Haider, et al.*, 2004], ESA ENVISAT (C-band) [*Baghdadi, et al.*, 2007], and Canadian RADARSAT-1/RADARSAT-2 (C-band) [*Leconte, et al.*, 2004]. Studies [*Baghdadi, et al.*, 2007; *Haider, et al.*, 2004; *Leconte, et al.*, 2004] have also demonstrated that SAR instruments at C-band measure soil moisture for bare soil with nearly 3-4% vol/vol retrieval error. However, with SAR C-band it is difficult to map soil moisture accurately from the soil surface covered with vegetation. *Schmullus and Furrer* [*Schumullius and Furrer*, 1992] examined backscattering from

soil under different vegetation conditions at various frequencies in L-, C-, and X-band at cross and like polarizations. They reported that backscattering is better related to soil moisture only at L-band frequency.

At present, there is no operational L-band radar satellite system. The upcoming Soil Moisture Active Passive (SMAP) mission of National Aeronautic and Space Administration (NASA) is a pathfinder-class concept for global mapping of soil moisture. The SMAP will have onboard low-frequency L-band radiometer (1.42 GHz) and radar (1.26 GHz). It will have soil moisture product derived from ~40 km resolution brightness temperature from the L-band radiometer and ~3 km resolution backscattering coefficients from the L-band radar with a revisit period of 2-3 days. The radar on SMAP platform is of particular interest here because it will provide a new perspective of L-band radar backscattering from a satellite platform. The primary objective of this study is to describe L-band radar backscattering coefficient under variety of terrain characteristics and vegetation conditions. The study also proposes a simple algorithm for determining stochastic surface roughness using synthetic radar data.

6.3. Modeling Active Microwave Sensing of Surface Soil Moisture

We hypothesize that a reliable spatio-temporal distribution of soil moisture is important for probabilistic characterization of backscatter by surface features in active microwave remote sensing. A distributed framework with Soil Vegetation Atmosphere Transfer (SVAT) modeling based on the work of *Das and Mohanty* [*Das, et al.*, 2008a] is implemented for spatio-temporal evolution of soil moisture for the study region. The

SVAT model incorporates Dobson's model [*Dobson, et al.*, 1985] to convert soil moisture to dielectric constant **ε**. Geophysical parameters (e.g., NDVI, soil texture, surface roughness) characterizing the study domain and estimated **ε** from SVAT modeling provided synthetic radar total backscatter. The radar backscatter for a vegetation-covered soil layer in both HH and VV polarizations is expressed as the sum of three components [*Ulaby, et al.*, 1996],

$$\sigma^t = \sigma^s \exp(-2\tau_o/cos\theta) + \sigma^v + \sigma^{sv} \quad (6.1)$$

where σ^t represents the total radar scattering cross-section, σ^s is the scattering contribution of the soil surface modified by the two-way vegetation attenuation, σ^v is the scattering cross-section of the vegetation volume, and σ^{sv} represents the multiple scattering interaction between the soil and vegetation. Subsequently the terminology vegetation backscattering and soil-vegetation backscattering are interchangeably used with volume scattering and surface-volume scattering, respectively.

In practice, theoretical and empirical models are used to model the scattering components σ^s, σ^v, and σ^{sv} [*Dobson and Ulaby*, 1986; *Dubois, et al.*, 1995]. In case of the above-ground biomass (vegetation) is lesser than 0.5 kg/m^2 second and third terms (σ^v and σ^{sv}) on the right side in eq. (1) become negligibly small. The atmospheric and ionospheric effect for the radar L-band is also negligible and could be ignored and then the soil surface backscatter σ^s can be modeled theoretically by Integral Equation Model (IEM) [*Fung, et al.*, 1992]. For a given radar configuration (i.e., wavelength, local incident angle and polarization), the IEM predicts the backscattering coefficient on a random surface depending on surface roughness (RMS height) *s* and its correlation

length *l*, and the relative dielectric constant *ε*. The IEM is tested in many studies including comparisons with data from Monte Carlo simulation, controlled laboratory study, truck-mounted scatterometer, and SIR-C/AIRSAR. For bare soil, there is a general confidence using the IEM in predicting L-band co-polarized backscattering signals (σ_{VV}^{s} and σ_{HH}^{s}) of a random rough surface. The RMS errors are commonly within 2 dB for backscattering when the surface roughness is well characterized. Studies [*Leconte, et al.*, 2004],[*Baghdadi, et al.*, 2002] have also shown that the results from IEM deviated when compared to truck-mounted scatterometer and SAR (airborne and spaceborne) measurements. The theoretical models like IEM can rarely invert data measured from natural environment because of restrictive assumptions made during their derivation. Well established alternative empirical methods are used in this study to circumvent the difficulties for modeling the backscattering signatures of bare surfaces. The empirical models for backscattering coefficient of bare soil σ_{VV}^{s}, σ_{HH}^{s}, and σ_{HV}^{s} are derived from experimental data. Dubois, et al. [1995] provide empirical expressions for σ_{VV}^{s} and σ_{HH}^{s} that is used in this study for the co-polarized backscatter,

$$\sigma_{HH}^{s} = 10^{-2.75} \cdot \left(\frac{cos^{1.5}\,\theta}{sin^{5}\,\theta} \right) \cdot 10^{0.028 \cdot \varepsilon' \cdot tan\,\theta} \cdot (ks \cdot sin\,\theta)^{1.4} \cdot \lambda^{0.7} \tag{6.2}$$

$$\sigma_{VV}^{s} = 10^{-2.35} \cdot \left(\frac{cos^{3}\,\theta}{sin^{3}\,\theta} \right) \cdot 10^{0.046 \cdot \varepsilon' \cdot tan\,\theta} \cdot (ks \cdot sin\,\theta)^{1.1} \cdot \lambda^{0.7} \tag{6.3}$$

where, θ is radar incidence angle**,** λ (cm) is the wavelength, *k* is the wave number, **s** is the surface RMS height, and **ε** is the real part of the dielectric constant. The cross

polarization component σ_{HV}^{s} can be computed from σ_{VV}^{s} using the empirical model given by [*Oh, et al.*, 1992]. The cross polarization component σ_{VH}^{s} is equal to σ_{HV}^{s} because of reciprocity property of radar scattering, as the response for HV and VH are identical.

The presence of vegetation biomass adds complexity and increase uncertainty in total radar backscattering. Vegetation canopies are complex structures in terms of the shapes and sizes of the scattering elements relative to wavelength. For radar backscatter modeling (unlike radiometric modeling) a uniform canopy assumption may not be adequate to describe the microwave-vegetation interactions. In this study it is assumed that, over the spatial extent of the 3-km radar footprints, the scattering is dominated by randomly-oriented components. Models for the co- and cross-polarized backscatter from vegetation represented as randomly orientated -structures are given by [*Ulaby, et al.*, 1986]. The expressions for the volume scattering ($\sigma_{VV}^{v}, \sigma_{HH}^{v}$) and surface-volume interaction terms ($\sigma_{HH}^{sv}, \sigma_{HV}^{sv}$) are mentioned below.

$$\sigma_{VV}^{v} = \sigma_{HH}^{v} = 0.74\omega\cos\theta\left[1 + 0.54\omega\tau_o - 0.24(\omega\tau_o)^2\right]\left[1 - exp\{-2.12\tau_o \sec\theta\}\right] \quad (6.4)$$

$$\sigma_{HV}^{v} = \omega\cos\theta\left[0.044\omega\tau_o - 0.018(\omega\tau_o)^2 + 0.006(\omega\tau_o)^3\right]\left[1 - exp\{-11.7\tau_o \sec\theta\}\right] \quad (6.5)$$

$$\sigma_{HH}^{sv} = 1.9\omega\cos\theta\left[1 + 0.9\omega\tau_o + 0.4(\omega\tau_o)^2\right]\left[1 - exp\{-1.93\tau_o \sec\theta\}\right]\times$$
$$\times exp\{-1.37\tau_o^{1.12} \sec\theta\}\, exp\{-0.84(ks)^2 \cos\theta\}\, r_h \quad (6.6)$$

$$\sigma_{HV}^{sv} = 0.013\omega\cos\theta\left[1 + 7.85\omega\tau_o + 7.9(\omega\tau_o)^2\right]\left[1 - exp\{-6.92\tau_o \sec\theta\}\right]\times$$
$$\times exp\{-1.02\tau_o^{1.38} \sec\theta\}\, exp\{-2.9(ks)^2 \cos\theta\}\left(\frac{r_v + r_h}{2}\right) \quad (6.7)$$

Where, τ_o is vegetation opacity, l is correlation length of surface roughness s, r_v and r_h are the Fresnel reflectivities and ω is vegetation parameter. The VV-polarized surface-

volume interaction term, σ_{VV}^{sv}, is small and thus neglected. To evaluate τ_o, total vegetation water content (VWC_c) was used as follows:

$$VWC_c = -0.3215\,(NDVI) + 1.9134\,(NDVI)^2 \quad (6.8)$$

where *NDVI* is normalized difference vegetative index. A woody component fraction f_T was used to scale the foliar water content derived from (8) to a corrected vegetation water content

$$VWC = VWC_c / (1 - f_T) \quad (6.9)$$

The nadir vegetation opacity τ_o is related to the columnar vegetation water content *VWC* (kg m^{-2}) and is given by:

$$\tau_o = b_o * VWC \quad (6.10)$$

were, the coefficient b_o depends on vegetation type [*Jackson and Schmugge*, 1991].

Our numerical study uses a Soil-Vegetation-Atmosphere-Transfer (model) [*Das, et al.*, 2008a] for soil moisture/dielectric constant modeling in conjunction with empirical models (eq. 1-10) for characterizing the spatial and temporal varibaility of microwave backscattering components. To generate synthetic backscattering data, normal random variability of 10% standard deviation was introdcued in the parameters (s, b_o, ω, and f_T) mentioned in Table 6.1 [*Zhan, et al.*, In press]. This synthetic data obtained from eq. 1 is considered as the total backscattering received by the satellite-based radar and is the basis for the characterization of uncertainty in radar backscattering (Section 6.4) and proposed algorithm (Section 6.5). The synthetic data is used because no such radar backscattering data exist for the study area (Section 6.7) for spatial and temporal characterization, and for use in the algorithm mentioned in subsequent sections for deriving surface roughness and vegetation backscattering components.

Table 6.1. Land cover classes, roughness parameters (s and h), albedo (ω), and vegetation parameters (b_o, f_T).

Class	**Category Name**	s (cm)	h	ω	b_o	f_T
1	Crop/mixed farming	1.5	0.15	0.05	0.13	0.2
2	Short grass	1.0	0.1	0.05	0.10	0.0
3	Evergreen needleleaf tree	1.0	0.1	0.12	0.10	0.8
4	Deciduous needleleaf tree	1.0	0.1	0.12	0.10	0.8
5	Deciduous broadleaf tree	1.0	0.1	0.12	0.12	0.8
6	Evergreen broadleaf tree	1.0	0.1	0.12	0.12	0.8
7	Tall grass	1.0	0.1	0.05	0.10	0.0
8	Desert	1.0	0.1	0.00	0.00	0.0
9	Tundra	1.0	0.1	0.05	0.10	0.0
10	Irrigated crop	1.0	0.1	0.05	0.11	0.0
11	Semidesert	1.0	0.1	0.05	0.10	0.0
12	Bog or marsh	1.0	0.1	0.05	0.10	0.0
13	Inland water	1.0	0.1	0.00	0.00	0.0
14	Evergreen shrub	1.0	0.1	0.05	0.11	0.0
15	Deciduous shrub	1.0	0.1	0.05	0.11	0.0
16	Mixed woodland	1.0	0.1	0.12	0.11	0.8
17	Short grass/crop	1.2	0.12	0.05	0.13	0.1
18	Tall grass/crop	1.2	0.12	0.05	0.13	0.1
19	Crop/mixed woodland	1.2	0.12	0.08	0.12	0.5
20	Crop/evergreen needleleaf tree	1.2	0.12	0.08	0.12	0.5
21	Crop/deciduous broadleaf tree	1.2	0.12	0.08	0.12	0.5
22	Irrigated crop/deciduous broadleaf tree	1.2	0.12	0.08	0.12	0.5
23	Short grass/mixed woodland	1.0	0.1	0.08	0.11	0.4
24	Evergreen needleleaf/short grass	1.0	0.1	0.08	0.11	0.4
25	Evergreen needleleaf/evergreen broadleaf	1.0	0.1	0.12	0.11	0.8

6.4. Method for Uncertainty Characterization in Radar Backscattering

Naturally occurring processes are chaotic and similar chaos is also observed in radar backscattering components. The knowledge on the behavior of radar backscattering is limited by their intrinsic complexity, which is the result of numerous

interacting geophysical parameters (e.g., vegetation canopy and surface roughness) and random errors (e.g., radio frequency interference) that contributes to the chaos. Sometimes it is related to the difficulties we have in describing or understanding radar backscattering components. To capture chaos and randomness in radar backscattering in diverse hydro-climatic, terrain, and vegetation, entropy theory defined by *Shannon* [*Shannon*, 1948] is used. According to the entropy theory, uncertainty in probability distribution of any variable is the negative expected value of the logarithm of the probability distribution function (PDF) of the variable. Shannon entropy H is defined as a function of probabilities p_i as

$$H = [\, I \,] = -\sum_{i=1}^{N} p_i \, log \quad p_i \tag{6.11}$$

Characteristically the increasing randomness of the variable decreases the skewness of the probability distribution, thus leading to increased entropy. Entropy takes on a maximum value when the probability distribution is uniform without any deflection, and it reduces to zero when a particular value of the variable occurs with probability of one. Again, the entropy-based methodology is applicable to any distribution and whether the distribution is a priori known or not. Direct application of the entropy theory can quantify the uncertainty in radar backscattering. The backscattering components σ^s, σ^v, and σ^{sv} can be charaterized as continous random variables for entropy based characterization.

6.5. A New Algorithm to Estimate Surface Roughness and Volume Scattering

Using the synthetic radar backscattering data, the study uses a new algorithm to determine the surface roughness and vegetation backscattering components as an alternative to using any of the aforementioned empirical models (eq. 4-7). In the proposed algorithm, the surface roughness parameter (s) and the vegetation backscattering (σ^v) are considered static for a small temporal scale (i.e., interstorm period). This is a resonable assumption based on the growth/decay status of vegetation in natural environment and soil surface getting modified after precipitation events. Also the parameters such as s and σ^v are considered not very dynamic for pasture and herbaceous fields for small temporal scale. On the other hand, special attention and treatment is required for a region having agricultural farmlands because of anthropogenic manipualtion (e.g., plowing and harvesting) that might change the backscattering components (σ^s, σ^v, and σ^{sv}) very abruptly. Therefore, in such conditions the assumption of constant s and σ^v might hold for few days only and may introduce error in the proposed approach. The backscattering due to soil-vegetation interaction componenet (σ^{sv}) is the most dynamic [*Njoku and Kong*, 1977] because along with vegetation it is greatly influenced by the temporal status of dielectric constant which is highly correlated to soil moisture evolution. Based on these assumptions and conditions, a new approach is proposed here for determining surface roughness and backscatter components. For co-polarized radar backscattering from a specific region for a particular day (x) is given as

$$\sigma_x^t = \sigma_x^s(-2\tau_o/cos\theta) + \sigma_x^v + \sigma_x^{sv} \quad (6.12)$$

where x = 1…n, represents a daily timestep within an interstrom period T. In other words the system has n sets of equations. By solving the n sets of equations simultaneously eliminated σ^v from all the equations as that component is considered constant across T. The backscattering from the soil surface σ_x^s has two unknowns, ε_x (dielectric constant for day x) and s in all the n equations. To compute dielectric constant reliable soil moisture at compatible resolution is essential. The SVAT model (mentioned in Section 5) provides reasonable distribution of state variable i.e., soil moisture at soil surface for ~3 km resolution. Subsequently Dobson's model [*Dobson, et al.*, 1985] relates soil moisture to equivalent dielectric constant. Now the system of n simultaneous equations comprise n+1 unknowns (i.e., s, σ_1^{sv},…, σ_n^{sv}). To solve n simultaneous equations with n+1 unknowns, we assumed $\sigma_1^{sv} \approx \sigma_2^{sv}$. The rationale of $\sigma_1^{sv} \approx \sigma_2^{sv}$ is that at the start of interstrom period and due to wet condition of soil surface the probability of $\sigma_1^{sv} \approx \sigma_2^{sv}$ is high. The assumption is even more appropriate for the region having high vegetation and also the region with soil texture having high percentage of clay fraction that retains high soil moisture. This assumption reduced the number of unknowns to n, leading to computation of s, σ^v, σ_1^{sv}…, σ_n^{sv}, for the interstrom period. The algorithm applied to certain regions for continuous interstrom periods could help study the temporal evolution and statistical characteristics of surface roughness s with changing season, precipitation, vegetation growth and vegetation water content.

6.6. SVAT Model

Reliable estimate of surface and root-zone soil moisture across the study is required to implement the algorithm mentioned in section 6.4. Therefore, we mainly focus the root-zone (~1 m depth) soil moisture at a spatial resolution of ~3 km. The disparity of scales between the horizontal (spatial resolution: ~3 km) and vertical (soil depth: 1 m) extents of the root-zone was the key consideration in formulating the SVAT modeling framework. The implementation of the model set up is similar to Das et al. [2008a]. Brief overview of the model framework at is provided for relevance of this study. For SVAT model simulation, the root-zone at every radar footprint within the study region is vertically discretized, with finer discretization near the soil layer interfaces and at the land-atmosphere boundary. Finer discretization near the top boundary and layer interfaces are used to handle the steep pressure gradient for the numerical simulations. Time-dependent flux-type top boundary conditions for each parallel soil column (matching the radar footprints) are used with precipitation distribution across the study region. Runoff and runon between adjacent footprints due to topography was considered on the land surface. The runoff from the one or more adjacent footprint of steepest descent according to flow routing is used as runon for the footprint under consideration. Given the relatively coarse horizontal scale with shallow root-zone, the parallel soil columns model ignores the lateral water fluxes across the adjacent soil columns and only predicts the vertical fluxes including infiltration, evapotranspiration, runoff, and deep percolation as parallel non-interacting stream-tubes concept. A probabilistic approach is adopted, by using an ensemble of state variables

(profile soil moistures) for all the radar footprints (~3 km). A state augmentation technique is applied by concatenating uncertain soil properties to state variables, forming composite vectors in the ensemble. The soil types from the CONUS soil database and the van-Genuchten shape parameters for the soil textural classes given by Unsaturated Soil Hydraulic Database (UNSODA) are used with ±20% uncertainty. The purpose of including uncertain soil properties in the ensemble is to address the assumption that it simulates model errors and subpixel variability present within a radar footprint. For best computational efficiency, one hundred members (composite vectors) were populated in the ensemble. The SVAT model is run 6 months ahead of year 2005, to tune the state of initial soil moisture profile. At each time step, final states (soil moisture) are determined by the ensemble of the one hundred replicated predictions made by the SVAT model for every radar footprint. The SVAT model used in the soil moisture modeling scheme is described briefly as follows.

We use the SWAP model [*Van Dam, et al.*, 1997] to simulate the processes of the soil-water-atmosphere-plant system. SWAP is a physically-based, hydrologic model that numerically solves the one-dimensional Richards' equation for simulating the soil moisture dynamics in the soil profile under different climatic and environmental conditions. Irrespective of scale, transient isothermal unsaturated water flow in non-swelling soil, Richards' equation used in SWAP is described by

$$\frac{\partial \theta}{\partial t} = \frac{\partial}{\partial z}\left[K\left(\frac{\partial H}{\partial z} + 1\right)\right] - S_a(H) \tag{6.13}$$

where θ is the soil water content (m^3/ m^3), z is the soil depth (m), H is the soil water pressure head (m), K is the unsaturated hydraulic conductivity (m/day), and $S_a(H)$ is the

root water uptake (m/day). Penman-Monteith equation [*Monteith*, 1965] was used to calculate potential evapotranspiration. The potential transpiration (T_p) and the soil evaporation (E_p) were partitioned using LAI. In the SWAP model soil moisture retention and hydraulic conductivity functions are defined by the Mualem-van Genuchten model [*van Genuchten*, 1980].

6.7. Study Area and Data

The Red-Arkansas river basin (Fig. 6.1) is selected for this study due to presence of diverse geophysical characteristics (topography, soil type and vegetation). The basin provides various combinations of these geophysical characteristics that are significant to study the spatio-temporal stochasticity present in radar backscattering. Three specific regions (Fig. 6.1) are selected as focus areas: i) Northwestern mountainous region (50,000 km^2), with elevation more than 1200 m from the sea level and having low LAI between 0 and 1.2 m^2/m^2. The land cover of this region is mostly dominated by high elevation alpine trees, deciduous trees and shrubs. ii) Central plains of farmlands/grasslands (38,000 km^2) with moderate elevation between 150 m and 500 m of rolling topography and having highly variable LAI between 1 and 5 m^2/m^2, peaking during the summer months. iii) Eastern plains, of low lying (elevation: 40 to 100 m) eastern region (38,000 km^2). The landcover of the eastern region is dominated by deciduous trees, grasslands and summer crops with moderate to high LAI of nearly1-6 m^2/m^2. Fig. 6.2 presents the diversity of soil type, vegetation, topography, and precipitation present across the basin. The study region is subhumid and receives heavy

to moderate rainfall distributed throughout the year. The other relevant datasets used in the study are summarized below:

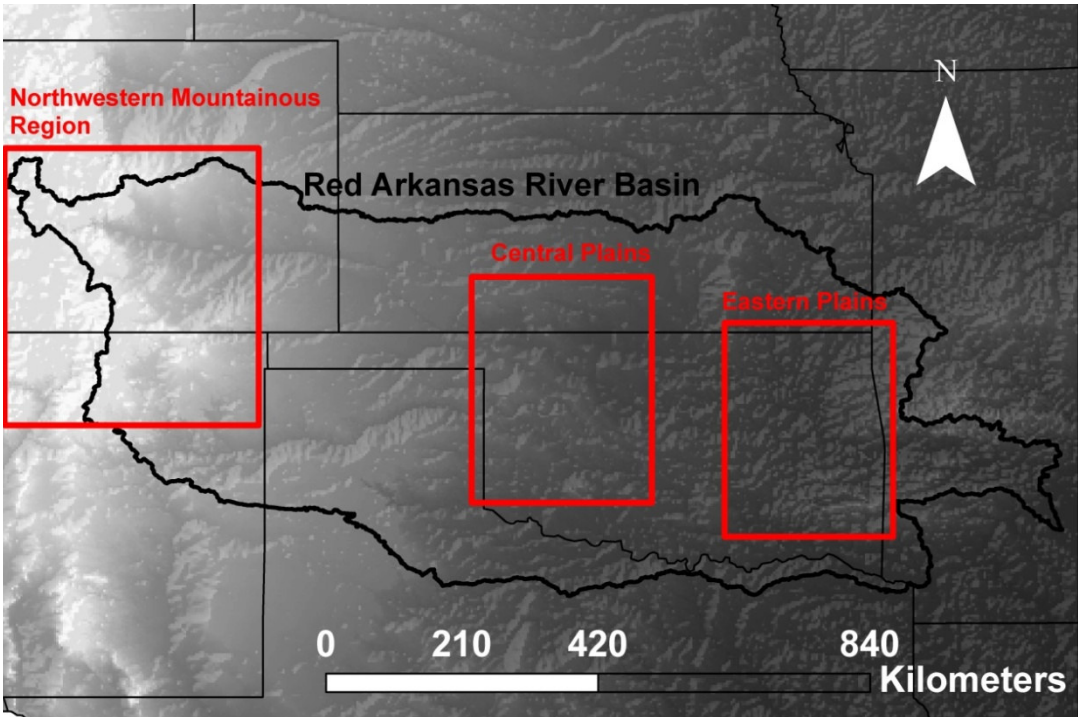

Figure 6.1. Red-Arkansas River Basin with highlighted region showing three focus study area: a) the Northwestern Mountainous Region, b) the Central Plains, and c) the Eastern Plains.

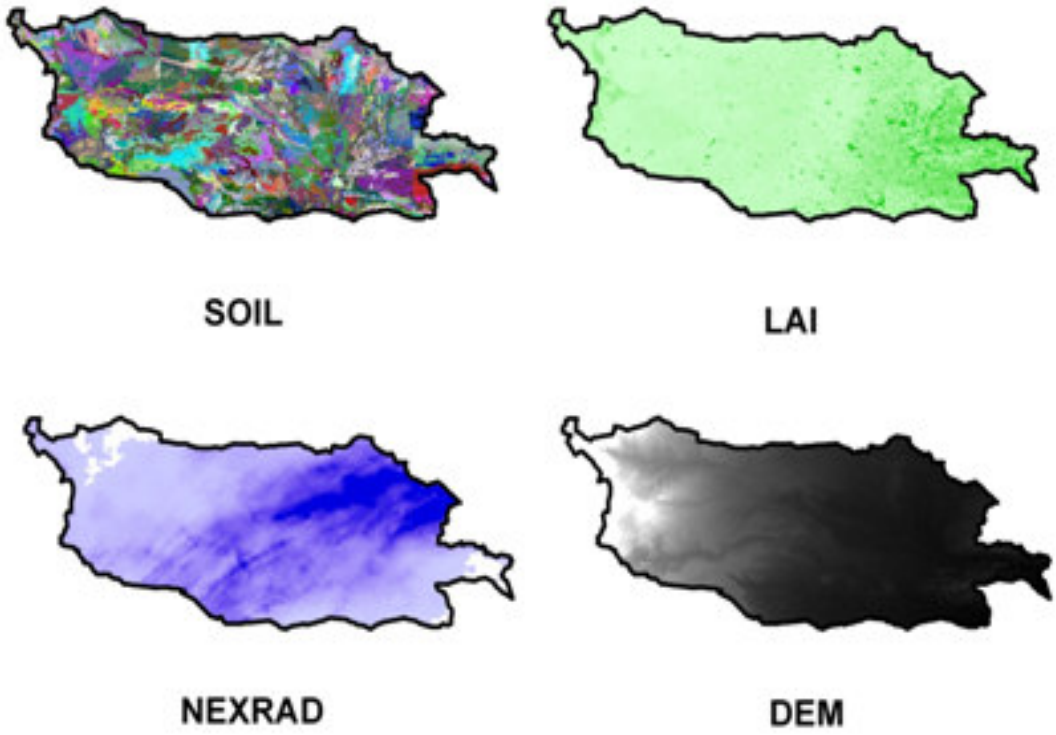

Figure 6.2. Sample data of Soil, LAI, Nexrad, and DEM of Red-Arkansas River basin.

Soil

The requisite soil parameters (e.g., %sand, %clay, bulk density and saturated hydraulic conductivity) data were derived from CONUS-SOIL (http://www.soilinfo.psu.edu/) which is a multilayer North American soil characteristic dataset.

NDVI and LAI

MODIS derived 16-day composite data of NDVI and LAI at ~1 km spatial resolution were obtained and resampled to ~3 km for the study.

Precipitation

Precipitation is arguably the most important forcing for spatio-temporal evolution of soil moisture. Quality-controlled ~4 km precipitation data [*Seo and Breidenbach*, 2002] based on multi-sensor (radar WSR-88D and rain gauge) estimates from National Weather Service (NWS) River Forecast Centers (RFCs) and resampled to ~3 km (matching SMAP-based L-band radar spatial resolution) is used for the study.

Meteorological Forcings

Other important forcings (e.g., min and max air temperature, relative humidity and incoming solar radiation) those are relatively spatially homogenous are extracted from the North American Regional Reanalysis (NARR) dataset. The NARR dataset resolution of ~32 km was further resampled to ~3 km to suit the study.

6.8. Results and Discussions

SVAT modeling based on a distributed modeling framework [*Das, et al.*, 2008a] that have an ensemble of appropriate boundary conditions and scaled parameters [*Das, et al.*, 2008b] [*Das, et al.*, 2008c] was used to simulate soil moisture, soil temperature, and evapotranspiration in the Red-Arkansas river basin at a spatial resolution of ~3 km for the year 2005. The soil moisture status and soil temperature profile for the surface/root zone were retrieved. Arbitrarily selected random error of 10% was introduced in the soil moisture values and the parameters (surface roughness, tree fraction, albedo, and vegetation opacity) in eq. 1-8. The random error of 10% was to make the synthetic

backscattering data more representative of chaos in the backscattering dynamics. The surface (i.e., top 5 cm) soil moisture from the simulation was used to compute total radar backscattering and its individual components (soil, vegetation, and soil-vegetation interaction). Figure 6.3 illustrates the estimated total backscattering and individual components at HH polarization (based on eq. 2) across the study river basin for the DOY 180, 2005. Visual examination of the backscattering values shows clear dependence on soil moisture. Mainly, backscattering based on HH/VV polarization was considered as the HV/VH cross polarization return was usually weaker than the like polarized return. Studies (e.g., [*Ulaby, et al.*, 1996]) have also demonstrated that backscattering are more sensitive at like polarizations (HH, VV) compared to cross polarization (VH, HV). Results presented in the subsequent figures (Fig. 6.4-6.12) are based on the average values of backscattering components within the study regions (i.e., the Northwestern mountainous region, the Central plains, and the Eastern plains). The results from the three focus areas are discussed below.

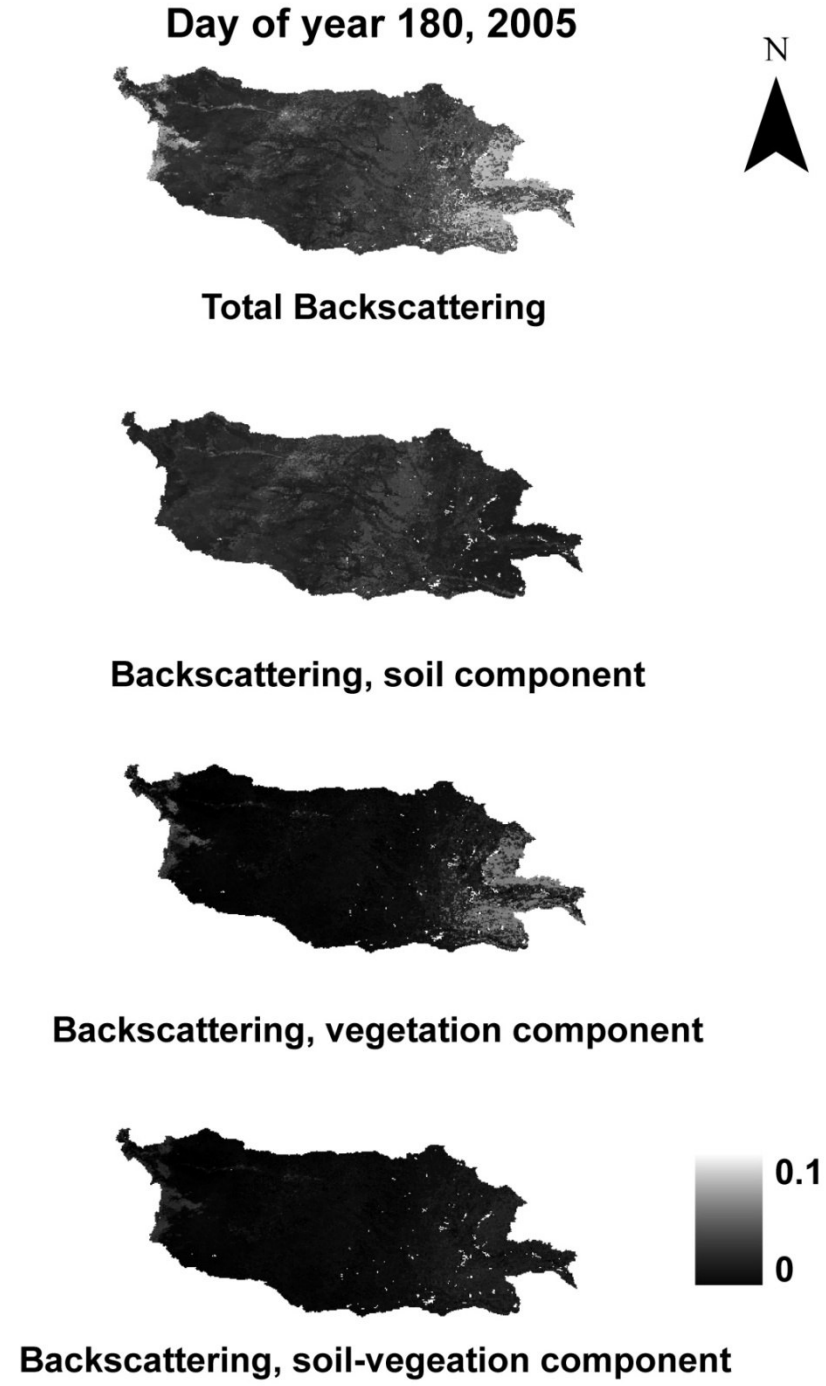

Figure 6.3. A sample of total and individual backscattering components at HH polarization for day of year (DOY) 180, 2005.

Northwestern Mountainous Region

This region is dominated by rugged topography and mountains, has low yearly average NDVI, and low average ambient temperature. The soil texture on surface is mostly sandy-loam or clay-loam. Low evapotranspiration rates throughout the year greatly influence the soil moisture evolution within the region. The average soil moisture of this region is nearly 0.25 (v/v) with occasional spikes due to precipitation events. As expected, the backscattering at HH/VV polarization (σ_{HH}^{s},σ_{VV}^{s}) from soil corresponds with soil moisture (Fig. 6.4a-b), although the variation and correspondence of σ_{HH}^{s} (Fig. 6.4a) with soil moisture evolution is not as pronounced as σ_{VV}^{s} (Fig. 6.4b), and is relatively constant throughout the year. Numerous investigations (e.g., [Njoku, et al., 2002]) have also shown that backscattering from soil having VV polarization (σ_{VV}^{s}) is more sensitive to soil moisture than σ_{HH}^{s}. The spikes in σ_{VV}^{s} are the result of high soil moisture after precipitation events (Fig. 6.4b). The time series of HH total backscattering (σ_{HH}^{t}) (Fig. 6.4a) makes a hump in the middle of the year due to increase in NDVI value that ultimately increase the HH vegetation (σ_{HH}^{v}) and soil-vegetation backscattering (σ_{HH}^{sv}) components. However, this phenomenon is not visible with VV polarization (Fig. 6.4b). It mainly resulted from the surface-volume (soil-vegetation) interaction term that has the characteristics $\sigma_{HH}^{sv} > \sigma_{VV}^{sv}$. For this region the overall trend in σ_{HH}^{t} could be attributed to the trends in σ_{HH}^{v} and σ_{HH}^{sv} backscattering components. To corroborate the finding, the backscattering components were plotted with the 16 days composite NDVI values shown in Fig. 6.5. It is interesting to note that the average of σ_{HH}^{t} from the region entirely corresponds with the trend of average NDVI. At L-band, the cross polarization

HV backscattering (σ_{HV}^{t}) is almost negligible for the region (Fig. 6.4c). However, the expected increase in σ_{HV}^{t} with increase in vegetation is not observed for the region.

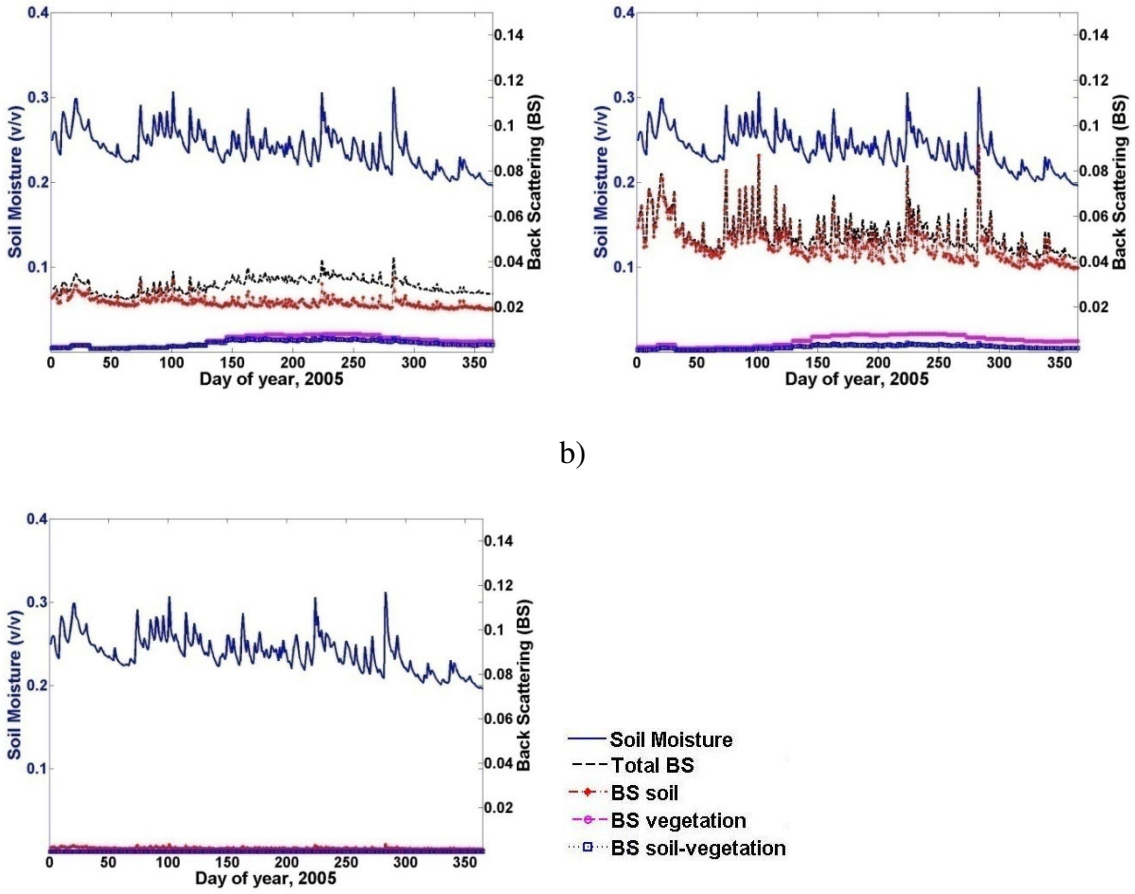

Figure 6.4. Mean soil moisture and mean backscattering components of the Northwestern Mountainous Region: a) at HH polarization, b) at VV polarization, and c) at HV polarization.

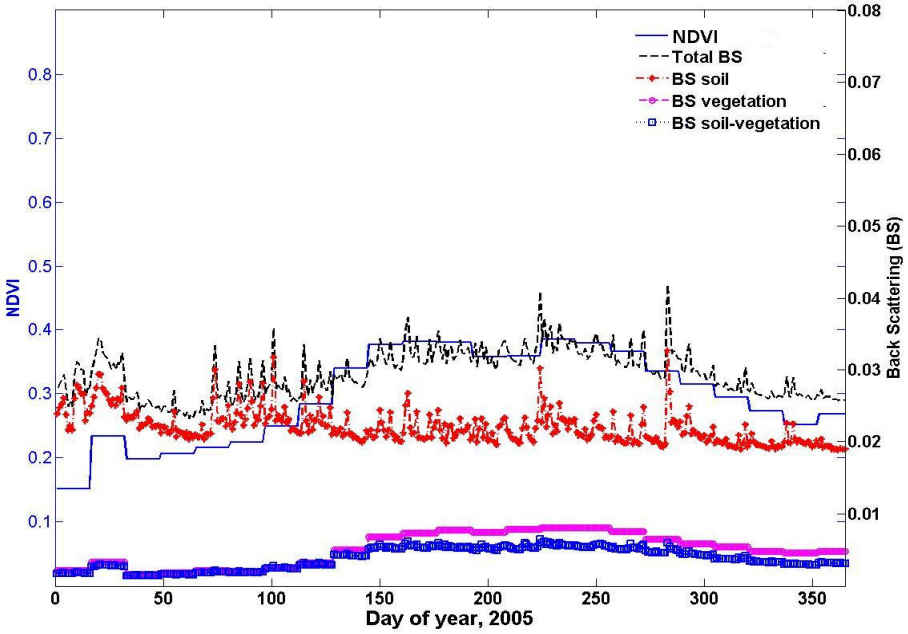

Figure 6.5. Mean NDVI and mean backscattering components of the Northwestern mountainous region at HH polarization.

Figure 6.6 highlights the uncertainty in terms of entropy associated with soil moisture and backscattering components for the Northwestern Mountainous Region. The consistently high entropy value for soil moisture evolution suggests more chaos in spatial organization of soil moisture (Fig 6.6a-b). The high entropy in soil moisture evolution for this region is attributed mostly to topographically-based distribution effects i.e., high elevation and steep mountain slopes result in high runoff/runon events. The difference in entropy values is distinct when the σ_{HH}^{S} and σ_{VV}^{S} components are compared. This property of σ_{VV}^{S} component having high entropy values is attributed to the higher sensitivity of σ_{VV}^{S} component to change in dielectric constant of soil medium with

respect to change in soil moisture. In contrast, high entropy is not visible in the σ_{HH}^{s} component (Fig. 6.6a). The entropy of σ_{HH}^{s} component for this region is relatively consistent for the whole study period. Another noticeable feature in Fig. 6.6a-b is the contribution of entropy of vegetation and soil-vegetation backscattering components in the overall response of HH/VV total backscattering ($\sigma_{HH}^{t}, \sigma_{VV}^{t}$) entropy. In case of HH polarization, the first harmonic of σ_{HH}^{t} entropy corresponds to the entropy of σ_{HH}^{v} and σ_{HH}^{sv} components, and the higher harmonic responds to the $\sigma_{\mathrm{HH}}^{\mathrm{s}}$ component. However, the entropy of σ_{VV}^{t} is almost unaffected by the entropy of σ_{VV}^{v} and σ_{VV}^{sv} component. The entropy of σ_{VV}^{t} only responds to the entropy of σ_{VV}^{s} component. This indicates that with sparse vegetation, the scattering in L-band at VV (σ_{VV}^{t}) polarization is dominated by the underlying surface and not by the vegetation and HH (σ_{HH}^{t}) polarization is influenced by the overlaying vegetation and the entropy of the HV backscattering (σ_{HV}^{t}) is insignificant (Fig. 6.6c). The mean plots in Fig. 6.4 shows the influence of the vegetation on total backscattering, but the entropy plot distinctly illustrates the effects in Fig. 6.6. The findings emphasize the dependence of σ_{HH}^{t} on vegetation (i.e., NDVI) as an important index for algorithm development for the high elevation mountainous region. However, in the actual radar backscattering form such mountainous region other factors that is not included in this study could also introduce uncertainty i.e., large variation of slope and aspect that creates a great variation of local incidence angles and illuminated area. It is assumed that the uncertainty due to variation of local incidence angles is a constant random error and could be ignored while interpreting the uncertainty due to system and geophysical parameters in trends of total radar backscattering for the region.

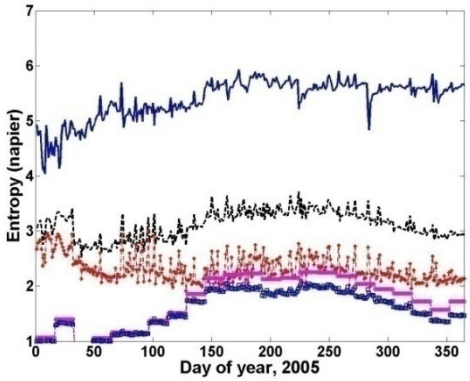

a)

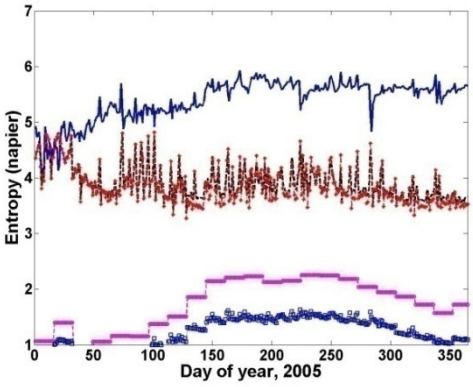

b)

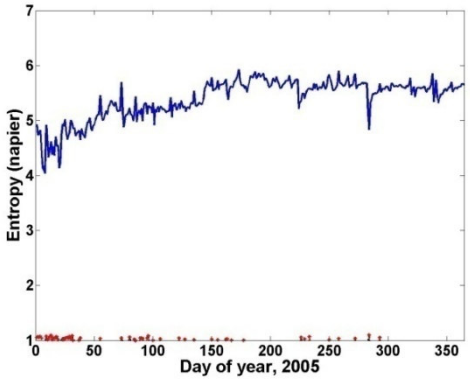

c)

Figure 6.6. Entropy of soil moisture and backscattering components of the Northwestern Mountainous Region: a) at HH polarization, b) at VV polarization, and c) at HV polarization.

Central Plains

The selection of the Central plains region is to analyze the effects of radar backscattering from the range and farm lands having rolling topography. As compared to the Northwestern mountainous region, the Central plains have a higher average NDVI

value throughout the year with slight increase in the summer months due to cropping, which is evident in Fig. 6.7. Favorable meteorological forcings and high soil moisture status promote high average NDVI for this region and resulting in a higher average evapotranspiration for the whole year. The meteorological forcings of this region is much more dynamic than the Northwestern mountainous region. The effect of evapotranspiration and dynamic forcings is conspicuous in highly variable soil moisture evolution (Fig. 6.8) that is induced by faster drydown. The region also maintains high average soil moisture values due to higher clay fractions found in the surface soil. All these geophysical attributes and state variables dynamics result in high radar backscattering components for the Central plains.

Even with high average NDVI value of this region, the σ_{VV}^{s} component is always higher and more sensitive to soil moisture evolution than the σ_{HH}^{s} component (Fig. 6.8a-b). The response to soil drydown is also better for σ_{VV}^{s} component. For this region, vegetation barely affects σ_{VV}^{t}, and σ_{VV}^{t} is dominated by σ_{VV}^{s} component (Fig. 6.8b). Like the Northwestern mountainous region, the σ_{HH}^{t} distinctly shows the contribution of σ_{HH}^{v} and σ_{HH}^{sv} component throughout the time series (Fig. 6.8a). The cross-polarization term HV (σ_{HV}^{t}) shows backscatter for this region, however, still insignificant in comparison to co-polarized HH/VV backscattering. The greater amount of σ_{HV}^{t} for the Central plains than that observed in the Northwestern mountainous region is also attributed to higher NDVI values (i.e., higher vegetation amount).

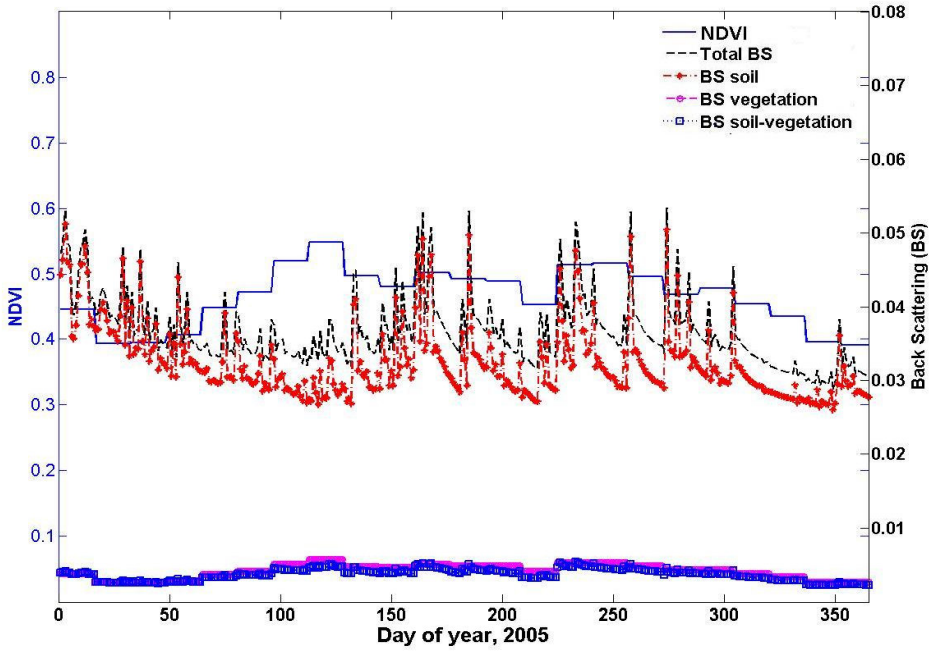

Figure 6.7. Mean NDVI and mean backscattering components of the Central Plains at HH polarization.

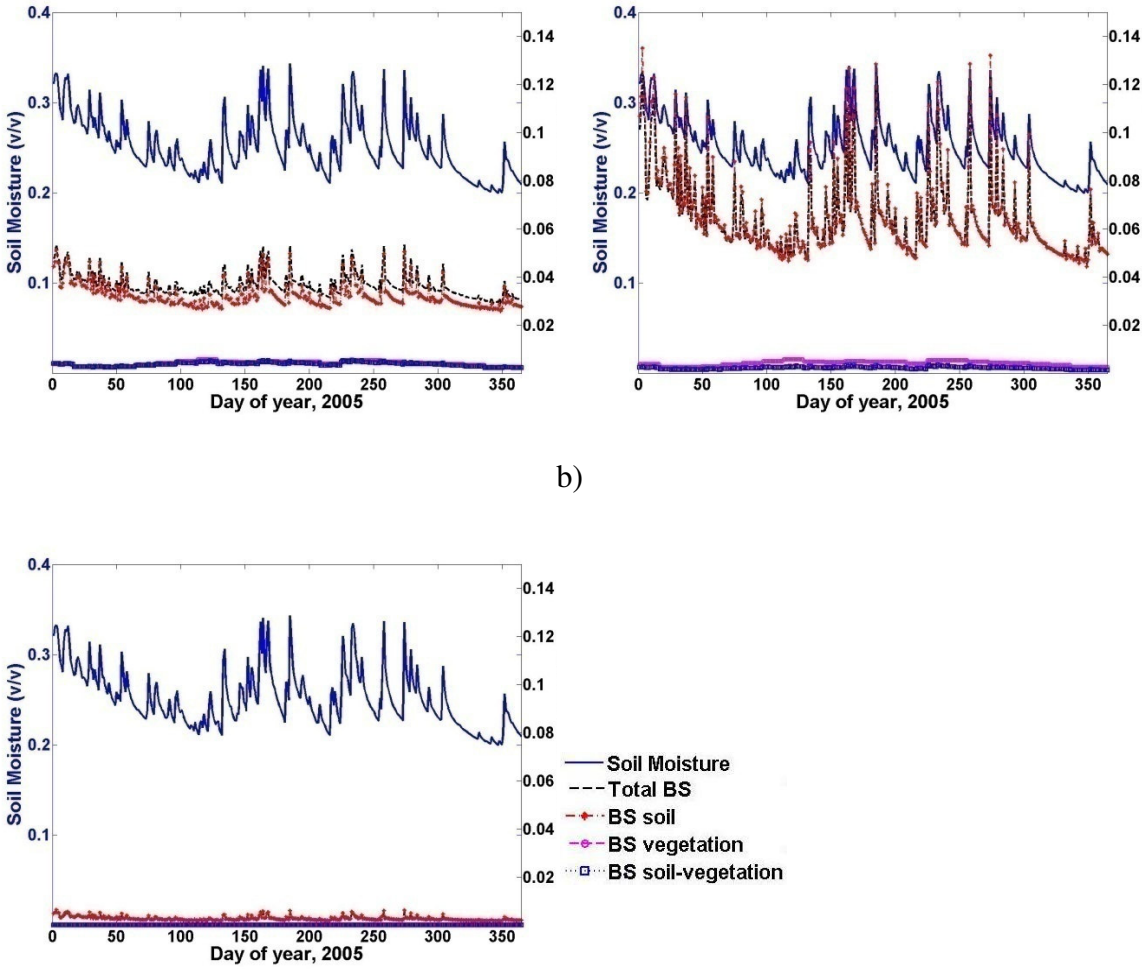

a) b)

c)

Figure 6.8. Mean soil moisture and backscattering components of the Central Plains: a) at HH polarization, b) at VV polarization, and c) at HV polarization.

The mean entropy of soil moisture (Fig. 6.9) shows high temporal variation which is typically observed due to uniform and widespread rainfall events that tends to saturate the soil surface and diminish the soil moisture variability. The entropy increases with natural drydown that is influenced by soil texture and crops of the region and this process is mainly prominent in the summer months. The entropy plots (Fig. 6.9a-b) of co-polarized HH/VV backscatter have a typical characteristic (i.e., the entropy of σ_{HH}^{s} and σ_{VV}^{s} is greater than the entropy of σ_{HH}^{t} and σ_{VV}^{t}) that was not observed in the Northwestern mountainous region. The reason behind this behavior in the Central plains region is the reduction in variability of σ_{HH}^{t} and σ_{VV}^{t} because volume backscattering by vegetation removes part of variability in σ_{HH}^{t} and σ_{VV}^{t} introduced by σ_{HH}^{s} and σ_{VV}^{s} components. Like the Northwestern mountainous region, the backscattering at HH polarization for this region captures more variability (high entropy) in σ_{HH}^{v} and σ_{HH}^{sv} components (Fig. 6.9a). The entropy of cross-polarization backscatter i.e., σ_{HV}^{t} also responds in this region, although they are very low and insignificant when compared to entropy of σ_{HH}^{t} and σ_{VV}^{t} (Fig. 6.9a-c).

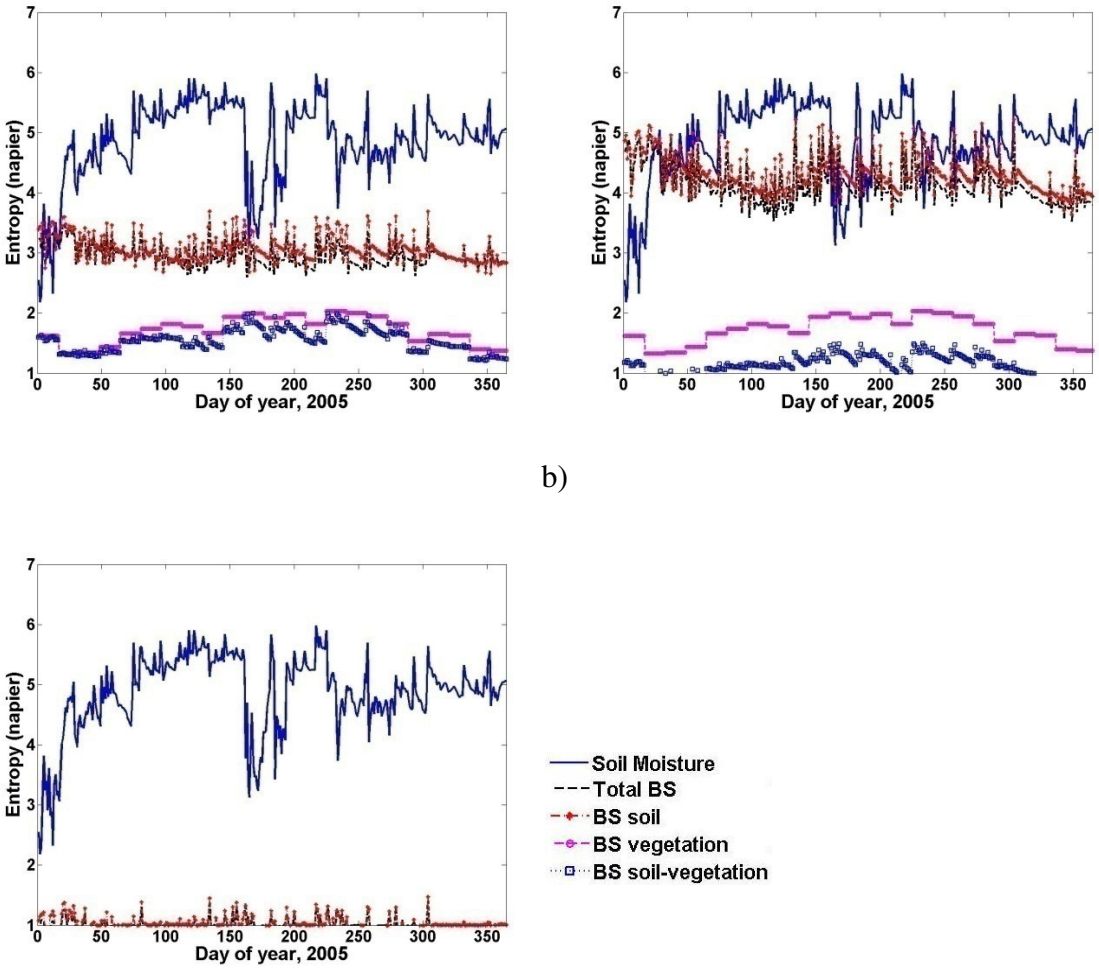

Figure 6.9. Entropy of soil moisture and backscattering components of the Central Plains: a) at HH polarization, b) at VV polarization, and c) at HV polarization.

Eastern Plains

This region was included in the study to assess the effects of high vegetation in L-band radar backscattering. The vegetation of this region is a mix of deciduous trees and croplands and has the highest average NDVI among the three study regions throughout the year (Fig. 6.10). The Eastern Plains resembles a typical low lying plain with little undulation and sandy soil texture on the land surface. The dense vegetation, sandy soil texture and dynamic forcings impart high evapotranspiration rates. Therefore, this region experiences highest surface soil moisture variability (Fig. 6.11), among the three study areas.

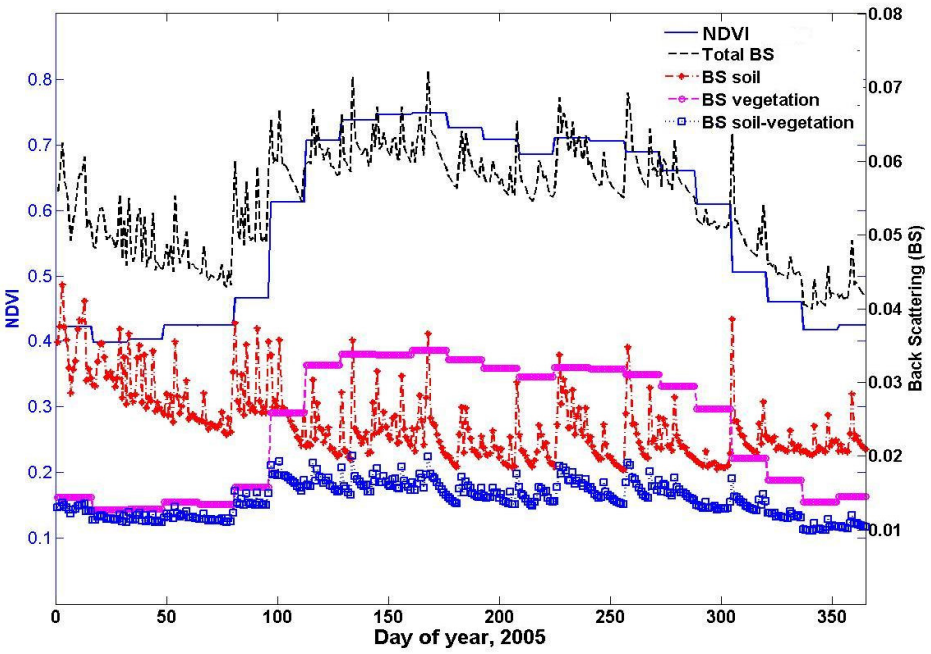

Figure 6.10. Mean NDVI and mean backscattering components of the Eastern Plains at HH polarization.

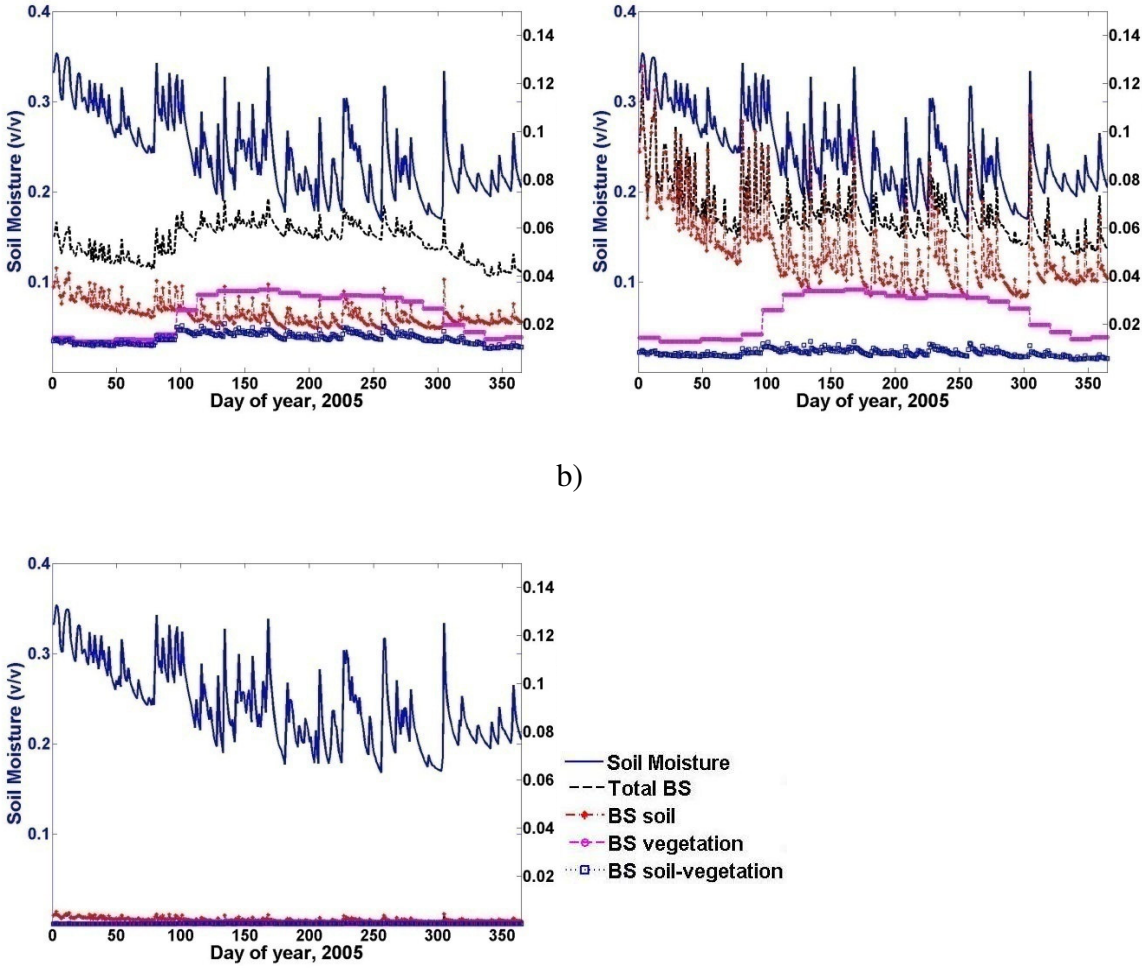

a) b)

c)

Figure 6.11. Mean soil moisture and backscattering components of the Eastern Plains: a) at HH polarization, b) at VV polarization, and c) at HV polarization.

Dense vegetation of this region contributes few special characteristics in HH/VV backscattering components. For most part of the year (especially spring and summer), the σ_{HH}^{v} component dominates the σ_{HH}^{s} (Fig. 6.11a), except on very wet days that leads to higher backscattering from σ_{HH}^{s}. Owing to dense vegetation, considerable amount of σ_{HH}^{sv} component is also observed (Fig. 6.11a). Furthermore, quite high backscattering form σ_{VV}^{v} polarization is also discovered (Fig. 6.11b). A notable exception for the Eastern Plains as compared to the observations in the other two regions is its higher vegetation backscattering for σ_{VV}^{v} than for σ_{HH}^{v} component (Fig. 6.11a-b). During spring and summer, the region experience an almost equal σ_{HH}^{t} and σ_{VV}^{t}, while it is not observed in the Central plains and the Northwestern mountainous region (Fig. 6.4a-b, Fig. 6.8a-b, Fig. 6.11a-b). This may be attributed to very rough surface features due to high vegetation. This increased roughness results in high volume scattering and tends to equalize σ_{HH}^{t} and σ_{VV}^{t} components. Similar findings are reported in other studies (e.g., [Dubois, et al., 1995], [Ulaby, et al., 1996]), and also demonstrated by geometrical optics and integral equation models. It is also evident from Fig. 6.11b that on dry days σ_{VV}^{v} polarization is nearly equal to backscattering from σ_{VV}^{s}.

As expected, the entropy of soil moisture is much higher than the backscattering components. A high variation in the entropy value of soil moisture indicates chaotic spatial organization influenced by precipitation and high evapotranspiration rate (Fig. 6.12). The entropy in Fig. 6.12a-b shows less temporal variability for total backscattering, as well as for soil, vegetation and soil-vegetation interaction components. Unlike the other two regions, the entropy of σ_{HH}^{v} component that is influenced by the diverse vegetation pattern is higher than entropy of other backscattering components (Fig. 6.12a). The predominant effect of vegetation also renders high entropy in σ_{HH}^{sv} and in fact has greater entropy than the entropy of σ_{HH}^{s}, except on very wet days. So, it is apparent that for high vegetation (high NDVI) the entropy of $\sigma_{\mathrm{HH}}^{\mathrm{t}}$ is primarily described by the entropy of σ_{HH}^{v} and σ_{HH}^{sv} components. However, the region lacks similar predominant effect of vegetation on entropy of $\sigma_{\mathrm{VV}}^{\mathrm{t}}$ (Fig. 6.12b). The backscattering from σ_{VV}^{s} component has a major contribution in characterizing the σ_{VV}^{t}, as it is clear from the entropy of σ_{VV}^{s} and σ_{VV}^{t} (Fig. 6.12b). The entropy of σ_{VV}^{v} is also quite significant that is normally not seen in other study region. The impact of high roughness in the region is also witnessed, due to almost equal entropy of σ_{HH}^{t} and σ_{VV}^{t}.

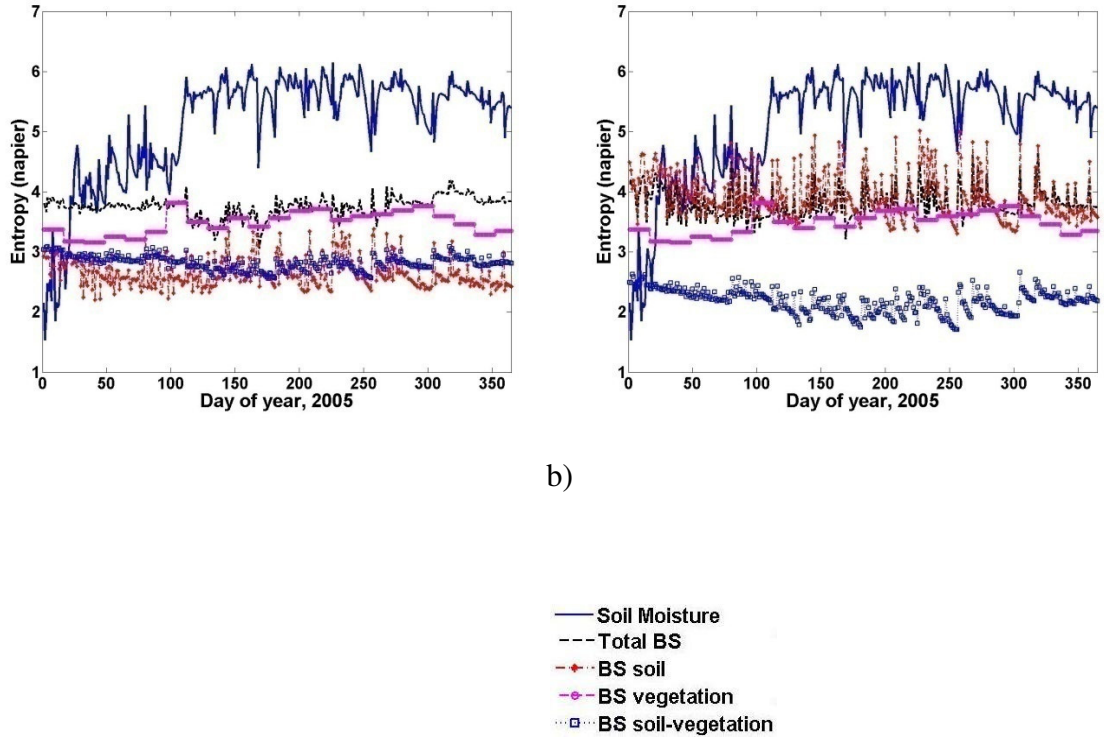

Figure 6.12. Entropy of soil moisture and backscattering components of the Eastern Plains: a) at HH polarization, b) at VV polarization, and c) at HV polarization.

Estimation of Surface Roughness and Volume Scattering

From the aforementioned results and discussions it is obvious that the total radar backscattering is a complex summation of individual backscattering components and is greatly affected by soil moisture, geophysical, and other system parameters. The new algorithm proposed here (Section 4) exploits the summation of radar backscattering components for determining certain geophysical parameters. Especially, the HH

polarization is used to evaluate surface roughness. As discussed in the above sections, the L-band HH polarization (σ_{HH}^{t}) is most sensitive to the presence of vegetation which influence the overall roughness characteristics. The algorithm uses the synthetic σ_{HH}^{t}, surface average soil moisture (~5 cm), soil temperature and precipitation data to estimate the surface roughness and vegetation backscattering. The assumptions and stochasticity in the algorithm introduce uncertainty in derived surface roughness estimates. The derived values of surface roughness depend on the inter-storm period, dielectric model and the assumption of static vegetation within the inter-storm period. In the study region, the validity of assumptions stands a better likelihood during spring and summer months, where the inter-storm periods are small. The smaller inter-storm period can capture the dynamics of variable surface roughness. However, for extended inter-storm events, the cumulative errors of algorithm assumptions (static vegetation within the inter-storm) and errors in the model and data may lead to an inferior estimate of surface roughness. For the Northwestern mountainous region, a randomly selected pixel, Fig. 6.13 shows the derived surface roughness and vegetation backscattering components. The result shows that the surface roughness from the algorithm is very similar to the values used in calculating the synthetic radar backscattering data. The surface roughness exhibits variability during spring and summer months, and are more reliable estimate due to shorter interstrom period. The algorithm-estimated vegetation backscattering component shows consistency with respect to derived surface roughness, sparse vegetation and soil backscattering component for the pixel. However, the derived vegetation backscattering parameter shows nearly 25% absolute errors, when compared to synthetic data for the

particular pixel. Similarly, other randomly selected pixels show absolute error ranging 20-30%. The errors in estimated vegetation backscattering are expected and are within - reasonable limits considering the simplified assumptions used in the algorithm. Figure 6.14 illustrate a randomly selected pixel from the Central plain region that exhibits typical characteristics of the surface roughness variability. Less variability and consistency in surface roughness parameter is found in the Central plain that also agrees with the existing ground conditions. The average surface roughness is slightly overestimated by 10%, when compared to the value used for calculating the synthetic data. The estimated vegetation backscattering for the pixel has nearly 31% absolute error. For the region, the absolute errors for estimated vegetation backscattering range from 23-36%. Similarly, Fig. 6.15 shows a randomly selected pixel in the Eastern plains. The maximum surface roughness is observed for the Eastern plains are consistent to the presence of dense vegetation that imparts to this attribute. However, the surface roughness is overestimated by nearly 20%. For the Eastern plains, an absolute error ranging between 25% and 35% is obtained for estimated vegetation backscattering. The algorithm performed reasonably well in approximating surface roughness of the study areas. In case of estimation of vegetation backscattering, the algorithm produced considerable errors. The major portion of errors in vegetation backscattering is the consequence of the mismatch of inter-storm period and NDVI 16 days composite data. However, with the future availability of satellite-based radar data at L-band, the problem of high error in vegetation backscattering is expected to reduce significantly by including the co-registered remote sensing of vegetation water content in the algorithm.

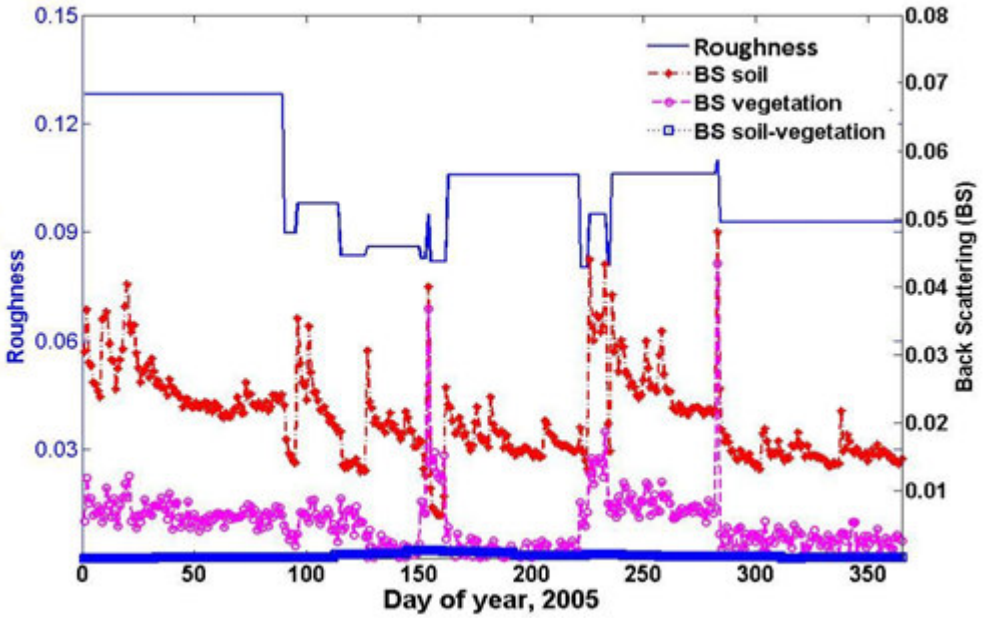

Figure 6.13. Algorithm based surface roughness and combined vegetation backscattering of the Northwestern Mountainous Region at HH polarization.

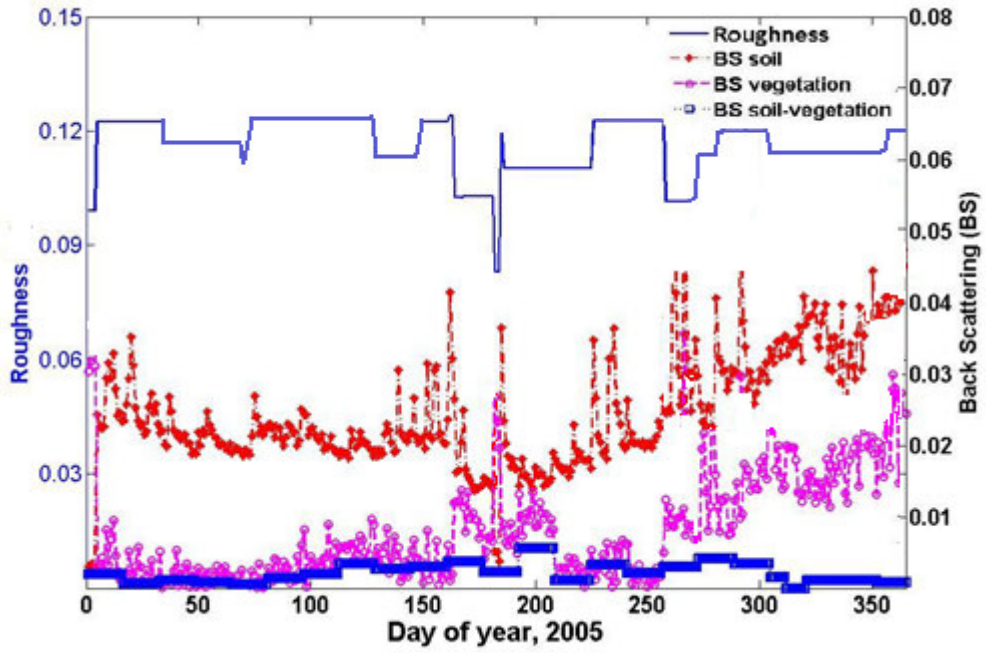

Figure 6.14. Algorithm based surface roughness and combined vegetation backscattering of the Central Plains at HH polarization.

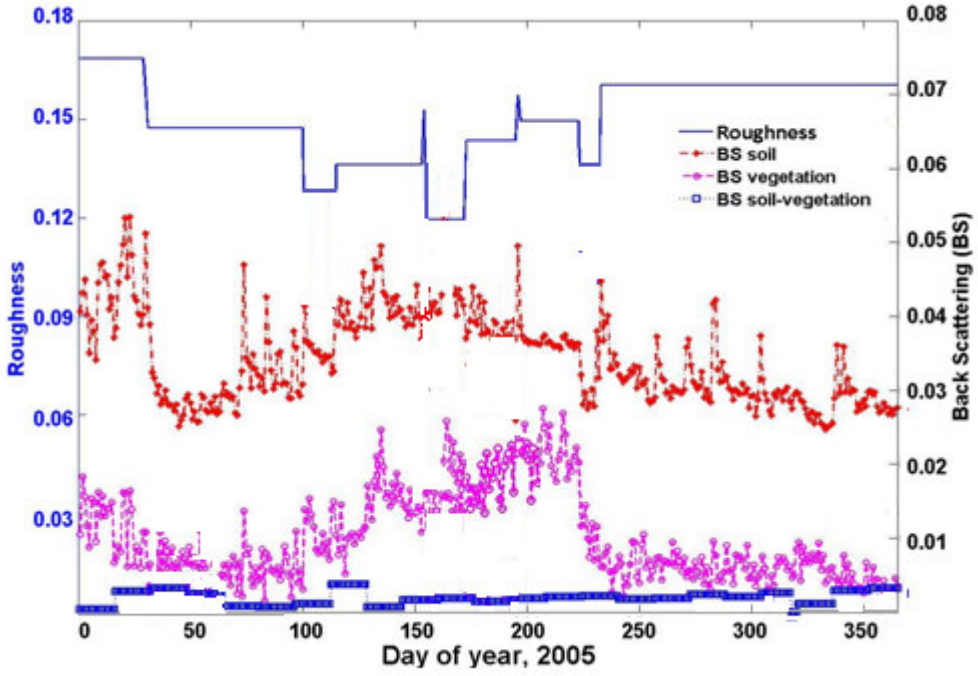

Figure 6.15. Algorithm based surface roughness and combined vegetation backscattering of the Eastern Plains at HH polarization.

6.9. Conclusion

In preparation for the upcoming soil moisture active passive (SMAP) mission our study focuses to characterize the L-band radar backscattering under different topography, meteorological conditions, and vegetation densities. Three regions in the Red Arkansas river basin were selected based on the attributes of topography and vegetation. Synthetic backscattering data with appropriate uncertainties were evaluated for the three regions and subjected to entropy-based characterization. Spatial averages at daily time step indicates important dynamics of total and individual radar backscattering components. Especially, the responses at HH and VV polarizations were investigated. Generally, the VV polarization of radar backscattering was found to be most sensitive to soil moisture status, whereas the HH polarization was most sensitive to vegetation status.

The mountainous region showed that with sparse vegetation, the scattering in L-band at VV (σ_{VV}^{t}) polarization is dominated by the underlying surface and not by the vegetation and HH (σ_{HH}^{t}) polarization is influenced by the overlaying vegetation, and the HV backscattering (σ_{HV}^{t}) is insignificant. For this region overall trend in σ_{HH}^{t} could be attributed to the trends in σ_{HH}^{v} and σ_{HH}^{sv} components. As expected, σ_{VV}^{t} is always greater than σ_{HH}^{t}.

The Central plains with moderate vegetation indicated that volume backscattering by vegetation removes part of the variability in HH/VV total backscattering ($\sigma_{HH}^{t}, \sigma_{VV}^{t}$) introduced by HH/VV soil backscattering component ($\sigma_{HH}^{s}, \sigma_{VV}^{s}$). The vegetation barely affects σ_{VV}^{t}, and σ_{VV}^{t} is dominated by σ_{VV}^{s}. The σ_{HH}^{t} polarization distinctly shows the

contribution of σ_{HH}^{v} and σ_{HH}^{sv} components. The region also experiences higher backscattering at σ_{VV}^{t} polarization as compared to σ_{HH}^{t}.

The Eastern plains with dense vegetation that imparts high roughness in the region witnessed almost equal σ_{HH}^{t} and σ_{VV}^{t} in magnitude. Unlike other regions, the σ_{HH}^{v} component is influenced by the diverse and dense vegetation pattern and is higher than the σ_{HH}^{s} component. Most of the variability in the σ_{HH}^{t} is captured by the σ_{HH}^{v} and σ_{HH}^{sv} components.

An algorithm using SVAT model and radar backscattering data is presented to derive stochastic surface-roughness and volume scattering by vegetation. The results were promising for estimation of surface-roughness. However, further studies and realistic radar data is required to reduce the errors in estimation of vegetation volume backscattering. The work advances our understanding in active microwave remote sensing of soil moisture with region specific characterizations of backscattering components. The entropy-based characterization scheme of backscattering dynamics for variety of soil, topographic and vegetation conditions will help improve the radar-based soil moisture retrieval for upcoming NASA SMAP mission.

CHAPTER VII

GENERAL CONCLUSION

Most of the research mentioned in Chapters II-VI pertaining characterization of soil physical parameters and hydrologic modeling for accurate soil moisture estimation is directed towards contributing to the understanding of soil moisture dynamics within and beyond the satellite footprint. Keeping in perspective the upcoming satellite missions (e.g., SMAP mission of NASA) for soil moisture remote sensing, new upscaling, downscaling, and data assimilation algorithm based on geophysical parameters for soil moisture spatial evolution are developed in these studies and the effectiveness is successfully demonstrated. Studies conducted in Chapters II-IV show the potential to quantify the subpixel variability and spatial evolution of soil moisture in different hydroclimatic regions. The physical controls of soil moisture spatial evolution are also identified. Results from studies conducted in semiarid hydroclimatic conditions of the Arizona region suggested soil texture as a primary physical control for surface and root zone soil moisture. However, the agricultural and grassland/rangeland landscapes of the Iowa and the Oklahoma regions, respectively, indicate that a complex combination of vegetation, precipitation pattern and soil texture dictates the surface soil moisture evolution across the spatial scales.

Effective application of soil moisture modeling with appropriate boundary conditions and modeling framework at field- to satellite footprint-scale that estimates stochastic soil hydraulic properties, surface feature attributes, and the radar

backscattering is also demonstrated. The new algorithm in Chapter V performed satisfactorily to characterize the saturated hydraulic conductivity at the field-scale. The algorithm developed in Chapter VI for characterization of surface features i.e., surface roughness and surface/volume backscattering is also achieved with reasonable success.

The future satellite mission, especially SMAP, will provide unique opportunity in form of regional-/global-scale data at varying resolutions to study the spatio-temporal scaling effect, hydrologic modeling, and data assimilation important for state variable and fluxes i.e., soil moisture and evapotranspiration. The technique developed in these studies may help unravel soil moisture spatio-temporal patterns, statistical characteristics, and spatial scaling issues in a variety of hydroclimatic conditions.

CHAPTER VIII

LIMITATIONS IN THE STUDIES AND RECOMMENDATIONS FOR FUTURE RESEARCH

The studies mentioned in this dissertation to estimate soil moisture at various spatial scales depend mostly on the data quality, and the hydrologic model parameters and structure. Assumptions, errors and uncertainties involved in the data, and the model parameter and structure directly impact on the output soil moisture estimates and their efficacy in subsequent applications. The implications of the data and the model in this dissertation are discussed hereafter.

Mostly, remote sensing data are used in the studies. The quality of remote sensing data largely relies on retrieval algorithm, systematic errors, and natural randomness/uncertainties involved in it. A basic assumption in the studies is also that the remote sensing data are representative of state/forcings at a specific spatial resolution. If the assumption is reasonably valid, then the data errors/uncertainties involved in soil moisture modeling are propagated forward in time and also degrade the model parameters. To some extent, the errors and uncertainties in remotely sensed soil moisture data are handled through data assimilation techniques. However, with the forcings data (e.g., rainfall, air temperature, and relative humidity) that bears a significant impact on soil moisture evolution, no such effort is made in the studies to improve the quality of forcings data by removing errors and uncertainties. So, a caveat for these studies is that the quality of forcings may have influenced the interpretation of results. Another aspect

of data needs special remark i.e., the satellite-based remotely sensed soil moisture measurements provide a snapshot at particular time on a daily basis and do not capture any information of subdaily soil moisture dynamics. As the model output are based on the average values of daily forcings; incorporating such remotely sensed daily snapshot into data assimilation may also lead to inferior soil moisture estimates. Uncertainties in geophysical data (e.g., soil, DEM, and vegetation) at coarse spatial resolution are other factors that introduces errors in the physical processes (i.e, infiltration, runon/runoff, and evapotranspiration), ultimately, affecting the reliability of outputs from the model.

The difficulties of obtaining unique and conceptually realistic parameter values have posed many challenges to hydrological modeling community for decades. The research conducted for this dissertation is also not immune to this aspect. Therefore, the model parameters uncertainties are another realm in these studies that warrant special attention. The effectiveness of a model to describe the states or outputs is constraint within the parameter domain. For the studies, the model parameters, which are difficult to measure or for which there are insufficient measurements, physical constraints, literature review, and past experience with the model, allowed to estimate the best and probable range of parameter values (e.g., van Genuchten soil parameters). Stochastic approaches are also implemented to describe the model parameters for these studies. The model parameters from a multivariate normal distribution whose mean and covariance are determined during the stochastic optimization techniques. On occasions, the limitations of parameters that affect the output states are especially encountered in semiarid regions. For example, the residual water contents are higher than the in-situ or

remotely sensed soil moisture. For all the studies, an ensemble of model parameter (i.e., soil hydraulic parameters) is used to make it more representative and capture the variability present within a specific spatial scale.

Model-structure is another grey area that is discussed here to highlight the implications of estimating soil moisture at varying scales. Model-structure uncertainty stem from the inability to truly represent the physical processes occurring on soil surface and in soil profile. The uncertainties introduced by the approximations used in the model affect the prediction of infiltration, runoff, and evapotranspiration that ultimately influence the soil moisture evolution. The model uses Richard's equation as the governing equation for the transport of soil moisture through the soil profile. However, the efficacy of Richard's equation is questioned at large spatial scale. Two approaches are normally used to overcome the shortcoming of implementing Richard's equation at large spatial scale. The first is through upscaling the Richard's equation (e.g., [*Mantoglou*, 1992]), and the second is by using scaled parameters (e.g., [*Ines and Mohanty*, 2008]). The studies in this dissertation use the second approach. Other forms of governing equations to model the transport of soil moisture through the soil profile are not used in the studies. A model averaging technique that uses various modeling concept and governing equation is recommended for future research use. The advantage of such technique is to compensate the limitations and drawbacks of a particular model by the strengths of other hydrologic models. The modeling framework used in these studies also requires special attention. A pseudo-3D framework is formulated that comprises 1D SVAT model for all the cell blocks and is connected overland. The

hypothesis is that the resultant flow of soil moisture is vertical in the top soil layer at coarse spatial scale. However, subsurface lateral transport of soil moisture induced by topography is expected among adjoining cell, especially, during wet conditions. This part is ignored in the studies that may lead to inferior soil moisture estimate during wet conditions.

Another important aspect that is completely overlooked in these studies is the effect of soil temperature on the movement of soil moisture. Soil temperature varies in response to change in the radiant, thermal, and latent heat exchange processes which take place primarily through the soil surface, therefore, influence the spatial evolution of surface soil moisture. The research mentioned in Chapters II-VI greatly depends on spatial evolution of surface soil moisture. This imposes another limitation on soil moisture outputs from the studies.

With the experience and insight gained from the studies, the following perspectives are recommended for future research:

- A 3D modeling framework is recommended to thoroughly simulate the spatio-temporal evolution of soil moisture. The significance of 3D hydrologic modeling also enhances with increase in resolution.
- Markov Chain Monte Carlo (MCMC) optimization technique is used in the studies to obtain optimal solution for model parameters. Optimization techniques (e.g., genetic algorithm, simulated annealing, stochastic tunneling, and particle swarm) other than MCMC could also be explored. It is recommended to use a technique that is closest to global optimization.

- Instead of using one SVAT model for simulating spatio-temporal evolution of soil moisture, a suite of models with Bayesian model averaging is recommended. This will boost the credibility by providing diverse modeling approaches.
- It is recommended to use subdaily time step in soil moisture simulation. This will capture diurnal soil moisture dynamics, and the data assimilation operation will be effective because of better temporal match between subdaily simulation output and remote sensing snapshot.
- To understand the influence and physical controls of geophysical parameter (i.e., soil, vegetation, DEM, and precipitation) on soil moisture spatial evolution, it is suggested to derive spatially continuous soil moisture at higher resolution (< 4 km resolution used Chapter 4).
- The studies in the dissertation use parameter upscaling to model soil moisture at varying spatial scales. For further studies, it is recommended to explore upscaling of the governing equations and compare with the parameter upscaling.

REFERENCES

Azevedo, A. S., R. S. Kanwar, and R. Horton (1998), Effect of cultivation on hydraulic properties of an Iowa soil using tension infiltrometers, *Soil Sci*, *163*, 22-29.

Baghdadi, N., M. Aubert, O. Cerdan, L. Franchistéguy, C. Viel, E. Martin, M. Zribi, and J. F. Desprats (2007), Operational mapping of soil moisture using synthetic aperture radar data: application to the touch basin (France), *Sensors*, *7*, 2458-2483.

Baghdadi, N., C. King, and J. P. Wingneron (2002), An empirical calibration of IEM model based on SAR data and measurement of soil moisture and surface roughness over bare soils, *International Journal of Remote Sensing*, *23*, 4325-4340.

Bindlish, R., T. J. Jackson, A. J. Gasiewski, M. Klein, and E. G. Njoku (2005), Soil moisture mapping and AMSR-E validation using the PSR in SMEX02, *Remote Sensing of Environment*, *103*, 127-139.

Bindlish, R., T. J. Jackson, A. Gasiewski, B. Stankov, M. Klein, M. H. Cosh, I. Mladenova, C. Watts, E. Vivoni, V. Lakshmi, and T. Keefer (2006a), Aircraft based soil moisture retrievals under mixed vegetation and topographic conditions, *Remote Sensing of Environment*, *112*, 375-390.

Bindlish, R., T. J. Jackson, A. J. Gasiewski, M. Klein, and E. G. Njoku (2006b), Soil moisture mapping and AMSR-E validation using the PSR in SMEX02, *Remote Sensing of Environment*, *103*, 127-139.

Bouma, J. (1980), Field measurement of soil hydraulic properties characterizing water movement through swelling clay soils, *J. Hydrol.*, *45*, 149-158.

Brooks, S. P., and G. O. Roberts (1998), Convergence assessment techniques for Markov chain Monte Carlo, *Stat Comput*, *8*, 319-335.

Burgers, G., P. J. van Leeuwen, and G. Evensen (1998), Analysis scheme in the ensemble Kalman filter, *Monthly Weather Review*, *126*, 1719-1724.

Burke, E. J., R. J. Gurney, L. P. Simmonds, and T. J. Jackson (1997), Calibrating a soil water and energy budget model with remotely sensed data to obtain quantitative information about the soil, *Water Resources Research*, *33*, 1689-1697.

Camillo, P. J., P. E. O'Neill, and R. J. Gurney (1986), Estimating soil hydraulic parameters using passive microwave data, *IEEE Transactions on Geoscience and Remote Sensing*, *GE-24*, 930-936.

Carsel, F. C., and R. S. Parrish (1988), Developing joint probability distributions of soil water retension characteristics, *Water Resources Research*, *24*, 755-769.

Celia, M. A., and E. T. Bouloutas (1990), A general mass-conservative numerical solution for the unsaturated flow equation, *Water Resources Research*, *26*, 1483-1496.

Chang, D. H., and S. Islam (2003), Effects of Topography, Soil properties and mean soil moisture on the spatial distribution of soil moisture: *A Stochastic Analysis, in Scaling Methods in Soil Physics*, edited by Y. Pachepsky, et al., pp. 193-225, CRC Press, Boca Raton, FL.

Choudhury, B. J., T. J. Schmugge, A. Chang, and R. W. Newton (1979), Effect of surface roughness on the microwave emission from soils, *J. Geophys.*, *84*, 5699-5706.

Claussen, M. (1998), On multiple solutions of the atmosphere-vegetation system in present-day climate, *Global Change Biol.*, *4*, 549-559

Coutadeur, C., Y. Coquet, and J. Roger-Estrade (2002), Variation of hydraulic conductivity in a tilled soil, *Europ. J. Soil Sci.*, *53*, 619-628.

Crosson, W. L., C. A. Laymon, R. Inguva, and M. P. Schamschula (2002), Assimilating remote sensing data in a surface flux-soil moisture model, *Hydrological Processes*, *16*, 1645-1662.

Crow, W. T., R. Bindlish, and T. J. Jackson (2005), The added value of spaceborne passive microwave soil moisture retrievals for forecasting rainfall-runoff partitioning, *Geophysical Research Letters*, *32*, doi:10.1029/2005GL023543.

Crow, W. T., and E. F. Wood (2003), The assimilation of remotely sensed soil brightness temperature imagery into a land surface model using Ensemble Kalman filtering: a case study based on ESTAR measurements during SGP97, *Adv Water Resour*, *26*, 137-149.

Crow, W. T., and E. F. Wood (1999), Multi-scale dynamics of soil moisture variability observed during SGP'97, *Geophysical Research Letters*, *26*, 3485-3488.

Cushman, J. H. (1990), An introduction of hierarchical porous media, in *Dynamics of Fluids in Hierarchical Media*, edited by J. H. Cushman, pp. 1-6, Academic Press, San Diego, CA.

Das, N. N., and B. P. Mohanty (2006), Root zone soil moisture assessment using remote sensing and vadose zone modeling, *Vadose Zone Journal*, *5*, 296-307.

Das, N. N., and B. P. Mohanty (2008), Temporal dynamics of PSR-based soil moisture across spatial scales in an agricultural landscape during SMEX02: a wavelet approach, *Remote Sensing of Environment*, 112, 522-534.

Das, N. N., B. P. Mohanty, M. H. Cosh, and T. J. Jackson (2008a), Modeling and assimilation of root zone soil moisture using remote sensing observations in Walnut Gulch Watershed during SMEX04, *Remote Sensing of Environment*, *112*, 415-429.

Das, N. N., B. P. Mohanty, and E. G. Njoku (2008b), An MCMC algorithm for upscaled SVAT modeling to evaluate satellite-based soil moisture measurements, *Water Resources Research*, *44*, W05416, doi:10.1029/2007WR006472.

Das, N. N., B. P. Mohanty, and E. G. Njoku (2008c), Statistics and probability density functions of soil moisture across large spatial scales. Submitted, under review, *Remote Sensing of Environment*.

daSilva, A. P., A. Nadler, and B. D. Kay (2001), Factors contributing to temporal stability in spatial patterns of water content in the tillage zone, *Soil Tillage Res.*, *58*, 207-218.

Delworth, T., and S. Manabe (1989), The influence of soil wetness on near-surface atmospheric variability, *J. Clim.*, *2*, 1447-1462.

Demarty, J., C. Ottlé, I. Barud, A. Olioso, J. P. Frangi, H. V. Gupta, and L. A. Bastidas (2005), Constraining a physically based Soil-Vegetation-Atmosphere Transfer

model with surface water content and thermal infrared brightness temperature measurements using a multi-objective approach, *Water Resources Research*, *41* W01010 10.1029/2004WR003275.

Dingman, S. L. (1994), *Physical Hydrology*, Macmillian, New York.

Dobson, M. C., and F. T. Ulaby (1986), Active microwave soil moisture research, *IEEE Transactions on Geoscience and Remote Sensing*, *GE-24*, 23–36.

Dobson, M. C., F. T. Ulaby, M. T. Hallikainen, and M. A. El-Rayes (1985), Microwave dielectric behavior of wet soil - part II: dielectric mixing models, *IEEE Transactions on Geoscience and Remote Sensing*, *GE-23*, 35-46.

Dubayah, R., E. F. Wood, and D. Lavallee (1997), Multiscaling analysis in distributed modeling and remote sensing: an application using soil moisture, in *Scale in Remote Sensing and GIS*, edited by D. A. Quatrocchi and M. Goodchild, pp. 93-112, Lewis Publishers, NewYork.

Dubois, P. C., J. Vanzyl, and T. Engman (1995), Measuring soil-moisture with imaging radars, *IEEE Transactions on Geoscience and Remote Sensing*, *33*, 915-926.

Dunne, S., and D. Entekhabi (2005), An ensemble-based reanalysis approach to land data assimilation, *Water Resources Research*, *41*, 10.1029/2004.

Engman, E. T. (1991), Applications of microwave remote-sensing of soil-moisture for water-resources and agriculture, *Remote Sensing of Environment*, *35*, 213-226.

Engman, E. T. (1995), Recent advances in remote-sensing in hydrology, *Reviews of Geophysics*, *33*, 967-975.

Engman, E. T., and R. J. Gurney (1991), *Remote Sensing in Hydrology*, Chapman and Hall, London, UK.

Entekhabi, D., H. Nakamura, and E. G. Njoku (1994), Solving the inverse problems for soil-moisture and temperature profiles by sequential assimilation of multifrequency remotely-sensed observations, *IEEE Transactions on Geoscience and Remote Sensing*, *32*, 438-448.

Evensen, G. (2003), The ensemble Kalman filter: Theoretical formulation and practical implementation, *Ocean Dynamics*, *53*, 343-367.

Famiglietti, J. S., J. W. Rudnicki, and M. Rodell (1998), Variability in surface moisture content along a hillslope transect: Rattlesnake Hill, Texas, *J. Hydrol.*, *92*, 210, 259.

Famiglietti, J. S., J. A. Devereux, C. A. Laymon, T. Tsegaye, P. R. Houser, T. J. Jackson, S. T. Graham, and M. Rodell (1999), Ground-based investigation of soil moisture variability within remote sensing footprints during the Southern Great Plains 1997 (SGP97) Hydrology Experiment, *Water Resources Research*, *35*, 1839-1851.

Feddes, R. A., P. J. Kowalik, and H. Zaradny (1978), *Simulation of Field Water Use and Crop Yeild*, John Wiley and Sons, New York.

Foley, J. A. (1994), The sensitivity of the terrestrial biosphere to climate change: A simulation of the middle Holocene, *Global Biogeochem. Cycles*, *8*, 505-525.

Fung, A. K., Z. Li, and K. S. Chen (1992), Backscattering from a randomly rough dielectric surface, *IEEE Transactions on Geoscience and Remote Sensing*, *30*, 356-369.

Gelman, A., J. B. Carlin, H. S. Stern, and D. B. Rubin (1995), *Bayesian Data Analysis*, CRC Press, Boca Raton, FL.

Georgakakos, K. P. (1996), Special issue - soil moisture theories and observations - preface, *J. Hydrol.*, *184*, 1-2.

Geweke, J. (1992), Evalutating the Accuracy of Sampling-based Approaches to the Calculation of Posterior Moments., Oxford University press, Oxford.

Gupta, R. K., R. P. Rudra, W. T. Dickinson, N. K. Patni, and G. J. Wall (1993), Comparison of saturated hydraulic conductivity measured by various field methods, *Trans. ASAE*, *36*, 51-55.

Gupta, R. K., R. P. Rudra, W. T. Dickinson, and G. J. Wall (1992), Stochastic analysis of groundwater levels in a temperate climate. , *Trans. Am. Soc. Agric. Engrs.*, *35*, 1167-1172.

Gupta, V., and E. Waymire (1990), Multiscaling properties of spatial rainfall and river flow distribution, *Journal of Geophysical Research*, *95*, 1999-2009.

Haar, A. (1910), Zur theorie der othogonalen funktionensysteme, Math. Ann, *69*, 331-371.

Haider, S. S., S. Said, U. C. Kothyari, and M. K. Arora (2004), Soil moisture estimation using ERS 2 SAR data: a case study in the Solani River catchment, *Hydrological Sciences*, *49*, 323-334.

Hawley, M. E., T. J. Jackson, and R. H. McCuen (1983), Surface soil moisture variation on small agricultural watershed, *J. Hydrol.*, *62*, 179-187.

Hillel, D. (1980), Measurement of unsaturated hydraulic conductivity of soil profile in situ in *Internal Drainage Methods*, pp. 213-220, Academic Press, New York.

Hills, R. G., D. B. Hudson, and P. J. Wierenga (1992), Spatial variability at the Las Cruces trench site in *Proc. International Workshop on Indirect Methods for Estimating the Hydraulic Properties of Unsaturated Soils*, pp. 529-538, University of Califorina, Riverside.

Houser, P. R., W. J. Shuttleworth, J. S. Famiglietti, H. V. Gupta, K. H. Syed, and D. C. Goodrich (1998), Integration of soil moisture remote sensing and hydrologic modeling using data assimilation, *Water Resources Research*, *34*, 3405-3420.

Houtekamer, P. L., and H. L. Mitchell (1998), Data assimilation using an ensemble Kalman filter technique, *Monthly Weather Review*, *126*, 796-811.

Hu, Z., Y. Chen, and S. Islam (1998), Multiscaling properties of soil moisture image and decomposition of large scale and small scale features using wavelet transform *International Journal of Remote Sensing*, *19*, 2451-2467.

Hu, Z. L., S. Islam, and Y. Z. Cheng (1997), Statistical characterization of remotely sensed soil moisture images, *Remote Sensing of Environment*, *61*, 310-318.

Ines, A. V. M., and P. Droogers (2002), Inverse modeling in estimating soil hydraulic functions: a genetic algorithm approach, *Hydrol Earth Syst Sci.*, *6*, 49-65.

Ines, A. V. M., and K. Honda (2005), On quantifying agricultural and water management practices from low spatial resolution RS data using genetic

algorithm: A numerical study for mixed-pixel environment, *Adv Water Resour*, *28*, 856-870.

Ines, A. V. M., and B. P. Mohanty (2006), Part 1. Near-surface soil moisture assimilation to quantify effective soil hydraulic properties using genetic algorithm: 1. Conceptual modeling, *Water Resources Research*, 44, doi:10.1029/2007WR005990.

Jackson, T. J., and T. J. Schmugge (1991), Vegetation effects on the microwave emission of soils, *Remote Sensing of Environment*, *36*, 203-212.

Jackson, T. J. (1993), Measuring surface soil moisture using passive microwave remote sensing, *Hydrol. Process*, *7*, 139-152.

Jackson, T. J., D. M. L. Vine, A. Y. Hsu, A. Oldak, P. J. Starks, C. T. Swift, J. D. Isham, and M. Haken (1999), Soil moisture mapping at regional scales using microwave radiometry: The Southern Great Plains Hydrology Experiment, *IEEE Transactions on Geoscience and Remote Sensing*, *37*, 2136-2151.

Jackson, T. J., R. Bindlish, A. J. Gasiewski, B. Stankov, M. Klein, E. G. Njoku, D. Bosch, T. L. Coleman, C. Laymon, and P. J. Starks (2005a), Polarimetric scanning radiometer C and X band microwave observations during SMEX03, *IEEE Transactions on Geoscience and Remote Sensing*, *43*, 2418-2430.

Jackson, T. J., R. Bindlish, A. J. Gasiewski, B. Stankov, M. Klein, E. G. Njoku, D. Bosch, T. L. Coleman, C. A. Laymon, and P. Starks (2005b), Polarimetric scanning radiometer C- and X-band microwave observations during SMEX03, *IEEE Transactions on Geoscience and Remote Sensing*, *43*, 2418-2430.

Jain, A. K., and R. C. Dubes (1988), *Algorithms for Clustering Data*, Prentice-Hall, Inc., Upper Saddle River, NJ.

Javaux, M., and M. Vanclooster (2006), Three-dimensional structure characterisation and modelling of transient fl ow in an undisturbed variably saturated heterogeneous monolith. , *J. Hydrol.*, *327*, 516-524.

Javaux, M., J. Vanderborght, R. Kasteel, and M. Vanclooster (2006), Three dimensional modeling of the scale- and flow rate-dependency of the dispersion in a heterogeneous unsaturated sandy monolith, *Vadose Zone Journal*, *5*, 515–528.

Kabat, P., R. W. A. Hutjes, and R. A. Feddes (1997), The scaling characteristics of soil parameters: From plot scale heterogeneity to subgrid parameterization, *J. Hydrol.*, *190*, 363-396.

Kalnay, E., M. Kanamitsu, R. Kistler, W. Collins, D. Deaven, L. Gandin, M. Iredell, S. Saha, G. White, J. Woollen, Y. Zhu, M. Chelliah, W. Ebisuzaki, W. Higgins, J. Janowiak, K. C. Mo, C. Ropelewski, J. Wang, A. Leetmaa, R. Reynolds, R. Jenne, and D. Joseph (1996), The NCEP/NCAR 40-year reanalysis project, *Am. Meteorol. Soc.*, *77*, 437-471.

Kavvas, M. L. (1999), On the coarse-graining of hydrological process with increasing scale, *J. Hydrol.*, *217*, 191-202.

Klute, A., and C. Dirksen (1986), Hydraulic conductivity and diffusivity: laboratory methods in *Methods of Soil Analysis*, 687-734 pp., American Society of Agronomy, Madison.

Kostov, K. G., and T. J. Jackson (1993), Estimating profile soil moisture from surface layer measurement- A review, *SPIE Proceedings*, *1941*, 125-136.

Kumar, P., and E. Foufoula-Georgiou (1993), A multicomponent decomposition of spatial rainfall fields 1. Segregation of large- and small-scale features using wavelet transforms, *Water Resources Research*, *29*, 2515-2532.

Kumar, P., and E. Foufoula-Georgiou (1997), Wavelet analysis for geophysical applications, *Reviews of Geophysics*, *35*, 385-412.

Leconte, R., F. Brissette, M. Galarneau, and J. Rousselle (2004), Mapping near-surface soil moisture with RADARSAT-1 synthetic aperture radar data, *Water Resources Research*, *40*, doi:10.1029/2003WR002312.

Leij, F. J., N. Romano, M. Palladino, M. G. Schaap, and A. Coppola (2004), Topographical attributes to predict soil hydraulic properties along a hillslope transect, *Water Resources Research*, *40*, doi:10.1029/2002WR001641.

Lewandowska, J., A. Szymkiewicz, K. Burzynski, and M. Vauclin (2004), Modeling of unsaturated water fl ow in double-porosity soils by the homogenization approach, *Water Resources Research*, *27*, 283–296.

Loague, K., and G. A. Gander (1990), R-5 Revisited .1. Spatial variability of infiltration on a small rangeland catchment, *Water Resources Research*, *26*, 957-971.

Loève, M. (1977), *Probability Theory*, 4 ed., Springer, Berlin.

Logsdon, S. D., and D. B. Jaynes (1996), Spatial variability of hydraulic conductivity in a cultivated field at different times, *Soil Sci Soc Am J*, *60*, 703-709.

Mantoglou, A. (1992), A theoretical approach for modeling unsaturated flow in spatially-variable soils - effective flow models in finite domains and nonstationarity, *Water Resources Research*, *28*, 251-267.

Margulis, S. A., D. McLaughlin, D. Entekhabi, and S. Dunne (2002), Land data assimilation and estimation of soil moisture using measurements from the Southern Great Plains 1997 Field Experiment, *Water Resources Research*, *38*, 1-18.

McBratney, A. B. (1998), Some considerations on methods for spatially aggregating and disaggregating soil information, *Nutr Cycl Agroecosys*, *50*, 51-62.

Meek, B. D., W. R. Detar, D. Rolph, E. R. Rechel, and L. M. Carter (1990), Infiltration-rate as affected by an alfalfa and no-till cotton cropping system, *Soil Sci. Soc. Am. J.*, *54*, 505-508.

Metropolis, N., and S. Ulam (1949), The Monte Carlo method, *J. Am. Stat. Assoc.*, *44*, 335-341.

Milly, P. C. D. (1988), Advances in modeling of water in the unsaturated zone, *Transp. Porous Media*, *3*, 491-514.

Mitchell, H. L., and P. L. Houtekamer (2000), An adaptive ensemble Kalman filter, *Monthly Weather Review*, *128*, 416-433.

Mohanty, B. P., R. S. Kanwar, and R. Horton (1991), A robust-resistant approach to interpret spatial-behavior of saturated hydraulic conductivity of a glacial till soil under no-tillage system, *Water Resources Research*, *27*, 2979-2992.

Mohanty, B. P., M. D. Ankeny, R. Horton, and R. S. Kanwar (1994), Spatial-analysis of hydraulic conductivity measured using disc infiltrometers, *Water Resources Research*, *30*, 2489-2498.

Mohanty, B. P., and R. S. Kanwar (1994), Spatial variability of residual nitrate-nitrogen under 2 tillage systems in central Iowa - a composite 3-dimensional resistant and exploratory approach, *Water Resources Research*, *30*, 237-251.

Mohanty, B. P., R. S. Kanwar, and C. J. Everts (1994), Comparison of saturated hydraulic conductivity measurement methods for a glacial-till soil, *Soil Sci. Soc. Am. J.*, *58*, 672-677.

Mohanty, B. P., J. S. Famiglietti, and T. H. Skaggs (2000), Evolution of soil moisture spatial structure in a mixed vegetation pixel during the Southern Great Plains 1997 (SGP97) Hydrology Experiment, *Water Resources Research*, *36*, 3675-3686.

Mohanty, B. P., and Z. Mousli (2000), Saturated hydraulic conductivity and soil water retention properties across a soil-slope transition, *Water Resources Research*, *36*, 3311-3324.

Mohanty, B. P., T. H. Skaggs, and J. S. Famiglietti (2000), Analysis and mapping of field-scale soil moisture variability using high-resolution, ground-based data during the Southern Great Plains 1997 (SGP97) Hydrology Experiment, *Water Resources Research*, *36*, 1023-1031.

Mohanty, B. P., and T. H. Skaggs (2001), Spatio-temporal evolution and time-stable characteristics of soil moisture within remote sensing footprints with varying soil, slope, and vegetation, *Adv Water Resour*, *24*, 1051-1067.

Monteith, J. L. (1965), Evaporation and environment, paper presented at the *Proceedings of the 19th Symposium of the Society for Experimental Biology*, New York.

Mualem, Y. (1976), A new model for predicting the hydraulic conductivity of unsaturated porous media, *Water Resources Research*, *12*, 513-522.

Muller, E., and H. Decamps (2001), Modeling soil moisture-reflectance, *Remote Sensing of Environment*, *76*, 173-180.

Nemes, A., M. G. Schaap, F. J. Leij, and J. H. M. Wosten (2001), Description of the unsaturated soil hydraulic database UNSODA version 2.0, *J Hydrol.*, *251*, 151-162.

Nielsen, D. R., J. W. Biggar, and K. T. Erh (1973), Spatial variability of field measured soil-water properties, *Hilgardia*, *42*, 215-259.

Njoku, E. G., and J. A. Kong (1977), Theory of passive microwave remote sensing of near-surface soil moisture, *J. Geophys.*, *82*, 3108-3118.

Njoku, E. G., and P. E. Oneill (1982), Multifrequency microwave radiometer measurements of soil-moisture, *IEEE Transactions on Geoscience and Remote Sensing*, *20*, 468-475.

Njoku, E. G., and D. Entekhabi (1995), Passive remote sensing of soil moisture, *J. Hydrol.*, *184*, 101-130.

Njoku, E. G., and L. Li (1999), Retrieval of land surface parameters using passive microwave measurements at 6 -18 GHz, *IEEE Transactions on Geoscience and Remote Sensing*, *37*, 79-93.

Njoku, E. G., W. J. Wilson, S. H. Yueh, S. J. Dinardo, F. K. Li, T. J. Jackson, V. Lakshmi, and J. Bolten (2002), Observations of soil moisture using a passive and active low-frequency microwave airborne sensor during SGP99, *IEEE Transactions on Geoscience and Remote Sensing*, *40*, 2659-2673.

Njoku, E. G., T. J. Jackson, V. Lakshmi, T. K. Chan, and S. V. Nghiem (2003), Soil moisture retrieval from AMSR-E, *IEEE Transactions on Geoscience and Remote Sensing*, *41*, 215-229.

Njoku, E. G., and S. K. Chan (2006), Vegetation and surface roughness effects on AMSR-E land observations, *Remote Sensing of Environment*, *100*, 190-199.

Nykanen, D. K., and E. Foufoula-Georgiou (2001), Soil moisture variability and scale-dependency of nonlinear parameterizations in coupled land-atmosphere models, *Adv Water Resour*, *24*, 1143-1157.

Oh, Y., K. Sarabandi, and F. T. Ulaby (1992), An empiral model and an inversion technique for radar scattering from bare soil surface, *IEEE Transactions on Geoscience and Remote Sensing*, *GE-30*, 370-381.

Oldak, A., Y. Pachepsky, T. J. Jackson, and W. J. Rawls (2002), Statistical properties of soil moisture images revisited, *J Hydrol.*, *255*, 12-24.

Pachepsky, Y., W. J. Rawls, and D. Gimenez (2001), Comparison of soil water retention at field and laboratory scales, *Soil Sci. Soc. Am. J.*, *65*, 460-462.

Paige, G. B., and D. Hillel (1993), Comparison of three methods for assessing soil hydraulic properties, *Soil Sci. Soc. Am. J.*, *155*, 175-189.

Paloscia, S., P. Pampaloni, L. Chairantini, P. Coppo, G. Gagliani, and G. Luzi (1993), Multifrequency passive microwave remote sensing of soil moistureand roughness, *International Journal of Remote Sensing*, *14*, 467-483.

Peck, A. J., R. J. Luxmoore, and J. L. Stolzy (1977), Effects of spatial variability of soil hydraulic properties in water budget modeling, *Water Resources Research*, *13*, 348-354.

Peters-Lidard, C. D., F. Pan, and E. F. Wood (2001), A re-examination of modeled and measured soil moisture spatial variability and its implications for land surface modeling, *Adv Water Resour*, *24*, 1069-1083.

Reichle, R. H., and R. D. Koster (2005), Global assimilation of satellite surface soil moisture retrievals into the NASA Catchment land surface model, *Geophysical Research Letters*, *32*, doi:10.1029/2004GL021700.

Reichle, R. H., R. D. Koster, J. R. Dong, and A. A. Berg (2004), Global soil moisture from satellite observations, land surface models, and ground data: Implications for data assimilation, *Journal of Hydrometeorology*, *5*, 430-442.

Reichle, R. H., D. B. McLaughlin, and D. Entekhabi (2002), Hydrologic data assimilation with the ensemble Kalman filter, *Monthly Weather Review*, *130*, 103-114.

Rodriguez-Iturbe, I., G. K. Vogel, R. Rigon, D. Entekhabi, F. Castelli, and A. Rinaldo (1995), On the spatial organization of soil moisture fields, *Geophysical Research Letters*, *106*, 2757-2760.

Roth, K. H., H. J. Vogel, and R. Kasteel (1999), The scaleway: a conceptual framework for upscaling soil properties, in *Modeling of Transport Process in Soil at Various Scales in Time and Space*, edited by J. Feyen and K. Wiyo, pp. 477-490, Wageningen Pers, Wageningen, The Netherlands.

Ryu, D., and J. S. Famiglietti (2005), Characterization of footprint-scale surface soil moisture variability using Gaussian and beta distribution functions during the Southern Great Plains 1997 (SGP97) hydrology experiment, *Water Resources Research*, *41*, W12433, doi:10.1029/2004WR003835.

Schmugge, T. J., P. Gloersen, and T. Wilheit (1974), Remote sensing of soil moisture with microwave radiometers, *Journal of Geophysical Research*, *79*, 317-323.

Schmugge, T. J., T. J. Jackson, and H. L. McKim (1980), Survey of methods for soil moisture determination, *Water Resour. Bull.*, *16*, 961–979.

Schmugge, T. J., J. M. Meeneely, A. Rango, and R. Neff (1977), Satellite microwave observations of soil moisture variations, *Water Resour. Bull.*, *13*, 265–286.

Schumullius, C., and R. Furrer (1992), Frequency dependence of radar backscattering under different moisture condition of vegetation covered soil, *International Journal of Remote Sensing*, *13*, 2233-2245.

Sellers, P. J., M. D. Heiser, F. G. Hall, S. J. Goetz, D. E. Strebel, S. B. Verma, R. L. Desjardins, P. M. Schuepp, and J. I. MacPherson (1995), Effects of spatial

variability in topography, vegetation cover and soil moisture on area-averaged surface fluxes. A case study using FIFE 1989 data, *Journal of Geophysical Research*, *100*, 25607-25629.

Seo, D.-J., and J. P. Breidenbach (2002), Real-time correction of spatially nonuniform bias in radar rainfall data using rain gauge measurements, *Journal of Hydrometeorology*, *3*, 93–111

Seyfried, M. S., and B. P. Wilcox (1995), Scale and the nature of spatial variability: field examples having implications for hydrological modeling, *Water Resources Research*, *31*, 173-184.

Shannon, C. E. (1948), C.E. Shannon, A mathematical theory of communication, *The Bell System Technical Journal XXVII*, 379–423.

Sharma, M. L., R. J. W. Barron, and M. S. Fernie (1987), Aerial distribution of infiltration parameters and some soil physical-properties in lateritic catchments, *J Hydrol.*, *94*, 109-127.

Sharma, S. K., B. P. Mohanty, and J. Zhu (2006), Including topography and vegetation attributes for developing pedo transfer functions in Southern Great Plains of USA, *Soil Sci. Soc. Am. J.*, *70*, 1430-1440.

Shih, S. F., and J. D. Jordan (1993), Use of Landsat thermal-IR data and GIS in soil-moisture assessment, *Journal of Irrigation and Drainage Engineering-ASCE*, *119*, 868-879.

Silverman, B. W. (1981), Using kernel density estimate to investigate multimodality, *Journal of the Royal Statistical Society, Series-B*, *43*, 97-99.

Simunek, J., K. Huang, and M. T. van Genuchten (1995), The SWMS_3D code for simulating water flow and solute transport in three-dimensional variably-saturated media. Version 1.0. *Research Report no. 139*, U.S. Salinity Laboratory, ARS. USDA-ARS, Riverside, CA.

Smajstrla, A. G. (1990), Agricultural field scale irrigation requirements simulation (AFSIRS) model, *Technical Manual*, University of Florida, Gainesville.

Smith, R. E., and B. Diekkruger (1996), Effective soil water characteristics and ensemble soil water profiles in heterogeneous soils, *Water Resources Research*, *32*, 1993-2002.

Tansly, K. J., and A. C. Millington (2001), Investigating the potential for soil moisture and surface roughness monitoring in dry lands using ERS SAR data, *International Journal of Remote Sensing*, *22*, 2129-2149.

Texier, D., N. d. Noblet, S. P. Harrison, A. Haxeltine, D. Jolly, S. Joussaume, F. Laarif, I. C. Prentice, and P. Tarasov (1997), Quantifying the role of biosphere-atmosphere feedbacks in climate change: Coupled model simulations for 6000 years BP and comparison with paleodata for northern Eurasia and northern Africa, *Clim. Dyn.*, *13*, 865-882.

Tomer, M. D., C. A. Cambardella, D. E. James, and T. B. Moorman (2006), Surface-soil properties and water contents across two watersheds with contrasting tillage histories., *Soil Sci. Soc. Am. J.*, *70*, 620-630.

Ulaby, F. T., P. C. Dubois, and J. van Zyl (1996), Radar mapping of surface soil moisture, *J Hydrol.*, *184*, 57-84.

Ulaby, F. T., R. K. Moore, and A. K. Fung (1986), *Microwave Remote Sensing Active and Passive*, Artech House, Inc., Norwood, MA.

Ulaby, F. T., and E. A. Wilson (1985), Microwave attenuation properties of vegetation canopies, *IEEE Transactions on Geoscience and Remote Sensing*, *23*, 746-753.

Vachaud, G., A. P. De Silans, P. Balabanis, and M. Vauclin (1985), Temporal stability of spatially measured soil water probability density function, *Soil Sci. Soc. Am. J.*, *49*, 822-828.

Van Dam, J. C. (2000), *Field-Scale Water Flow and Solute Transport. SWAP Model Concepts, Parameter Estimation and Case Studies*, Wageningen University, The Netherlands.

Van Dam, J. C., J. Huygen, J. G. Wesseling, R. A. Feddes, P. Kabat, and P. E. V. Van Waslum (1997), Theory of SWAP version 2.0: Simulation of water and plant growth in the soil–water–atmosphere–plant environment., *Technical Document 45*, Wageningen Agricultural University and DLO Winand Staring Centre, The Netherlands.

van Genuchten, M. T. (1980), A closed-form equation for predicting the hydraulic conductivity of unsaturated soils, *Soil Sci. Soc. Am. J.*, *44*, 892-898.

Wager, M. G., and H. P. Denton (1989), Influence of crop and wheel traffic on soil physical properties in continuous no till corn, *Soil Sci. Soc. Am. J.*, *53*, 1206-1210.

Wang, J. R. (1980), The dielectric properties of soil-water mixtures at microwave frequencies, *Radio Sci.*, *15*, 977-985.

Wang, J. R., and B. J. Choudhury (1995), Passive microwave radiation from soil: examples of emission models and observations, in *Passive Microwave Remote Sensing of Land-Atmosphere Interactions*, edited by B. J. Choudhury, et al., pp. 423-460, VSP, Utrechts, The Netherlands.

Wang, J. R., and T. J. Schmugge (1980), An empirical model for the complex dielectric permittivity of soil as a function of water content, *IEEE Transactions on Geoscience and Remote Sensing*, *GE-18*, 288-295.

Wang, J. S. Y., and T. N. Narasimhan (1992), *Distribution and Correlations of Hydrologic Parameters of Rocks and Soils*, University of California, Riverside.

Warrick, A. W., and D. R. Nielsen (1980), *Spatial Variability of Soil Physical Properties in the Field*, Academic Press, New York.

Wesseling, J. G., and J. G. Kroes (1998), *A Global Sensitivity Analysis of the Model SWAP*, DLO Winand Staring Centre, Wageningen, The Netherlands.

Western, A. W., R. B. Grayson, and G. Blöschl (2002), Scaling of soil moisture: A hydrologic perspective, *Annual. Review Earth Planet Sciences*, *30*, 149-180.

Whitaker, J. S., and T. M. Hamill (2002), Ensemble data assimilation without perturbed observations, *Monthly Weather Review*, *130*, 1913-1924.

Wierenga, P. J. (1985), Spatial variability of soil water properties in irrigated soils, pp. 112-129, Proceedings of a Workshop of the ISSS and the SSSA, Las Vegas, NV.

Yeakley, J. A., W. T. Swank, L. W. Swift, G. M. Hornberger, and H. H. Shugart (1998), Soil moisture gradients and controls on a southern Appalachian hillslope from drought through recharge, *Hydrology and Earth System Sciences*, *2*, 41-49.

Zhan, X., P. Houser, J. P. Walker, and W. Crow (In press), A method for retrieving high-resolution surface soil moisture from hydros L-band radiometer and radar observations, *IEEE Transactions on Geoscience and Remote Sensing*, *44*, 1534-1544.

Zhang, D. X. (1999), Nonstationary stochastic analysis of the transient unsaturated flow in randomly heterogeneous media, Water Resources Research, *35*, 1127-1141.

Zhu, J., and B. P. Mohanty (2002), Spatial averaging of van Genuchten hydraulic parameters for steady-state flow in heterogeneous soils: a numerical study, *Vadose Zone Journal*, *1*, 261-272.

Zhu, J., and B. P. Mohanty (2003), Upscaling of hydraulic properties of heterogeneous soils, in *Scaling Methods in Soil Physics*, edited by Y. A. Pachepsky, et al., pp. 97-118, CRC Press, Boca Raton, FL.

VITA

Name:	Narendra Narayan Das
Address:	BAEN, Scoates Hall, TAMU-2117, Texas A&M University College Station, Tx-77843, USA
Email Address:	nndas@yahoo.com
Education:	B.En., Chemical Engineering, National Institute of Technology, Raipur, India (formerly: GEC Raipur), 1992
	M.S., Biological and Agricultural Engineering, Texas A&M University, 2005
	Ph.D., Biological and Agricultural Engineering, Texas A&M University, 2008